Thermal Cycling Creep of a Fiber Reinforced Aluminum Alloy

Von der Fakultät Chemie der Universität Stuttgart
zur Erlangung der Würde eines Doktors der Naturwissenschaften (Dr. rer. nat.)
genehmigte Abhandlung

Vorgelegt von

Alexander Flaig

aus Göppingen

Hauptberichter:	Prof. Dr. phil. E. Arzt
Mitberichter:	Prof. Dr. rer. nat. F. Aldinger
Tag der mündlichen Prüfung:	27.09.2000

Institut für Metallkunde der Universität Stuttgart
und Max-Planck-Institut für Metallforschung

Stuttgart 2000

Abstract

In the present work, the creep behavior of a metal-matrix-composite was investigated under thermal cycling creep conditions. The material was an eutectic Al-Si matrix that had been reinforced with 15 vol.% of discontinuous alumina fibers.

Advanced high-temperature mechanical testing techniques were used together with specifically designed testing procedures to measure the stress dependent rate of deformation during thermal cycles. The influence of the maximum temperature, of the thermal amplitude, of high-temperature dwell times, of the sign of loading and of the reinforcement orientation were especially studied.

At low stresses, a creep acceleration compared to isothermal conditions was found and the apparent stress exponent decreased to low values. The material showed pronounced transitional behavior upon load changes. An analysis of the strain evolution in individual cycles showed evidence of substantial inelastic deformation which was for the biggest part compensated between half-cycles.

A simple continuum mechanical model was set up which approximated the investigated composite by a stack of two tightly bonded and homogeneously deforming slabs. The model was used to predict the creep rates and the in-cycle strain evolution on the basis of calculated internal stresses under thermal cycling creep conditions. The experimental observations were interpreted and discussed in comparison to the simulation results. The observed phenomena could be explained on the basis of the model.

The material showed pronounced transitional behavior on loading and unloading. This transient creep and the overall envelope shape of the thermal cycling creep curve was further investigated with stress cycling creep experiments. The phenomenon of back-creep was utilized to investigate effects of load transfer from the matrix to the fibers and to conclude on the overall evolution of the composite strain rate.

Kurzfassung

In der vorliegenden Arbeit wurde das Kriechverhalten eines Metall-Matrix-Verbundwerkstoffes unter thermozyklischen Bedingungen untersucht. Bei dem Verbundwerkstoff handelt es sich um eine eutektische Al-Si Legierung, die mit 15 Vol.% diskontinuierlicher Aluminiumoxid-Fasern verstärkt wurde.

Fortgeschrittene Methoden der mechanischen Hochtemperaturprüfung wurden verwendet, um in speziell angepassten Versuchsabläufen die spannungsabhängige Verformungsrate während der thermischen Zyklen zu messen. Speziell untersucht wurden die Einflüsse der Maximaltemperatur, der thermischen Amplitude, von Haltezeiten bei hoher Temperatur, des Vorzeichens der Belastung und der Orientierung der Verstärkung untersucht.

Bei geringen Spannungen wurde im Vergleich zu isothermen Bedingungen eine Beschleunigung des Kriechens gefunden und der beobachtete Spannungsexponent sank auf kleine Werte. Eine genaue Analyse der Dehnungsentwicklung in einzelnen Zyklen lieferte Belege für das Vorhandensein beträchtlicher inelastischer Dehnungen, die sich von Halbzyklus zu Halbzyklus gegenseitig größtenteils kompensierten.

Ein einfaches kontinuumsmechanisches Modell wurde aufgestellt, das den untersuchten Verbundwerkstoff durch zwei aufeinander gestapelte, fest miteinander verbundene und sich homogen verformende Platten annäherte. Das Modell wurde verwendet, um auf Basis von berechneten inneren Spannungen die Kriechraten und die innerzyklische Dehnungsentwicklung unter thermozyklischen Bedingungen zu erklären und vorherzusagen. Die experimentell gemachten Beobachtungen wurden im Vergleich zu den Simulationsergebnissen interpretiert und diskutiert. Die beobachteten Phänomene konnten auf Basis des Modells erklärt werden.

Das Material zeigte ein ausgeprägtes Übergangsverhalten beim Be- und Entlasten. Dieses Übergangskriechen und der gesamte Verlauf der Einhüllenden der thermozyklischen Kriechkurve wurde mit Hilfe von spannungszyklischen Kriechexperimenten näher untersucht. Das Phänomen des Rückwärts-Kriechens nach äußerer Entlastung wurde ausgenutzt, um Effekte der Last-Übertragung von der Matrix auf die Fasern zu untersuchen und um auf die Entwicklung der Dehnrate eines Verbundwerkstoffes zurückzuschließen.

Preface

This dissertation is an account of work which has been carried out at the “Max-Planck-Institut für Metallforschung” in Stuttgart, Germany, and at the “Institut für Metallkunde” of the University of Stuttgart under the supervision of Prof. Dr. Eduard Arzt between January 1995 and December 1999.

I would like to thank Prof. Dr. Eduard Arzt for giving me the opportunity to carry out this work parallel to my obligations as a teaching assistant at his Institute and for granting me great freedom in the choice and treatment of the topic.

I would also like to thank Prof. Dr. Fritz Aldinger for kindly taking on the task of secondary examiner for this work.

I am greatly indebted to Dr. Alexander Wanner for his enduring interest in this work and for his seemingly unlimited patience. The numerous stimulating discussions with him were the source of many ideas which now make up a substantial part of this work.

Table of Contents

List of Symbols and Abbreviations

Composite Nomenclature

Basically, composite nomenclature follows the simple denotation “chemical matrix symbol” / “chemical reinforcement symbol”. The matrix material can be further qualified by anteposition of “hp” (for “high purity”) or “cp” (for commercial purity) or by appending an alloy index number. The reinforcement symbol is often preceded by the specification of the weight or volume content. A subscript after the reinforcement symbol denotes the reinforcement morphology: “*p*” = particles, “*platelets*” = platelets, “*w*” = whiskers, “*f*” = fibers, “*DS*” = directionally solidified eutectic. If necessary, the production route is also given in brackets placed behind the composite denotation: “(PM)” indicates production on a powder metallurgical route, “(cast)” means production by casting.

Examples:

Al 6061 / 20 vol.% SiC_w (PM)	aluminum 6061 alloy, reinforced by silicon carbide whiskers with a volume fraction of 20 percent. Production by powder metallurgical processing.
cp Al / 15 vol.% Al_2O_{3f} (cast)	aluminum of commercial purity, reinforced by alumina fibers with a volume fraction of 15 percent. The composite was made by casting.

Abbreviations

MMC	Metal Matrix Composite
TCC	Thermal Cycling Creep
CCA	Cyclic Creep Acceleration
CCR	Cyclic Creep Retardation
TECS	Thermoelastic Coefficient of Stress
CTE	Coefficient of Thermal Expansion
SEM	Scanning Electron Microscopy
VP-SEM	SEM with variable pressure
BS	Back Scattered Electrons
SE	Secondary Electrons
TEM	Transmission Electron Microscopy
ODF	Orientation Distribution Function

WHZ	Work Hardened Zone
MISP	Mismatch Induced Superplasticity

Symbols

α	Coefficient of thermal expansion CTE [1/K] (physical)
α_{inst}	Instantaneous CTE [1/K] (physical)
α_{20}	Technical CTE [1/K] with respect to room temperature
a	Time exponent, used for describing primary creep
a, b	Major and minor radii of fiber section ellipses [µm]
a_{ij}	Fiber orientation tensor
A	Power-law creep pre-exponential factor [$MPa^{-n} \cdot s^{-1}$]
A*, A’	Proportionality factors for primary creep laws
B	Factor in the power-law creep equation containing the thermal activation term and the pre-exponential factor [$MPa^{-n} \cdot s^{-1}$]
C_c, C_m, C_r	Stiffness tensors of composite, matrix and reinforcement
d	Average fiber thickness [µm]
D_{act}	Thermal activation term
E	Young’s modulus
ε	Strain. All strains are given as true strains unless indicated otherwise
ε^{anel}	Anelastic strain
ε^{c}	Creep strain
ε^{el}	Elastic strain
ε^{eq}	Equivalent strain
ε_{frac}	Fracture strain
ε^{inel}	Inelastic strain
ε_{init}	Strain after initial heat treatment
ε_{l}	Total strain that has accumulated since application of a thermal or mechanical load (including elastic, anelastic, thermal and inelastic strain). In experiments with repeatedly applied load: strain since first application of load.
ε_{pc}	Strain increment in a complete thermal cycle
ε^{pl}	Plastic strain

ε_{prim}	Strain in the primary creep regime
ε_t	Technical strain
$\varepsilon_{\ to\ min.}$	Strain to minimum strain rate (strain at which the primary creep transient ends)
$\Delta\varepsilon_f$, $\Delta\varepsilon_b$	Forward and backward creep strain in cyclic creep testing
$\dot{\varepsilon}$	Strain rate [1/s]
$\dot{\varepsilon}_{SS}$	Steady state creep rate [1/s]
θ	Inclination angle about a plane normal [deg, rad]
ϕ	In plane rotation angle [deg, rad]
ϑ	Inclination towards a horizontal line [deg, rad]
f_m, f_r	Volume fraction of matrix/reinforcement
f_{Scale}	Scaling factor
F_n	Weighting function for cutting of inclined fibers
I	Identitiy Matrix
I_1, I_3	Constants used in the definition of Eshelby Tensors (according to Brown and Clarke (1975))
k	Calibration factor for strain measurements
k_E	Ratio of reinforcement and matrix elastic moduli
L	Average fiber length [µm]
L_0	Specimen (extensometer) gage length [mm]
λ_{ij}	Transformation matrix
n	Stress exponent in power-law creep
ν	Poisson's ratio
p_1, p_2, p_3	Unit vector components
P, Q, R	Constants used in the definition of Eshelby Tensors (according to Brown and Clarke (1975))
Q_{app}	Apparent activation energy
R	Gas Constant [J/(K·mol)]
R_a	Arithmetic average roughness [µm]
$R_{p0.1}$, $R_{p0.2}$	0.1% and 0.2% yield stress

s, s_e	Fiber aspect ratio, section ellipse aspect ratio
σ	Stress [MPa]
σ_A	Externally applied stress tensor
σ^{eq}	Von-Mises equivalent stress [MPa]
$\langle\sigma\rangle_p$	Volume-averaged stress tensor in phase p [MPa]
σ_y	Uniaxial yield stress [MPa]
S	Eshelby Tensor
t	Time [s]
t_c	Duration of a thermal cycle
t_l	Time at load.
T	Temperature [K]
T_{eq}	Equivalent temperature. Average temperature of a thermal cycle, weigthed for the diffusion coefficient [°C]
T_{esf}	Effective stress-free temperature. Temperature in a thermal cycle, where the volume averaged matrix and reinforcement stresses are zero [°C]
T_{min}, T_{max},	Minimum and maximum temperature of a thermal cycle [°C]
ΔT	Amplitude of a thermal cycle (T_{max}-T_{min}) [K]
ΔT_c	Critical thermal cycle amplitude to induce matrix plasticity [K]
$\Delta V/V$	Phase transformation strain
x, y, z	Global coordinate system used to describe specimen orientation
x', y', z'	Local coordinate system
ψ	Probability distribution function of orientation

Subscripts

i (1, 2, 3)	Orientation index indicating principal direction
p (c, m, r)	Phase index referring to *composite, matrix, reinforcement*

1 Introduction

Metals and alloys are reinforced with stiff phases to improve their performance but sometimes this introduces unwanted weaknesses. An example is the sensitivity of metal matrix composites (MMCs) to changing temperatures. This is brought about by the differences in the thermal expansion coefficients of the metallic matrix and the ceramic reinforcement, which cause an internal strain mismatch when the temperature is varied. This strain mismatch can give rise to large internal stresses. When the temperature is cycled, these stresses are continually regenerated and this can enhance the creep deformation of MMCs. This phenomenon has been termed “thermal cycling creep” (TCC) and has been subject of research for many years.

The acceleration of deformation is especially pronounced when the cyclically induced stresses become substantially larger than the applied stresses. Under such conditions the thermal cycling creep rates become proportional to the applied stress i.e. the apparent stress exponent approaches unity. The high amount of strain rate sensitivity can give rise to superplastic deformability. Another consequence of thermal cycling under such conditions is that the TCC curves exhibit no transitional behavior. Such behavior has been observed in the past in many investigations for a variety of different MMCs. It seems, however, that in many cases the investigated material combinations and the test conditions were chosen such that a particularly high creep enhancement could be observed. Almost all findings and interpretations therefore originate from investigations of idealized materials or even model materials. TCC behavior of metal matrix composites has been investigated theoretically using continuum theory as well as micromechanical modeling and the fundamental phenomenology of thermal cycling creep acceleration has been successfully explained by these models.

The composite behavior under thermal cycling conditions is not only of great academic interest. Aluminum based MMCs, for example, have already found application in automotive engine environments where thermal cycling is definitely an issue. In this work, the TCC-behavior of a technical aluminum alloy, reinforced with discontinuous alumina fibers, has been widely investigated. This composite system is one of the very few series applications of short fiber reinforced metals. The material is used as local reinforcement in diesel engine pistons and there it is subjected to both mechanical and thermal cyclic loads.

One of the aims of the present work is to test the performance of the material under thermal cycling conditions that are close to use conditions. Furthermore it is to be investigated which aspects of the present knowledge on thermal cycling creep can be recognized in the present technical material and, if necessary, the present understanding of TCC is to be refined and extended.

2 Literature

When materials have to be optimized for a structural application, it is usually strength and/or stiffness that is to be improved. Reinforcing a material with a stiffer second phase has proved to be an effective way to do so. The underlying concept is the principle of load sharing. An applied external load is distributed amongst the phases of a composite according to their elastic and plastic properties and the volume fraction, the shape and the orientation of the reinforcement. In composites with metallic or polymer matrices, low-strength phases are reinforced by high-stiffness phases, because the stiffer phase does not only raise the stiffness of the composite, but also reduces the average stress in the matrix effectively.

This load-partitioning between the components of a composite frequently changes the basic phenomenology of the material's response to an applied stress, as compared to single-phase materials. Especially for plastic deformation or under creep and/or thermal cycling conditions, metal matrix composites can behave quite differently than unreinforced metals. The key to the understanding of these differences lies in understanding the evolution of stress in the metallic matrix phase. In the following, some basic textbook knowledge related to the internal stresses in MMCs is briefly revisited. This knowledge is required to understand the literature concerning the isothermal creep and thermal cycling creep properties of MMCs which is reviewed afterwards.

2.1 Stresses in MMCs

Stresses in materials arise when they are subjected to a strain or when a spontaneous strain is impeded.

2.1.1 Origin

In composites, the straining of one phase can be impeded by the other. When two well-bonded phases are strained by different amounts, the mismatch in strain causes stresses in each phase. In this work, three different types of strain are distinguished: elastic, thermal, and inelastic strain. Each type of strain can cause strain mismatch between the phases and thus can give rise to internal stresses.

Elastic Strain Mismatch

Under external load, the individual phases are strained according to their individual stiffnesses. If they have different stiffness, the tight bonding causes a strain mismatch. The volume averaged stresses in the stiffer phase (reinforcement) will be higher than the externally applied stress, while the more compliant phase will experience a lower average stress. As long

as no inelastic strains are involved, the amount of load transfer is proportional to the applied load. The proportionality constant depends, amongst other things, on the difference between the elastic constants of the constituents and their volume fraction. Higher stiffness differences and high reinforcement volume fraction lead to higher reductions in the matrix stress.

Thermal Strain Mismatch

The matrix and the reinforcing phase of an MMC usually have different coefficients of thermal expansion (CTE). Changing the temperature will thus cause a strain mismatch between them. When no inelastic strains are involved, then the induced stresses are proportional to the change in temperature. The proportionality constant will be called *thermoelastic coefficient of stress*. It is the first differential of stress σ_p in the phase p with respect to temperature T for purely elastic deformation: $d\sigma_p/dT\big|_{elastic}$. The abbreviation *"TECS"* will also be used frequently. This coefficient is proportional to the difference in CTEs, $\Delta\alpha$, and again to the elastic properties and the volume fraction of the phases. It also depends on the reinforcement morphology and its orientation distribution.

In MMCs the CTE of the matrix phase is usually larger than that of the reinforcement. As a consequence, the thermoelastic coefficient of stress for the matrix is negative. This means that cooling increases the matrix stress, while heating decreases it. When a composite is cooled from production temperature, where the strain misfit is zero, to room temperature, the matrix will experience tensile stresses.

Inelastic Strain Mismatch

In MMCs, the matrix can undergo creep or time-independent plastic strain. A stiff reinforcement, which is tightly bonded to the matrix has to make up the misfit strain by straining elastically and so its stress changes. Inelastic deformation of the matrix thus results also in load transfer from the matrix to the reinforcement.

Stress Relaxation

The above mentioned sources of strain mismatch often give rise to high stresses in the reinforcement. The stored elastic strain energy provides a driving force for relaxation of these stresses. This can happen by a series of mechanisms that have in common that they help to decrease the strain misfit between the matrix and the reinforcement. Such processes are reinforcement-fracture (Brechet et al. (1991), Llorca (1995), Favier et al. (1995)), reinforcement-matrix debonding (Favier et al. (1995)), matrix cavitation (Whitehouse and Clyne (1993)), reinforcement relaxation by interface diffusion (Rösler et al. (1991), Sato and Kuribayashi (1993)) or any inelastic matrix deformation (creep, plasticity, interfacial diffusion, recrystallization).

2.1.2 Mathematical Treatment

Stresses in MMCs can be calculated by considering the misfit strains in the composite. A relatively widespread method to do so is the so-called Eshelby method. It is based on the insight that an ellipsoidal elastic inclusion in an infinite matrix has a uniform state of stress at all points within it. Eshelby (1957) developed a technique to represent an actual inclusion by an inclusion made of the matrix material (an "equivalent homogeneous inclusion") with a certain misfit strain (the "equivalent transformation strain") and an identical stress. An excellent review of the method and its application to composites has been given by Withers et al. (1989). A well comprehensible introduction to the topic can be found in the book by Clyne and Withers (1993). The method is strictly valid only for ellipsoidal inclusions in an infinite matrix and for purely elastically accommodated misfit. For non-dilute systems, the matrix is approximated by an effective medium in a so-called "mean-field"-approach. This elegant mathematical trick leads to lower bound estimates of the composite properties (Pedersen (1983)).

The Eshelby method with the mean-field approach leads to the following equation for the composite stiffness tensor C_c and the composite CTE tensor α_c (Clyne and Withers (1993)):

$$C_c = \left[C_m^{-1} - f_r \cdot \{(C_m - C_r)\cdot[S - f_r(S-I)] - C_m\}^{-1} \cdot (C_m - C_r)\cdot C_m^{-1}\right]^{-1} \qquad \textbf{(2-1)}$$

$$\alpha_c = \alpha_m - f_r \cdot \{(C_m - C_r)\cdot[S - f_r(S-I)] - C_m\}^{-1} C_r(\alpha_r - \alpha_m), \qquad \textbf{(2-2)}$$

Here, C_m and C_r are the stiffness tensors of the matrix and the reinforcement, respectively, f_r is the volume fraction of reinforcement and I is the identity matrix. S is the Eshelby-tensor, which is a fourth-rank tensor that relates the constrained strain (tensor) of an elastically homogeneous ellipsoidal inclusion to the inclusion's unconstrained transformation strain (tensor). It represents the shape and the orientation of the inclusions and depends on the reinforcement geometry and the Poisson's ratio of the matrix. α_m and α_r are the thermal expansion tensors of the matrix and the reinforcement.

The amount of the volume averaged mean matrix stress $\langle\sigma\rangle_m$ due to an external load as well as the thermoelastic coefficient of stress $d\langle\sigma\rangle_m/dT$ can also be easily derived from the equations that are given by Clyne and Withers (1993):

$$\langle\sigma\rangle_m = \left(f_r \cdot C_m \cdot (S-I)\cdot\{(C_m - C_r)\cdot[S - f_r(S-I)] - C_m\}^{-1}\cdot(C_m - C_r)\cdot C_m{}^{-1} + 1\right)\cdot\sigma_A \qquad \textbf{(2-3)}$$

and

$$\frac{d\langle\sigma\rangle_m}{dT} = f_r \cdot C_m \cdot (S-I)\cdot\{(C_m - C_r)\cdot[S - f_r(S-I)] - C_m\}^{-1}\cdot C_r\cdot(\alpha_r - \alpha_m), \qquad \textbf{(2-4)}$$

where σ_A is the applied stress tensor and T is the temperature. The misfit-generating "transformation strains" can be added up so that the combined effects of an external load and a thermally induced misfit (due to ΔT) on the mean matrix stress can also be calculated:

$$\langle \sigma \rangle_m = f_r \cdot C_m \cdot (S - I) \cdot \{(C_m - C_r) \cdot [S - f_r (S - I)] - C_m\}^{-1} \cdot \left[C_r \cdot (\alpha_r - \alpha_m) \cdot \Delta T + (C_m - C_r) \cdot C_m^{-1} \cdot \sigma_A + \sigma_A \right] \quad \textit{(2-5)}$$

The components of the Eshelby tensor S can be found in textbooks (e.g. Clyne and Withers (1993) or Mura (1987)) for various aligned reinforcements of certain geometry (spheres, oblate and prolate spheroids, fibers, plates). Averaged Eshelby tensors have been calculated for reinforcements that are not aligned but have certain special orientation distributions. Johannesson and Ogin (1995) have calculated an average Eshelby tensor for fibrous reinforcements in a 2D-planar arrangement (see Appendix A.1). Johannesson and Pedersen (1998) have extended this averaging routine with the aid of a computer algebra program to arbitrary transversely isotropic orientation distributions (see Appendix A.2).

2.1.3 Measurement of Internal Stresses

Stresses cannot be measured directly. What can be measured is elastic strain. Internal elastic strains in metals are usually measured by diffraction techniques. The underlying principle is based on the distortions of the crystal lattice that cause (Bragg) diffraction peaks to shift in the spectrum. From these peak-shifts, one can deduce the elastic strains and possibly the stresses. The principle and its application to various materials is extensively reviewed in the book by Noyan and Cohen (1987).

Diffraction techniques have been used extensively to measure internal stresses in MMCs. Conventional X-ray diffraction at room temperature is relatively widespread. A survey of internal stress measurements on aluminum based MMCs has been given by Ericsson et al. (1993). Since then, X-ray diffraction has also been applied for measurements at high temperatures (e.g. Weiland and Johannesson (1995), Weiland et al. (1998)) and during thermal cycling (e,g, Weiland and Ericsson (1995), Li et al. (1998)). A basic drawback of the technique is that it provides only near-surface information due to the limited penetration depth of the X-rays. Thermal neutrons do not have this drawback because they exhibit a much higher penetration depth. Therefore neutron diffraction techniques have been used by various groups to measure the mean lattice strains in the bulk of MMCs during room temperature deformation (e.g. Allen et al. (1992), and to measure thermally induced stresses at rising temperatures (e.g. Majumdar et al. (1991), Ceretti et al. (1994)) and during thermal cycling (Withers et al. (1987)). The major drawback of neutron diffraction is the low flux of the sources, which makes measuring times very long (on the order of hours) and thus unsuitable for the investigations of dynamic processes. In the case of thermal cycling, this has been

overcome by applying a stroboscopic technique which measures lattice strains at various points in a thermal cycle, averaged over many cycles (Daymond and Withers (1997)). More recently, synchrotron X-rays with high energy and flux have become available with new third-generation synchrotron facilities. Those X-rays have been employed to study internal strain evolutions at short measuring times without the need of a stroboscopic technique (Daymond and Withers (1996)). It seems obvious that this technique will be exploited further in the future to study dynamic processes in MMCs.

From the survey of the diffraction studies on aluminum based MMCs by Ericsson et al. (1993), it is apparent that the bulk of the internal stress measurements have been made on Al-matrix composites reinforced with SiC particles and whiskers. This trend has continued to the present date. This is probably due to the high modulus and CTE mismatch between the aluminum matrix and silicon carbide reinforcement that give rise to large, well measurable misfit strains. Moreover, the SiC phase is usually single crystalline cubic and therefore also well suited for lattice strain determination.

A general problem with diffraction techniques is that absolute stresses can only be determined when the unstrained lattice parameter d_0 is also measured with sufficient accuracy. This is a tedious, often impossible task. Therefore, most diffraction results are only presented in terms of the evolution of (relative) internal strains, without calculating stresses from them.

2.2 Isothermal Creep of MMCs

A short fiber reinforcement usually increases the creep strength of metals and alloys. The reason for this is the above mentioned load transfer from a deforming matrix to the stiff reinforcement (for a review see Clyne and Withers (1993)). This load transfer reduces the effective stress in the matrix progressively, so that the creep rate decreases continuously. For continuously reinforced MMCs, this process may go on until, at infinite time, all the load is borne by the reinforcement. MMCs with short fibers, however, usually exhibit a steady state creep regime. This can be thought of as a dynamic equilibrium between load transfer to the fibers and stress relaxation processes (damaging or non-damaging) that unload the fibers (see 2.1.1). Alternatively, one can think about part of the matrix creep strain occurring without introducing additional strain misfit (e.g. flow around fiber ends). A steady state is then reached when the matrix stress is such that the rate of creep that induces misfit assumes the same values as the rate of creep that induces no misfit become equal. The initial transient creep is thus a “built-in” feature of such composites, irrespective of whether the creeping phase shows primary creep or not.

Due to the potential application of MMCs at elevated temperatures, many investigations on the isothermal creep of a wide variety of composite materials have been published. In their

book *"An Introduction to Metal Matrix Composites"*, Clyne and Withers (1993) give a short review of experimental data and theoretical models for creep of MMCs.

In the following, at first the phenomenology of MMC creep, simple models and considerations of the influence of primary creep will be briefly reviewed. A more detailed review, which will be given afterwards, is confined to those publications that have focused on creep in composite systems that are similar to the one used in this work, i.e. aluminum-based alloys, reinforced with discontinuous alumina fibers (Al/Al_2O_{3f}). The present understanding of the creep of discontinuously reinforced MMCs will be critically summarized at the end of this chapter in Section 2.5.

2.2.1 General Findings and Basic Models

Most experimental creep investigations of fibrous composites have the following in common: 1) The composite creep strength is higher than that of the unreinforced matrix. 2) The stress exponent for power-law creep and the thermal activation are higher for the reinforced material.

The first point is not surprising, given that effective load transfer to the fibers can take place (note that for particulate reinforcement, the creep strength is sometimes lowered, e.g. Whitehouse and Winand (1999), Whitehouse et al. (1998)). High stress exponents for composite creep have been observed in the system Al/SiC (e.g. Nieh (1984), Pickard and Derby (1990)). Threshold-stress concepts have been put forward (Mishra and Pandey (1990)) to rationalize these high stress exponents. It must be noted that pronounced thresholds had been found only rarely in experiments. Nevertheless, there has been much speculation about the origin of a threshold stress for MMCs in literature. It has been attributed to dispersion strengthening of the matrix due to introduction of a fine oxide dispersion during powder-metallurgical processing (Park et al. (1990)). Mishra and Pandey (1990) have explained it with the stress-independent pinning of subgrains by the reinforcement, using the substructure-invariant creep approach by Sherby et al. (1977). Nardone and Prewo (1986) have ascribed the threshold stress to internal stresses from thermal strain misfit that oppose creep deformation.

The effect of internal load transfer as a possible cause for the high creep stress exponents observed on MMCs has been investigated by Dragone and Nix (1990). They showed analytically that load transfer to an array of *isolated* aligned fibers results in a composite creep law which has the same activation energy and the same stress exponent as the matrix material. In a subsequent finite element model (FEM) study (Dragone and Nix (1992)), they found that load transfer to an *interconnected fiber network* could give rise to high stress exponent, if it was combined with progressive evolution of damage in the fiber network during creep. Their experimental results and their model will be considered in more detail in one of the following subsections.

Models for Steady State Creep

Simple rule-of-mixture equations for two-phase composites with two creeping phases have been given by McLean (1994), based on iso-strain assumptions between the phases. More elaborate models, based on the shear-lag theory have been developed by De Silva (1968), Mileiko (1970), McLean (1972), Kelly and Street (1972) and others. All these models, however, can only be applied to aligned short fiber composites and they all predict only steady state creep and no creep transitions. Goto and McLean (1991a, Goto and McLean (1991b) have adapted the approach by Kelly and Street (1972) and have additionally assumed a deforming interface layer around the elastic fibers. They calculated creep curves with a progressively decreasing strain rate until steady state was obtained and they showed the marked influence that weak interfaces have on creep strength. Mori et al. (1997) claimed to have shown that a steady-state in a discontinuously reinforced metal could be achieved only when diffusion and/or sliding at the reinforcement interface takes place. They have been disproved, however, by Sato et al. (1998), who showed that a steady state can be reached with only matrix plastic (creep) flow operating.

Transient creep

Numerous FEM investigations of MMC creep with particles (e.g. Mori et al. (1997)), continuous fibers (e.g. Durodola et al. (1994)), aligned short fibers (e.g. Dakshinamurthy and Pollock (1998)) and misoriented short fibers (Sorensen (1993)) have been undertaken. They all capture the effect of transient creep due to load transfer from the matrix to the fibers, without incorporating primary creep behavior in the matrix constitutive law. None of these investigations focused on the influence of the reinforcement on the composite creep stress exponent or its thermal activation energy for creep.

In an FEM study of the creep of an aluminum-based composite with TiC particles as reinforcement, Davis and Allison (1995) stated that the steady-state creep rate was only dependent on the matrix steady-state creep rate and the reinforcement fraction. Furthermore they confirmed that the elastic/plastic properties of matrix and reinforcement do affect the transitional behavior but not the final rates. They incorporated primary matrix creep of the matrix in the form of a t^{-a} strain-rate dependence in their model and found that the composite material asymptotically approached the same behavior (t stands for time). The prediction for the beginning of primary creep, however, was rather poor.

In another continuum mechanics FEM analysis of the primary creep of a SiC particle reinforced aluminum alloy, Atkins and Gibeling (1995) found that the primary-like effect due to load transfer is minimal compared to the strain transient caused by true primary creep of the matrix. They also reported that the stresses no longer change once a constant creep rate of the composite is established.

2.2.2 Creep of Al/Al_2O_{3f} Composites

The study by Dragone and Nix (1992) is one of the few investigations of creep of aluminum based composites, reinforced with Al_2O_3 fibers (Al/Al_2O_{3f}), published so far. They investigated the steady state and transient creep of an Al-5 wt.%Mg alloy, reinforced with 26 vol.% short alumina fibers in a random-planar arrangement, in the temperature range 200-400 °C. The steady state creep stress exponents were above 12, which is very high compared to the measured matrix stress exponent of 3. They observed distinct primary creep and large anelastic strains after unloading and attributed them to load transfer between fibers and matrix. During loading, elastic strain energy is stored in the fibers and when the load is removed, this elastic strain energy provides a driving force for back-creep. They found that the amount of strain recovered depends non-linearly on the external stress. Higher absolute stresses led to larger strain recovery after 10 minutes of unloading. The authors do not specify, for how long or to what strain the specimen was initially loaded at each stress. They also do not report on the recovery behavior for repeated loading and unloading. The creep behavior was modeled with a 2-dimensional finite element model, with a matrix capable of elastic and power-law creep deformation and an interconnected random-planar fiber network, represented by connected elastic beam elements. With this model, they succeeded in predicting the anelastic unloading behavior reasonably well – although the initial rate for back-flow was overestimated. A second loading and recovery is less well predicted and the authors claim that this is due to neglect of substantial damage that has happened during the second loading phase to the fiber network. They suggest that progressive loading and an increasing damage to the fiber network result in a reduction of the driving force for backflow and thus in a reduction of the recovered strain. However, they give no experimental evidence for this assumption. Their FEM model has another drawback: It fails in the prediction of the long-term creep rates of the composites. This is due to the assumption of a continuous reinforcement. In their synopsis the authors speculate that the incorporation of creep damage to the fiber network in the model could remedy this.

Dlouhy et al. (1993) have studied creep in two aluminum-based alloys with 15 vol.% short alumina fibers (random-planar arrangement) at 350 °C. They found a high degree of creep strengthening and stress exponents that were raised compared to the matrix (10 instead of 5). Based on microstructural observations they have put forward a micromechanical model for creep, which encompasses transitional behavior (Dlouhy et al. (1995)). They claim that three elementary processes are involved in the creep of a short-fiber MMC: 1) loading of the fibers by the formation of a work hardened zone (WHZ), 2) a recovery process which decreases the dislocation density in the WHZ and 3) breakage of fibers. The work hardened zone (WHZ) around the fibers was interpreted as an arrangement of dislocation loops. This WHZ causes load transfer from the matrix to the fibers. In continuum mechanics it could be interpreted as a plastic strain mismatch between the phases. This load transfer is opposed by the recovery mechanism, during which dislocation loops move to the fiber end, shrink and annihilate. The

reduction in dislocation density contributes to the creep stain, but does not increase the plastic strain mismatch. In this way the load in the fibers is reduced. Once the dislocation density in the WHZ is high enough to induce a critical stress, multiple breakage of fibers starts to occur. Fiber breakage accelerates the recovery process because the travel distance for the dislocation loops to annihilate is reduced. The authors point out that, under all their assumptions, *"creep is never microstructurally steady"*, i.e. no long-term steady state creep rate is achieved. Primary creep is governed by load transfer and recovery. Before a dynamic equilibrium between the rate of load transfer and the recovery rate is established, the stress in the fibers is high enough to break them. Tertiary creep, governed by recovery and fiber breakage is the consequence. Eggeler (1994) points out that fiber fracture relaxes only part of the elastic energy stored in the fibers, and that the subfibers can be newly loaded by the surrounding matrix. Dlouhy and Eggeler have not presented experimental data or modeled results regarding the back-flow of their MMC. In a short note (Dlouhy and Eggeler (1994)), however, they discuss the aforementioned results by Dragone and Nix. They claim that both the over-estimate of the initial back-flow rate and the under-estimate of the total strain in the later stages of creep are due to disregarding a recovery process that reduces the elastic energy stored in the fibers.

Liu and Bathias (1994) performed uniaxial creep experiments on two hypoeutectic Al-Si alloys, reinforced with 20 vol.% of alumina fibers with supposedly 3D-random orientation. In their investigation they focused on a short-term negative creep region that followed after a conventional primary creep transient. The negative creep disappears as the load is raised above a critical stress. The authors attribute the occurrence of negative creep to the "randomly oriented fibers strongly resisting dislocation creep of the matrices" without giving further details.

A technical aluminum alloy that was reinforced with 15 vol.% of Al_2O_3 (Saffil) fibers has been investigated for its creep rupture life by Nam and Han (1998). Like the aforementioned investigators, they also found high stress exponents for creep in the MMC (about 12) and lower ones in the matrix material (about 4). They found that the creep rupture life was proportional to the $(n\text{-}1)^{th}$ power of stress, where n is the stress exponent of power-law creep. While the matrix material showed normal creep rupture by growth and coalescence of pores (equiaxed dimples on the fracture surface), the MMC failed by brittle shear fracture (elongated dimples).

Investigations of Creep Damage

Komenda and Henderson (1993) have investigated the influence of the homogeneity of fiber densities on the creep rupture times of an Al-3 wt.%Cu alloy reinforced with 10, 20 and 30 vol.% of Al_2O_3 (Saffil) fibers. They quantified the fiber homogeneity in terms of the ratio of standard deviation of the diameter of fiber free zones to the mean zone diameter. In their

work, it was found that the stress needed for a rupture time of 1000 hours decreased linearly with increasing inhomogeneity.

Sorensen (1991) employed FEM creep modeling with a 2D unit-cell approach to model creep of whisker-reinforced aluminum. He found a low influence of fiber clustering on creep rates, compared to the large effect on plastic deformation (Christman et al. (1989)). Fiber clustering in his work, however, is discussed in terms of periodic arrangements of whiskers in pairs (due to the unit-cell approach), and not to large-scale variations in reinforcement density.

Whitehouse et al. (1998) studied cast as well as powder-metallurgically produced aluminum alloys, reinforced with 10 and 20 vol.% of Al_2O_3 (Saffil) fibers, that were extruded after production. Matrix cavitation adjacent to fiber ends was found to be the dominant damage mechanism. Cavitation was particularly pronounced in clustered regions. The authors propose that this damage and not load transfer dominated the creep strain evolution of the MMC.

2.3 Isothermal Creep under Cyclic Loading Conditions

The isothermal creep behavior of materials can be altered when the externally applied load is cyclically varied during the experiment. In the present work, experiments under such loading conditions will be called “stress cycling creep experiments”. A few studies dedicated to the creep behavior of materials in such stress cycling creep experiments have been published. The experiments usually employ symmetric triangular or square wave cycles of stress with cycling periods in the region of 1 to 60 seconds. They are thus very similar to slow load-controlled fatigue tests under creep condition. Most investigations center on the question whether creep is accelerated or retarded by load cycling.

Cyclic Creep Acceleration and Retardation

The two contrary phenomena have been termed *“cyclic creep acceleration”* (CCA) and *“cyclic creep retardation”* (CCR). Hereby, creep rates determined from the envelopes of the stress cycling creep curves are directly compared to static creep rates. Usually no correction is made for the time spent at low or zero stresses. Both, CCA and CCR have been observed in pure polycrystalline and single crystalline metals, alloys, dispersion strengthened materials and also in MMCs. A general trend is that CCA occurs at rather low temperatures and high stresses, while CCR is mostly found at high temperatures and low stresses (Lee and Nam (1988)).

It has been tried to explain CCA by different theories. Cross slip based theories assume that piled up screw dislocations can overcome obstacles by cross slip during off-load periods and easily glide away upon re-loading. Other theories are based on point defects such as excess vacancies. These are produced mechanically by non-conservative jog motion and they enhance

diffusion controlled creep, which is reflected in a lowering of the apparent activation energy for creep. Both types of theories, cross-slip and point-defect based ones, have been reviewed by Lee and Nam (1988).

Kimmerle et al. (1986) investigated the frequency dependence of stress cycling creep rates of a dispersion strengthened superalloy. They observed CCR and found that the creep rate decreased when the cycle duration became shorter. To explain this behavior, they assumed that during forward creep (under load), the strain could be divided into two components, a recoverable and a non-recoverable one. Only the non-recoverable component contributed to the cyclic creep strain. They demanded that recoverable strain had to take place over a certain time before non recoverable creep could occur. The time remaining for non-recoverable creep was shortened when the cycle duration was shortened and therefore the stress cycling creep rate decreased for shorter cycles. As a physical explanation they proposed a mechanism based on climb controlled dislocation glide. Under load, dislocations bow out between strong pinning points and during the phase of recoverable strain storage, they climb over weaker pinning points. Upon load removal, they can completely un-bow again. Non-recoverable creep occurs when the dislocation has sufficient time to climb over the strong pinning points. In their reasoning the authors neglect that when the cycle duration is shortened, the time for recovery is also shortened and then less time is needed to restore the recoverable strain on loading. The explanation of Kimmerle, Nardone and Tien can only rationalize CCR behavior.

Stress Cycling Creep of MMCs

Stress cycling creep experiments have also been performed on MMCs. Tjong et al. (1999) observed CCR behavior with cp-Al / 20 vol.% SiC_w (PM) which they investigated at 325-375 °C. They used sawtooth cycles with a frequency of 0.5 Hz and almost complete unloading. They found a deceleration by 3 orders of magnitude and explained it using the same rationale as Kimmerle et al. The same explanation was also used by Liu et al. (1997b), who found CCR in Al 6061 / 28 vol.% SiC_w at 350 °C. At temperatures of around 200 °C, however, they found CCA, which was more pronounced for higher cycle frequencies (see also Liu et al. (1997a)). In this case they employed explanations based on the generation of excess vacancies that had been given for pure metals (see above). All these dedicated stress cycling creep investigations on MMCs have in common that short cycle times were used. They do not consider effects of load transfer and strain energy storage in the reinforcement, probably because these are believed to gain importance only at very low frequencies with long relaxation times.

No investigations of stress cycling creep on MMCs with long recovery times have been found in literature. It was mentioned above (see 2.2.2) that Dragone and Nix (1992) studied the creep recovery behavior upon load removal in a short fiber MMC. They, however, investigated only singular back creep curves but not multiply repeated unloadings. They also did not

address effects of recovery on the stress cycling creep rate or on the damage evolution. This will be done in the present work for a short fiber-reinforced aluminum alloy.

2.4 Thermal Cycling Creep of MMCs

Thermal cycling under creep conditions can lead to increased creep rates and pronounced dimensional changes in a variety of materials. This is expected when thermal cycling induces considerable strain misfits (and thus internal stresses) in the material that are repeatedly regenerated. The phenomenon has been termed *"thermal cycling creep"* and will be frequently abbreviated "TCC" in this work*.

The probably first report on this phenomenon was made by Cottrell (1955). He reported on the possibility of creep enhancement in polycrystalline α-uranium due to neutron irradiation or thermal cycling. Without experimental evidence, he predicted that the high anisotropy of CTE in α-U would give rise to large internal stresses, because the grains would mutually constrain their individual thermoelastic deformation. He pointed out that the acceleration of creep would be highest when the applied stresses are low: *"This is because […] most of the work of deformation is done by the internal stresses and the role of the external stress is merely to guide the local plastic deformation such a way that their average […] has a non-vanishing component in the direction of the stress."* Cottrell's suppositions were experimentally confirmed later on. A more recent study is the one by Wu et al. (1987).

Examples of misfit-accelerated creep due to thermal cycling have been found in

1) materials with an anisotropic CTE, such as U, Zn, Cd … (e.g. Lobb et al. (1972), Wu et al. (1987), Pickard and Derby (1991)),
2) materials that undergo phase transformations with density changes, such as U, Fe, Ti … (e.g. Greenwood and Johnson (1965), Zwigl and Dunand (1998), Schuh and Dunand (1998))
   and
3) two- or multi-phase materials with CTE differences between the phases such as MMCs (Wu and Sherby (1984), Pickard and Derby (1990), Chen and Daehn (1991))

In the following, the basic phenomenology of thermal cycling creep will be summarized. Afterwards, existing models for the prediction of thermal cycling creep rates are reviewed.

* The use of the term "creep" in "thermal cycling creep" does not necessarily mean that creep deformation is a dominant deformation mechanism or involved at all. The term is only used to indicate that the testing temperature lies in a region where isothermal creep deformation can be expected.

2.4.1 Phenomenology

Two typical results from TCC investigations are presented in Figure 2.1a and b in terms of Norton plots of strain rate $\dot{\varepsilon}$ vs. applied stress σ. They were chosen here because they are thought to be representative for most experimental investigations of TCC in a variety of materials. In these plots, three basic features of TCC that have been identified in the literature (see e.g. Derby (1991)) are visible:

1) At low applied stresses the creep rate under thermal cycling conditions is higher than for isothermal creep (at a comparable temperature).
2) At low applied stresses the strain rate is proportional to the applied stress, i.e. the stress exponent of creep approaches unity.
3) At high stresses the stress exponent approaches values for isothermal creep (at a comparable temperature).

Furthermore, most investigators report that in the region where the stress exponent is low, no transitional behavior (comparable to primary creep) was found, i.e. the strain per cycle was constant from the first thermal cycle. It was also frequently reported that TCC was only observed when the thermal excursion was higher than a critical value. This was attributed to matrix plasticity being induced beyond a critical thermal excursion ΔT_c.

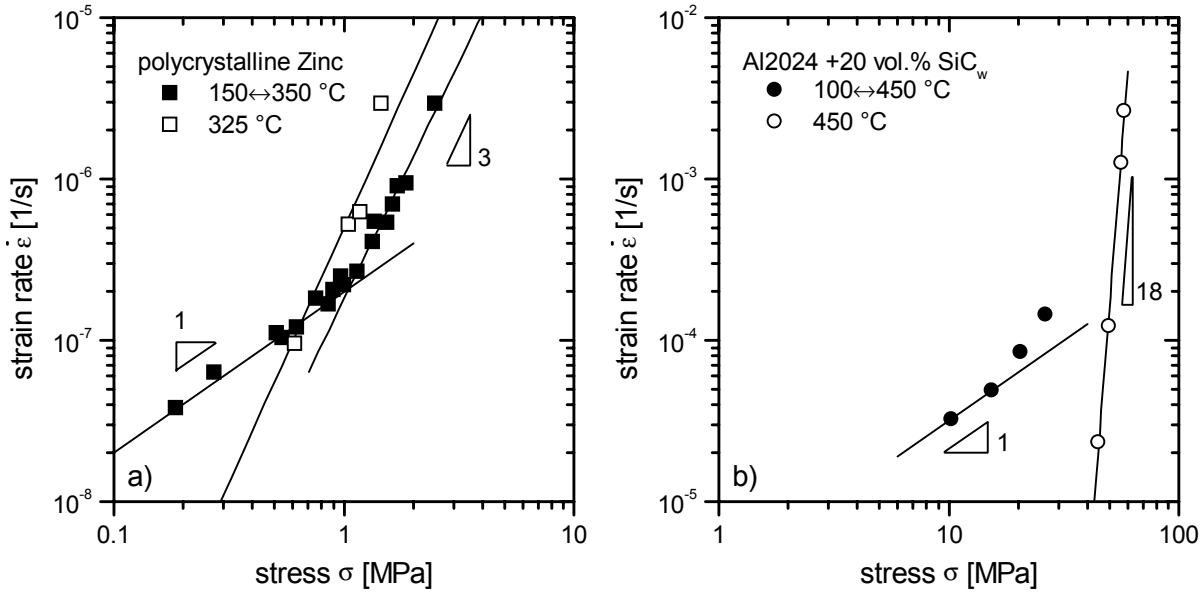

Figure 2.1: *Examples for typical thermal cycling creep behavior. a) TCC of polycrystalline Zinc (Lobb et al. (1972)) b) TCC of a metal matrix composite consisting of an aluminum based matrix with 20 vol.% of SiC whiskers (Wu and Sherby (1984)).*

The low apparent stress exponent is equivalent to a high value of strain rate sensitivity. This can result in the inhibition of necking and thus fulfils a necessary condition for superplastic deformation (Avery and Backofen (1964)). Indeed, superplastic deformability under TCC conditions has been shown for all of the above cases. To distinguish it from the classical *"microstructural superplasticity"* or *"fine-grained superplasticity"* this has been called

"transformation superplasticity" (for the case of metals undergoing phase transformation) and *"internal stress superplasticity"* (in the field of MMCs). The expression *"mismatch induced superplasticity – MISP"* used by Chen and Daehn (1991), seems to be the most appropriate formulation. It is, however, rarely used.

2.4.2 Materials, Experiments and Evaluation

The most popular MMC system for the investigation of thermal cycling creep seems to be the system Al/SiC. Just like in the field of measurement of internal stresses (see Section 2.1.3), the system Al/SiC is attractive because of the large difference in CTE between the constituents. A compilation of aluminum-based composites with discontinuous reinforcements that have been investigated under thermal cycling creep conditions is given in Table 2.1.

Composite	Reinforcement volume fraction	Orientation	Thermal cycle	Reference
cp Al / SiC_w	10%	aligned	400↔175 °C	Daymond and Withers (1997)
Al 2024 / SiC_w	20 %	aligned, random	450↔100 °C	Wu and Sherby (1984)
Al 2024 / SiC_w	10%, 20%	aligned	450↔100 °C	Hong et al. (1988)
Al 6061 / SiC_w	20%	aligned	450↔100 °C	Daehn and Gonzalez-Doncél (1989)
Al 6061 / SiC_w	15%	aligned	150↔50 °C	Toitot et al. (1990)
cp Al / SiC_p	5% - 40%		450↔130 °C 350↔130 °C 200↔80 °C	Pickard and Derby (1990)
Al 2024 / SiC_p	10%, 20%		450↔100 °C	Goncales-Doncel and Sherby (1996)
Al 7090 / SiC_p	15%		200↔70 °C	Le Flour and Locicéro (1987)
cp Al / $Si_{platelets}$	13.6% (eutectic)	random	300↔165 °C	Chen and Daehn (1991)
Al / Al_3Ni_{DS}	10% (eutectic)	aligned	400↔300 °C	Kitazono et al. (1996)
cp Al / Al_2O_{3f}	10%, 20%	aligned	340↔140 °C	Furness and Clyne (1991b)

Table 2.1: *Aluminum based composites with discontinuous reinforcement that have been investigated under thermal cycling creep conditions (loaded thermal cycling).*

Most TCC studies were conducted using standard creep rigs, equipped with radiant furnaces and forced air cooling. In many cases, the effect of superplastic deformability was also addressed. Therefore most experiments were conducted under tensile loading. Compressive tests have also been conducted by Wu and Sherby (1984), Hong et al. (1988) and Kitazono et

al. (1996). Possible differences in TCC behavior between tensile and compressive loading were not addressed or reported.

Thermal cycling creep strains were commonly measured as strain increments from cycle to cycle. The experimentators usually refrained from highly resolved strain measurements, most probably because standard extensometers are not capable of measuring high strains, as they occur in superplastic deformation, with the high resolutions that are necessary for this. An exception are the works by Furness and Clyne (1991a) and Daymond and Withers (1997), who both used a laser scanning extensometer to measure strains within the thermal cycles. Continuous strain measurement during the thermal cycles has also been performed in the present work. The methods to evaluate these in-cycle strains are therefore discussed in Chapter 4 “Experimental”, Section 4.3.1.

In the previous section, it was stated that materials that showed accelerated thermal cycling creep displayed no transitional behavior when the load was changed abruptly. This was also reported for most studies with MMCs, but not for all. Le Flour and Locicéro (1987) and Toitot et al. (1990) reported strong initial transients i.e. 10 and more cycles until a constant strain per cycle was reached. It is remarkable that in these two investigations, thermal cycles at particularly low temperatures were used. This trend has been confirmed by Daymond and Withers (1996), who explicitly investigated the strain transients during the initial cycles. They found that at high temperatures and high thermal amplitudes (400↔175 °C) only one cycle was needed to achieve a state of constant strain per cycle, while it took three cycles at lower temperatures and lower thermal excursions (325↔175 °C).

2.4.3 Models for Thermal Cycling Creep

Several models and theoretical considerations have been put forward to explain and predict TCC behavior for the different materials. These can be roughly divided into three groups:

1) Models based on cyclic plasticity (“Enhanced plasticity models”, Derby (1991)). These assume that the induced strain misfit is large enough to cause plasticity, biased by the external load in every cycle.
2) Models based on repeated creep under the combined action of internal and external stresses (“Enhanced creep models”, Derby (1991)).
3) Calculations using the Finite Element method. With these, it is tried to accurately predict the matrix stress state during thermal cycling based on continuum mechanics. Appropriate constitutive material laws are employed to consider inelastic effects and how these affect the evolution of the matrix stress and the global strain response of the material.

These three types of modeling approaches will now be addressed in turn.

Cyclic Plasticity Models

A very important model, on which many other TCC models are based, is the model for transformation plasticity by Greenwood and Johnson (1965), which in turn is based on an earlier model by Anderson and Bishop (1962). An excellent review of the Greenwood and Johnson model, along with a brief overview of various refinements to it, can be found in the recent publication by Zwigl and Dunand (1997). Only the most important assumptions and simplifications will be outlined here.

Greenwood and Johnson considered an ideally plastic material which undergoes a phase transformation. During this transformation, the strain misfit becomes high enough to cause plastic flow in the weaker phase. They add the transformation strain $\Delta V/V$ to the plastic strain which is induced in the weaker phase to get the internal strain mismatch. Then they use the Levy-von Mises flow rule*, to link this internal strain tensor to the plastic yield stress σ_y. After introducing strain compatibility conditions, they arrive at an expression for the deviatoric stress component in loading direction, which is a function of the transformation strain and the total strain. To simplify this expression, Greenwood and Johnson assume that the total strain is much smaller than the transformation strain, ($\varepsilon << \Delta V/V$) and after an integration which considers all possible orientations of the phase transformation strain, they arrive at the following formula for the total strain $\Delta\varepsilon$ after two transformations per cycle:

$$\Delta\varepsilon \approx \frac{5}{3}\frac{\Delta V}{V}\frac{\sigma}{\sigma_y} \qquad \textbf{(2-6)}$$

The above simplification leads to the prediction that the strain per cycle (and thus the TCC rate) scales linearly with the applied stress σ. Furthermore, it is seen that the creep rate is proportional to the induced strain mismatch and that higher yield stresses σ_y will lead to lower strain rates. Analytical expressions have been obtained for the case of less strict simplifications (Zwigl and Dunand (1997)) and for these, a deviation from the linear stress / strain rate dependence is found for higher strain rates (and thus higher stresses).

Derby (1985) adapted the Greenwood and Johnson model (making use of the Levy-von Mises equations) for the case of CTE mismatch in MMCs. He assumed an ideal plastic matrix and aligned rigid short fibers as reinforcement with a difference in CTE of $\Delta\alpha$. The matrix yields as soon as the thermal excursion ΔT exceeds the critical value ΔT_c. His expression differs from the one by Greenwood and Johnson only in the mismatch strain term:

$$\Delta\varepsilon \approx \frac{5}{3}\frac{\sigma}{\sigma_y}\Delta\alpha\cdot\left(\Delta T - \Delta T_c\right) \qquad \textbf{(2-7)}$$

* The Levy-von Mises flow rule states that the strain rate in a certain direction is proportional to the deviatoric stress component in this direction.

An identical expression was given by Greenwood and Johnson (1965) (taken from Anderson and Bishop (1962)) where $\Delta\alpha$ is the difference in CTEs for the crystallographic axes of uranium.

Despite the basic features that can be explained by these models (strain rate proportional to stress at low stresses, critical thermal excursion), they have one obvious drawback: They do not consider any time dependent processes such as creep and stress relaxation. In the case of MMCs, other approaches have been made to consider creep. Some of these are reviewed in the following section.

Enhanced Creep Models

A purely creep-based model for thermal cycling creep was proposed by Sherby and co-workers (Wu et al. (1987)). As a starting point, they assumed that deformation in the matrix is accomplished by diffusion-controlled dislocation creep, which they describe by the empirical Garofalo creep equation (a hyperbolic sine relation). Their key supposition is that *"at any given time during thermal cycling, half of the moving dislocations are influenced by an internal stress (+σ_i) that aids their motion and the remaining half of the moving dislocations are influenced by an internal stress (-σ_i) that opposes their motion"*. Next, they assumed that these two groups of dislocations contribute independently to the global deformation. They arrived at a relation that reflects the basic phenomenology of thermal cycling creep:

$$\dot{\varepsilon} \sim \tfrac{1}{2}\sinh\left(\frac{\sigma+\sigma_i}{\sigma_{pbd}}\right)^n + \tfrac{1}{2}\,\mathrm{sgn}(\sigma-\sigma_i)\cdot\sinh\left(\frac{\sigma-\sigma_i}{\sigma_{pbd}}\right)^n \qquad \textbf{(2-8)}$$

(σ_{pbd} is the stress at which the power-law breaks down to an exponential creep law). In this simplified formulation of their creep law, one can see that for applied stresses σ that are much higher than the internal stresses σ_i, the creep law simplifies to the Garofalo creep equation. When the external stress is low, however, the term $(\sigma\pm\sigma_i)/\sigma_{pbd}$ becomes low and the two hyperbolic sine functions can be approximated by linear functions. Then, Sherby and co-workers expand the resulting power-law and eliminate all terms above second order as negligible. Finally they arrive at an expression that states the linear dependence of strain rate on applied stress σ for low stresses:

$$\dot{\varepsilon} \sim \sigma_i^{\,n-1} \cdot \sigma \qquad \textbf{(2-9)}$$

Their creep expression is well suited to fit experimental data of TCC rates. It is, however, difficult to make predictions with it because it does not specify the amount or even the origin of the internal stress. As a consequence, σ_i is mostly a fit-parameter. Moreover, to make equation 2-9 predictive requires to introduce difficult-to-obtain *average* quantities such as the diffusion coefficient and the internal stress, because these change during a thermal cycle.

It would be more desirable to have a model which takes into account the nature of changing internal strain misfits and changing matrix creep rates right away. Such a model would necessarily be a numerical one because the accepted exponential creep equations in combination with exponential thermal activation terms can usually not be integrated analytically. Such a numerical approach has been followed by the next model.

Daehn and Gonzalez-Doncél (1989) have put forward a 2-dimensional (plane strain) model that is based on the assumption that matrix deformation in an aligned MMC takes place by shear between the fibers. They neglected effects at the fiber ends (especially flow around them) and assumed homogeneity in the matrix. For their simple geometrical arrangement, which is defined by the fiber aspect ratio and the volume fraction, they could calculate the shear stress state in the matrix, incorporating the thermally induced stress. From this, a power-law creep rate was calculated and resolved for its component in the loading direction. For a small time step, the strain increment in the loading direction was calculated and via a strain compatibility condition, it caused a change in the matrix (and fiber) stress. With a computer program, they finally calculated the complete strain and stress evolution for a thermal cycle in small increments. They used the model to fit experimental creep data for composite systems of Al/SiC_w (e.g. Daehn and Gonzalez-Doncél (1989)) and even particulate systems (Al/Si: Chen and Daehn (1991)) and found good agreement with experimental findings. They could reproduce the behavior at low loads and the transition to isothermal behavior for higher stresses. Moreover, their model was probably the first one that included a dependence on the cycling frequency and the shape of the thermal cycle (apart from its amplitude). It also captured the effect of progressive load transfer to the fibers, because of a strain compatibility condition between the matrix and the fibers together with an increasing inelastic matrix strain. Note that Clyne and Withers (1993) erroneously deny this ability of the Daehn and Gonzalez-Doncél model. Daehn and Gonzalez-Doncél point out that they made gross simplifications, especially of the internal stress state, to make the problem tractable. Still they consider it to be predictive, because it captures the effect of cyclic internal inelastic strains which become irreversibly biased by an applied load *"in a physically reasonable manner"*.

FEM Calculations

A general problem of FEM studies of composite deformation is the limited complexity of the structure that can be modeled within reasonable computing time. It is especially difficult to capture the statistical character of the spatial, orientational and size distribution of the reinforcement in a real composite. Therefore, most FEM models for composites employ a so called unit-cell approach, in which the real microstructure is approximated by a periodic arrangement of identical cells that contain a limited number of reinforcement structures (usually a single fiber or particle segment).

Zhang et al. (1991) employed such a unit-cell approach in an FEM investigation of the geometry used in the Daehn and Gonzalez-Doncél model. They used plane strain elements and an isotropic, elastic-perfectly plastic constitutive law for the matrix. The fibers were assumed to be ideally rigid, with no elastic or plastic deformation. The thermal strain misfit during thermal cycling caused rather uniform plastic deformation in a zone surrounding the central portion of the fibers and plastic strain concentrations near the fiber ends. Substantial plastic extension of the composite was only found when the plastic zones became interconnected. As for the dependence of strain rate on the applied stress, qualitatively, the same behavior was predicted as with the closed-form model by Daehn and Gonzalez-Doncél (1989). The FEM model was also used to study the influence of reinforcement morphology (aspect ratio of the fibers, volume fraction). The authors reported that the influence of the morphology is only very small.

An other interesting computational study of TCC in a Al/SiC_w composite was published by Daymond and Withers (1997). Two simple three-dimensional fiber arrangements were modeled (staggered and aligned). To model the inelastic deformation of the matrix, a perfectly plastic law with a temperature dependent yield stress and additionally a power-law creep law was utilized. The authors point out that the matrix should rather be modeled with a kinematically hardening plasticity law. To compensate for the weakness introduced by the non-hardening law, they adjusted the matrix yield stress for a better agreement with experimental results. Their results were reported in the form of the evolution of the mean axial inelastic strain components during thermal cycling. They individually investigated the case of only plastic deformation and of combined creep and plastic deformation. One basic result was that under the used conditions, creep contributed substantially to the cyclic strain evolution in the composite. Especially at the high temperature end of the thermal cycle, creep took over from plasticity as the dominant deformation mechanism. The authors also pointed out that creep deformation in the model tended to be more localized than plastic deformation, due to the high stress exponent. Their results will be discussed in comparison to results from this work in more detail in Section 7.3.

2.5 Theoretical Understanding of Creep in MMCs – the State of the Art

Isothermal Creep of Discontinuous MMCs

As mentioned above, the creep properties of many different MMCs have been investigated experimentally with great care and detail. Models for the creep behavior of discontinuously reinforced MMCs are, however, mostly confined to the description of the load transfer process and in addition only available for idealized geometries (such as aligned short fibers). Such

models are usually based on continuum mechanics and they cannot be adapted easily for MMCs with arbitrary reinforcement orientation distributions. Multidirectional reinforcement by comparatively long but discontinuous fibers, for example, is beyond the scope of the present models.

A major shortcoming of present creep models is the neglect of damage. While damage processes such as fiber fracture and interfacial debonding are a vital part of most creep models in the field of continuously reinforced MMCs, such processes are rarely considered in models for discontinuous reinforcement (particles or short fibers). Experimentally, the damage evolution in discontinuously reinforced MMCs has received broader attention just in the last four or five years. However, there is still a notable lack of experimental techniques with which processes of load transfer and damage during creep can be studied simultaneously. Another remarkable issue regarding the understanding of creep damage in MMCs is that, compared to other material classes such as superalloys or technical ceramics, relatively few investigations have been combined with transmission electron microscopy (TEM) studies. This is most probably due to severe problems with the production of TEM specimens from MMC material. The usually large size of the reinforcing phase makes the investigation of representative sample volumes additionally difficult.

Only one model, namely the above mentioned model by Dlouhy and Eggeler, combines a load transfer concept with damage evolution. It was noted above that this model was based on microstructural observations that were obtained by TEM. To date, it seems to be the most advanced model for isothermal creep of a fibrous MMC. It is, however, difficult to apply because of its complexity and because it has to be implemented numerically. It has to be pointed out that the Dlouhy/Eggeler model is still a one-dimensional model in which real fiber orientation distributions have to be approximated by an effective volume fraction of aligned fibers.

All in all, isothermal creep of MMCs is at present best understood for systems with continuous unidirectional fiber reinforcement. For this idealized case the concept of load transfer and reinforcement damage is utilized in predictive models. With growing complexity of the reinforcement morphology, the modeling of load transfer and the incorporation of damage processes becomes increasingly difficult and has only rarely been realized in theoretical models.

Thermal Cycling Creep

The most striking phenomena of creep under thermal cycling conditions in MMCs, namely stress exponents of one and superplastic deformability, have been explained by the simple considerations that have already been formulated for the case of transformation plasticity: Generally speaking, internal stresses are biased by a small externally applied stress. The influence of this “disturbance” on the rate of deformation is linear when the disturbance is small.

The simple models based on cyclic plasticity (see 2.4.3) can explain the low stress exponents and the existence of a critical thermal excursion. These models can be applied only for idealized conditions because they neglect time dependent deformation and the effects of load transfer and damage. A series of numerical models have successfully attempted to consider at least time dependent deformation processes and load-transfer-effects. However, just like in the field of isothermal creep modeling, these models are limited to idealized geometries (aligned short fibers) and they still neglect effects of damage.

Thermal cycling creep has been mainly investigated in terms of steady state cyclic creep rates as a function of applied stress. The evolution of thermal cycling creep curves, which is especially interesting when the internal stresses and the applied stress are comparable in size (high applied stresses and/or low thermal cycle amplitudes), has been investigated only very rarely – even with the latest numerical models that could well be applied to such problems.

Contributions of the Present Work

The present work provides detailed experimental studies of thermal cycling creep behavior especially in the above mentioned realistic case where internal and externally applied stresses are comparable in size. The found behavior will be compared to results from a simple model (see Chapter 6) which is based on continuum mechanics and which focuses on the evolution of internal stresses. Among the numerical models described in section 2.4.3 the model used in the present work is most similar to the model by Daehn and Gonzalez-Doncél (1989) with respect to its numerical basis and implementation. The model also uses a special geometry which comes closest to an MMC with a 2D planar array of fibers. It will be widely used to study the applicability of such continuum mechanics approaches to the case of TCC and the considerations should provide a basis for more detailed studies of micromechanical processes.

The model still neglects damage processes. As mentioned above, damage in discontinuous MMCs is generally not considered quantitatively even under isothermal conditions (with the exception of the Dlouhy and Eggeler model). In the present work, it is tried to narrow the gap between theoretical modeling of MMC-creep and the phenomenological understanding of the load-transfer and damage process by introducing a newly developed testing technique with which the processes of load transfer and damage can be studied simultaneously under isothermal creep conditions. The phenomenological interpretation of results from these tests provides possibly important information for the setting up of future creep models that consider damage.

3 Material

The experiments were done on a fiber reinforced piston alloy – a composite system that is one of the very few series applications of short fiber reinforced metals. It was produced by squeeze infiltration of fiber preforms by the company MAHLE GmbH, Stuttgart, Germany. The material was obtained as infiltrated plates of size 250×100×20 mm^3 that were machined from ingots. The plates incorporated a reinforced region of size 55×75×20 mm^3 in the center, according to the dimensions of the preform. A sketch of such a plate is shown in Figure 3.1, where also the orientations with respect to the faces of the plates are denoted.

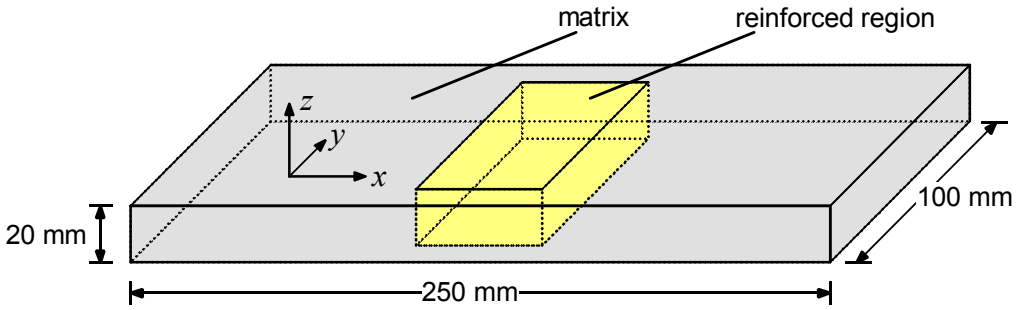

Figure 3.1: *Orientational denotation for a plate that was cut from an ingot with a reinforced region.*

3.1 Aluminum Alloy Al Si12Cu1Mg1Ni1

The piston alloy that forms the matrix is a slightly hypoeutectic aluminum-silicon alloy with additions of copper, magnesium and nickel (proprietary name M124 F). Its composition is given in Table 3.1. Due to the low room temperature solubility of silicon in aluminum, almost all of the 12 wt.% (13.6 vol.%) of silicon form brittle platelet precipitates with diameters of up to 50 µm (see Figure 3.3). The other alloying elements and impurities, in addition to their solution and precipitation hardening effects, form a variety of brittle intermetallic phases (Paul and Exner (1990)). Especially the presence of magnesium and thus the possible formation of fine Mg_2Si precipitates makes the matrix age hardenable.

Si	Cu	Mg	Ni	Fe	Mn	Zn	Ti	Al
11-13	0.8-1.3	0.8-1.3	1.3	0.7	0.3	0.3	0.2	rest

Table 3.1: *Nominal composition of the piston alloy M124 F in weight percent.*

In Figure 3.2 the solidification microstructure of the matrix alloy in the unreinforced regions of an ingot can be seen. Large dendrites of proeutectic aluminum as well as the silicon and intermetallic precipitates in the interdendritic spaces are clearly visible. Shape and size of the precipitates are shown in Figure 3.3. It has been shown by Bär (1992) that the silicon precipi-

tates together with the intermetallic phases form a continuous three-dimensional network with low mechanical stability.

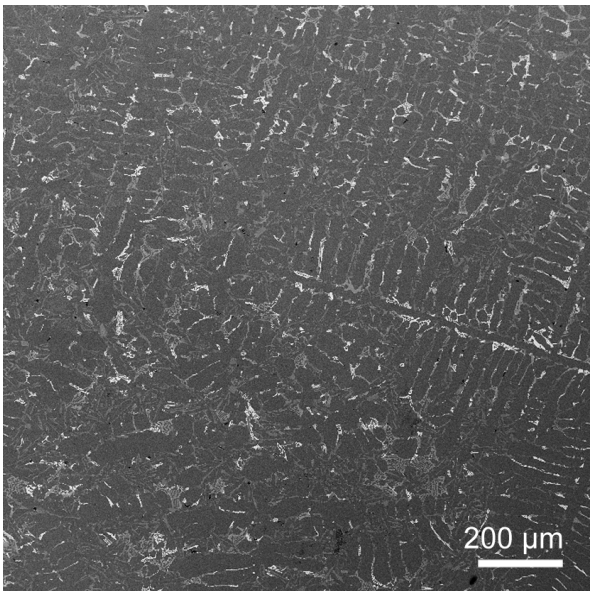

Figure 3.2: *Dendritic solidification microstructure of the unreinforced Al-12Si alloy. variable-pressure scanning electron microscopy (VP-SEM), back-scatterd electron (BS) detection.*

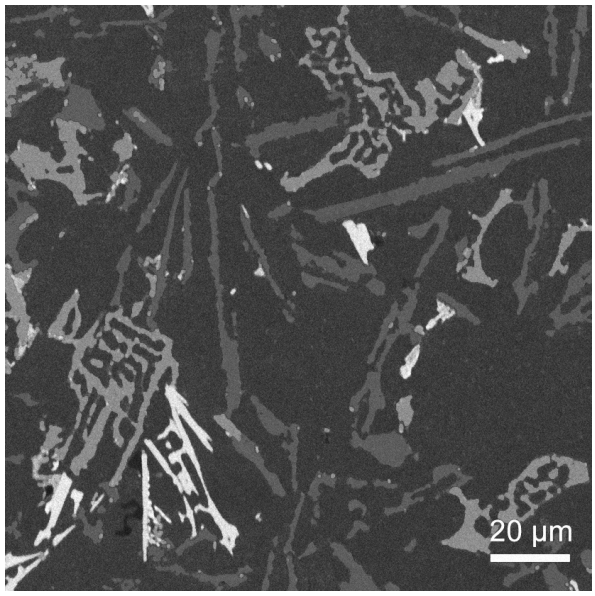

Figure 3.3: *Size and shape of the various phases that are present in the piston alloy. Darkest: Matrix Al, dark gray: Si-platelets, middle gray chinese script and light: other intermetallic phases, see Paul and Exner (1990) for details. VP-SEM, BS detection.*

3.2 Composite

The reinforcing phase is 15 vol.% of δ-Al_2O_3-fibers (“Saffil RF”, by ICI). The fiber properties are listed in Table 3.2. Preforms are commonly fabricated from a liquid suspension of these fibers by a combined sedimentation and draining process. It is also common to simultaneously compress the preform in order to establish the desired volume fraction of fibers. A small addition of binder helps to increase the stability and therefore makes the preform easier to handle. Although the fibers often tend to align in a plane perpendicular to the sedimentation direction, it is yet possible to get much less pronounced degrees of orientation up to complete 3D-random orientation.

To produce the composite material, the preform is heated and put in a pre-heated die, where it is infiltrated with melt at high pressures of usually more than 100 MPa. The high pressure is needed to feed freezing shrinkage during solidification. The infiltration and solidification procedure takes only few minutes.

Manufacturer	ICI
Composition	95-97 % Al_2O_3, 3-4% SiO_2 [a,b,c]
Density ρ [g/cm^3]	3.5 [b], 3.3 [d]
Young's Modulus E [GPa]	285 [b], 300 [a,c,d]
Poisson's ratio ν	0.2 [a]
Tensile strength σ_m [MPa]	1500 [a,b], 2000 [c,d]
Coefficient of thermal expansion α [10^{-6}/K]	7.7 [b], 7.5 [d]
median fiber diameter d [µm]	3.2 [f], 3.5 [a], 3 [b]
median fiber length L [µm]	50-200 [e], 100-300[d]

Table 3.2: *Properties of Saffil RF© fibers according to: [a] ICI), [b] Clyne and Withers (1993), [c] Hegeler et al. (1994), [d] Müller-Schwelling and Röhrle (1988), [e] Henning and Neite (1994), [f] this Work*

Figure 3.4 shows the typical microstructure of the fiber reinforced region in a cross section perpendicular to the *z*-direction (see Figure 3.1 for the orientational denomination) at low magnification. The fibers are visible as black dots and lines and at higher magnifications (see Figure 3.5) as dark section ellipses. The fiber arrangement has no pronounced large-scale homogeneity: considerable variations in the local fiber content and limited regions where the fibers cluster with parallel alignment are clearly visible. However, a slightly preferential orientation of fibers in the *yz*-plane is to be noticed. At higher magnification, the matrix precipitates can be seen, yet smaller and finer than in the unreinforced matrix, probably owing to heterogeneous nucleation at the fiber interfaces. In regions with very low fiber content, the microstructure closely resembles the unreinforced regions of the ingot with its dendritic solidification microstructure. SEM investigation of the reinforced material revealed a small amount of pores that are usually found next to fibers (see Figure 3.5).

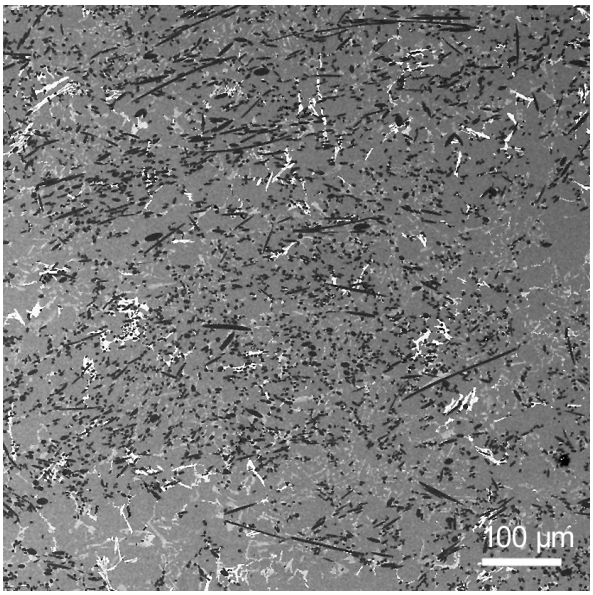

Figure 3.4: *Metallographic section of the composite material (vertical: x-axis, horizontal, y-axis). Fibers are visible as dark dots and lines. No large scale homogeneity is found, but a slightly preferential orientation of fibers in the yz-plane is observed. VP-SEM, BS detection.*

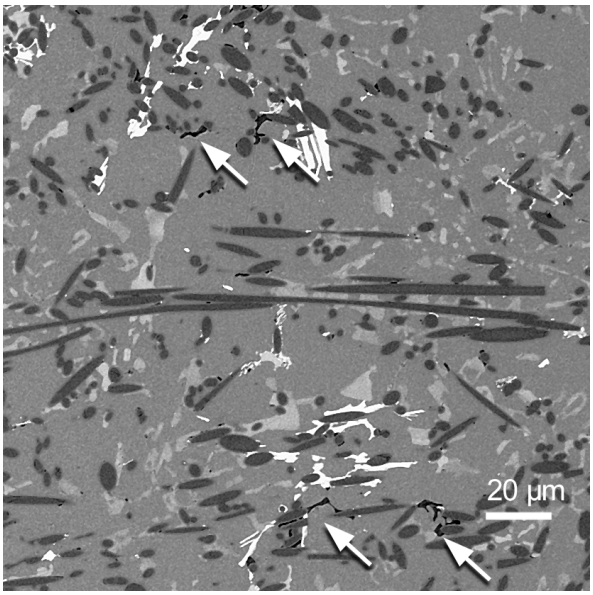

Figure 3.5: *Detail of Figure 3.4. The fibers are visible as dark section ellipses alongside with the silicon platelets and the other phases of the matrix material. Infiltration pores were repeatedly found and they were mostly associated with fibers (see arrows). VP-SEM, BS detection.*

3.3 Heat Treatment and Aging Behavior

After squeeze infiltration, the ingots were subjected to a T6 heat treatment. This comprises homogenization for 1 h at 480 °C, quenching in oil and aging of 24 h at room temperature and 9 h at 215 °C (according to manufacturer's specifications).

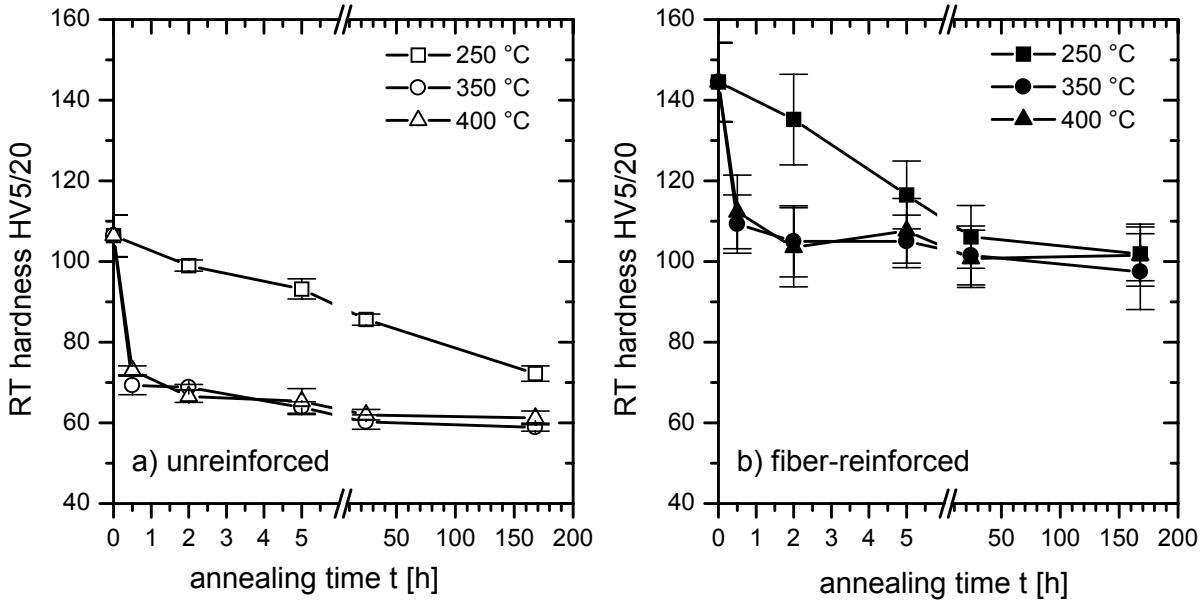

Figure 3.6: *Evolution of room-temperature hardness with time for annealing at various temperatures from peak-aged condition: a) unreinforced matrix alloy, b) composite material.*

Mechanical testing at high temperatures, as performed in this work, usually involves heating the sample to testing temperature and allowing for temperature homogenization prior to testing. During this time, over-aging of the matrix alloy can happen and therefore the aging behavior of the already peak-aged material was investigated by hardness measurements. The results are shown in Figure 3.6. It can be seen that for annealing above 350 °C about 75 % of the total hardness loss is achieved within 30 minutes. This applies to both the unreinforced matrix and the composite material. It is also worth noting that the Saffil reinforcement does not substantially accelerate the aging process. This complies with earlier findings on the same material by Bär et al. (1993) and on a Saffil reinforced Al-2024 alloy (Chen and Chao (1995)).

3.4 Temperature Dependent Properties

For the interpretation of thermal cycling experiments, the temperature dependence of material properties is important. In this section, the temperature dependence of yield stress, elasticity, and thermal expansion are briefly summarized.

Yield Stress

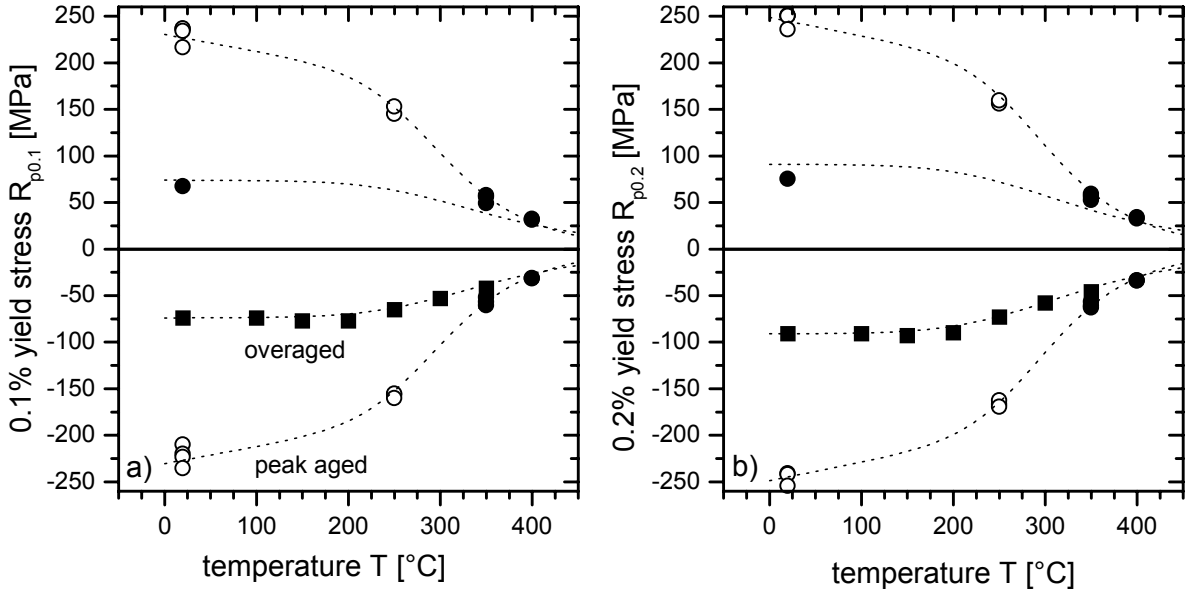

Figure 3.7: *Yield stress of the matrix alloy: a) $R_{p0.1}$ yield stress, b) $R_{p0.2}$ yield stress. Open symbols: peak-aged (as supplied), closed symbols: over-aged 1h@350 °C*

Monotonic tensile and compressive tests were performed to evaluate the flow curves of the unreinforced matrix material. A set of peak aged samples (as supplied) and a set of over-aged samples were tested at a constant crosshead speed of 0.6 mm/min. The 0.1% and 0.2% yield stresses are given in Figure 3.7. It can be seen that tensile and compressive yield stresses are equal in the whole temperature range. The 0.1% yield stress for the over-aged matrix alloy is about 75 MPa from room temperature up to 200 °C and then decreases to 42 MPa at 350 °C. The room temperature yield stress of the over-aged matrix is only a third of the yield stress at

peak-aged condition. However at 350 °C and for higher temperatures, the yield stresses for the two aging conditions start to coincide. This is due to fast over-aging at the high temperatures (see Section 3.3), which takes place during a 30 minute dwell at test temperature prior to testing.

Elastic Properties

The elastic properties of the matrix alloy and the composite were measured at room temperature by Bidlingmaier (1999) with the impulse-echo method. For both materials, no pronounced anisotropy was found so that the elastic properties were assumed to be macroscopically isotropic (Bidlingmaier et al. (1997)). Bidlingmaier's results are summarized in Table 3.3.

	matrix alloy	**composite**
Shear modulus G [GPa]	30.2 ± 0.6	35.8 ± 0.8
Young's modulus E [GPa]	80 ± 1.8	94 ± 2.2
Poisson's ration ν []	0.33 ± 0.02	0.31 ± 0.02

Table 3.3: *Elastic constants at room temperature; data taken from Bidlingmaier (1999).*

The temperature dependence of the shear modulus was measured with a torsion pendulum at frequencies of about 2.5 Hz. The results are shown in Figure 3.8. Between room temperature and 250 °C the temperature dependence of the matrix shear modulus is linear with a coefficient of -0.014 GPa/K. Above that range, the curve becomes successively steeper. At 400 °C the shear modulus is 22.4 GPa. If one assumes Poisson's ratio to be constant in the relevant temperature range, the temperature dependence of Young's modulus *E* shows the same characteristics as the shear modulus. *E* changes from 80 GPa at room temperature to 60 GPa at 400 °C.

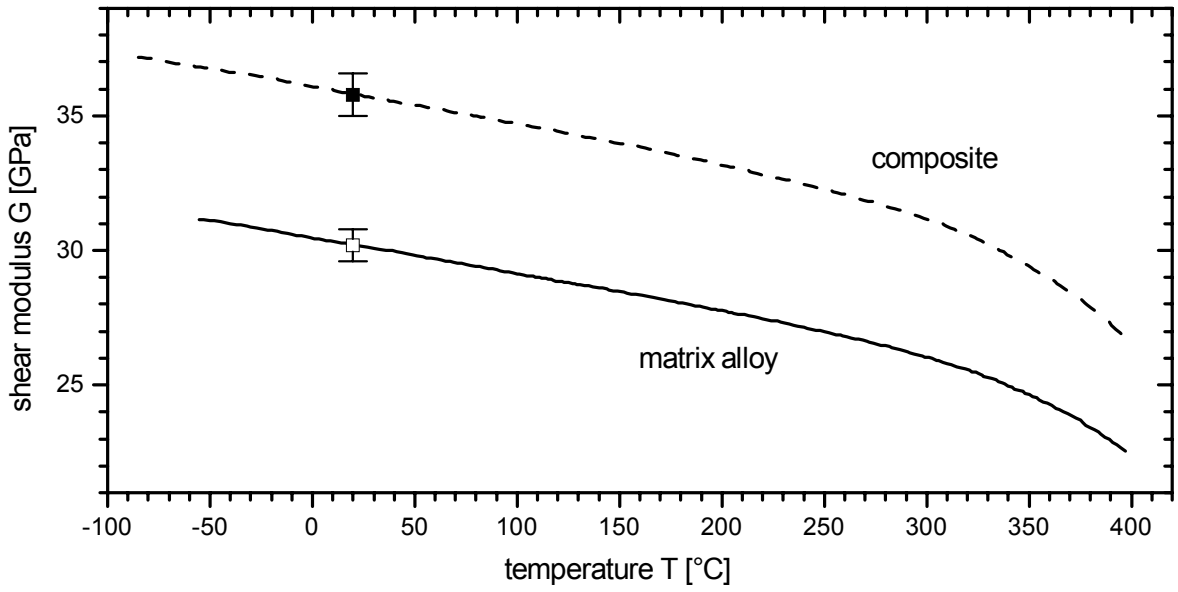

Figure 3.8: *Temperature dependence of the shear modulus as measured in a torsion pendulum. The value at room temperature were take form Table 3.3.*

Thermal Expansion

The thermal expansion was measured with a single pushrod dilatometer Model DIL 402 C by NETZSCH with a tube-type sample carrier and pushrod made from quartz. Cylindrical samples of the matrix alloy with a diameter of 6 mm and a length of 25 mm were subjected to temperature cycles from room temperature to 480 °C at heating and cooling rates of 0.5 K/min. The thermal expansion curve is shown in Figure 3.9a. It is seen that the heating and cooling curve almost coincide. The technical coefficient of thermal expansion (CTE) α_{20} and the physical CTE – both for the heating curve – are plotted in Figure 3.9b. The CTE values are also summarized in Table 3.4 for selected temperatures and compared to data for pure Al.

Temperature T [°C]	50	100	150	200	250	300	350	400	450
tech. CTE α_{20} [10^{-6}/K]	19.7	20.0	20.6	21.1	21.7	22.2	22.7	23.0	23.4
phys CTE α [10^{-6}/K]	19.5	20.8	22.0	22.8	24.7	25.1	25.4	25.5	25.1
tech. CTE α_{20} [10^{-6}/K] pure aluminum[(a)]		23.6		24.5		25.5		26.4	

Table 3.4: *Coefficient of thermal expansion (CTE) for the matrix alloy in comparison to pure aluminum.*
[(a)]Humsicker et al. (1979)

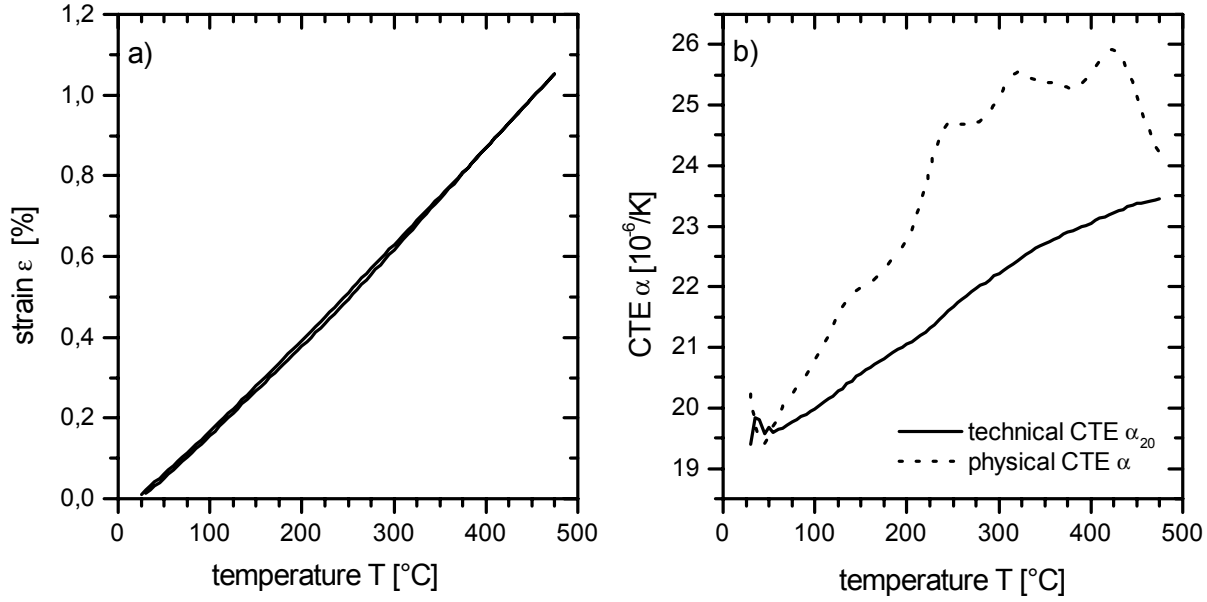

Figure 3.9: *Thermal expansion of the matrix alloy: a) heating and cooling curve (0.5 K/min), b) for the heating curve: technical coefficient of thermal expansion* $\alpha_{20} = (l-l_{20°})/l_{20°} \cdot 1/(T-20°)$ *and physical CTE* $\alpha = d\varepsilon/dt$

3.5 Isothermal Creep

Isothermal creep of the matrix material and the composite has been investigated under tension and compression at various temperatures and loads by Bidlingmaier and Wolf. Bidlingmaier tested the material in a standard creep rig under tensile loading at 350 °C (Bidlingmaier et al. (1996a)), and at 250 and 400 °C (Bidlingmaier et al. (1996b)). Wolf (1997) investigated the stress dependence at 350 °C. He also investigated the temperature dependence in the range from 325 to 400 °C to assess the apparent activation energy for creep. Bidlingmaier's tensile specimens were oriented with the loading axis in y-direction, whereas Wolf's compressive specimens had z-orientation (cf. Fig. 3.1). Their experimental results are summarized in the following sections.

Minimum Creep Rates

In the Figures 3.10a and -b it can be seen that the reinforcement enhances the material's creep resistance and that it also increases the apparent stress exponent. The apparent stress exponent varies considerably for different temperatures. This may well be due to the small number of data points and the substantial scatter in the test results. The open symbol in Figure 3.10b denotes a data-point that was obtained within the present work for a specimen that was oriented in x-direction (Bidlingmaier's specimens had y-orientation). It can be seen that the specimen orientation has no significant influence on the minimum isothermal creep rate. From this, one can conclude that either a) the specimen microstructure is insensitive to the orienta-

tion i.e. no texture is present or b) the creep rate of the specimens is insensitive to texture. In Chapter 5, it will be shown that the latter is the case.

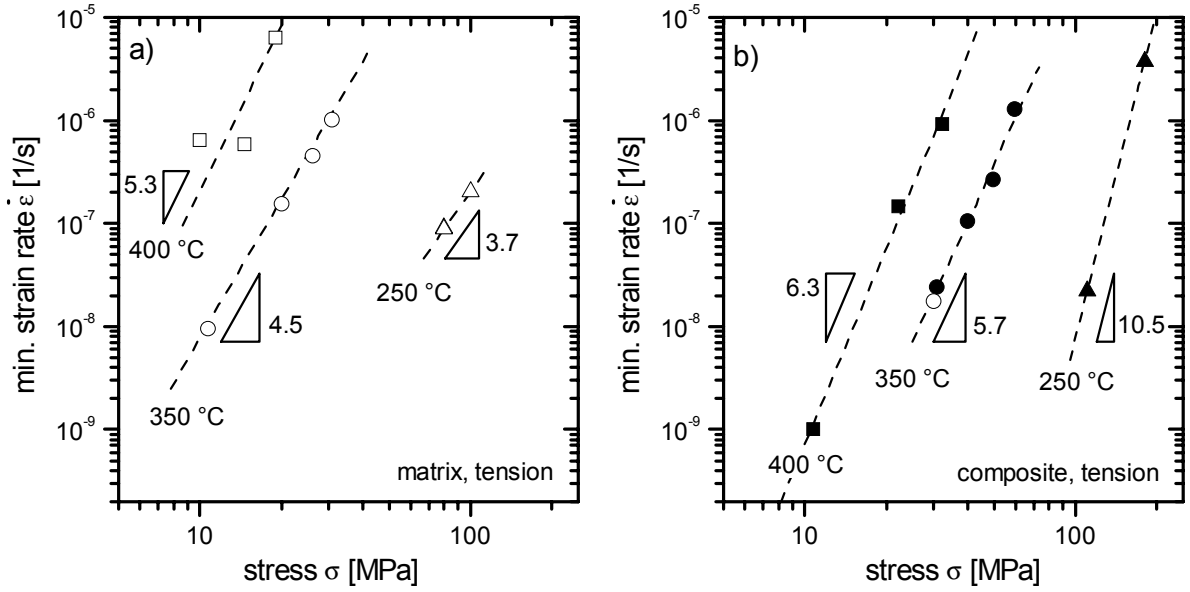

Figure 3.10: *Tensile creep rates of a) the matrix alloy and b) the composite material at 250, 350 and 400 °C, measured by Bidlingmaier et al. (1996a). Apparent stress exponents n_{app} are also given. The open circle in b denotes an experiment with a specimen that had a different orientation – see text for details.*

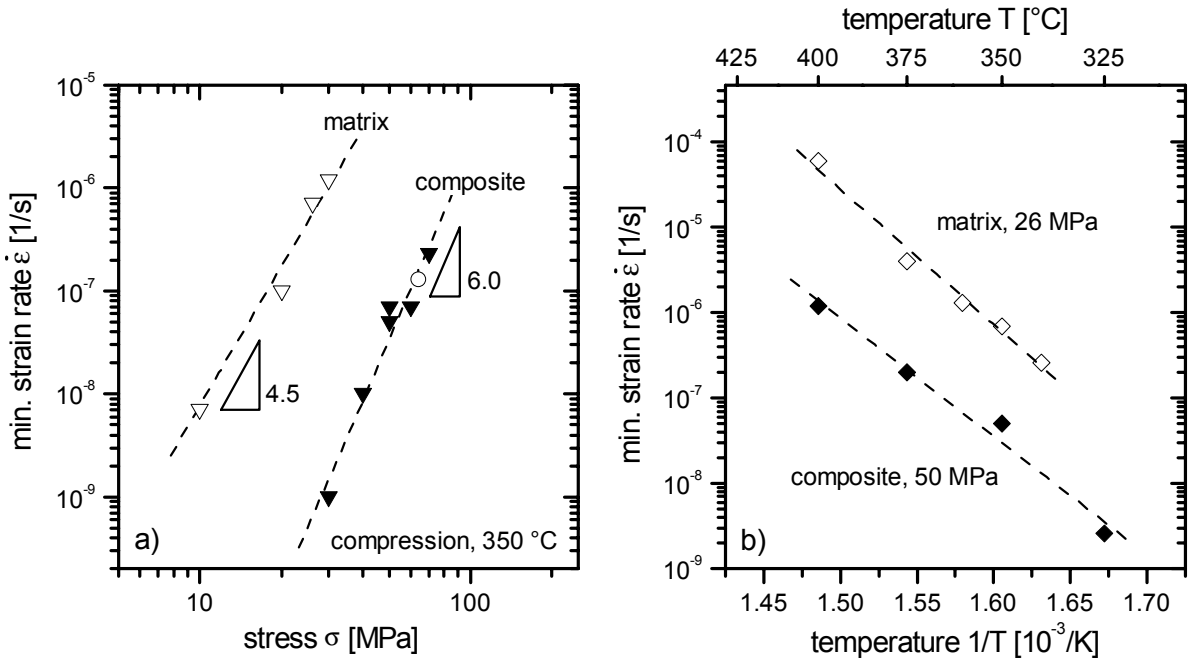

Figure 3.11: *Compressive creep rates of the matrix alloy and the composite material as measured by Wolf (1997): a) at 350 °C and various stresses and b) at a fixed stress and for various temperatures. The open circle in a) denotes an experiment that was done in the testing setup used in this work.*

By comparing the tensile and the compressive creep data (Figures 3.10 and 3.11a), one can see that the creep rate of the matrix alloy is insensitive to the sign of loading. For the reinforced material, however, it is found that the compressive creep rates are much lower than the tensile

creep rates. This tension-compression asymmetry has been explained by Bidlingmaier et al. (1998) on the basis of differences in the damage evolution under the following assumptions: 1) The reinforcement is assumed to be macroscopically untextured, 2) the matrix and the fibers are in iso-strain condition 3) the creep rate is dominated by progressive breaking of fibers as the composite is strained beyond the elastic limit of the fibers and 4) fibers break only in tension. The asymmetry is caused by the geometry: For tensile tests, the fibers that break are the ones that are oriented *parallel* to the loading direction and for compression, the ones that lie *perpendicular* to the external load fracture. However, if the constancy-of-volume condition for plastic or creep deformation holds, the amount of strain perpendicular to the loading direction is only half of the axial strain. Thus under compressive loading it takes twice the strain until the fibers start to break than under tensile loading. This consideration has been experimentally confirmed by Bidlingmaier with acoustic emission measurements of fiber fractures under plastic deformation of the composite at room temperature Bidlingmaier (1999).

The apparent activation energies for creep under compression were determined by Wolf from an Arrhenius-type plot of $\ln(d\varepsilon/dt)$ against $1/T$ (like in Figure 3.11b) and were reported to be Q_{app}=294 kJ/mol for the matrix alloy and Q_{app}=249 kJ/mol for the composite.

The creep properties of the matrix and the reinforcement are important inputs for the numerical simulations of the present study which will be described in Chapter 6. The parameters for semi-empirical creep equations (stress exponents n_{app}, activation energies Q_{app}) can be estimated from the experimental data of Bidlingmaier and Wolf. This analysis is also given in Chapter 6.

Transient Behavior and Fracture

In Figure 3.12 the transient creep behavior is shown in plots of strain rate vs. strain of Bildlingmaier's data (Bidlingmaier et al. (1996a)). It can be seen that the matrix creep rate decreases rapidly, goes through a minimum at relatively small strains and displays no pronounced steady state. The minimum creep rate is reached at around 0.2% irrespective of the applied load. The composite, in contrast, exhibits a prominent transitional regime up to around 0.55-0.75% strain. The strain to minimum strain rate appears to depend slightly on the applied stress: For higher stresses, higher strains to minimum are needed. While the matrix creeps with steadily increasing rate up to a fracture strain of around 15%, the composite displays a seemingly long secondary regime and fracture occurs abruptly at only 1.5 to 1.8% strain. In all these data there is some uncertainty of at least ±0.1%. Bidlingmaier and Wolf focused on the measurement of minimum strain rates because they were mainly interested in the assessment of apparent stress exponents and activation energies. To facilitate the conduction of their experiments, they applied the load not instantaneously but gradually over about half a minute.

As a consequence, the starting point of measurement was not well documented and there was considerable ambiguity about the origin of strain and time in their data.

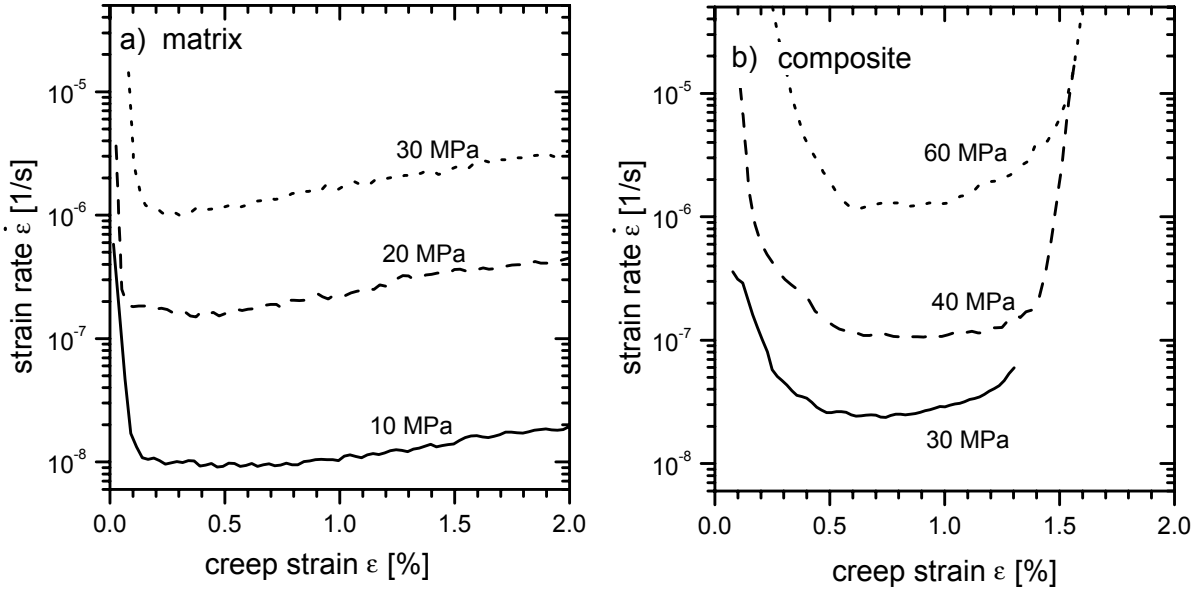

Figure 3.12: *Transient creep behavior under tensile stress for a) the matrix and b) the composite material. The matrix displayed only limited primary and secondary creep. After the initial transient a steady increase of strain rate until fracture was observed. The composite exhibited pronounced transient creep until steady state was reached at comparably high strains depending on the applied stress.*

3.6 Material Properties –the Present Knowledge

The following mechanical properties can be regarded as well-known for the material under investigation: The aging characteristics, the elastic properties and the plastic deformation behavior (including damage evolution). The creep behavior has also been covered experimentally especially in the temperature region around 350 °C. The behavior under tensile and compressive creep loading, stress exponents and activation energies have been well established. There is, however, still need in interpretation of the transient creep behavior and the damage evolution under creep conditions.

A very similar composite material (20 instead of 15 vol.% of fiber reinforcement) has been widely examined with respect to its isothermal fatigue behavior, mostly to determine the improvement of fatigue life compared to the unreinforced matrix alloy (Seitz et al. (1991), Bär (1992)). The material's behavior under thermal cycling conditions, which might be important in automotive engine environment, has not been investigated to date. This topic will be covered in the present work.

4 Experimental

The following experimental methods were used in the present work: For the characterization of the material's microstructure, standard metallographic techniques including quantitative image analysis were applied (Section 4.1). Mechanical tests were performed using a customary electro-mechanical testing machine which was suited for high temperature testing (Section 4.2). Self-written computer programs enabled special testing procedures which will be described in Section 4.3.

4.1 Microstructural Characterization

4.1.1 Specimen Preparation

Cross sections of the composite material and the matrix alloy were prepared by standard metallographic techniques. After cutting metallographic samples from the ingots or from tested specimens they were wet ground with *Struers 1200 silicon carbide grinding paper* (grain size ≈14 µm; US-Standard 600). They were polished subsequently with 6, 3, and 1 µm diamond paste for about 120 seconds at each grain size. It was necessary to keep the polishing times rather short, in order to avoid reliefs. The last step was a polish of 30-40 seconds with *Buehler Mastermet 2*, a (supposedly) non-crystallizing colloidal silica suspension. This polish greatly enhances the phase contrast for optical microscopy but it also leads to a slight embedding of silica particles in the soft matrix. Apart from that, it was found that the surface damage, introduced by the metallographic preparation was negligible.

4.1.2 Microscopy and Image Analysis

Most of the samples were examined by standard optical microscopy after testing to check for noticeable features or damage in the microstructure. If porosity was to be examined, scanning electron microscopy was preferred to optical microscopy.

It has been noted in Section 3.2 that there appears to be a particular plane with slightly preferential orientation of fibers. Quantitative image analysis was performed to investigate the nature of the global orientation distribution of fibers in the matrix, and to possibly quantify the reinforcement texture. A *Leica Quantimet Q500IW* (software version 2.2) system with an optical microscope and a video camera were used for image acquisition, processing and analysis. The procedure is outlined in the following.

Image Processing

The specimen is viewed and focused in the optical microscope at a magnification of 500:1. Images are acquired by a video camera which produces a digital 8-bit grayscale image of 760×570 pixel (see Figure 4.1a). A single square pixel has a size of 0,17×0,17 μm^2, so that the image size is 129.2×96,9 μm^2. At this magnification, an image typically contains about 100 sections of fibers. A fiber with a diameter of 3 µm which is cut normal to its rotational axis by the image plane shows up in the image with an average area of 244 pixels. The magnification is thus high enough to detect single fibers with sufficient accuracy while there are still enough fibers per image present to make the procedure efficient.

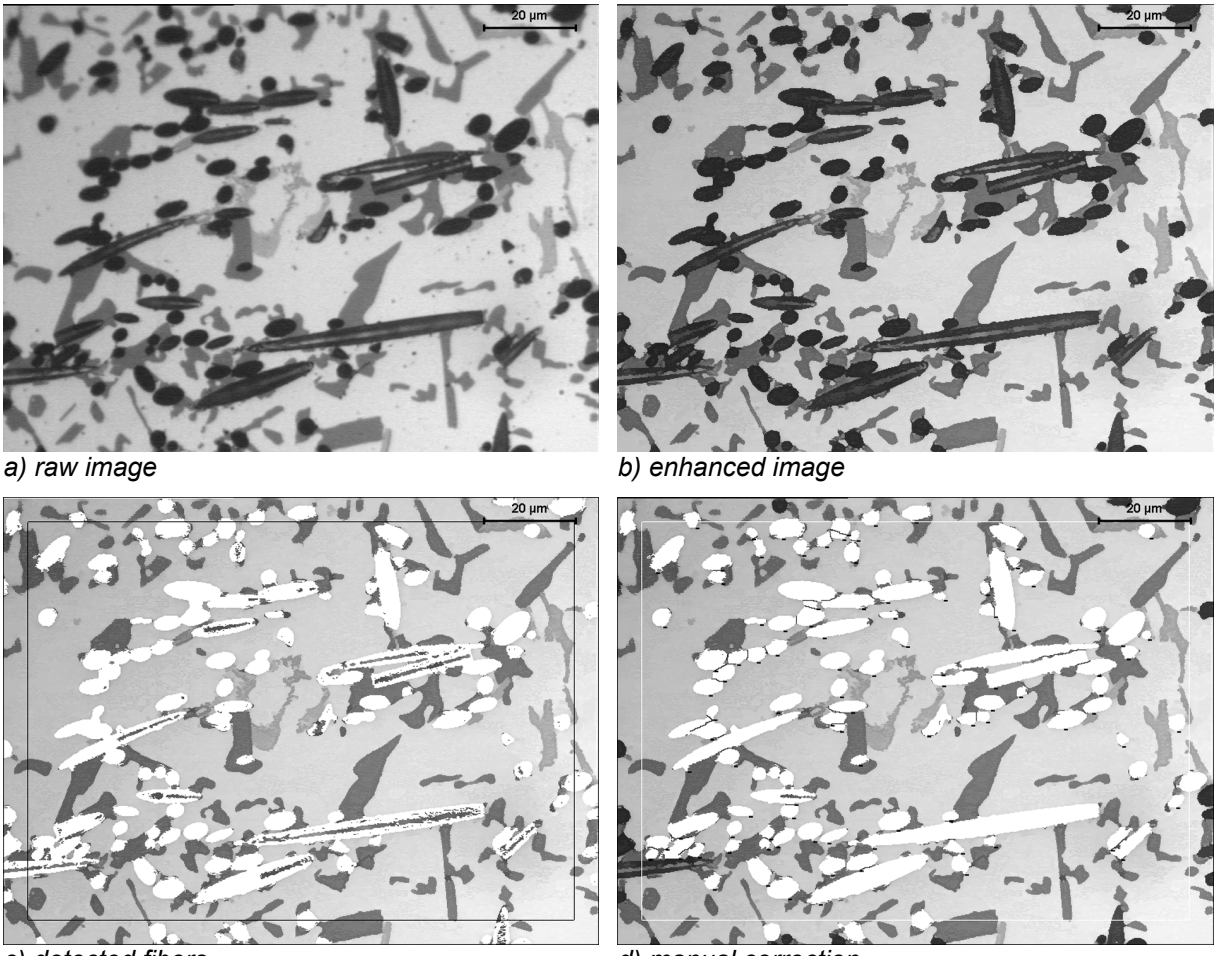

a) raw image *b) enhanced image*

c) detected fibers *d) manual correction*

Figure 4.1: *Sequence of images, representing four important steps of image analysis for the composite material. Optical microscopy.*

After acquisition, the image is digitally enhanced. Edges are sharpened, noise and dust are removed and areas with pixels of similar intensities are connected to regions of identical gray-scale value (see Figure 4.1b). Then the threshold grayscale value for the detection of the fibers, which are the darkest phase, is set manually. The now binarized picture is shown in Figure 4.1c superimposed on the enhanced image. White regions represent the detected fibers. This first binarized picture usually needs some editing before features of the fiber sections can be measured automatically. Adjacent fibers must be separated manually to avoid that they are

detected as one connected region in the binarized picture. The partial transparency of the fibers poses some additional problems. Fibers that are sectioned at a low angle often have a light core that is not detected as belonging to the fiber phase. These open regions were filled in the binarized picture manually. It has been tried to obscure the light cores by sputter coating the metallographic samples with gold. However, it was found that at a film thickness sufficient to cover the fiber transparency, the contrast between the fibers and the silicon precipitates was reduced to an unacceptable level.

Finally the computer automatically removes those of the detected fibers that intersect the image border (very long fiber sections are excluded from this routine). Now the software measures certain values for the whole edited binary picture (e.g. the area fraction of the fiber-phase) and for each detected fiber.

Analysis of Fiber Orientation

In the following analysis, the fibers are assumed to be cylindrical and straight and to have an average length of L=150 µm (see Tab. 3.2). The features that are relevant for the determination of the spatial orientation of the fibers are the maximum and minimum diameters of the section ellipses $2a$ and $2b$ and the inclination of the longest axis to the horizontal ϑ (see Figure 4.2). The fiber orientation is described in a Cartesian coordinate system. The z-axis is perpendicular to the section plane, the y-axis lies on the horizontal and the x-axis is the vertical of the section image (see Figure 4.2).

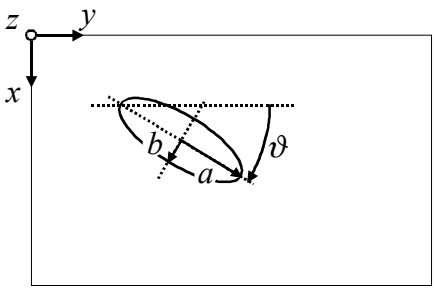

Figure 4.2:. *Elliptic cross section of a fiber. Data that are measured are the longest and smallest diameters* $2a$ *and* $2b$ *and the inclination towards the horizontal* ϑ

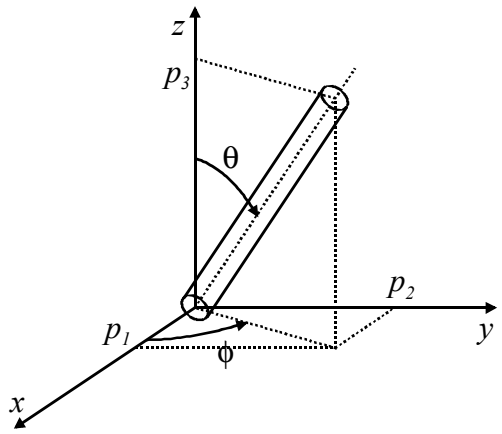

Figure 4.3: *Spatial fiber orientation with angular denotation.*

The spatial orientation of a fiber in a Cartesian coordinate system is determined by the angles θ (inclination away from z) and ϕ (rotation of the fiber's xy-projection about z starting from x) or alternatively by a vector p=(p_1,p_2,p_3) (see Figure 4.3). These parameters are related to the measured values by the following formulae:

$$\theta = \arccos(b/a), \qquad \textbf{(4-1)}$$

$$\phi = \pi/2 - \vartheta\,, \tag{4-2}$$

$$p_1 = \cos\phi \cdot \sin\theta = \sin\vartheta \cdot \sin\left(\arccos\left(b/a\right)\right), \tag{4-3}$$

$$p_2 = \sin\phi \cdot \sin\theta = \cos\vartheta \cdot \sin\left(\arccos\left(b/a\right)\right), \tag{4-4}$$

$$p_3 = \cos\theta = b/a\,. \tag{4-5}$$

The determination of fiber orientation from the elliptical cross-sections lacks accuracy in certain angular ranges. The error for θ becomes quite significant when the measured ellipse aspect ratio is low. Below $s_e = 1.41$ ($\theta < 45°$), the relative error is larger than 12% ($\Delta\theta > 5.5°$). Above 60° ($s_e = 2$), the error drops below 5% ($\Delta\theta < 2.8°$). The uncertainty in the measurement of ϑ also depends on the measured aspect ratio. For aspect ratios of more than 1.5 the accuracy of the angular measurement was found to be better than ±2.5°. A more detailed consideration of the accuracy of fiber orientation measurement is given in Appendix B.

4.1.3 Fiber Orientation Tensor

It was shown above how the orientation of individual fibers can be measured from a polished cross-section. Now, a convenient way to describe the statistics of orientation of a representative number of fibers in the specimen will be outlined. The most general characterization of the fiber orientation state is the probability distribution function for orientation $\psi(\theta,\phi)$ (see e.g. Tucker and Advani (1994)). This function gives the probability of finding a fiber between θ and $(\theta+d\theta)$ and ϕ and $(\phi+d\phi)$. Though being the most universal description, the orientation distribution function is quite difficult to handle. A simpler approach, which has become more and more popular in the last decade especially in the field of polymer composite engineering, is the calculation of an *orientation tensor*, which in principle is a volume average of orientation distribution. It completely represents the distribution function in three dimensions with an accuracy according to the order of the tensor (higher order tensors give more exact representations). A good review of the history and properties of orientation tensors and examples for their application was given by Advani and Tucker (1987).

The second-order orientation tensor is defined as follows:

$$a_{ij} = \oint p_i p_j \psi(p)\,dp \tag{4-6}$$

The main diagonal components a_{11}, a_{22} and a_{33} of this tensor measure the degree of orientation in the three principal axes x, y and z of the section coordinate system. The off-diagonal elements give the in-plane (a_{12}) and out-of-plane (a_{13}, a_{23}) rotations. For 3D random fiber orientation, the orientation tensor would be

$$a_{ij}^{3D} = \begin{pmatrix} 1/3 & 0 & 0 \\ 0 & 1/3 & 0 \\ 0 & 0 & 1/3 \end{pmatrix},$$

for a random-planar arrangement in the *xy*-plane of the section, it would be

$$a_{ij}^{2D} = \begin{pmatrix} 1/2 & 0 & 0 \\ 0 & 1/2 & 0 \\ 0 & 0 & 0 \end{pmatrix}.$$

The tensor components can be determined experimentally from a sample of fiber orientations that have been determined by image analysis of polished cross sections like in the previous Section (see e.g. Mlekusch (1999)). In this case, a discrete sample of N orientations instead of a continuous orientation function is used, and therefore the integration in Eq. 4-6 is replaced by a summation:

$$a_{ij} = \frac{\sum_{n=1}^{N} \left(p_i p_j\right)_n F_n}{\sum_{n=1}^{N} F_n} \qquad \textbf{(4-7)}$$

The probability for a fiber to be intersected by the plane of polish is dependent on the inclination angle θ and the fiber length L. A weighting function F_n for the n-th fiber is needed to account for this. The probability for a fiber to appear on the *xy*-section is proportional to the fiber's projected height $L \cdot \cos(\theta)$ on the z-axis. The weighting function is therefore:

$$F(\theta, L) = \frac{1}{L \cdot \cos(\theta)} \qquad \textbf{(4-8)}$$

This weight has to be cut off at a critical inclination θ_{crit}. Bay and Tucker (1992) suggest that this should be done at

$$\theta_{crit} = \arccos\left(\frac{d}{L}\right), \qquad \textbf{(4-9)}$$

which is the inclination that is measured for a fiber that lies perfectly parallel to the sectioning plane and has a projected height of the fiber diameter d. For high aspect ratios, as they appear in the material studied here, the cutoff region is very narrow so that the weighting function can be approximated without further refinement:

$$F(\theta, L) = \frac{1}{L \cdot \cos(\theta_{crit})} = \frac{1}{d} \quad \text{for} \quad \theta > \theta_{crit} \qquad \textbf{(4-10)}$$

A detailed study of the stereological issues and an error estimation for measurements of this kind was given by Bay and Tucker (1992).

It has to be pointed out that, from a single cross section, only the tensor components a_{11}, a_{22}, a_{33} and a_{12} can be determined. This is because fibers with the orientation (θ, ϕ) or (θ, $\phi+\pi$) have identical cross-sections. As a consequence, for each individual elliptic fiber cross section, only the absolute values of the tensor components $(a_{13})_n$ and $(a_{23})_n$ can be determined, but not their sign. The ambiguity of the out-of-plane rotations a_{13} and a_{23} can be overcome by assuming special symmetry conditions and using inclined cross sections (Mlekusch (1999)). Alternatively, one can also take three perpendicular cross sections and determine the ambiguous tensor components in one cross section coordinate system from the a_{12}-components of the other two sections. In this work, the latter approach has been followed. Three polished sections with axes aligned parallel to the global ingot coordinate system (see Figure 3.1) have been made and prepared and analyzed as described in Section 4.1.1 and 4.1.2. The results obtained are given in 0.

4.2 Mechanical Testing

In thermal cycling creep tests, a sample is subjected to a constant external load and to simultaneous cyclic temperature changes, while the strain evolution with time is measured. A testing system with which this can be achieved has to consist of eight components that have to be carefully adjusted to each other: 1) the sample, the loading system including 2) the testing rig with load cell and load control circuitry, 3) the specimen grips, 4) an extensometer for strain measurement, the heating system including 5) the temperature controller, 6) the heater and 7) a thermometer and finally 8) computer hardware with a software program for experiment control and data acquisition and storage.

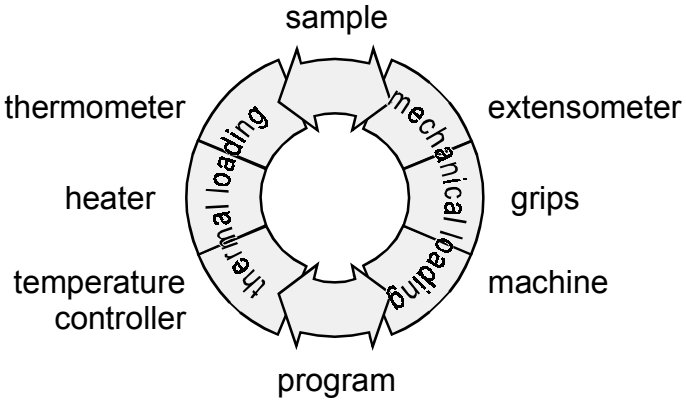

Figure 4.4: *Components of a testing system for thermal cycling creep experiments*

The requirements for thermal cycling creep tests are very similar to those for thermomechanical fatigue testing, where temperature cycles are synchronized with simultaneous strain cycles. In this work, a testing system which had previously been used for low cycle fatigue (Elzey (1989)) and thermomechanical fatigue tests (Joos (1995)) was adapted to perform thermal cycling creep tests.

4.2.1 Testing Rig

The thermal cycling creep tests were performed in an uniaxial electro-mechanical testing machine model RMC100 by Schenck-Trebel. The screw-driven machine has a maximum load capacity of 100 kN in compression or tension and can be operated in closed loop load- or strain-control. The machine is equipped with a digital interface, which makes it possible to control tests with a personal computer.

4.2.2 Specimen

For tensile tests, cylindrical button-head specimens with an elongated hourglass shape were used. The length and diameter of the parallel gage section were 15 and 7 mm, the exact dimensions are given in Figure 4.5a. These samples were cut from the partially reinforced plates described in Section 3.2, so that the whole gage-section, the transition radii and a part of both shoulders were reinforced with fibers. Following the orientational denotation given in Figure 3.1, the tensile samples that can be produced from the plates have *x*-orientation. The gage lengths of the tensile samples were diamond ground and successively polished with 7, 3, 1, and 0.2 µm diamond suspension on a lathe.

For compressive tests, smaller cylindrical samples with a length of 18 mm and a diameter of 9 mm were used. These could be cut in *x*-, *y*- or *z*-orientation from the fiber reinforced plate regions. On some of these samples two parallel side faces were ground to enable ultrasonic measurements of elastic constants or observation of changes in surface morphology. Specimen dimensions are given in Figure 4.5b and c.

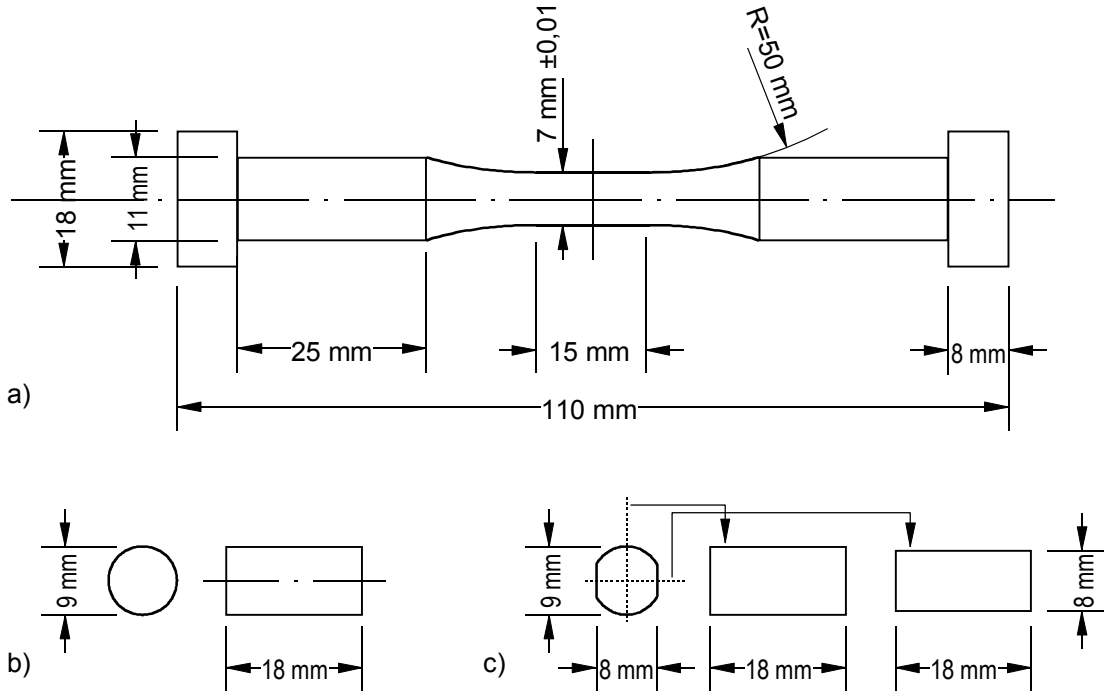

Figure 4.5: *Specimen geometry for a) tension/compression specimen, b) compression specimen and c) compression specimen with parallel side faces.*

The two different sample geometries required very different setups with respect to gripping and heating. These will be described in the following sections.

4.2.3 Grips

For tension tests the sample is gripped by a split flange that exerts pressure on the inside face of the button head when it is screwed to the loading rod. A stainless steel punch between the specimen end and the water cooled loading rod diminishes the heat loss at the sample end while still allowing for moderate cooling rates. An additional locking ring on the split flanges is necessary to assure even distribution of the flange pressure. For the compressive specimens, the setup is far simpler: The sample is held between two hard metal punches that are placed on plate fixtures which are screwed to the loading rods. For compressive tests that were run to total strains of more than -5%, a suspension of boron nitride was used as a lubricant between the specimen and the hard metal punches to minimize friction at the specimen ends. Figure 4.6 shows the grip assembly for the tension and the compression specimens.

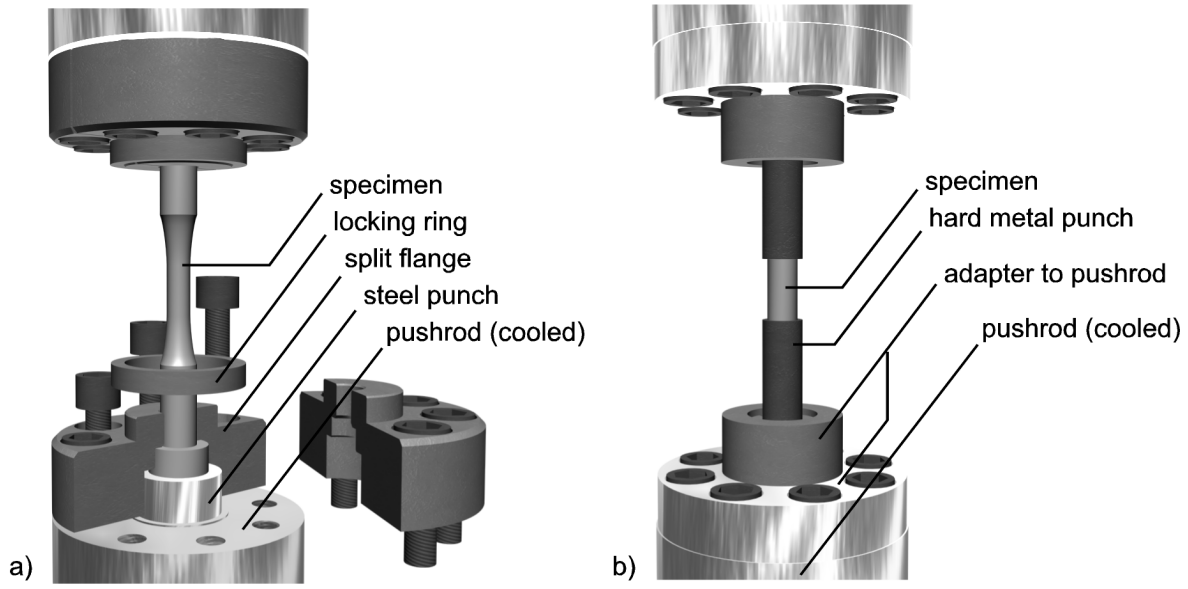

Figure 4.6: *Grip assembly for a) tension-compression tests and b) compression only test*

For good reproducibility of testing results, it is necessary to achieve a high degree of axial alignment. According to ASTM standard E139-83 for creep tests of metallic materials ASTM (1983), bending strains should not exceed 10%. Bending strains were measured according to the code of practice EUR 16138 EN (Bressers (1995)) and were found to be about 5% or lower if the flange screws were mutually tightened very carefully. Good specimen alignment however takes much practice and experience on the part of the experimentator. It was found that slight uneven tightening of the screws can result in bending strains of more than 50%.

4.2.4 Heating System

In this work, a 5 kW induction heater by Hüttinger (model TIG 5/300) was used together with self-built cooled copper coils. The specimens are mounted in the center of the coil and heated by direct coupling to the specimen and to the grips or punches. A relatively low induction frequency of about 50 kHz is used to reduce the skin effect. Great care has been taken in the design of the induction coils for the two different sample geometries. It was found that the coil geometry and position relative to the specimen was very important to minimize temperature gradients in the gage length.

At first, the poor coupling of the aluminum based materials could be enhanced by using a square cross section for the coil tubing instead of the conventional round copper tubes. For the tension/compression samples, a coil with two tight windings at each shoulder and an inner diameter of 22 mm was designed. This helped to avoid hot spots in the middle of the gage section to which these samples were very susceptible. For the compression samples a similar coil was used (see Figure 4.7). Due to the fact that the hard metal punches coupled better to the coil than the sample itself, an additional winding in the middle of the gage section was introduced to prevent overheating at the sample ends. Initially it had been tried to overcome this problem by replacing the hard metal punches by ceramic punches. However in that case the cooling rates were inadmissibly low.

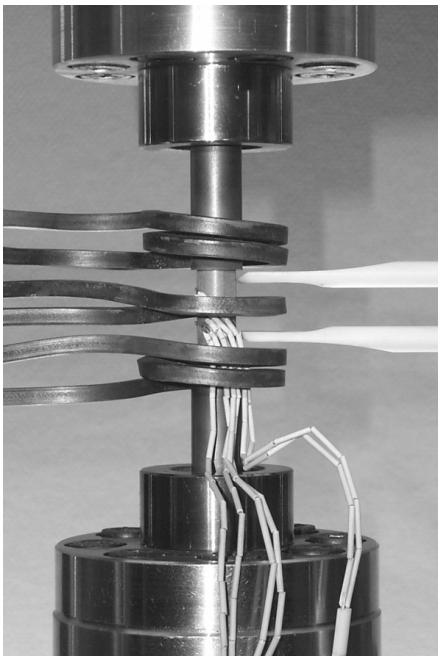

Figure 4.7: *Compressive testing setup (cf. Figure 4.6b). The specimen is equipped with three thermocouples and the side-contact extensometer is put up to the specimen from the right. The inductive coil has two windings at the top and the bottom and one central winding.*

Temperature measurement was accomplished using several Ni/NiCr (Type K) thermocouples that were spot-welded equally spaced along the gage length. The central thermocouple was used for temperature control and was connected to a Dimension II Series 8700 Process Controller by RESEARCH INC. Temperature setpoints were either programmed directly into the controller or given externally by an analog signal from a programmable function generator

(WAVETEK arbitrary waveform generator model 75). The signals from the remaining thermocouples were fed into a Keithley 2000 digital multimeter equipped with a Model 2001 TCSCAN thermocouple scanner card. Usually, a total of five thermocouples (including the controlling thermocouple) was used with tensile specimens and three thermocouples with the compression specimens. With this setup, the temperature distribution along the gage length could be monitored throughout an experiment.

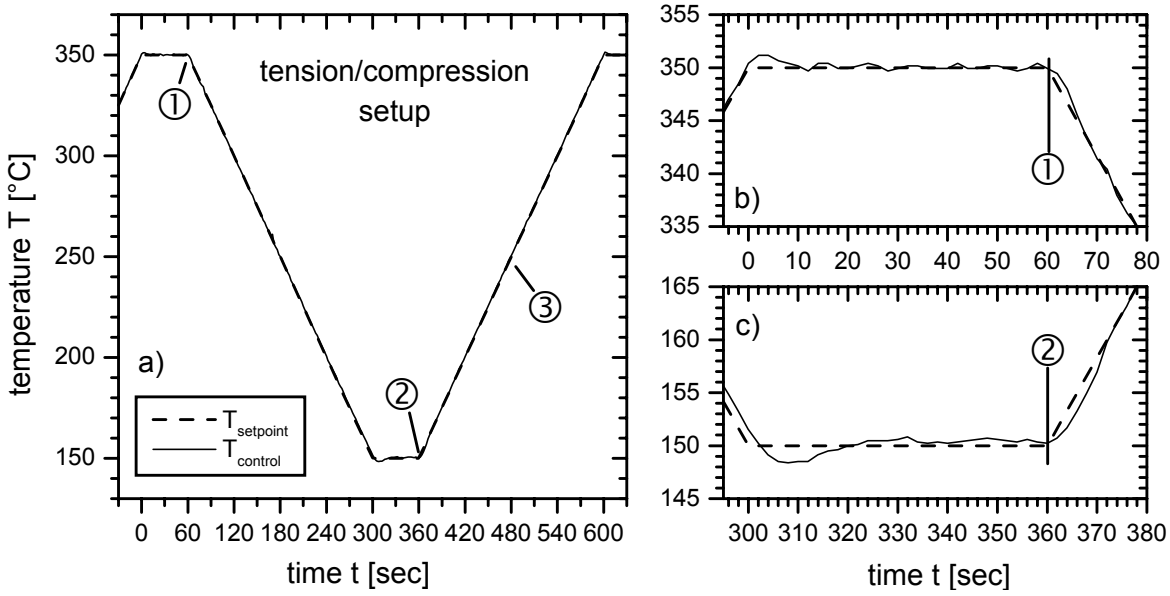

Figure 4.8: *Standard temperature-time cycle with a tensile specimen: a) full cycle, b) high-temperature dwell enlarged and c) low temperature dwell enlarged*

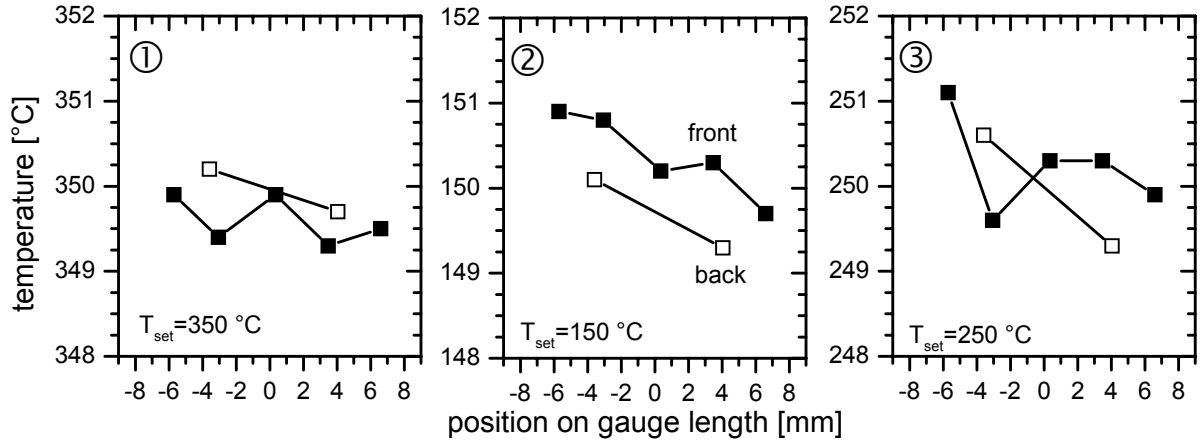

Figure 4.9: *Temperature distribution on the gage length of a tensile specimen at the end of the high-temperature dwell (①), at the end of the low temperature dwell (②) and in the middle of the heating ramp (③) for standard thermal cycles (350 °C - 150 °C, 600 sec. period, 1 minute dwell).*

One sample of each type was specially prepared with eight thermocouples, five on the front and three on the back of the gage length. These samples were used to optimize the temperature distribution during the design of the induction coils, to adjust the control parameters of the temperature controller and to measure the thermal gradients during the testing of different temperature cycles. Results from tests with these samples are shown in Figures 4.8 to 4.11. For the tension setup the control parameters of the temperature controller

were set to yield a maximum overshoot of 1.7 K and a maximum time-lag of 2 seconds compared to the setpoint signal at the extreme points of a typical temperature cycle like it was used in this work (see Figure 4.8). The respective values for the compressive setup were 2.6 K overshoot (at the low temperature dwell) and 3 seconds time-lag. A comparison of the readings from the thermocouples at certain characteristic temperatures during a standard cycle showed that the temperature distribution along the gage length was homogeneous well within 2 K (see Figures 4.9 and 4.11). Finally, the radial temperature gradient was tested using a tensile specimen with five shielded thermocouples mounted into holes that were drilled into the sample from the side. The core temperatures were also found to fall into the 2 K homogeneity bounds.

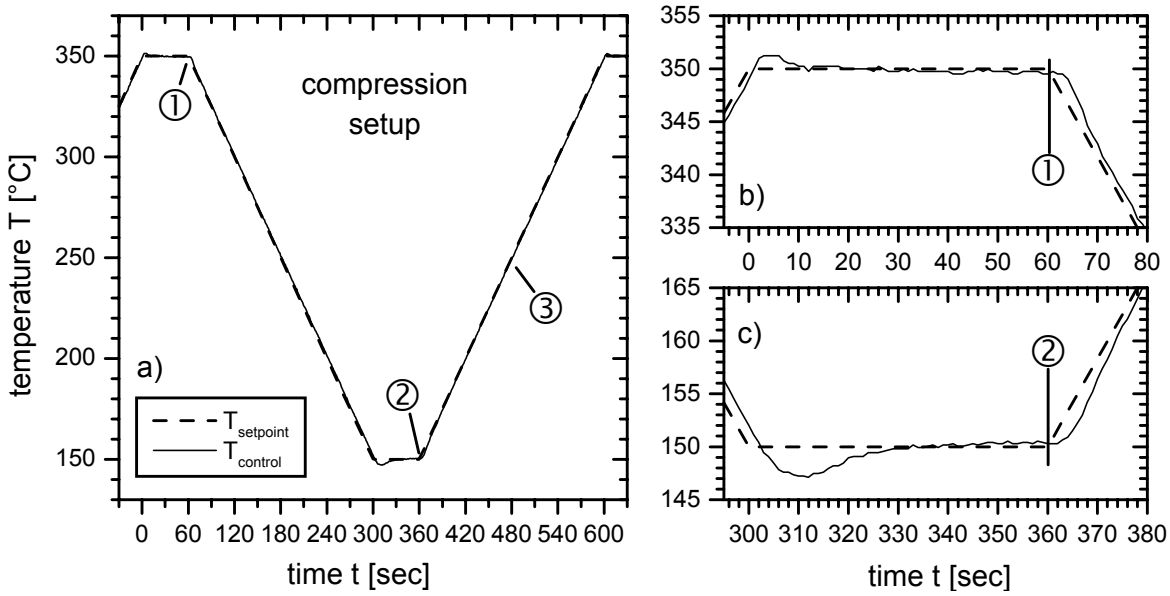

Figure 4.10: *Standard temperature-time cycle with compression specimen: a) full cycle, b) high-temperature dwell enlarged and c) low temperature dwell enlarged*

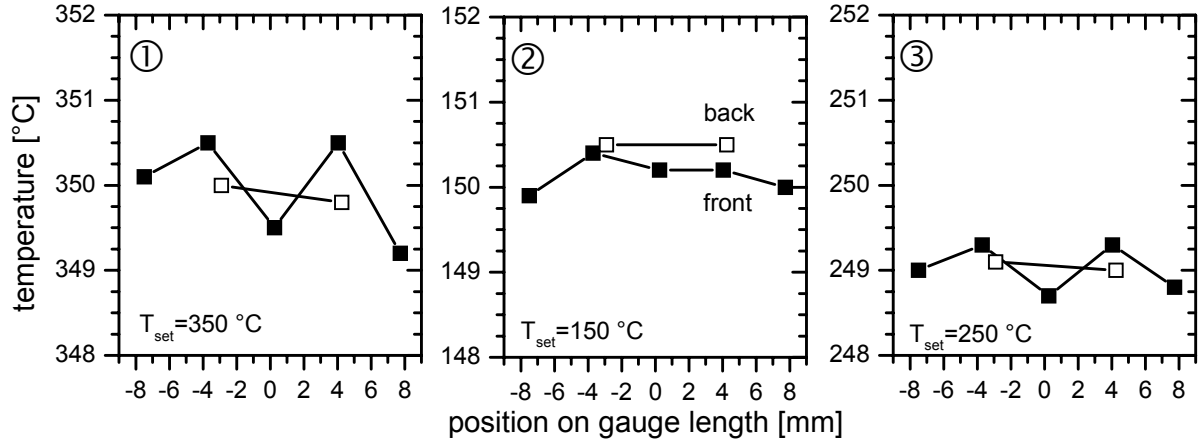

Figure 4.11: *Temperature distribution on the gage length of a compression specimen at the end of the high-temperature dwell (①), at the end of the low temperature dwell (②) and in the middle of the heating ramp (③) for standard thermal cycles (350 °C - 150 °C, 600 sec. period, 1 minute dwell).*

For the thermal cycles with a 600 second period and 350 °C and 150 °C as the extreme temperatures, the specimen temperature follows the command signal quite well. If the minimum

temperature is set to lower values, say 100 °C, deviations from the desired cooling curve occur and the time-lag becomes longer. This, however, does not increase the thermal gradients within the specimen.

4.2.5 Strain Measurement

The specimen strain in the gage section was measured using a high-temperature side-contact extensometer by Schenck. It is based on a standard clip-on extensometer with resistor strain gages, which is connected to two ceramic rods with straight knife edges at one end. The ceramic rods are mounted on a leaf spring that serves two purposes: first it presses the tips of the rods with a constant force against the specimen and second it is the hinge of the lever system that transmits the specimen strain via the rods to the clip-gage. The technical strain ε_t is calculated from the conditioned voltage readings V as

$$\varepsilon_t = \frac{V \cdot k}{f_{Scale} \cdot L_0}, \qquad \textbf{(4-11)}$$

with k being the calibration constant of the extensometer and f_{Scale} being the scaling factor (amplification of the output voltage). In the following, the different contributions to the error of extensometry will be briefly discussed.

- *Voltage measurements*. It has been found that the voltage readings at constant strain scatter within 5 mV in the signal range of ±10 V. This scatter can be numerically reduced to less than 1 mV by averaging over multiple measurements at constant strain. This technique however is not applicable to dynamic measurements. The resolution of the 12-bit analog to digital converter has the same magnitude: about 1 mV within ±2 V, 2.5 mV within ±5 V and 5 mV within ±10 V. The non-linearity of the voltage measurements was found to be less than 0.1% within ±10 V. The scaling factor f_{Scale} can be set to 1:1, 1:2 or 1:5 manually. The error of the amplification is already considered in the non-linearity of the voltage measurements.
- *Calibration factor*. The calibration factor k is given by the geometry of the extensometer and the properties of the resistor strain gages. Calibrating the extensometer with a calibration device employing a drum micrometer gave a factor k of 0.1501 mm/V with a non-linearity smaller than 0.2%.
- *Gage length*. The largest error in measuring the strain is introduced by the determination of the initial gage length L_0. Before each experiment, the extensometer was put up against a double notched bar with a known notch separation of 13 mm and strain measurement was zeroed. Then the extensometer was put up to the sample and the initial gage length was calculated from the strain readings. After that, the strain readings were zeroed again. In an analysis of over 50 experiments within 24 months, the mean gage length was found to be 12.887 mm with a standard deviation of 0.026 mm and maximum deviation of less than

±0.08 mm. This statistical analysis gives a relative error of less than 0.6% for the gage length determination. It however neglects systematic errors that may be introduced by the non-linearity of the voltage measurements (<0.1%) or an error in the calibration constant k (<0.2%). Adding up all these errors, the relative error for the L_0-determination is less than 0.9% (≈0.12 mm).

In Table 4.1, errors for strain measurement are given at different strains and different settings for the signal scaling. It can be seen that the relative error is usually less than 1.5%. If however strains from one and the same experiment are compared to each other (e.g. when the opening of a strain hysteresis during a thermal cycle is calculated), the result does no longer depend on the initial gage length L_0 and so the error from L_0-determination is eliminated. In this case, the accuracy becomes better than 0.6% (or $4 \cdot 10^{-5}$ in absolute values) for the frequent case of low strains and high signal amplifications.

tech. strain []	**$1 \cdot 10^{-3}$**	**$1 \cdot 10^{-3}$**	**$1 \cdot 10^{-2}$**	**$1 \cdot 10^{-2}$**	**$2 \cdot 10^{-2}$**	**$2 \cdot 10^{-2}$**	**$2 \cdot 10^{-2}$**	**$5 \cdot 10^{-2}$**	**$5 \cdot 10^{-2}$**
Scaling	1:2	1:5	1:2	1:5	1:1	1:2	1:5	1:1	1:2
calibration k	0.1501 [mm/V]								
linearity error	< 0.2 %								
gage length L_0	12.887 [mm]								
Error	< 0.9 %								
voltage [V]	0.1717	0.4293	1.7171	4.2928	1.7171	3.4342	8.5856	4.2928	8.5856
noise [V]	< 0.0050 V								
digital resol. [V]	0.0010	0.0010	0.0010	0.0024	0.0010	0.0024	0.0049	0.0024	0.0049
linearity error	< 0.1 [%]								
voltage error [%]	3.01	1.26	0.39	0.22	0.39	0.25	0.16	0.22	0.16
strain error (relative) [%]	4.11	2.36	1.49	1.32	1.49	1.35	1.26	1.32	1.26
strain error []	**$4.1 \cdot 10^{-5}$**	**$2.4 \cdot 10^{-5}$**	**$1.5 \cdot 10^{-4}$**	**$1.3 \cdot 10^{-4}$**	**$3.0 \cdot 10^{-4}$**	**$2.7 \cdot 10^{-4}$**	**$2.5 \cdot 10^{-4}$**	**$6.6 \cdot 10^{-4}$**	**$6.3 \cdot 10^{-4}$**

Table 4.1: *Errors for strain measurement at various strains and for different scaling. All values refer to technical strains.*

4.2.6 Computer Control and Data Acquisition

Figure 4.12 shows the setup of the measuring system in a block diagram: A customary personal computer was interfaced to various devices via a GPIB-Bus (IEEE 488) or a serial bus so that most of the functionality of the devices was controllable by a self-written software

running on that computer. The software serves two purposes, namely data acquisition and experiment control.

- Experiment control. A single experiment was programmed as a sequence of isothermal or thermal cycling segments with individual loads, temperatures and data acquisition rates. For each segment, a set of data limits (maximum and minimum strain or load, maximum number of cycles etc.) was given. When one of them was exceeded, the experiment was continued with the next segment or ended automatically.
- Data acquisition. During an experiment, time, strain, load and all thermocouple readings were measured with a frequency of usually 0.5 Hz. All data were stored to hard disk in a separate file for each segment of the experiment.

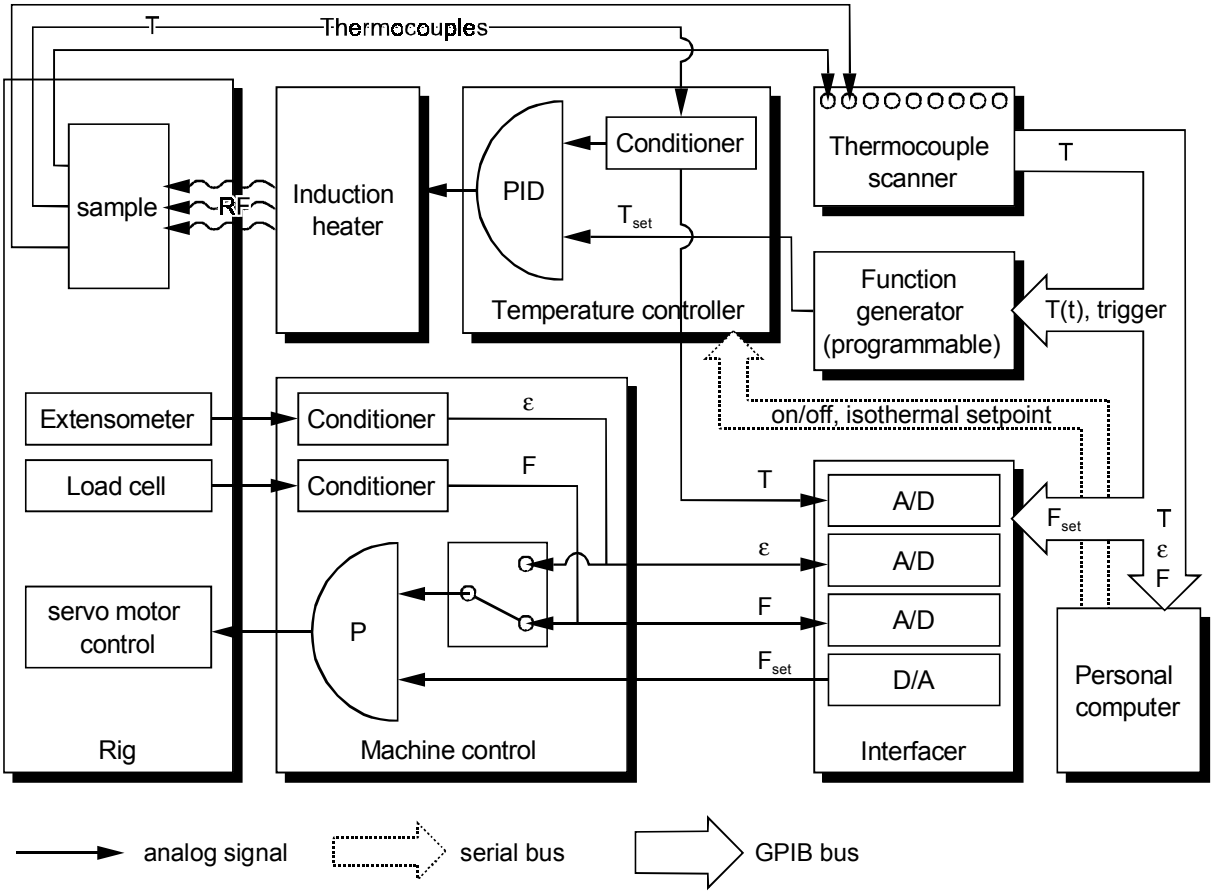

Figure 4.12: *Block diagram of the testing system circuitry.*

4.3 Experiments and Evaluation

A great variety of experiments can be performed with the setup and controlling software described in section 4.2.6. In the following, the general procedures of several kinds of experiments that have been performed within this work are described. In the results section, frequent reference will be made to these testing procedures.

4.3.1 Thermal Cycling Creep Tests

TCC-Test with Initial Load-Free Cycling

The specimen, equipped with thermocouples, is mounted in the testing machine under zero load control and the extensometer is attached. It is then heated to an annealing temperature and kept there for some time to overage the matrix alloy. Then the specimen is subjected to a number of thermal cycles until a stable strain-temperature hysteresis is reached. After the initial load-free cycling stage, the desired external load is applied and held constant for the rest of the experiment. The thermal cycling creep test is run until specimen fracture occurs. Load, temperature distribution and strain are measured and recorded continuously throughout the experiment.

An example for such a test is shown in Figure 4.13. The evolution of the true strain and the applied load are plotted against time. The origin of the time scale is always set to the point where the external load is first applied. The initial heat treatment (over-aging) consisted of a 30-minute dwell at 350 °C and was followed by 26 load-free thermal cycles. Afterwards, a tensile load of 40 MPa was applied. Specimen fracture occurred at the beginning of cycle number 86.

The thermal cycle used in this experiment was a standard 350↔150 °C cycle with a cycle duration of t_c=10 minutes, including dwell times of 1 minute at the extreme temperatures and linear heating and cooling ramps (see Figure 4.8). The cycles start with the high-temperature dwell.

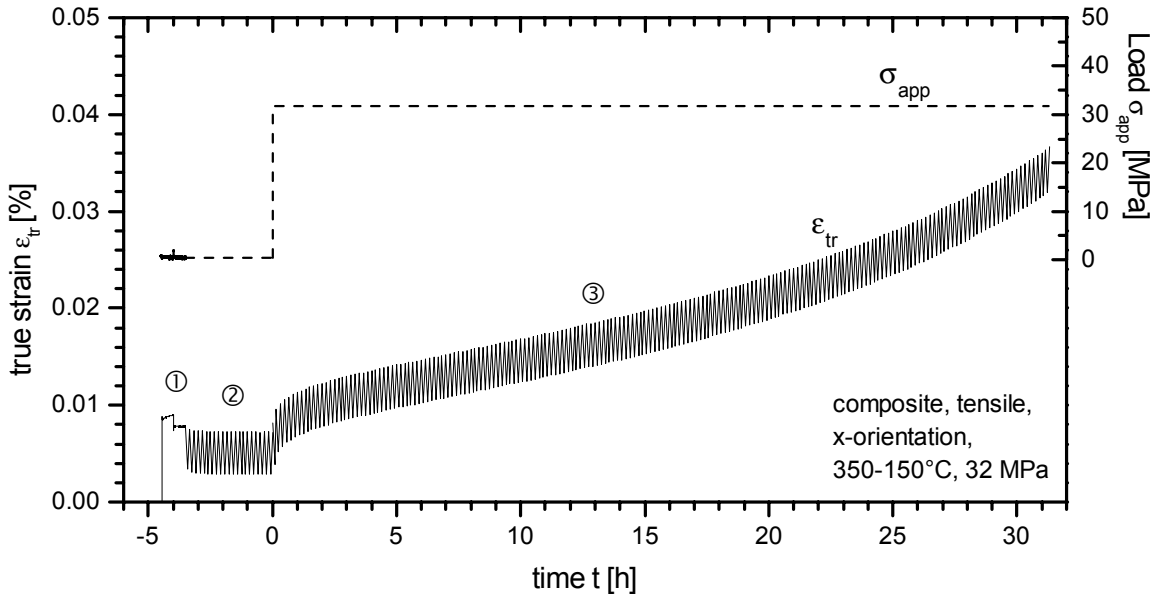

Figure 4.13: *TCC-test with initial load-free cycling. Stages of the experiment are: ① thermal treatment, ② load-free thermal cycling and ③ thermal cycling with an applied creep load of 32 MPa.*

This test type had to be slightly modified for compressive tests: Instead of mounting the specimens under zero load, a slight compressive pre-load of less than 1.5 MPa had to be

applied to ensure gripping of the specimens during the thermal treatment and the initial load-free cycling segments. The compressive experiments were ended at a certain strain or when a defined number of cycles was reached.

Other experiments were performed in which the test sequence was further modified with respect to the thermal cycle (higher amplitude ΔT, other maximum and minimum temperatures T_{min} and T_{max}). In Chapter 5, where the test results are presented, it is distinguished between tests with standard cycles (350↔150 °C) and cycles with a T_{max} higher than 350 °C.

TCC-Test with Stepwise Loading

In order to accelerate the experimental procedure and to save specimen material, creep experiments are often conducted in a stepwise manner, where a single specimen is tested at various external loads, with only few percents of strain at each stress level. Those stepwise creep tests can be applied only if the tested material exhibits pronounced secondary creep and when transient as well as tertiary creep are limited. In conventional creep testing, such a stepwise loading technique is frequently called “single sample technique”. This type of test is also relatively wide spread in thermal cycling creep testing. In the scope of this work, such tests were conducted as follows: The initial heat treatment and load-free cycling stages were performed as described above. The following loaded thermal cycling stages were each run to a certain strain (typically < 1%) or to a defined number of cycles before the load was changed for the next segment. The load was usually incremented a few times before it was reduced again to a low level in order to check for reproducibility of the individual creep rates.

An example for the output of such a test is given in Figure 4.14. A compressive specimen of the matrix alloy was mounted in the testing machine under a gripping stress of -1.5 MPa. The initial treatment consisted of a 1 hour anneal at 400 °C, followed by 30 thermal cycles under the gripping stress. The thermal cycles in this experiment had the same form as the standard cycles mentioned before with the exception that the maximum and minimum temperatures were 400 and 200 °C. Under these conditions, the matrix alloy showed measurable thermal cycling creep deformation already at the gripping stress. In this case, the term “load-free cycling” for the initial segment seems inappropriate. The expression is nevertheless used for sake of consistency. After the initial treatment, the stress was increased to -4, then -6, -8. -10 and -12 MPa. For the final segments, a stress level of again -4 MPa was set. The control program ended each segment when a previously defined amount of strain (which included the elastic strain from the stress change) had accumulated. The limiting strains for each segment were chosen according to the applied stresses. For low stresses, strains of typically 0.3 or 0.4% were chosen, while for the higher stresses, where the (average) strain rate was higher, the strain limit was set to 0.6 to 1%. The control program was also capable to end a segment after a given number of cycles.

The whole testing sequence included series of segments, where not the stress but the cycle duration was changed. This was done at one low stress level and also at one high stress level, to assess the time-dependence of the thermal cycling creep rate.

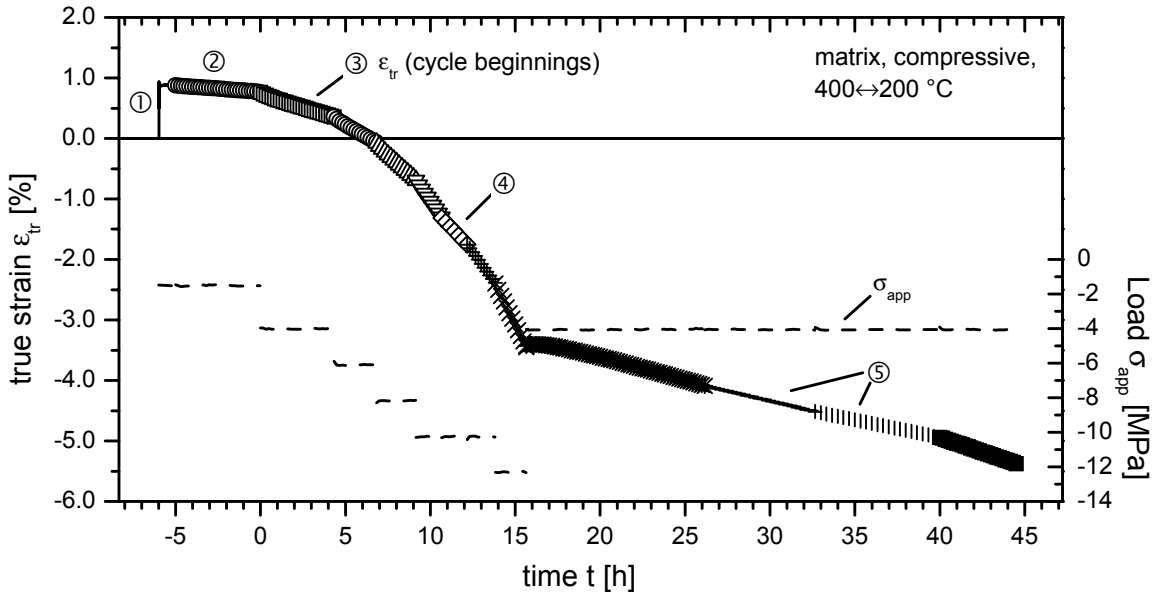

Figure 4.14: *TCC test with initial load-free cycling and stepwise loading. Only the strain readings at the beginning of each cycle are shown. Phases of the experiment were: ① thermal treatment, ② load-free thermal cycling and ③ loaded thermal cycling with increasing stresses. ④ and ⑤ indicate a variation of cycle duration for successive segments at constant stress.*

Evaluation of Thermal Cycling Creep Rates

TCC tests were usually evaluated from plots of true strain versus time, where only the strain readings at the very beginning of each cycle are plotted (see Figure 4.14). After a data smoothing operation (averaging over adjacent data points), derivatives of these curves were taken and the minimum of the derivatives was referred to as the thermal cycling creep rate. Apart from the minimum creep rate at a given stress, the transitional behavior after load changes was found to be of interest. Therefore, the results of the TCC tests will be frequently presented as plots of absolute strain rate (logarithmic) vs. accumulated creep strain (linear) in the results section.

The determination of thermal cycling creep rates was limited with respect to applicable stresses and the time that one is ready to invest into a single test. The lowest applicable stresses that were held sufficiently stable by the testing machine were around 1 MPa (this is about the gripping stress applied on the compressive samples). In most cases, such low stresses led to very low creep rates. Strain rates below 10^{-8} 1/s were rarely measured, because such experiments were very time-consuming, especially when the transitional regime was pronounced.

Evaluation of Strain Evolution in Individual Thermal Cycles

Different researchers have successfully attempted to gain insight into the mechanisms involved in thermal cycling creep by examining the strain evolution in individual thermal cycles. This was done by directly measuring phase strains using diffraction techniques (Daymond and Withers (1996), Daymond and Withers (1997)) or by precisely measuring the macroscopic strain evolution (Furness and Clyne (1991b), Gordon and Clyne (1993), Daymond and Withers (1997)). The commercial composite investigated in the present work was not suited for diffractive strain measurements: The multi-phase matrix was highly alloyed with presumably strong local variations in composition and the fibers had a weak texture and were nanocrystalline. The experimental setup described above, however, was well suited for precise strain measurements and so the route of investigating macroscopic strain changes was followed.

If one considers the measured macroscopic strain evolution, the view is obstructed most of the time by (recoverable) thermoelastic expansion strains, which are usually much larger than the inelastic contribution. A straightforward way to overcome this problem would be to subtract experimentally determined thermal expansion curves from the measured TCC cycles. This, however, will give misleading results, because inelastic strains that occur during load-free cycling are neglected. Alternatively, one can subtract *calculated* thermal expansion curves for purely thermoelastic deformation from the measured strains (done e.g. by Furness and Clyne (1991b)). These calculations, however, are usually based on a simplified composite model and the approximations made in such a model introduce uncertainties in the analysis.

In this work, it was chosen to follow an approach by Daymond and Withers Daymond and Withers (1997). They presented the in-cycle strain evolution in terms of the so-called "instantaneous CTE" α_{inst}, which is simply the first differential of measured strain with respect to temperature[*]. This does of course not overcome the principal problem that inelastic strains occur in both loaded and unloaded cycles. Taking derivatives is a good way to bring out the slight changes in the thermal strain hysteresis due to applied load, without having to modify the primary experimental data by some strain compensation method.

As useful as the instantaneous CTE is, it is hard to determine meaningful derivatives from the experimentally acquired strain data. The main reason for this is the noise level of the strain measurement which is high compared to the considered inelastic strain effects. This can be overcome in part by applying suitable data smoothing methods. In this work, the following smoothing procedure was employed: First, the strain and temperature vs. time curves were

[*] The CTE is usually defined for thermal expansion with no external load applied. Daymond and Withers nevertheless used the term "instantaneous CTE" also for loaded thermal cycling. Their terminology was adapted here because of its simplicity and for consistency with the literature. Moreover, most of the inelastic strain within a thermal cycle is fully reversed and the share of not reversed inelastic strain due to the applied load is comparatively small.

averaged over several (typically 4 or 5) subsequent cycles, provided that the residual strain per cycle was more or less constant in all of these cycles. Then the $T(t)$- and $\varepsilon(t)$-curves were separately subjected to a Fast-Fourier-Transform (FFT) smoothing operation, which filtered out frequencies above 0.1 Hz (the sampling rate was 0.5 Hz). After that, the data was reorganized to give a strain with temperature ($\varepsilon(T)$) cycle which was split up in a heating and a cooling half-cycle. The two half-cycles were then numerically differentiated to give the final curves of instantaneous CTE. It should be noted here that all attempts to approximate the raw data by an analytical function and then taking the derivative of the best fit gave less reliable curves and frequently misleading results.

4.3.2 Isothermal Stress Cycling Creep Tests

A series of experiments were performed in which not the temperature but the applied stress was cycled*. After the initial heat treatment, the applied stress was changed from segment to segment between the creep stress and the low gripping stress, so that after each creep segment, the material was allowed to recover for some time. The purpose of these tests was to investigate back-creep of the material and to determine the material's ability to store elastic strain energy in the reinforcements.

An example for such an experiment is shown in Figure 4.15. Like in the TCC tests, the specimens were subjected to the standard in-situ over-aging treatment after they had been mounted in the testing machine. Afterwards a standard isothermal creep test under load control was undertaken. When the creep strain had increased by a certain increment (typically below 1%), the load was removed (or reduced to the gripping load) and the material was allowed to recover for a certain time (6 hours). After this time, the load was reapplied until the desired strain increment was again reached. This loading/unloading sequence was repeated until a certain total strain ε_t had accumulated. The strain increment under load will subsequently be called "forward strain increment" $\Delta\varepsilon_f$ and the strain that was recovered during the unloaded phase will be called "backward strain" $\Delta\varepsilon_b$. Both quantities include the elastic strain from applying or removing the load as well as the immediate anelastic response. Figure 4.15 shows the strain-time curve for such a test with a forward strain increment of 0.6 %.

* Such tests are frequently referred to as "cyclic creep" tests in the literature. In this work, the term "stress cycling creep" is preferred in order to clearly distinguish it from thermal cycling creep.

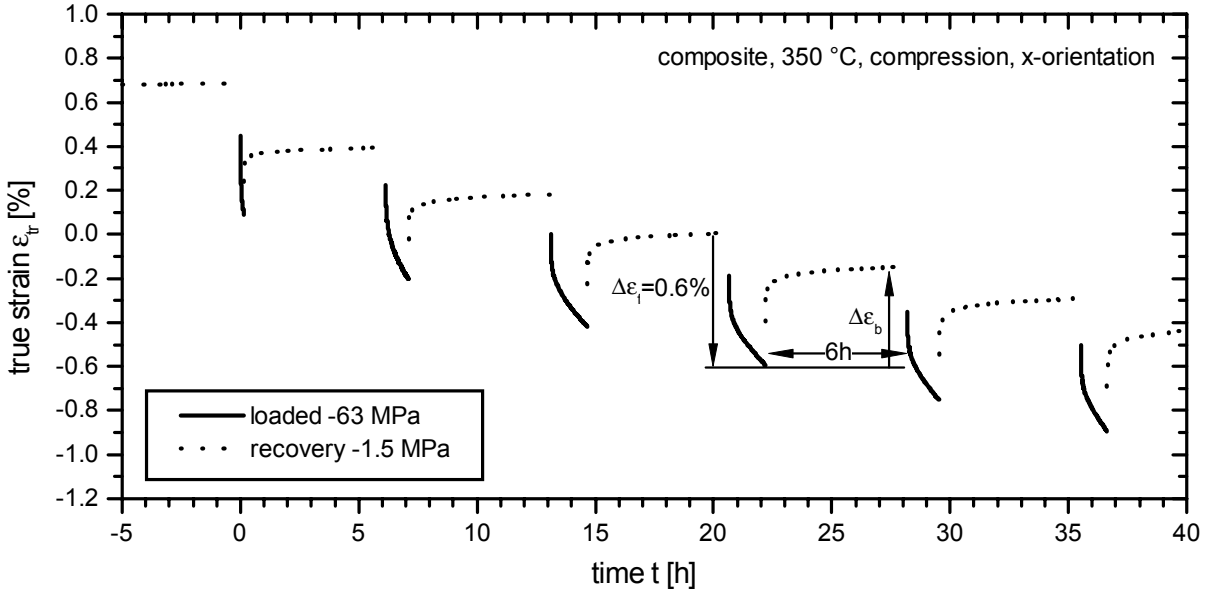

Figure 4.15: *Stress cycling creep test. The first segments of a stress cycling creep test at 350 °C for the composite material are shown. The test parameters were: forward straining at -63 MPa until a strain increment $\Delta\varepsilon_f$ of 0.6% was reached and subsequent recovery at -1.5 MPa for 6 hours.*

5 Results

The results of the experimental work are grouped into five sections in this chapter. Initially the results from image analysis of the composite material, which was done to quantitatively characterize the orientation distribution of the reinforcement phase, are presented. Then, the bulk of the experimental results, namely those from thermal cycling creep tests, are summarized in two sections. Measured creep rates and the net strain curves are presented at first, followed by the strain evolution in individual thermal cycles. In the fourth section, results from isothermal stress cycling creep experiments are supplemented. The chapter is closed with a brief report on the material damage that was found after mechanical testing.

5.1 Reinforcement Microstructure

Detailed image analysis has been carried out for three mutually perpendicular sections of the composite material. The axes of the sections were aligned with the axes x, y and z of the global ingot (plate) coordinate system. Unless indicated otherwise, this global ingot coordinate system will be used throughout this section and the results chapter.

Of each metallographic section, more than 25 images, each containing around 60-120 fibers, were taken and analyzed as described in Chapter 4.

5.1.1 Fiber Thickness

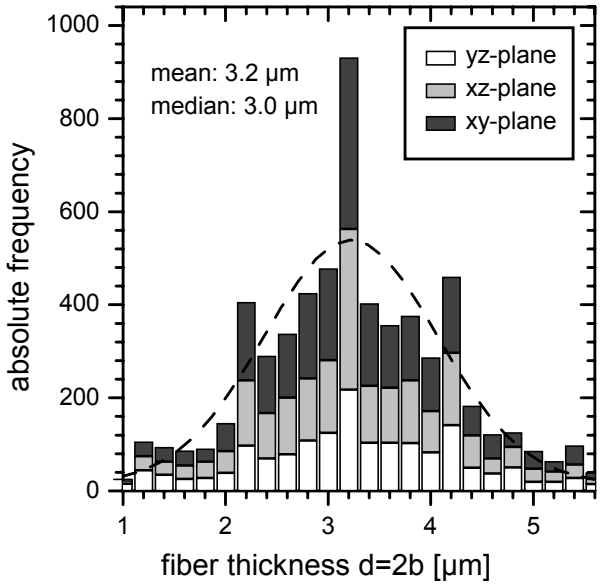

Figure 5.1: *Frequency distribution of fiber thickness as measured by quantitative image analysis.*

The thickness of an individual fiber can be determined from its elliptical cross section. The small semiaxis of the ellipse is the thickness of the sectioned fiber. This value was automatically measured by the image analysis software. In Figure 5.1 a histogram of the thickness distribution is given for the three perpendicular sections. The arithmetic mean thickness was

3.2 µm with a measuring error of 0.2 µm, the median thickness was 3.0 µm. No correlation between the fiber thickness and any orientational parameter of the fiber was found. Thick fibers had the same orientation distribution as thinner ones, i.e. the orientational distribution of fiber thickness was uniform.

5.1.2 Fiber Orientation Tensor

Global Orientation Tensor

The fiber orientation of each individual fiber has been determined with the techniques described in Section 4.1.2. A first graphical representation of the orientation state is given in Figure 5.2. In this diagram, the normalized frequency of in-plane orientations ϕ was plotted in polar diagrams for each metallographic section. The frequencies were corrected with the weighting function $F(\theta)$ (Eq. 4-8). Apart from this correction, this diagram contains no information about the inclination of the fibers. The single polar plots are all oriented in the same local coordinate system (x', y', z'). Also given are the axes of the global ingot coordinate system. From these in-plane fiber orientations, one can already see that there is a preferential orientation of fibers perpendicular to the (global) x-axis. Within this plane, orientational components in z-direction seem to be more strongly represented than the y-direction. Furthermore, the preferential plane appears to be tilted a little along the z-axis.

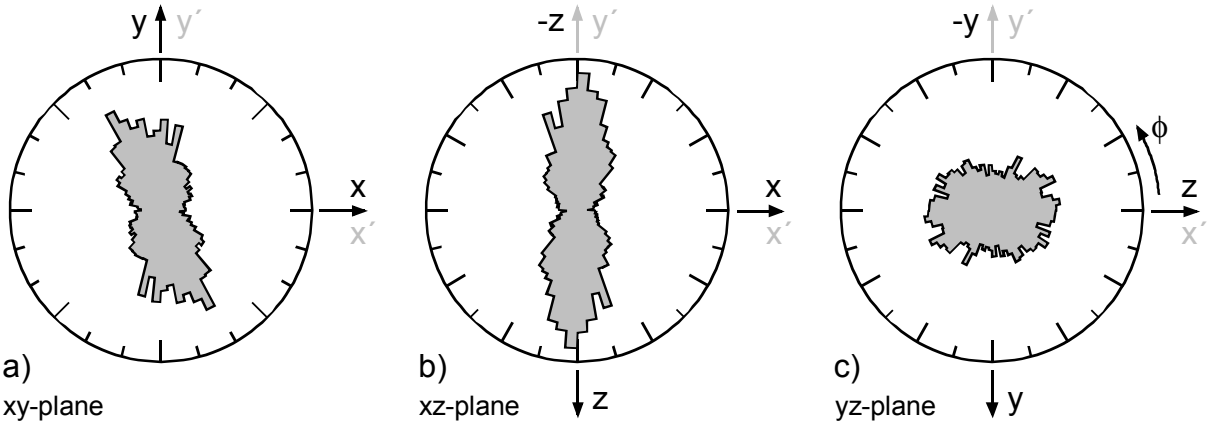

Figure 5.2: *Frequency of the orientation ϕ of the elliptic fiber cross sections in one specific plane: a) in x-y-plane, b) in x-z-plane, c) in y-z-plane. The data are corrected with the weighting function Eq. 4-8. In each diagram, the local (section) coordinate system (x´, y´, z´), which is always identical, is given along with the global (ingot) coordinate system (x, y, z).*

The orientation tensors for these sections were determined according to Equations 4-7 and 4-8 – except for the 13- and 23-components. It has been pointed out in Section 4.1.3 that these components cannot be determined from a single cross section because their sign is ambiguous for an individual fiber. The three orientation tensors that were determined from the metallographic sections, each in its individual coordinate system, were then transformed into the global coordinate system by the transformation rule

$$a_{ij} = \lambda_{ij} \cdot a'_{ij} \cdot \lambda^T_{ij}. \qquad \textbf{(5-12)}$$

Here a_{ij} and a'_{ij} are the orientation tensors in the global (ingot) and local (metallographic section) coordinate system and λ_{ij} and λ^T_{ij} are the transformation matrix and the transposed transformation matrix. The λ_{ij} are the directional cosines between the axes of the different coordinate systems. The local orientation tensors and their transformation to the global coordinate system are given in Table 5.1. The transformation matrices for the orientational relations that are shown in Figure 5.2 are also given there.

Section:	OT in local (section) CS a'_{ij}	Transformation matrix λ_{ij}	OT in global (ingot) CS a_{ij}
xy-plane	$a'^{xy}_{ij} = \begin{pmatrix} 0.21 & -0.045 & ? \\ -0.045 & 0.42 & ? \\ ? & ? & 0.37 \end{pmatrix}$	$\lambda_{ij} = \begin{pmatrix} 1 & 0 & 0 \\ 0 & 1 & 0 \\ 0 & 0 & 1 \end{pmatrix}$	$a^{xy}_{ij} = \begin{pmatrix} 0.21 & -0.045 & ? \\ -0.045 & 0.42 & ? \\ ? & ? & 0.37 \end{pmatrix}$
xz-plane	$a'^{xz}_{ij} = \begin{pmatrix} 0.18 & 0.003 & ? \\ 0.003 & 0.53 & ? \\ ? & ? & 0.29 \end{pmatrix}$	$\lambda_{ij} = \begin{pmatrix} 1 & 0 & 0 \\ 0 & 0 & -1 \\ 0 & 1 & 0 \end{pmatrix}$	$a^{xz}_{ij} = \begin{pmatrix} 0.18 & ? & 0.003 \\ ? & 0.29 & ? \\ 0.003 & ? & 0.53 \end{pmatrix}$
yz-plane	$a'^{yz}_{ij} = \begin{pmatrix} 0.44 & -0.003 & ? \\ -0.003 & 0.35 & ? \\ ? & ? & 0.22 \end{pmatrix}$	$\lambda_{ij} = \begin{pmatrix} 0 & 0 & 1 \\ 0 & -1 & 0 \\ 1 & 0 & 0 \end{pmatrix}$	$a^{yz}_{ij} = \begin{pmatrix} 0.22 & ? & ? \\ -0.045 & 0.35 & 0.003 \\ ? & 0.003 & 0.44 \end{pmatrix}$

Table 5.1: *Orientation tensors as determined from three perpendicular cross sections. Also given are the transformation matrices for the transformation into the global coordinate system and the transformed orientation tensors.*

The diagonal elements of the three transformed tensors should be the same when each cross section contains a representative sample of the global fiber orientation distribution. This was not the case here because of limited sampling and due to the inhomogeneity of the reinforcement. Nevertheless, it was found that the a_{11}-component was always the lowest and the a_{22} and a_{33} components lay closer to each other than to the a_{11}-component. This showed that the fibers were preferentially oriented in the *yz*-plane (perpendicular to the *x*-axis) although the degree of alignment was relatively weak so that still a good portion of fibers had random-3D orientation.

To obtain the complete global fiber orientation tensor, the diagonal tensor components were averaged over all three sections. The local a'_{12}-components were taken to yield the off-diagonal elements. Finally the orientation tensor is given as:

$$a_{ij} = \begin{pmatrix} \frac{1}{3}\left(a^{xy}_{11} + a^{xz}_{11} + a^{yz}_{11}\right) & a'^{xy}_{12} & a'^{xz}_{12} \\ a'^{xy}_{12} & \frac{1}{3}\left(a^{xy}_{11} + a^{xz}_{11} + a^{yz}_{11}\right) & -a'^{yz}_{12} \\ a'^{xz}_{12} & -a'^{yz}_{12} & \frac{1}{3}\left(a^{xy}_{11} + a^{xz}_{11} + a^{yz}_{11}\right) \end{pmatrix} = \begin{pmatrix} 0.20 & -0.045 & 0.003 \\ -0.045 & 0.35 & 0.003 \\ 0.003 & 0.003 & 0.44 \end{pmatrix}$$

The fibers were preferentially oriented in the *yz*-plane with a slight preference of the *z*-direction. In Figure 5.3a this orientation distribution is schematically visualized. The plane of preferential orientation was slightly tilted about the z-axis (a_{12} is largest, a_{13} and a_{23} are very small and can be neglected). This tilt can be due to misalignment of the metallographic section during preparation.

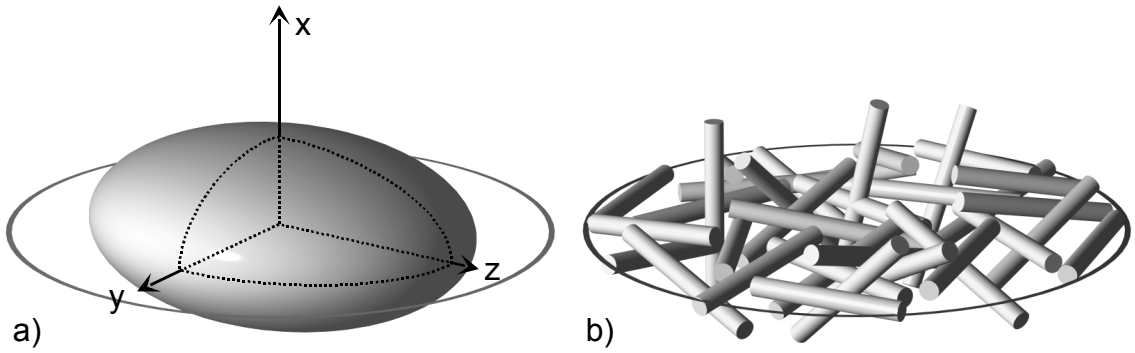

Figure 5.3: *a) Ellipsoid representing the fiber orientation distribution as it is given by the measured orientation tensor. b) Schematic of the orientation of a selection of fibers. Note the preferential orientation of fibers in the yz-plane.*

Local Variations

The above tensor describes the volume averaged orientation state for the whole composite. In this simple description, the local variation of the fiber orientation distribution is of course lost. These local variations can be shown at least qualitatively if the tensor components are not determined for three complete sections but for every single image. In Figure 5.4 some local tensor components $a'_{ij,n}$ that have been obtained from the *n*-th image in the *xy*-section are plotted. It can be seen that there is substantial scatter in the data. Nevertheless, a'_{11} is in general lower than a'_{22} and a'_{33}, which are again very similar.

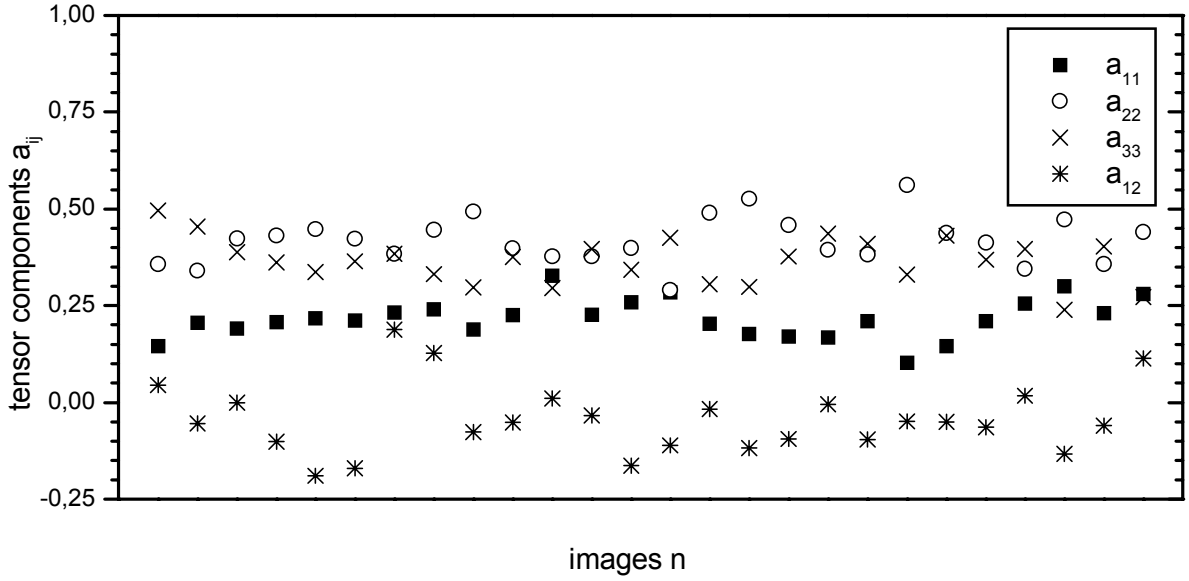

Figure 5.4: *Fiber orientation tensor components for 26 individual images on the xy-plane.*

Relevance of the Image Analysis Results

The results obtained in this section show that the reinforcement was textured and that anisotopic behavior could be expected in mechanical tests. In the following Sections 5.2-5.4, this anisotropy will be considered and experiments will be distinguished according to the specimen orientation. The quantification of the reinforcement texture in the form of an orientation tensor will be of great help in Chapter 6, where material properties are compared to theoretical predictions. The orientation tensor will be used there to determine an Eshelby tensor (see also Appendix A.2) with which thermoelastic properties of the material can be predicted (Sections 6.3.1 and 6.3.4).

5.2 Strain Rates for Thermal Cycling Creep

In the following two sub-sections, composite TCC rates are given first for cycles with low mean temperatures and thermal amplitudes and secondly for more intense thermal loading. In a third sub-section the TCC rates for the matrix material without the reinforcement are presented.

5.2.1 TCC Behavior for 350 ↔ 150 °C Cycles

All test that are presented in this section employed the 350 to 150 °C thermal cycle that was shown in section 4.2.4. The cycle duration was 10 minutes with constant linear heating and cooling rates and dwell times of 1 minute at the upper and lower temperature. The initial heat treatment comprised 30 minute anneals at 400 °C and 350 °C. Load-free cycling lasted for at least 20 cycles before the load was applied. The evolution of strain during this load-free cycling phase is addressed in the following sub-section. Afterwards, results from tensile TCC tests are given as a starting point. Compressive test for various specimen orientations were made to find out whether a tension/compression asymmetry was present under thermal cycling conditions as it had been found in the isothermal case.

Initial Load-Free Cycling

During the load-free cycling, the specimens changed their shape: Within 30 cycles, they contracted in x-direction by approximately -0.09% and they expanded in y- and z-direction by half that value. This behavior is displayed in Figure 5.5 for the first 20 cycles. Although the absolute strain per cycle decreased steadily, no saturation to a constant strain was observed within 50 cycles.

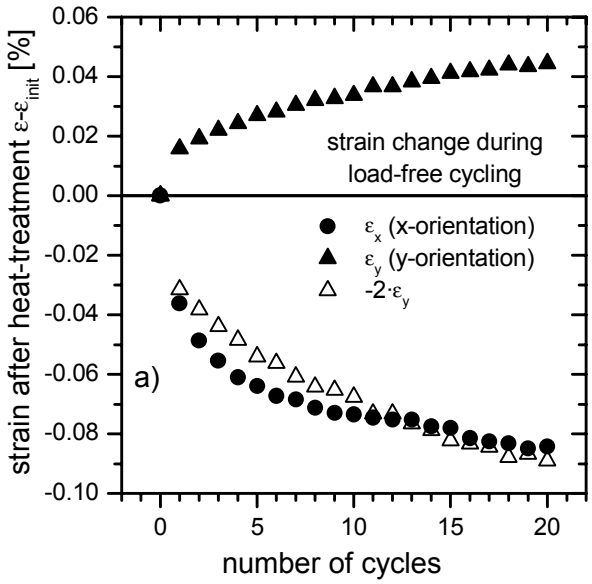

Figure 5.5: *Strain evolution during 20 cycles of load-free cycling. Only the strain readings from the very beginning of each cycle are shown. The specimens contracted in the x-direction and they expanded by half of that value in y- and z-direction.*

Tensile Tests, X-Orientation

Tensile specimens could only be produced with the loading axis in x-direction, which was the direction perpendicular to the plane of preferential fiber orientation (see Section 4.2.2). Three typical tensile TCC-experiments – for a very low, a comparatively high and an intermediate external stress – are shown in Figure 5.6.

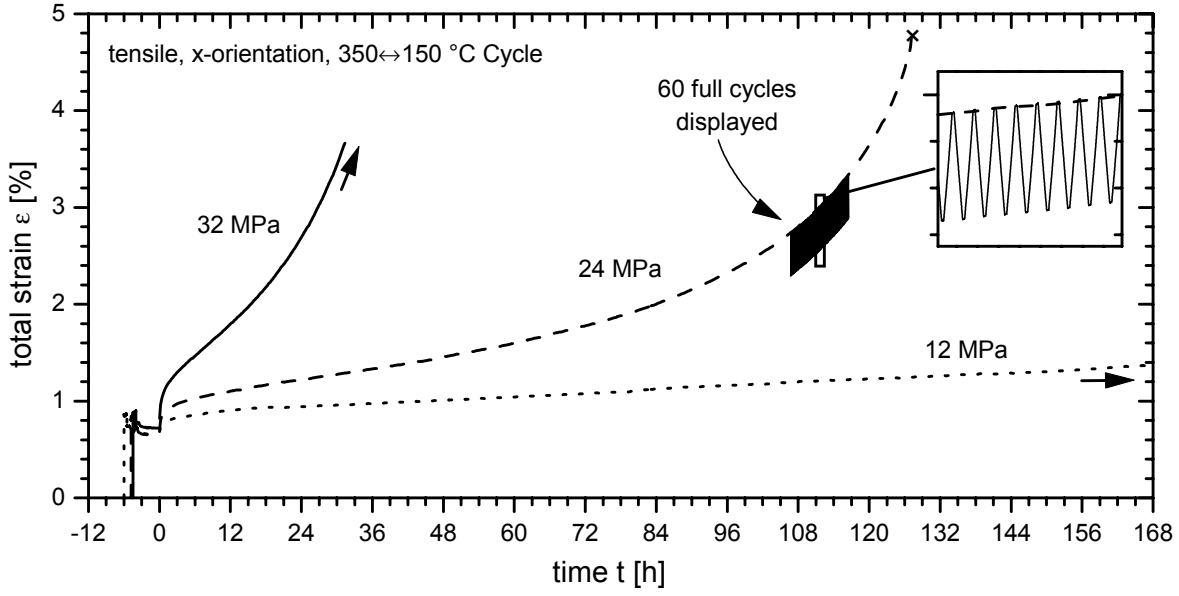

Figure 5.6: *Selected tensile TCC experiments (x-orientation). Strain vs. time for three samples tested at stresses of 12, 24 and 32 MPa. Only the strain readings at the very beginning of each cycle are shown. The plot includes the initial strain due to heating and over-aging of the specimen and due to the load free cycling prior to loading.*

During the load free cycling stage, the specimens contracted slightly in the x-direction (around 0.2% within 20 cycles, see above). After loading, the material displayed a pronounced transitional behavior in all three cases, until a minimum creep rate (i.e. a minimum strain per cycle) was reached. For the high stress, this took about 30, for the lower stresses over 100 cycles.

The minimum creep rate prevailed only for a rather low number of cycles, after which the strain rate started to increase progressively. The test at the lowest stress had been aborted before this increase was observed. In analogy to the three stages of conventional creep, the stages of the overall strain evolution for the thermal cycling creep experiments will from here on be called “primary” or “transitional regime”, “steady state regime” and “tertiary stage”.

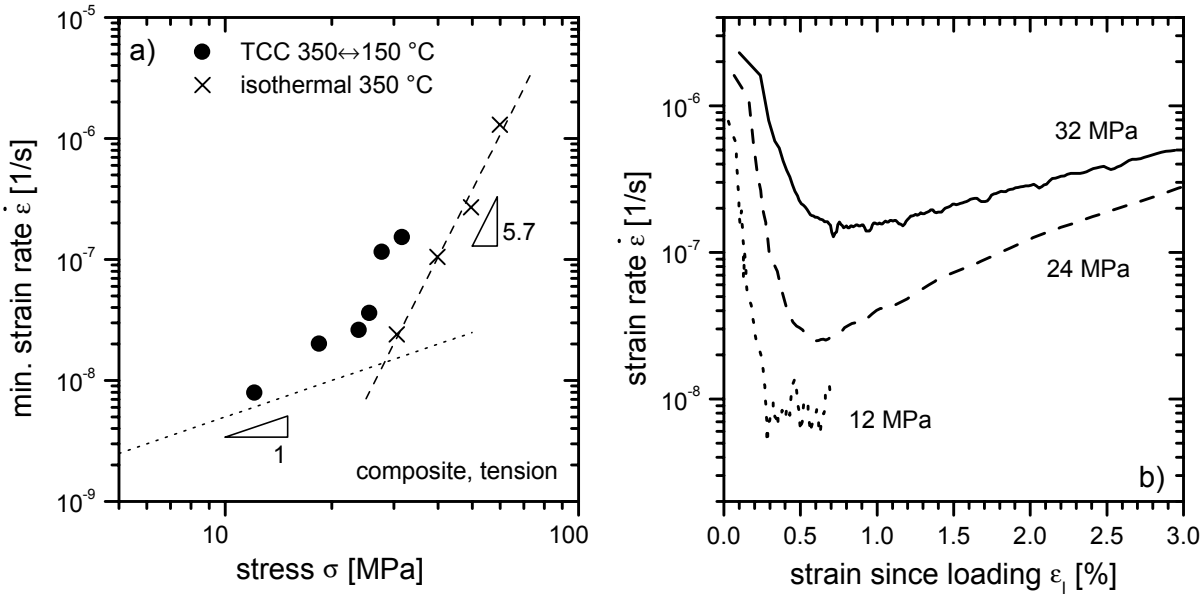

Figure 5.7: *TCC-rates for standard tensile tests in x-orientation. For comparison, the isothermal creep rates at maximum temperature (y-orientation) are given and a guideline with a slope of 1 is drawn. b) transitional behavior for three selected loads: strain rate vs. the strain that had accumulated since the load had been applied. ε_l includes the elastic strain.*

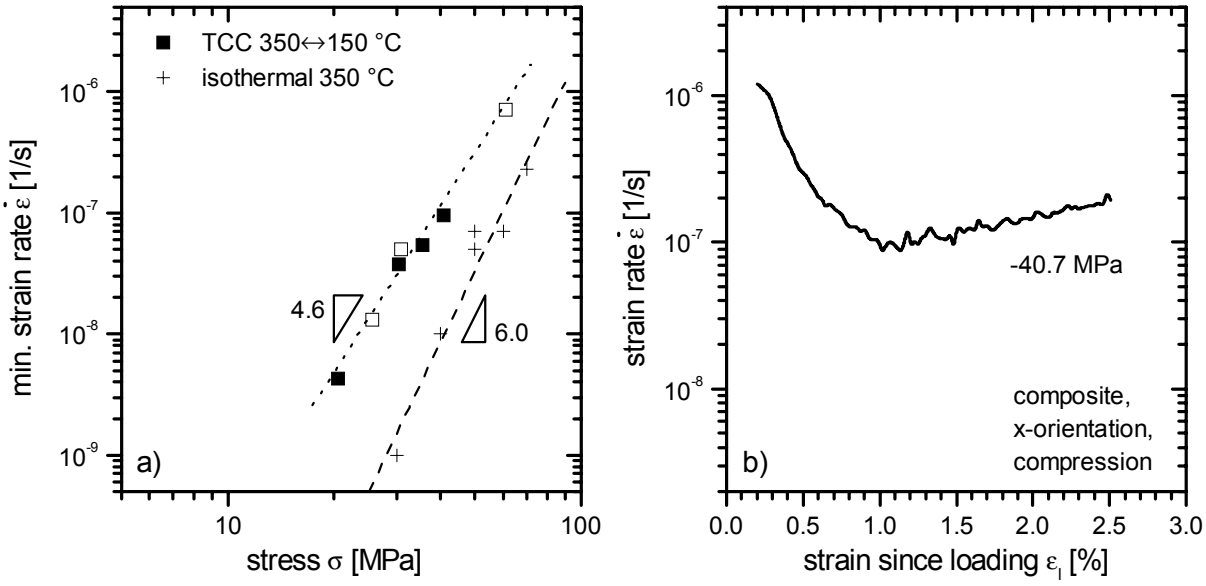

Figure 5.8: *TCC-rates for compressive tests in x-orientation (standard cycle). For comparison, the isothermal compressive creep rates at 350 °C are also shown. Open symbols denote rates that were obtained from the second or a following loading segment in experiments with stepwise incremental loading. b) transitional behavior for a test at -40 MPa, where steady state was reached at slightly more than 1% of creep strain.*

The minimum strain rates from the tensile TCC creep tests (350↔150 °C) with x-orientation are shown in Figure 5.7a. It can be seen that in the stress range under investigation, the TCC-rates were generally higher than the isothermal creep rates at peak temperature. At the higher stresses, the apparent stress exponent of thermal cycling creep approached the one for isothermal behavior, at the low stresses the stress exponent decreased substantially. Yet the classical slope-one-regime of thermal cycling creep at low loads could not be observed in the stress-range investigated.

The initial transitional behavior following the load change is displayed in Figure 5.7b, where the strain rate (determined from the strains per cycle) is plotted versus the strain accumulated since the time of loading. The strain at which the steady state was reached shifted to lower values for decreasing stresses: At 32 MPa, the steady state was reached at around 0.7%, for 24 MPa at around 0.6% and for the lowest load at less than 0.4%.

Only the specimen at 24 MPa was tested until fracture. The fracture strain since loading (including the elastic strain) was 4.1%. In the isothermal case, the fracture strains were always smaller than 1.8% Bidlingmaier et al. (1996a).

Compressive Tests, X-Orientation

The thermal cycling creep behavior depended on the sign of the external load. As in the isothermal case, the creep rates were considerably lower in compression (see Figure 5.8a) than in tension (see section 3.5). Yet thermal cycling still enhanced the creep rate compared to the isothermal case. In the stress range investigated, the thermal cycling creep rates were an order of magnitude higher than the isothermal creep rates. The apparent stress exponent was fairly constant over the whole stress range and with a value of 4.6, it was not much less than the apparent stress exponent for the isothermal case (6.0). The strain rate evolution of one selected compressive creep curve, given in Figure 5.8b, showed a similar transitional behavior as observed for tensile loading. However, if one compares tensile and compressive tests with similar minimum creep rates (Fig. 5.8b and 5.7b), it can be seen that the strain at which the steady state was reached was considerably larger in the case of compression. In the case of isothermal creep, no such difference in the transitional strain was found. This can be seen in comparing Bidlingmaier's and Wolf's data (Bidlingmaier et al. (1996a), Wolf (1997)).

Compressive Tests, Y- and Z-Orientation

On changing the orientation of the specimens from *x*- to *y*-orientation the thermal cycling creep rates decreased even further. The loading axis was then no longer *perpendicular* but *parallel* to the plane of preferential fiber orientation. For the two specimens that were tested, the creep rates lay in between those for TCC in x-orientation and the isothermal creep rates at peak temperature (compare Figures 5.9a and 5.8a). The stress exponent estimated from the two data points is 4.7. The transitional behavior, which is shown in Figure 5.9b, showed the

same stress-dependence as for x-orientation in tension: Lower stresses led to shorter transitions. The compression creep curve for the higher load did not differ substantially from the one for x-orientation. For both orientations, the minimum creep rate was reached at slightly more than 1% of creep strain.

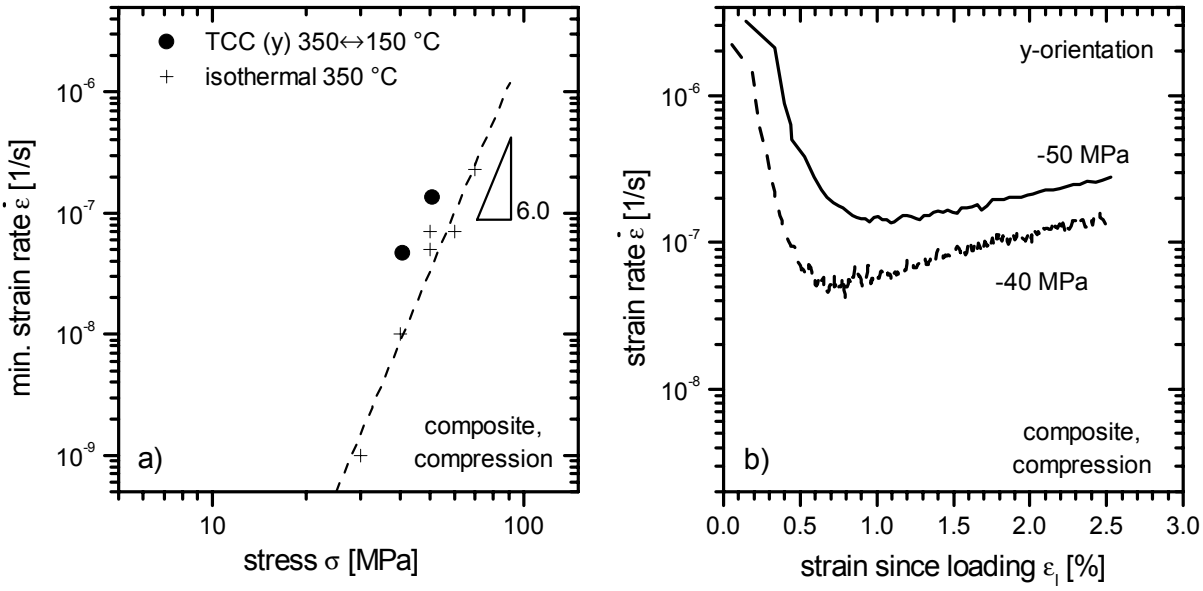

Figure 5.9: *a) Rates for two compressive TCC-experiments in y-orientation (standard cycle). b) transitional behavior for these test.*

5.2.2 Effect of Cycling to Higher Temperatures

The maximum temperature of 350 °C in the standard cycles was chosen to roughly reflect service conditions in an engine environment. It could be seen in the previous section that for the standard cycles, the strains per cycle were very small – especially at low loads – and thus difficult to measure experimentally. In order to get better insight in the behavior at low loads, a few test series were performed with thermal cycles that went to comparatively high maximum temperatures. In the following, the term "high-temperature cycle" will be used for cycles with a T_{max} higher than 350 °C.

These high-temperature cycles resulted in higher strain rates, lower apparent stress exponents and shorter transitional regimes. Under these conditions, time- and specimen-saving tests with stepwise loading could be more reasonably conducted. Interesting investigations such as studying the influence of the thermal excursion or studying the influence of a high-temperature dwell time could be made using only few specimens. Results from these investigations are presented in the following sub-sections.

X-Orientation

Two tests were performed with specimens in x-orientation. The thermal cycle was similar to the standard cycle, with identical cycle duration (600 seconds) and dwell times of 1 minute at

the extreme temperatures. However, the maximum and minimum temperatures were altered, which also changed the rates for the linear heating and cooling ramps. The rates that are shown in Figure 5.10 were determined from TCC-tests with stepwise increasing loads (single sample technique), starting with the lowest load. It can be seen that in both cases the apparent stress exponent became small for very low loads. The stresses were, however, not low enough to reach a slope of one. At higher stresses, the apparent stress exponent increased to values close to those for isothermal creep. Further comparisons of the curves are not meaningful because of the differences in both the thermal cycle and the sign of loading.

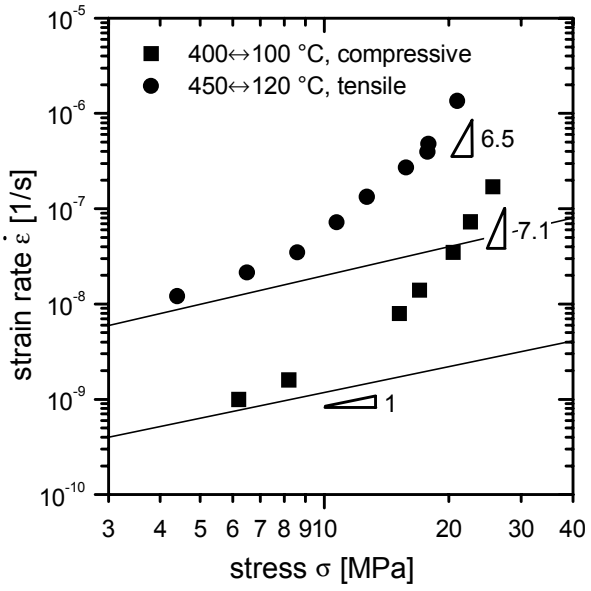

Figure 5.10: *TCC rates for specimens in x-orientation tested with high-temperature cycles. The rates were obtained from tests with stepwise incremental loading. At low loads, the apparent stress exponent approached unity, at high loads it was close to the values for isothermal creep.*

Influence of Thermal Amplitude

For a tensile specimen (*x*-orientation), a special experiment was conducted to assess the influence of the magnitude of the thermal excursion on the TCC rate. In this experiment, the specimen was kept at a stress of 8.5 MPa in tension while the amplitude of the thermal cycles was altered every 50 cycles. The maximum temperature of the cycles was always 450 °C and each cycle included a dwell time of 1 minute at T_{min} and T_{max}. The heating and cooling rates of the linear ramps were kept constant at (±)50 K/min (0.833 K/s). This means that upon changing the minimum temperature of a cycle, the cycle duration was also changed. The amplitude was varied from 50 K (450↔400 °C) up to 370 K (450↔80 °C). The sequence of the cycle types was not ordered. Usually, a 50-cycle segment with a high amplitude was followed by 50 cycles with a lower amplitude and vice-versa. Average strain rates were determined from the last 30 cycles of each segment. Because the cycle duration was varying with the amplitude, it was better to quantify the TCC rate in terms of strain per cycle rather than by the average strain rate. The results are presented in Figure 5.11. The average strain per cycle stayed at a relatively low level with considerable scatter up to a thermal excursion of 250 °C. For high cycle amplitudes of 300 °C and higher, the strain per cycle rose above that level. A data point

from the 450↔120°C experiment that was shown in Figure 5.10 for the same load fell well within the trend (open symbol in Figure 5.11). The load was also 8.5 MPa and the parameters of the thermal cycle were the same except for the higher heating and cooling rates.

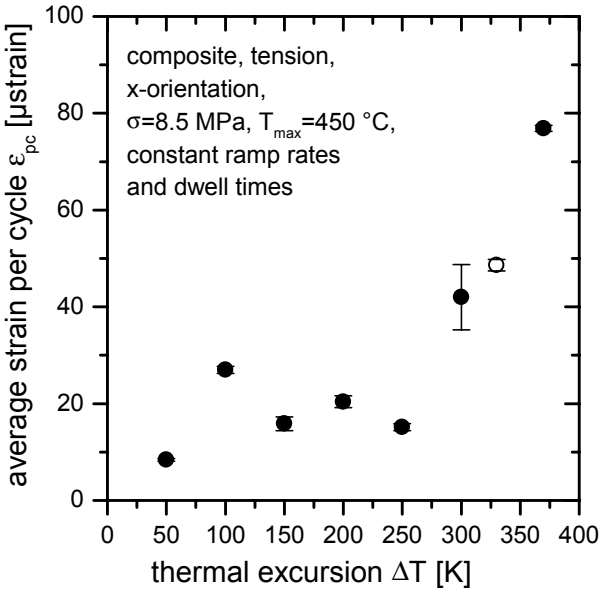

Figure 5.11: *Influence of the thermal amplitude on the strain per cycle. Tensile test (x-orientation) at a constant load of 8.5 MPa. Ramp rates were 50 K/min, dwell times of 1 minutes were introduced at T_{max} and T_{min}. T_{max} was always 450 °C. It can be seen that the average strain per cycle in general was low but rose with increasing cycle amplitude. The open symbol denotes a data point from a TCC experiment that was shown in Fig. 5.10 (cycle parameters are the same except for the heating/cooling rates, which are higher).*

Regarding the transitional behavior, it was found that after a change in cycle amplitude, the strain evolution underwent a measurable transition of up to 5 cycles until a steady strain rate was achieved. This is remarkable because the externally applied load was not changed throughout the experiment. If the amplitude of the cycle was lowered, the TCC-strain rate became initially high and sank to the steady state value. If the cycle amplitude was increased, an inverse transition was observed, i.e. the TCC rate was initially negative until again a positive steady state TCC-rate was established. The higher the change in thermal amplitude was, the more pronounced was the transitional behavior. However, the transitions are much smaller that those that are commonly found upon load changes.

Influence of High-Temperature Dwell

The effect of the high-temperature dwell on the TCC behavior was studied by a series of compression tests on specimens with *y*-orientation. The temperature was cycled between 450 and 100 °C with linear heating and cooling ramps of 240 seconds and a lower dwell time of 60 seconds. High-temperature dwell times of 0, 60 and 360 seconds were investigated, corresponding to overall cycle periods of 540, 600 and 900 minutes. The tests were conducted with the stepwise loading procedure, starting with the lowest load. The average thermal cycling creep rates from the steady state are shown in Figure 5.12a. In Figure 5.12b), the corresponding strains per cycle are given.

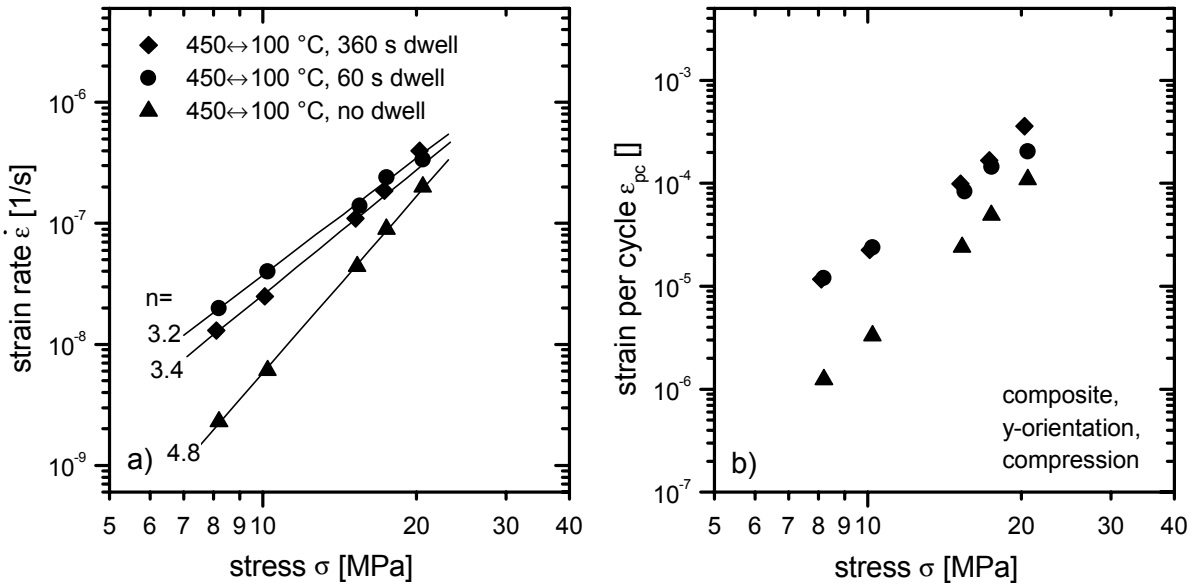

Figure 5.12: *TCC rates and strains per cycle for changing the high-temperature dwell time of the thermal cycle. The rates for each type of cycle were measured in compressive TCC tests with stepwise increasing load on a single specimen (y-orientation). The extreme temperatures were 450 and 100 °C, the linear heating and cooling ramps took 4 minutes, and the low-temperature dwell time was 1 minute. The high-temperature dwell was varied from no dwell (0 seconds) over short dwell (60 seconds) to long dwell (360 seconds).*

The lowest average strains per cycle and creep rates were found for the case when no high-temperature dwell was employed. Although a short high-temperature dwell in each cycle increased the average strain per cycle substantially (especially at low loads), the even longer dwell time led to no further increase. Along with the increasing rates, the apparent stress exponents became lower. The stress exponents were roughly the same for both tests with high-temperature dwell times.

5.2.3 Thermal Cycling Creep (TCC) Behavior of the Matrix Alloy

The matrix alloy itself can be considered as a composite with an aluminum matrix and 12 wt.% of silicon platelets and intermetallic phases as reinforcements. In fact, in TCC tests it was found that the matrix alloy exhibited a composite-like increase of the average creep rate and a decrease in the apparent stress exponent. Minimum strain rates from TCC tests with stepwise loading are shown in Figure 5.13. For the standard 350↔150 °C cycle, the minimum creep rate had an apparent stress exponent of n_{app}=2.5 (compared to 4.5 for isothermal creep at $T_{\max}$) which was constant in the investigated stress range. For cycles to higher temperatures, this was no longer so. The apparent stress exponent decreased with decreasing load down to a value of n_{app}=1.2 (for a 400↔100 °C cycle, see Figure 5.13b and c).

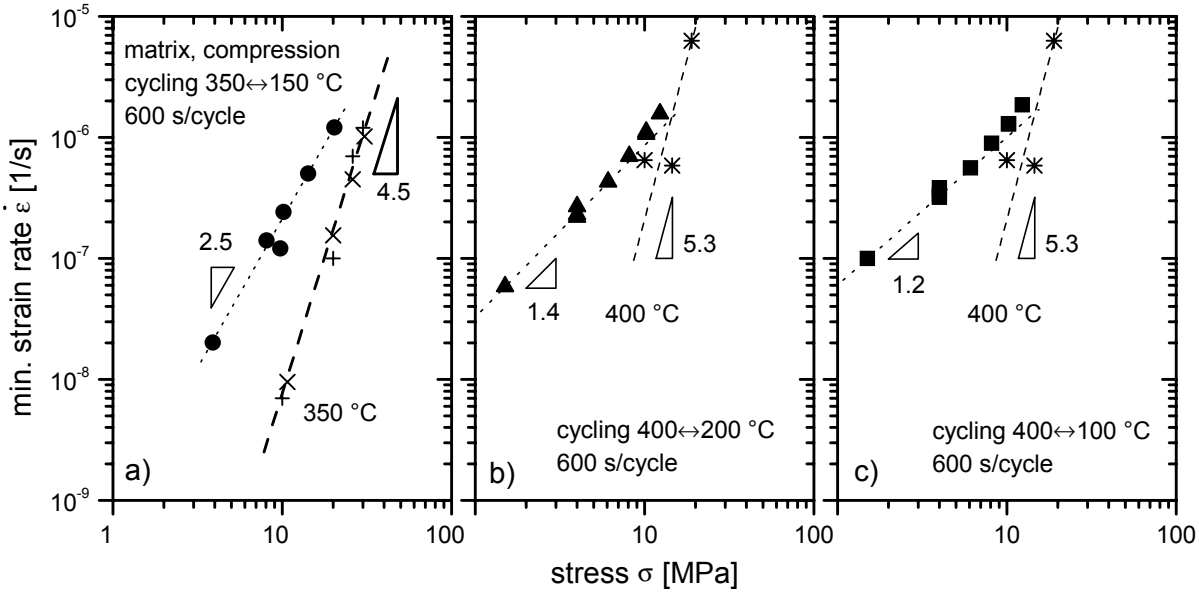

Figure 5.13: *Thermal cycling creep rates for the matrix material (compressive) a) standard cycles 350↔150 °C, b) cycling 400↔200 °C and c) thermal cycling 400↔100 °C. Cycle duration was 10 minutes, with linear heating and cooling and 1-minute dwell times at T_{max} and T_{min}. For comparison, isothermal creep rates at T_{max}, (Bidlingmaier et al. (1996a)) are given.*

5.2.4 Summary of TCC Strain Rate Results

TCC for Standard Cycles

For all standard TCC-tests that were performed in the present work, the minimum creep rates were always higher than isothermal creep rates measured at the maximum temperature of the cycle. A tension/compression asymmetry, like it was found for isothermal creep, was also present under thermal cycling conditions. This kind of behavior has not been published before for thermal cycling creep of MMCs. Moreover, the TCC-rates showed an orientation dependence: For *x*-oriented specimens (loading perpendicular to the plane of preferential fiber orientation) the rates were higher than for *y*-orientation. The apparent stress exponents were found to be generally lower than for isothermal creep but still larger than one. Only for tensile loading (*x*-orientation) did the stress exponents become substantially lower and could be suspected to reach unity for lower loads.

The envelope creep curves themselves displayed only a very short secondary stage and extensive transitional stages. Such pronounced TCC transients have been reported only very rarely and only for thermal cycles with particularly low temperatures (see Section 0). The transient creep was found to be more pronounced the higher the stresses were. If creep curves with comparable minimum strain rates were compared, then the compressive tests seemed to exhibit longer creep transients than the tensile ones. A distinct orientation dependence was, however, not observed.

TCC for High-Temperature Cycles

The high-temperature experiments showed the same principal behavior as the standard TCC: The TCC rates were increased compared to the isothermal creep rates at T_{max} – especially at low loads. The apparent stress exponents became also substantially lower and close to unity in the lower end of the investigated stress range. The same principal orientation dependence and the dependence on the sign of loading were also observed. The biggest differences to the standard cycles were found regarding the overall form of the creep curves: The high-temperature (and high-amplitude) experiments exhibited much shorter creep transients.

The average strain per cycle increased considerably when the thermal amplitude of the cycle (for a fixed T_{max}=450 °C) was increased above around 250 K (T_{min}<200 °C). For lower amplitudes, a finite strain per cycle was measurable but it was low and more or less constant. Such behavior has been attributed to the presence of a critical amplitude ΔT_c beyond which the matrix yields. It will be discussed in Chapter 7 whether this is the case for the present material as well.

The average strains per cycle became noticeably lower when the 60 second dwell time at T_{max} was omitted of the cycle. When the dwell time was increased to 6 minutes, however, the strain per cycle stayed more or less the same.

5.3 In-Cycle Strain Evolution

Only few investigations of the in-cycle strain evolution during TCC were reported in literature and in no case a systematic study on the influence of testing parameters has been presented. Thus, in this work, the primary purpose of the in-cycle strain analysis was to find out whether differences in the creep rates and the overall TCC curve were reflected in systematic differences in the in-cycle strain evolution.

The in-cycle strain evolutions were determined for various representative cycles from selected TCC experiments. As described in Section 4.3.1, the results are presented in the form of instantaneous CTE curves. At first, the standard 350↔150 °C experiments are dealt with. In a second section, the analysis of high-temperature cycles is presented.

5.3.1 Standard Tests

Load-Free Cycling

When the composite specimens were cycled from 350 to 150 °C without external load, they exhibited a small hysteresis in the strain-temperature curve. As a consequence, the first differential of strain with respect to temperature – which is called instantaneous CTE – was different for heating and cooling half-cycles. This can be clearly seen, when Figures 5.14a and

b) are compared. The specimens with *x*-orientation had an almost linear cooling curve i.e. the instantaneous CTE was approximately constant with temperature. The heating curve, in contrast, had a lower instantaneous CTE at the lower end of the cycle and a much higher one the high-temperature end. Moreover, a little shoulder was reproducibly found at around 250 °C. As expected, the curves for the two specimens with *x*-orientation coincided very well. The small undulations in all curves were mostly due to noise in the basic data and should not be over-interpreted. The instantaneous CTE in *y*-direction was found to be always smaller than in *x*-direction. Furthermore, the heating/cooling asymmetry was reversed for *y*-orientation: Now it was the cooling curve which lay initially below and at high temperatures above the instantaneous CTE for heating. In *y*-direction, no almost linear strain-temperature behavior was found – neither for heating nor for cooling.

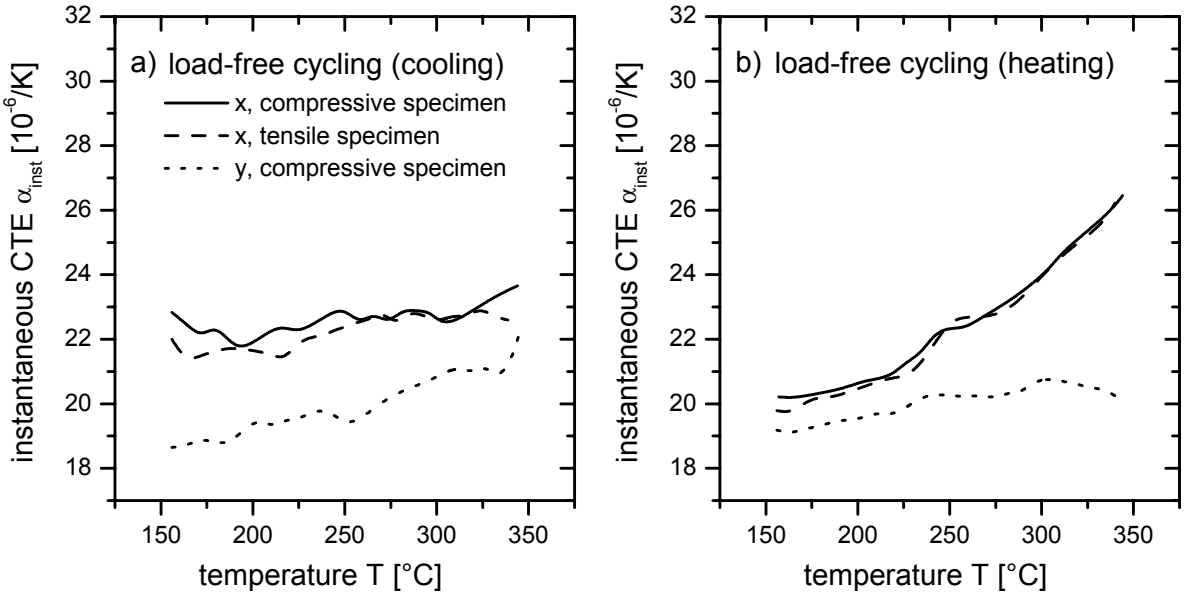

Figure 5.14: *Instantaneous CTE for load-free cycling in standard 350↔150 °C tests. a) cooling curves for x-orientation reflected the linear thermal contraction behavior in this direction. The cooling curve in y-direction had a lower CTE and showed a clear decrease of CTE for lower temperatures. b) the heating curves for x-orientation started at lower CTE values and ended at higher CTEs than the cooling curves. The CTE in y-direction lay below the one for x-direction and were less temperature dependent than the cooling-CTE in y-direction.*

A good test for the validity of the analysis that leads to the CTE-curves and for the quality of the measurements is the calculation of a volume-averaged instantaneous CTE. The volume averaged thermal expansion should show no thermal hysteresis because the volume of the specimen has to be constant at a given temperature[*]. It is assumed that the *y*- and *z*-directions are equivalent so that the volume averaged instantaneous CTE is given by

[*] The tiny volume changes due to internal elastic strains are neglected in this analysis.

$$\alpha_{inst,V} = \frac{1}{3}\left(\alpha_{inst,x} + 2\alpha_{inst,y}\right). \qquad \textbf{(5-13)}$$

The results of this analysis are given in Figure 5.15. It can be seen that no significant differences were present between the volume averaged CTEs for heating and cooling.

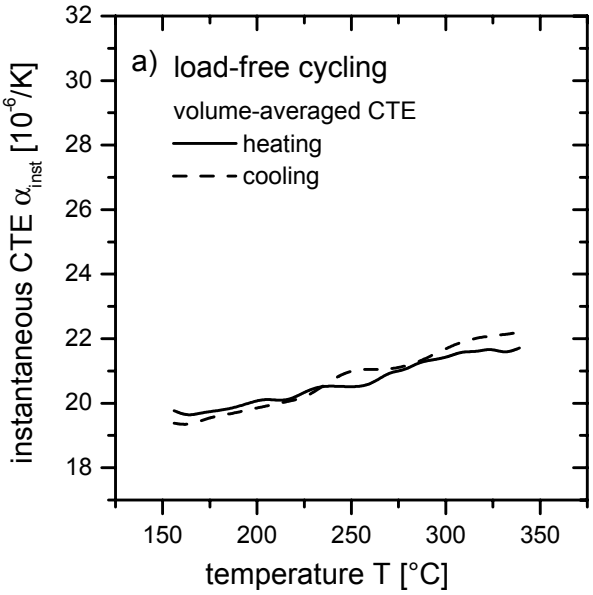

Figure 5.15: *Volume-averaged instantaneous CTE (see Eq. 5-13). The heating and cooling curves coincided well so that the volume averaged thermal strain cycle showed no hysteresis.*

Loaded Thermal Cycling

The instantaneous CTEs changed when the material was loaded. In Figure 5.16b), this can be seen most clearly for the heating curves: For tensile loading, the material expanded more readily at the high-temperature end of the cycle than without external load. For compressive loading, the instantaneous CTE was lowered in the same temperature range. Up to around 270 °C, all the heating curves showed the same CTE values. The tensile heating curve started to deviate from the unloaded curve at 270 °C, the compressive curve deviated not before 290 °C were reached. The small deviation of the compressive heating curve at the low temperature end of the heating cycle could not be reproduced in other experiments. The cooling curves that were shown in Figure 5.16a were virtually unchanged by the external loading. Only at the very beginning of the cooling curve was a significant enhancement of the thermal contraction found for compressive loading.

The cycles shown in Figure 5.16 were taken from the region of minimum TCC-rate in the experiment. In the following Figures 5.17 and 5.18, the same curves are shown in comparison to the instantaneous CTE from very "early" (the second loaded cycle) and "late" cycles. In the tensile case (Figure 5.17), the cooling curves stayed more or less the same throughout the experiment. Only for the first few cycles (see cycle #2) are they shifted to slightly lower values. For heating, the instantaneous CTE curve was initially very steep – especially at the high-temperature end – but it flattened as the TCC experiment proceeded to the region of minimum strain rate. At higher strains, when the specimen was already in the tertiary regime, the instantaneous heating CTE was increased again. For tensile TCC experiments that were

continued to failure of the specimen, it was found that the instantaneous heating CTE could become very high in the last few cycles before fracture – considerably higher than it had been in the first few cycles.

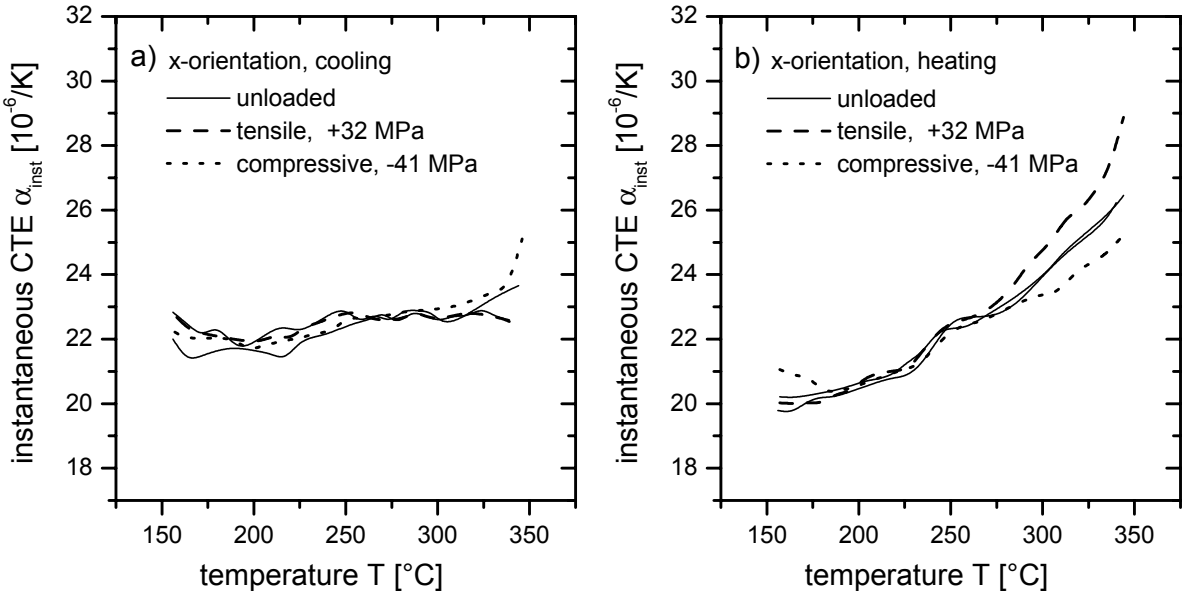

Figure 5.16: *Instantaneous CTE for standard TCC-cycles and x-orientation. The cycles are taken from regions of minimum strain rate. For comparison, the instantaneous CTE for load-free cycling of the same specimens are also given. a) cooling curves b) heating curves.*

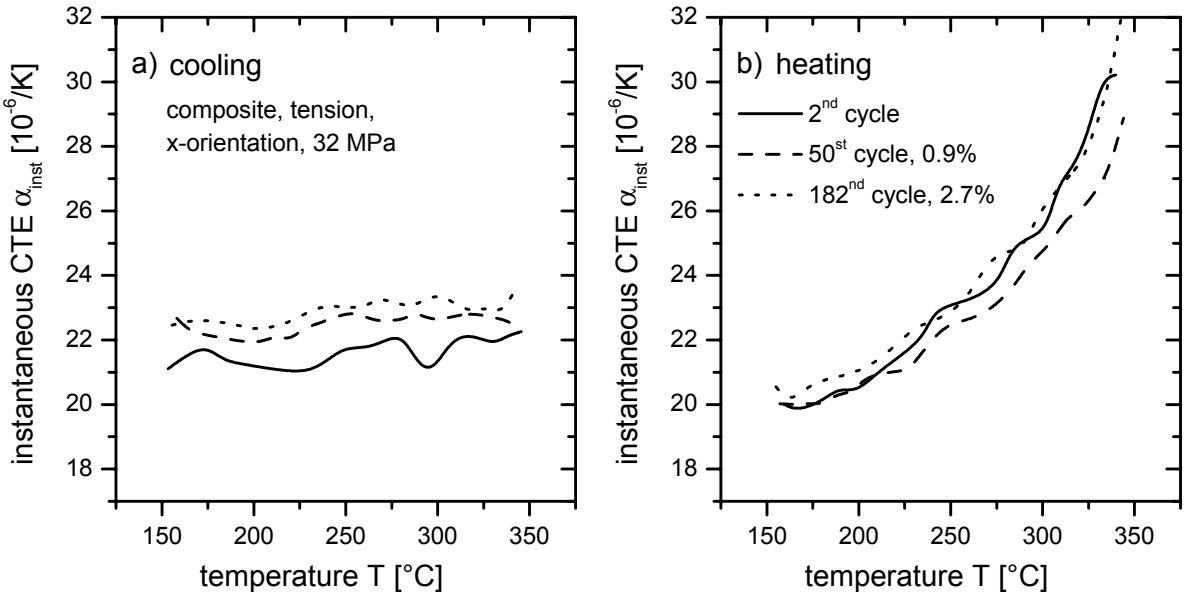

Figure 5.17: *Tensile TCC test: Instantaneous CTE for early, intermediate and late cycles. The specimen had x-orientation and the load was 32 MPa. The cycles number 2, 50 (at 0.9% strain) and 182 (at 2.7% strain) are given. a) cooling curves. b) heating curves.*

The same comparison was made for a compressive TCC test in Figure 5.18. The intermediate and the late cycle showed almost identical instantaneous heating and cooling CTEs. Only the

early cycle exhibited a different behavior. For cycle #2, the cooling CTE was considerably raised and the respective curve was more erratic: At the very beginning of the second cooling cycle, the contraction was much stronger than for the intermediate and late cycles. It furthermore showed a pronounced shoulder at around 270 °C. The heating CTE curve of cycle #2 bowed downwards at the high-temperature end. The deviation from the intermediate and late cycle heating curves started at about 220 °C.

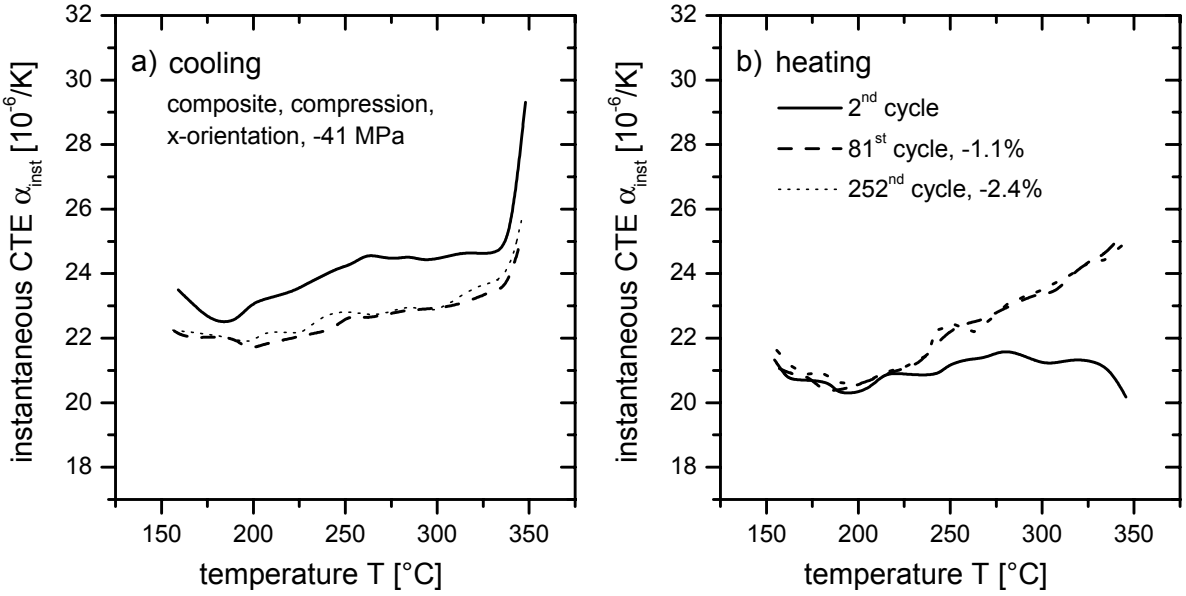

Figure 5.18: *Compressive TCC test: Instantaneous CTE for early, intermediate and late cycles. The specimen had x-orientation and the load was -41 MPa. The cycles number 2, 81 (at -1.1% strain) and 252 (at -2.4% strain) are given. a) cooling curves. b) heating curves.*

5.3.2 High-temperature Cycles

Variation of Amplitude

In Figure 5.11, results from a tensile TCC test with cycles to 450 °C and various thermal excursions were presented. The instantaneous CTE curves for selected cycles from this experiment are given here. All these cycles had the same high-temperature dwell times and the same heating and cooling rates. In Figure 5.19a it can be seen that all cooling curves coincided, no matter how low the minimum temperature was. The cooling curve was not as linear as it was for most of the (tensile) standard cycles. The instantaneous CTE curve was rather *S*-shaped with a steep segment between 260 and 330 °C and rather constant values above and below. The instantaneous heating CTE curves were found to differ a lot for various thermal excursions. For the cycle with 300 K thermal excursion, the heating CTE started at 150 °C with values below the cooling curve. Upon heating, the CTE increased steadily with increasing slope until about 430 °C. At this point, the slope of the curve reverted and for the last 20 K the CTE dropped a little. The instantaneous heating CTE curves for lower thermal amplitudes had roughly the same shape, but they were shifted to higher temperatures. Simul-

taneously, the range of heating CTEs was narrowed down: Compared to the 300 K cycle, the heating CTE of the 50 K cycle started at higher values and ended at much lower ones.

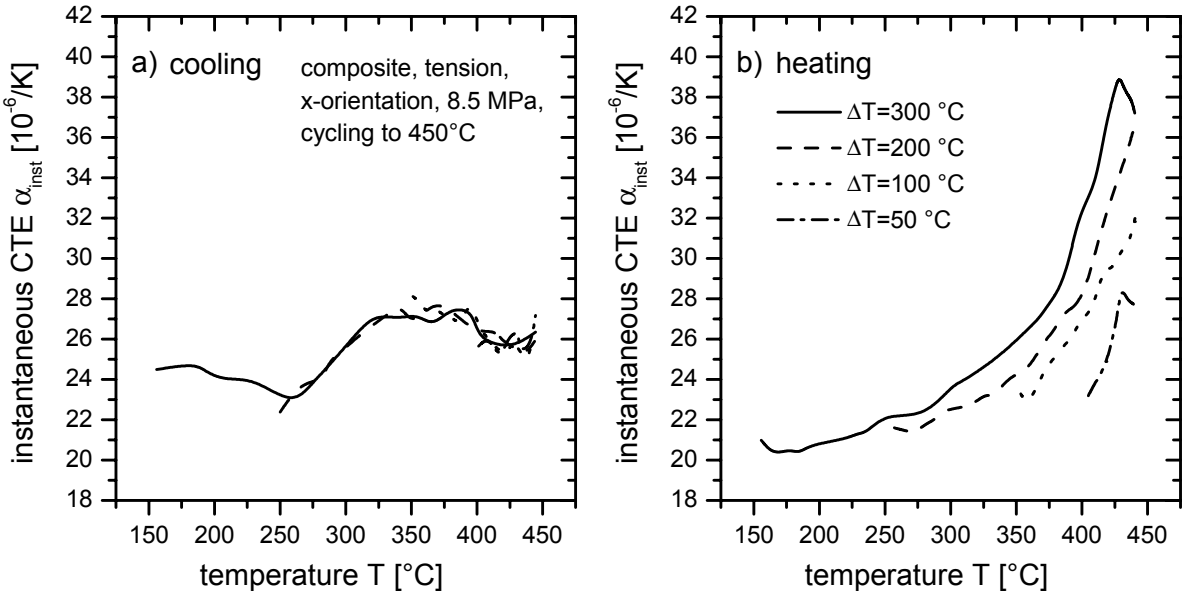

Figure 5.19: *Instantaneous CTE for a tensile TCC test at 8.5 MPa, where the cycle amplitude was changed (see page 66 for details of the cycle shape). The instantaneous CTE is given for excursions of 300, 200, 100 and 50 K. It is remarkable that the cooling CTEs (a) were always the same, while the heating CTEs (b) were shifted to higher temperatures for smaller excursions.*

Influence of Dwell Time

It was shown in Section 5.2.2 that the strain per cycle was significantly influenced by the high-temperature dwell time. Experiments with high-temperature dwells of 60 and 360 seconds exhibited both the same strains per cycle and these were higher than for a TCC test without dwell. Instantaneous CTE curves from these three tests (for *y*-oriented samples) are shown in Figure 5.20. The general shapes of the heating and cooling curves were the same as for the standard load-free cycles for *y*-oriented samples (see Figure 5.14). However, they were extended to higher and lower temperatures. Above 350 °C, the heating-CTE dropped to values as low as at the low temperature end of the curve. All three cooling curves coincided as well as the three heating curves.

No pronounced differences were found in the instantaneous CTE curves for the different dwell times. This is why the strain evolution during the dwell time was investigated further: In Figure 5.21, the strain-time curves during the 60-second and 360-second dwell at 450°C are shown. Both curves displayed non-linear behavior, similar to transient creep. The accumulated strains were -0.011 and -0.016 % for the short and long dwell time and in both cases, this strain was higher than the strain per cycle. This means that part of the strain that had accumulated during the high-temperature dwell was recovered during the following thermal cycle.

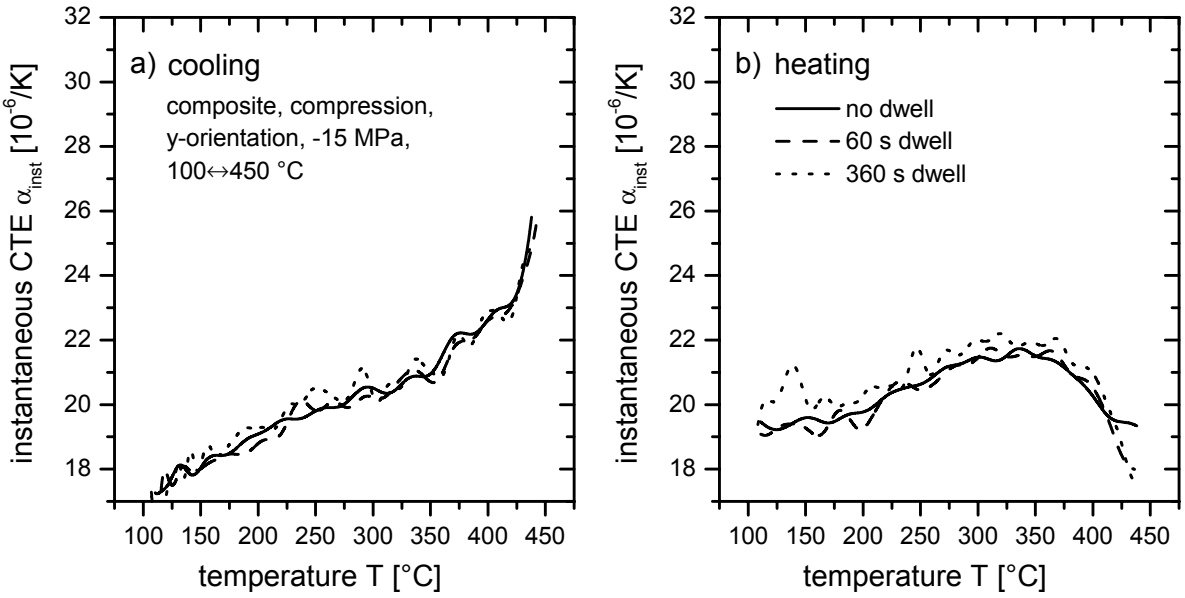

Figure 5.20: *Instantaneous CTE for a three compressive TCC test (y-orientation) at 15 MPa. The cycles differed in the high-temperature dwell time (see Page 67 for details). Nevertheless, the cooling CTEs (a) and the heating CTEs (b) coincided for all three curves.*

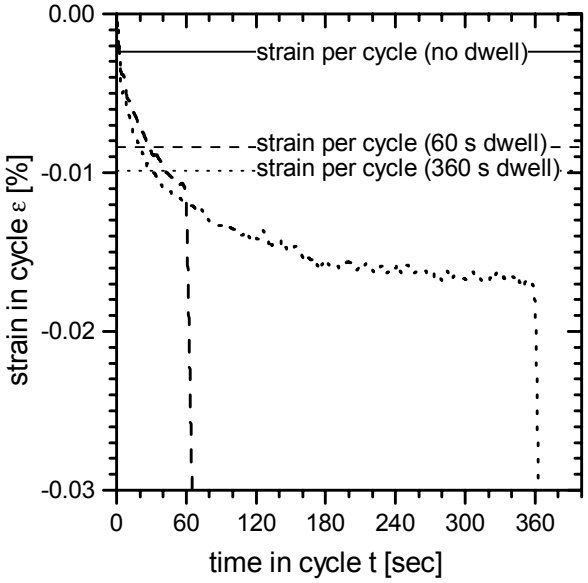

Figure 5.21: *Strain evolution during high-temperature dwell times of 60 and 360 seconds (-15 MPa, 450 °C). It can be seen that the strain that had accumulated during the high-temperature dwell was larger than the strain per cycle.*

5.3.3 Summary of the Observed In-Cycle Strain Evolution

The instantaneous CTE curves were generally markedly different for heating and cooling, i.e. a strain-temperature hysteresis was always present. When instantaneous CTE curves for various test conditions were compared, it was found that differences in the composite deformation were usually found in the heating curves– especially at the high-temperature end – but that the cooling curves stayed more or less the same.

The instantaneous CTE curves and what their form can tell about the evolution of inelastic strains and internal stresses will be discussed in detail in Chapter 7.

5.4 Stress Cycling Creep Behavior

To complement the TCC tests that were described in the previous section, some stress cycling creep tests were performed. The temperature was kept constant at 350 °C and the applied stress was cycled between a creep stress and zero stress (or the low stress necessary to grip compressive samples) at a very low frequency. It is reasonable to assume that the composite stores elastic strain energy in the reinforcement when a load is applied and creep deformation takes place. The stress cycling creep tests were performed to investigate to what extent this strain is released in the form of back-creep if the load is removed.

Stress cycling creep tests are characterized by the temperature, the creep- and recovery-stresses and the times or strains in the creep/recovery phases (see Section 4.3.2). In this work, the experiments were done with *x*-oriented specimens at 350 °C in compression. The external stress was cycled between -63 MPa and the gripping stress of about -1.5 MPa. The stress changes were applied instantaneously. Various forward creep strains were used together with a fixed recovery time of 6 hours. The results from those experiments are given in the following.

Compressive Tests

In Figure 5.22a, the amount of back creep with increasing creep strain is shown for three different forward strain increments. In all three cases, the amount of recovered strain became almost constant after a number of cycles. The total forward strain needed to achieve this constant back creep was found to depend on the forward strain increment.

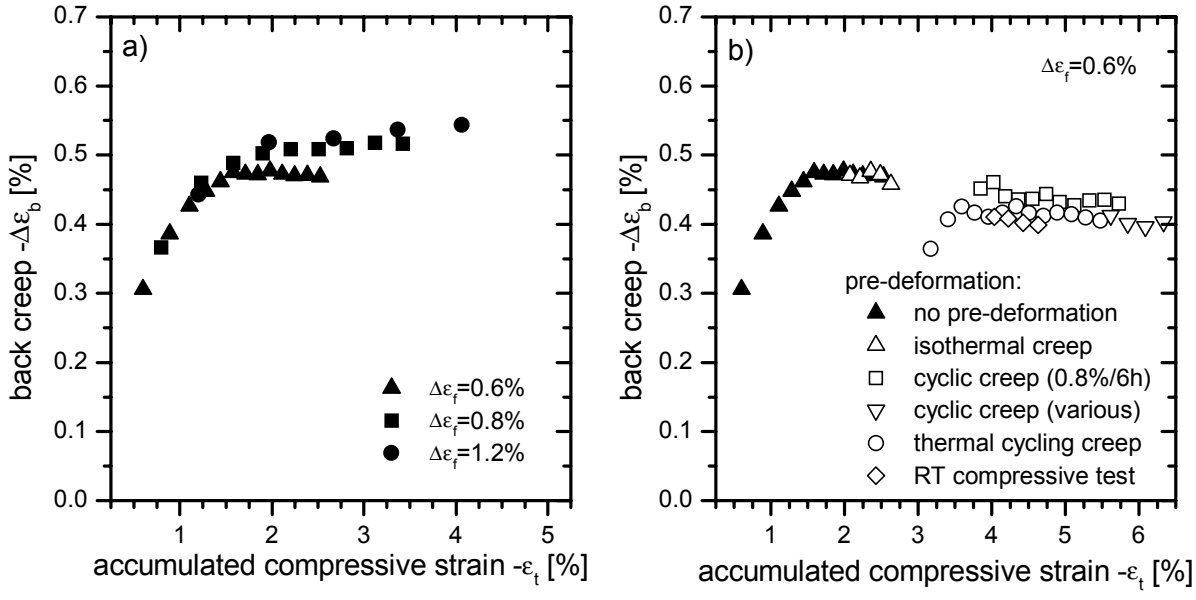

Figure 5.22: *a) Isothermal stress cycling creep tests at 350 °C with creep/recovery stresses of -63/-1.5 MPa. The specimens were loaded until 0.6%, 0.8% or 1.2% of forward creep strain were reached and subsequently allowed to recover for 6 hours. The evolution of the recovery strain with the accumulated total creep strain is shown. b) Back creep strain for stress cycling creep with a forward strain of 0.6%, following various types of pre-deformation. The recovery strain decreased only very moderately with increasing accumulated creep strain and was independent of the type of pre-deformation.*

In a series of experiments, the specimens were deformed to large strains with different types of tests. The intention was to cause different amounts of damage to the reinforcement. Afterwards, a stress cycling creep test with a forward creep strain of 0.6% was performed in order to find out whether the reinforcement damage had affected the tendency for back-creep. The back creep strains from these tests are shown in Figure 5.22b. The recovery strain showed only a very moderate decrease with increasing total creep strain. Furthermore, in all cases the recovery strain was almost the same at the same total accumulated strain, irrespective of the type of pre-deformation.

In Figure 5.22a it was shown that recovery depended slightly on the amount of the forward strain increment. A closer look on this is given in Figure 5.23, where the amount of backward strain at a certain total strain (-2.75% accumulated creep strain) of different samples is plotted against the amount of the prior forward strain. For small forward strain increments, the large total strain was reached in an incremental technique with large-increment stress cycling creep preceding small-increment stress cycling creep. For very low forward strain increments (below around 0.3%), almost all the strain was recovered within 6 hours. The back creep strain increased with increasing forward strains. Although the degree of increase diminished progressively, no upper limit for back creep was observed up to forward strain increments of around 3%. It is to be noted here that even at the end of the 6-hour load-free segment, the specimen still exhibited measurable back-creep: The back creep rate was low but not zero.

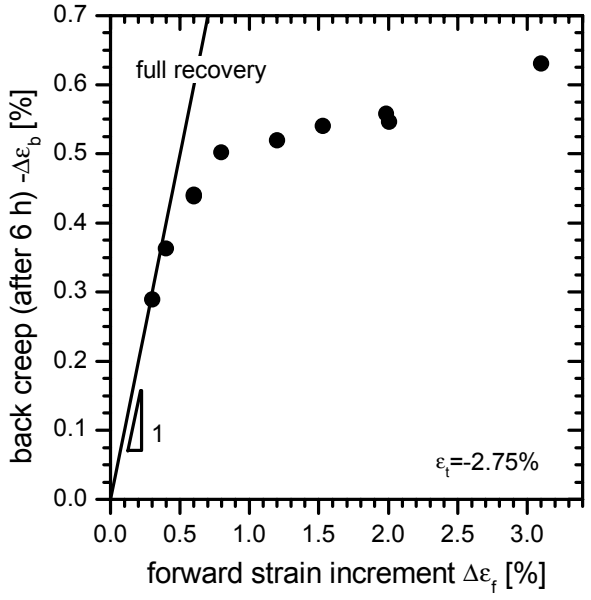

Figure 5.23: *Amount of back-creep for different forward creep strain increments. The recovered strain increased with increasing forward strain increments and no upper limit was found up to around 3% of forward strain.*

Tensile Test

Under tensile conditions, only slightly different observations were made. A single tensile stress cycling creep experiment was conducted at an external stress of 50 MPa and a stress of 0 MPa during recovery. The forward strain increment was chosen to be +0.4% and the recovery time was again 6 hours. The back creep strains from this experiment are shown in Figure 5.24. A maximum of 0.34% back creep was found at 1.2% tensile creep strain. After

four further cycles, where the amount of recovered strain decreased slightly, the specimen fractured. The total strain to fracture was 1.53%. This fracture strain matches well with the strains to failure for standard isothermal creep experiments (see section 3.5).

The overall shape of the back-creep strain vs. total strain curve was similar to the ones for the compressive experiments. In both cases, no dramatic decrease in the recovery ratio was found for larger strains. While in the tensile case the specimen failed as soon as the back creep started to become lower, the compressive specimens exhibited only a slight decrease of the recovery strains up to relatively large strains. It is remarkable that under tension (at the smaller external stress) the maximum recovery strain is reached at smaller total strains than under compression (at the larger stress).

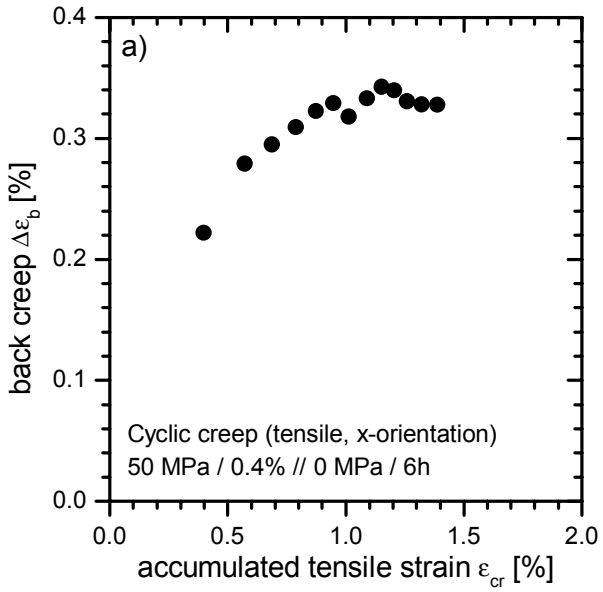

Figure 5.24: *Tensile isothermal stress cycling creep test at 350 °C with creep / recovery loads of +50/0 MPa, a forward strain increment of 0.4% and a recovery time of 6 hours. The fracture strain was 1.53%.*

Rates of Stress Cycling Creep

An interesting question was how the creep rate of the composite was influenced by the repeated unloading during stress cycling creep. In order to compare stress cycling creep curves directly to data from static creep experiments, data in the recovery phases had to be removed from the strain vs. time curves. In Figure 5.25a two cyclic creep curves are shown, where only the data from the loaded segments are concatenated. For comparison, a static compressive creep curve (-63 MPa, 350 °C) is also given. In Figure 5.25b, the respective strain rate vs. total strain curves are plotted. The overall shape of the creep curve was always the same. In each experiment, the strain to minimum strain rate was about 1.2%. Pronounced primary and tertiary creep regimes were found while the regime of steady state creep was very narrow. It can be clearly seen that the stress cycling creep experiments yielded higher creep rates. The creep acceleration seems to be linked to the number of creep recovery segments per time (or strain), because lower forward strain increments led to higher creep rates.

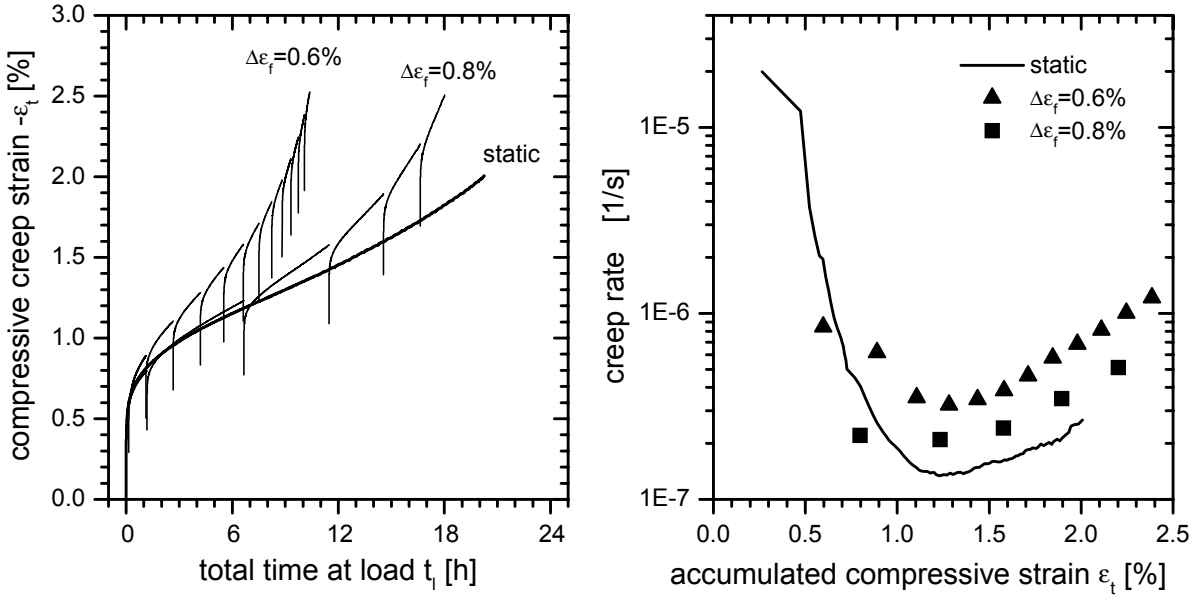

Figure 5.25: *Stress cycling creep compared to static creep. a) strain vs. time curves where only the loaded segments are shown; data from the recovery segments are removed. b) strain rate vs. strain curves. For the cyclic creep curves, only the very last measurements in the loaded segments were taken and differentiated with respect to the time at load. It can be seen that, for all three curves, the strain to minimum strain rate lay at about 1.2%.*

5.5 Damage

Damage due to TCC testing can be observed on different size scales. In the following, these observations will be grouped into "macroscopic" and "microscopic". All discovered damage features that were larger than the typical inter-fiber spacing were termed "macroscopic", although a microscope was sometimes helpful in viewing them. These will be presented in the first of the following two sections.

5.5.1 Macroscopic Observations

Strain to Failure

A series of tensile TCC-tests with standard cycles were run until fracture of the specimen. The strain to failure was determined as the total strain from directly before application of the load until final fracture minus the elastic strain, calculated with a measured elastic modulus of 76.4 GPa at 350 °C (see Section 3.4, Figure 3.8). The results for various loads and amounts of isothermal pre-creep are summarized in Figure 5.26. For comparison, fracture strains measured by Bidlingmaier et al. (1996a) for isothermal creep are also given. These lay between 1.5 and 1.8% (cf. Section 3.5). The TCC fracture strains scattered around 4.1% with considerable variation. Just like in the isothermal case, the fracture strain for TCC showed no pronounced dependence on the applied load (Figure 5.26a). It also seemed to be independent of the amount of isothermal pre-creep (Figure 5.26b).

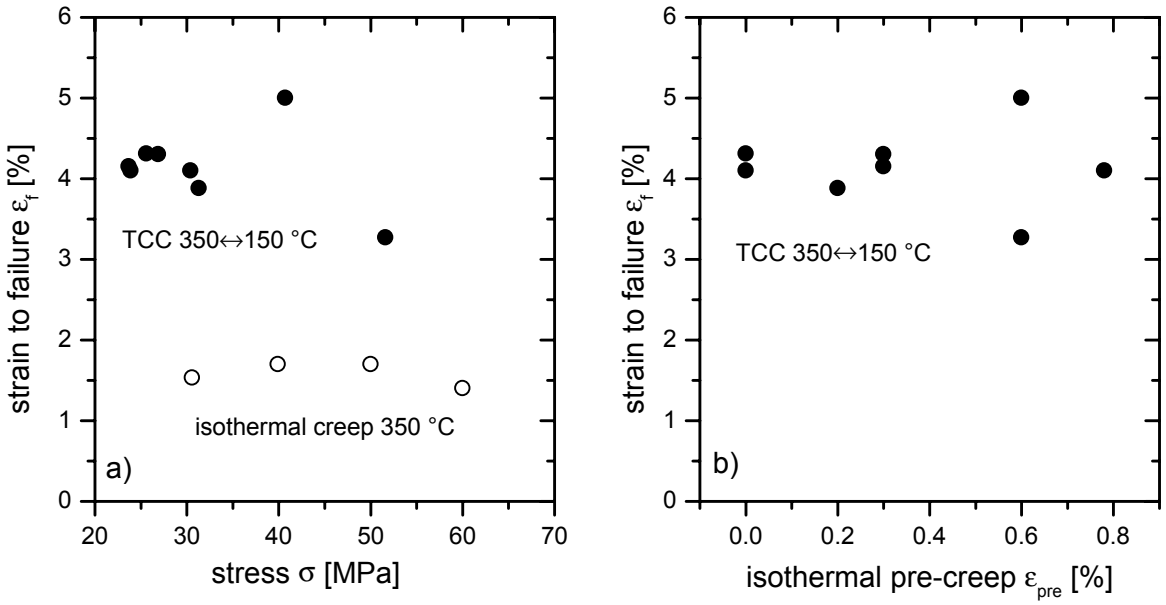

Figure 5.26: *Strain to failure for tensile thermal cycling creep (x-orientation), 350↔150 °C. a) Strain to failure for different stresses and different amounts of pre-creep, plotted against stress. No pronounced dependence was found. For comparison, fracture strains for isothermal creep at 350 °C measured by Bidlingmaier et al. (1996a) are also given. b) Same TCC data as in a) but plotted against the amount of pre-creep. Again, no correlation between fracture strain and pre-creep could be observed.*

Fracture Surface

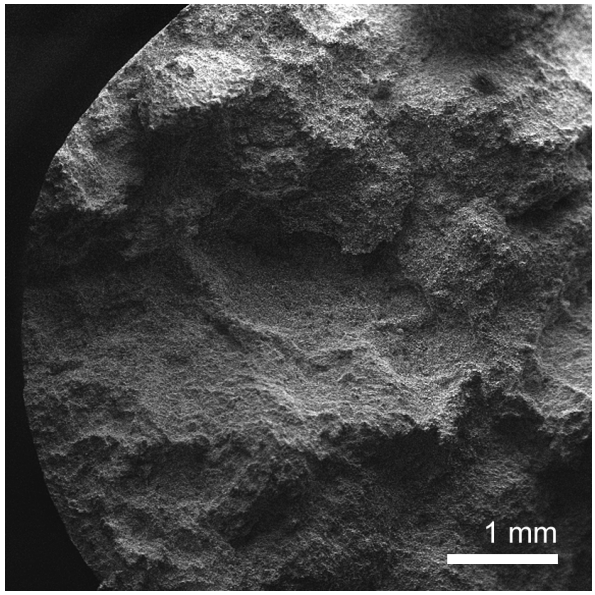

Figure 5.27: *The typical fracture surface of a tensile composite specimen after a TCC test is very rugged on a macroscopic scale. No indications were found for starting sites and cyclic growth of macroscopic cracks. SEM, SE detection.*

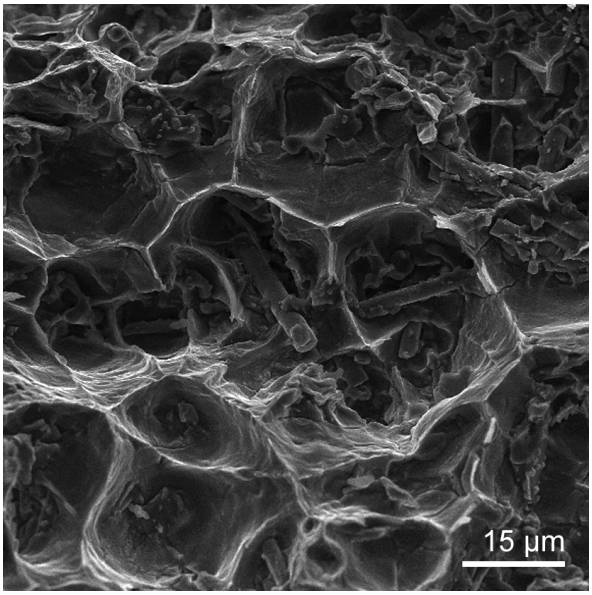

Figure 5.28: *Fracture surface detail that shows evidence (equiaxed creep dimples) for classical creep fracture by growth and coalescence of creep voids. SEM, SE detection.*

The fracture surfaces of tested tensile TCC specimens were very rugged on a macroscopic scale. In some cases, sideways fissures with millimeters in depth were found. No indication was found for the initiation and cyclic growth of macroscopic cracks. Only one out of 8 frac-

ture surfaces went through one of the thermocouples that had been spot-welded to the specimen surface, although those would have been obvious starting points from which damage could have emanated. At higher magnifications, equiaxed creep dimples were found all over the fracture surface. Apparently, macroscopic damage by growth and coalescence of pores led to final fracture. Elongated dimples that would have been evidence for shear rupture could only rarely be observed. No pronounced fiber pull-out or debonding was found. Fibers that stuck out from the fracture surface always had remains of matrix material sticking to them. This indicated good bonding between the matrix and the fibers.

Surface Roughening

On all tested specimens, surface roughening was observed. An image of a compression specimen that was deformed under stress cycling creep conditions up to -6% of strain is given in Figure 5.29. The initially polished surface had become very rough during testing and a characteristic surface topography with bands of hills and valleys had built up. These features became clearly visible with the naked eye for strains larger than 1.5% under all kinds of creep deformation (tensile, compressive, cyclic, thermal cycling). It was found that surface valleys were usually associated with regions of low fiber content. This is illustrated in Figure 5.30 where a cross section of a tensile TCC specimen with a fracture strain of 5% is shown.

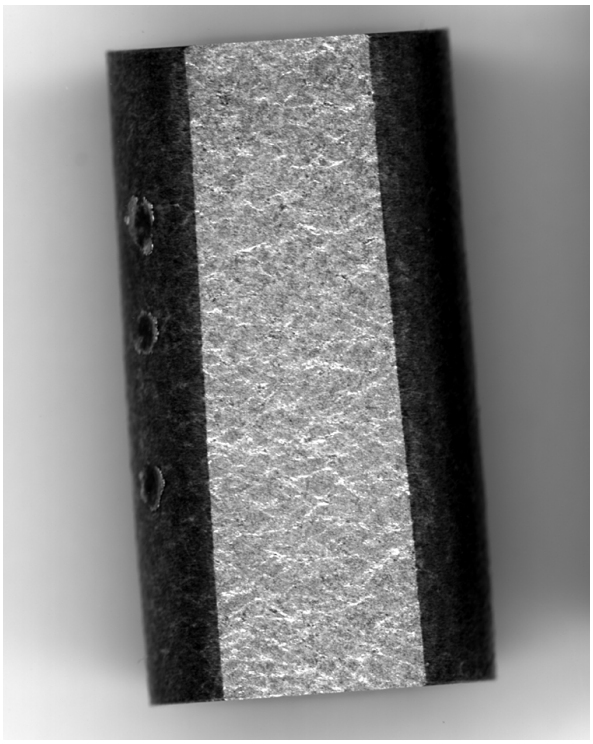

Figure 5.29: *Compressive specimen after stress cycling creep to a strain of -6%. Note that the initially polished surface shows a high amount of roughness. Specimen diameter is 9 mm.*

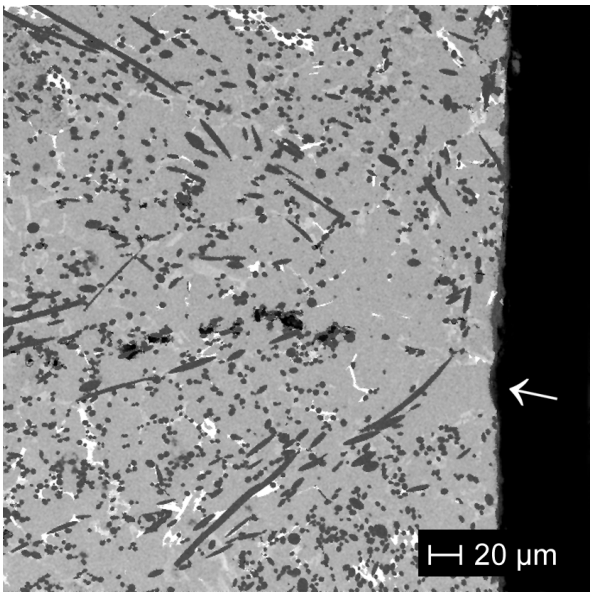

Figure 5.30: *Longitudinal cross section of a tensile TCC specimen strained to 5%. Note that the characteristic surface trenches are usually associated with regions of low fiber content. Loading direction vertical. VP-SEM, BS detection.*

The surface roughness of tensile specimens with various fracture strains was measured with a DEKTAK3 surface profilometer. The measured profiles are shown in Figure 5.31. They were measured in the direction of the tensile axis. For each one, the arithmetic average roughness R_a (arithmetic average deviation form the mean line) is also given. It was found that the surface roughness increased non-linearly with increasing creep strain. The occurrence of fracture was not correlated with a certain roughness.

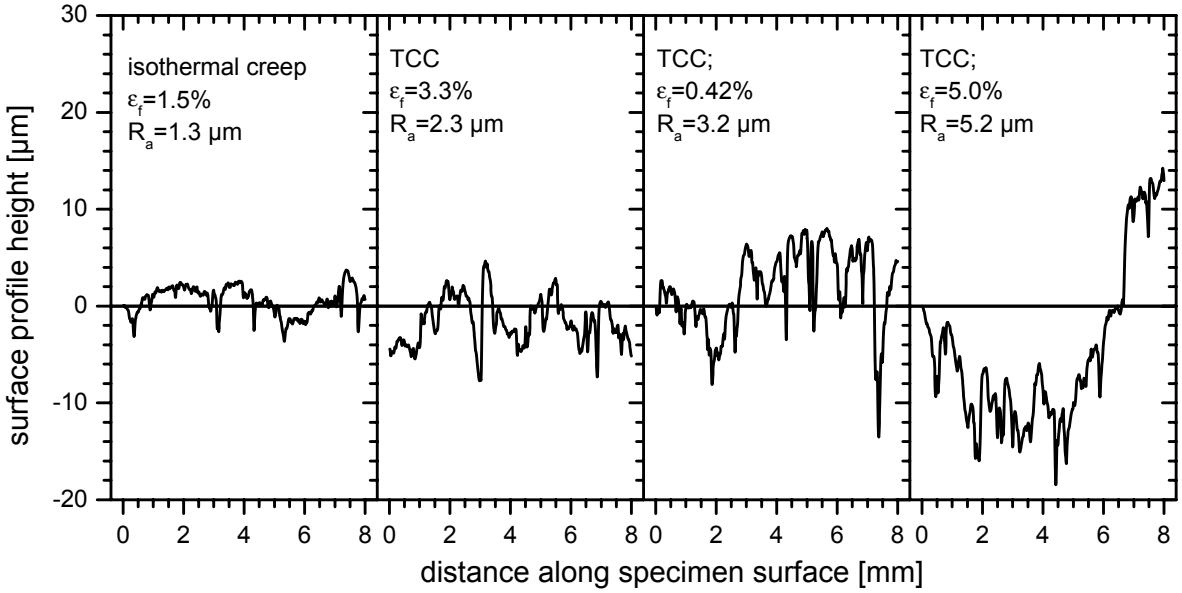

Figure 5.31: *Surface profiles of tensile specimens tested to different fracture strains. The arithmetic average roughness R_a increased non-linearly with the fracture strain ε_f. The measuring direction was parallel to the tensile axis.*

5.5.2 Microscopic Damage

Pores

Longitudinal metallographic cross sections of broken tensile TCC specimens revealed vast assemblies of pores in the matrix that had grown and coalesced to cracks perpendicular to the loading direction (Figure 5.32). It was found that these assemblies were mostly associated with fiber free-regions. Either adjacent regions of low fiber content had been linked up by a series of pores or the pores had aligned along the boundary of a fiber-free region. These typical pore arrangements were found all over the cross section, with no pronounced concentration near the specimen surface or the fracture surface. They were exclusively found under tensile loading conditions, not in compression. Such pore arrangements were not found under tensile isothermal creep conditions.

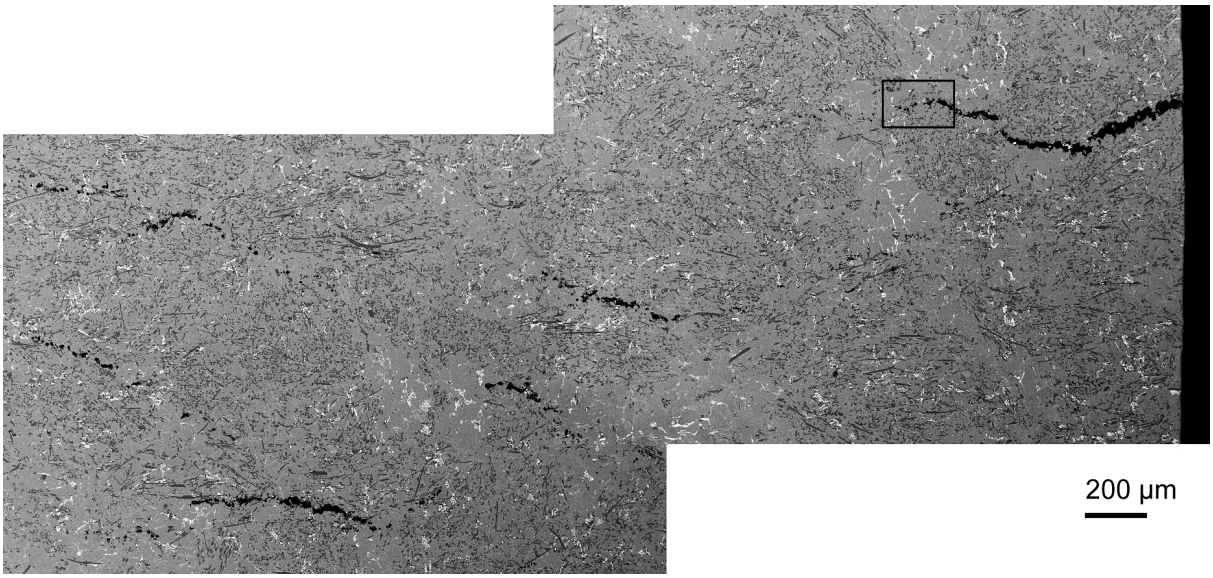

Figure 5.32: *Typical pore arrangement as seen on a longitudinal cross section of a tested TCC-specimen (5% strain). Tensile loading, the loading direction was vertical. VP-SEM, BS detection.*

In the wake of these pore arrangements, an increased amount of microscopic damage, such as particle cracking, matrix cracking or fiber fracture was frequently observed. An example for this is shown in Figure 5.33.

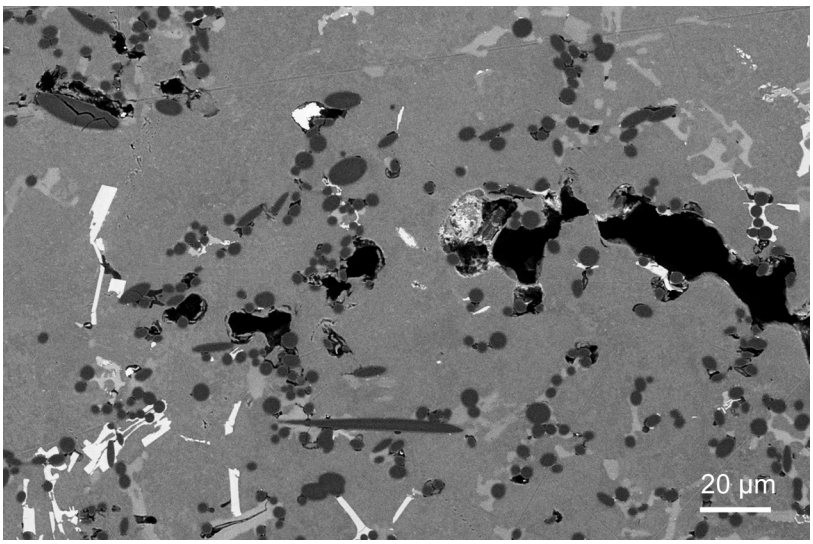

Figure 5.33: *Creep pores after a tensile TCC test. Detail from Figure 5.32. Note the increased amount of microscopic damage such as matrix, particle or fiber cracks in the wake of the pore assembly. VP-SEM, BS detection*

Fiber Fracture

Only a limited number of fiber fractures were found in the metallographic investigations, even when the fracture strain or the compressive creep strain of the specimens had been large. As mentioned above, fiber fracture occurred more frequently in the wake of pore assemblies in tensile specimens. An example for fiber fracture in a compressive specimen is given in Figure 5.34. It is clearly seen that the region between the fiber fracture surfaces is filled with matrix

material. Open cracks were observed only in very rare instances. The gaps could have been filled by deformation processes or as a result of the metallographic preparation (smearing). Silicon precipitates or intermetallic phases were never found in the gap between the fracture surfaces. This indicates that the fractures did not occur before or during the infiltration process.

An orientational dependence of fiber fracture was not observed. In most tensile specimens, it was almost impossible to find fibers that were aligned with the loading direction (*x*-orientation), and these were usually not damaged. In compressive specimens, fiber fracture appeared to be more frequent in fibers that were aligned perpendicular to the loading direction. Precise statements can, however, not be made without extensive image analysis and statistics. Such an analysis of fiber fractures was performed by Wolf (1997) for tensile and compressive creep samples that both had the direction of loading in the plane of preferential fiber orientation. He found a clear orientational dependence of fiber fractures with preferred fracture of aligned fibers in tension and preferred fracture of transverse fibers in compression (see also Bidlingmaier et al. (1998)).

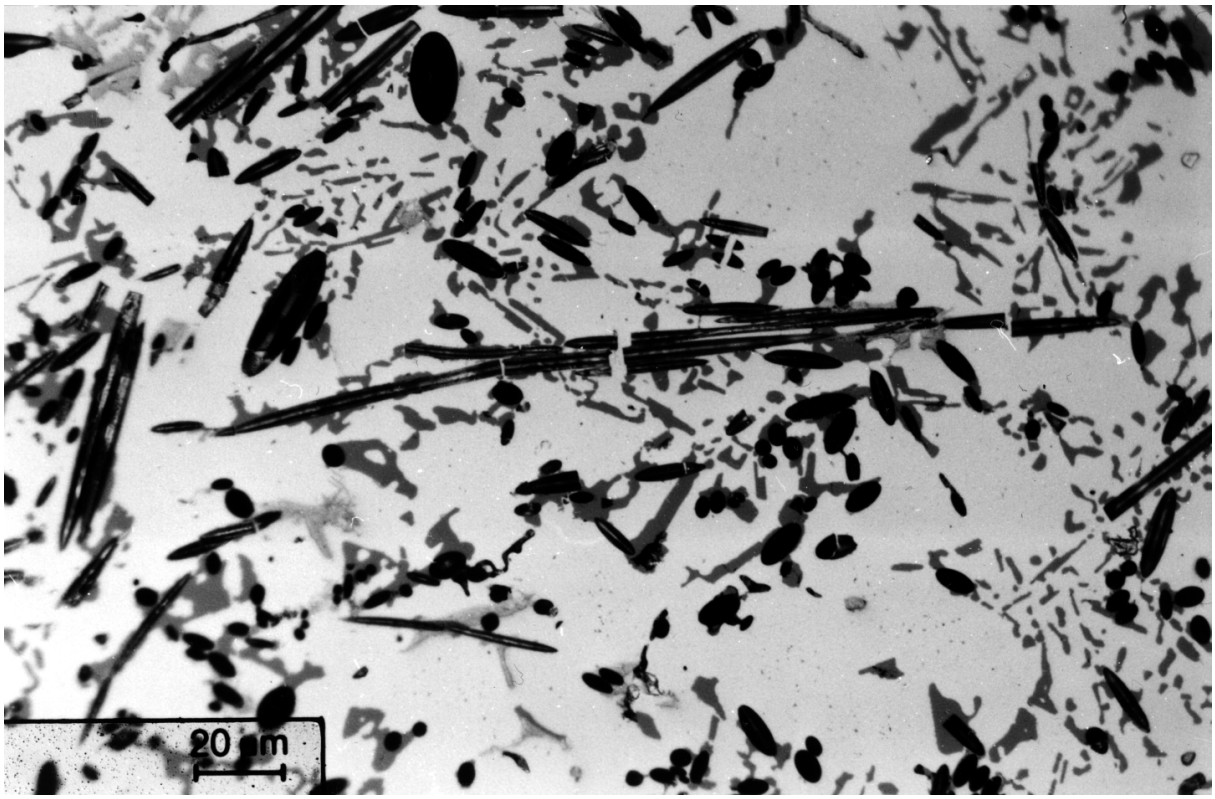

Figure 5.34: *Fiber fracture in a TCC-tested compression specimen (longitudinal section) The loading axis was vertical. Note that the gaps between the fiber fracture surfaces are filled with matrix material. Optical microscope.*

5.6 Summary of the Most Important Results

By quantitative metallographical analysis it was shown that the reinforcement was textured. This means that for all mechanical tests, attention has to be paid to the orientation of the specimen. The orientational distribution of fibers was quantified by an orientation tensor. The quantification of the orientation distribution facilitates comparison to past and future results from other researchers and it is essential when numerical predictions of physical and mechanical properties are to be made.

Under thermal cycling conditions, the rate of deformation of the MMC was always higher than under isothermal condition at the maximum temperature of the thermal cycle. This kind of behavior has also been reported in the literature for other MMCs.

In some aspects, however, the behavior observed in the present study differed from the classical thermal cycling creep (TCC) behavior described in the literature. Although the apparent stress exponents were found to be generally lower than for isothermal creep, they were still larger than one – even at very low applied stresses. Another remarkable result is that the envelope creep curves displayed pronounced transient behavior upon load changes. This transient creep was more pronounced the higher the stresses and the lower the temperatures were. The origin of these discrepancies will be addressed in Chapter 7.

The above mentioned reinforcement-texture was well reflected in the orientational dependence of the TCC-rates: The creep rates were higher when the specimen was loaded perpendicular to a plane of preferential fiber orientation. Moreover, the creep rates depended on the sign of loading (lower creep rates were found under compression). These two observations are not only important issues for mechanical design with this material but they also give information about the underlying deformation processes. As will be shown in the following chapters, conclusions on the deformation processes can also be drawn from the strain hystereses observed within the individual thermal cycles.

The deformation processes in the material were further investigated with stress cycling creep experiments in which the applied stress was switched back and forth between the creep stress and zero stress at varying time intervals. The most important result of these tests was that the composite material was able to recover considerable amounts of creep strain after unloading. The amount of recovered strain was found to depend on the total amount of previously accumulated creep strain but also on the amount of strain since the last recovery. When the stress cycling creep experiments were compared to uninterrupted isothermal creep experiments, it was found that the creep rates under load were slightly higher. This means that the creep deformation of the material is accelerated if the load is not applied constantly.

These results are of great importance for the practical application of this kind of material as service conditions generally include varying stresses and varying temperatures.

6 Calculations

For the interpretation of results that were presented in the previous chapter, it is desirable to calculate the evolution of internal stresses under thermal and/or load-cycling conditions for comparison. In the following, a so-called slab-model will be described, which provides such estimates for a simplified geometry. At first, its basic assumptions, its implementation and its fundamental limitations will be addressed. In a second section, the slab-model will be calibrated with parameters to yield predictions for the composite material. Finally, the prediction of basic physical properties will be presented in order to check the validity of the calculations. In Chapter 7, the slab-model will be used to predict thermal cycling creep rates and in-cycle strain evolution. These predictions will be compared to the experimental findings.

6.1 The Slab Model

The slab model in a simple form has been used to approximate a long-fiber reinforced composite by a stack of two cuboid slabs that represent the matrix and the reinforcement, with relative thicknesses proportional to the respective volume contents (Clyne and Withers (1993)). Considering the symmetry, it is quite obvious that the slab arrangement is most useful in modeling a random planar distribution of continuous fibers. The degree of abstraction increases as the composite geometry is changed to discontinuous fibers with a preferential orientation in one particular plane. It cannot be expected that the behavior of the investigated composite is predicted with high accuracy by such a slab model. Due to this simplicity, however, the model can be set up to consider the complex interplay of elastic loading, thermal expansion, creep relaxation and plastic flow. This will be shown in the following sections.

6.1.1 Basic Assumptions and Equations

A two-phase composite, consisting of a stack of cuboid slabs that are tightly bonded together is considered. It is assumed that one principal axis of the stress tensor coincides with the direction of stacking. This axis is denoted with the index “1”.

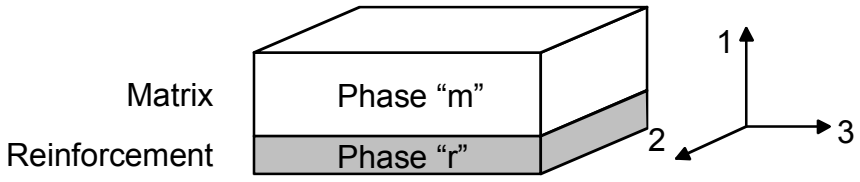

Figure 6.1: *Slab model: graphic representation and orientational denotation*

Both phases are allowed to undergo elastic deformation, thermal expansion and inelastic deformation (i.e. creep and/or plasticity). All material properties are assumed to be isotropic for each phase and the strains in the slabs are assumed to be uniform. The principal strains ε_{ip} in the phase p are thus given by the following equations:

$$\varepsilon_{1p} = \frac{1}{E_p}\sigma_{1p} - \frac{\nu_p}{E_p}\sigma_{2p} - \frac{\nu_p}{E_p}\sigma_{3p} + \alpha_p \Delta T + \varepsilon_{1p}^{inel}, \qquad \textbf{(6-1 a)}$$

$$\varepsilon_{2p} = \frac{1}{E_p}\sigma_{2p} - \frac{\nu_p}{E_p}\sigma_{1p} - \frac{\nu_p}{E_p}\sigma_{3p} + \alpha_p \Delta T + \varepsilon_{2p}^{inel}, \qquad \textbf{(6-1 b)}$$

$$\varepsilon_{3p} = \frac{1}{E_p}\sigma_{3p} - \frac{\nu_p}{E_p}\sigma_{1p} - \frac{\nu_p}{E_p}\sigma_{2p} + \alpha_p \Delta T + \varepsilon_{3p}^{inel}. \qquad \textbf{(6-1 c)}$$

The elastic strains are given by the principal stresses σ_{ip} in the phases and Young's modulus E_p and Poisson's ratio ν_p according to Hooke's law. The thermal strain is the product of the phase's coefficient of thermal expansion α_p (CTE) and the temperature change ΔT. The contribution of inelastic strain in the phase p in the direction i is represented by ε_{ip}^{inel}.

In the stacking direction, the phase strains simply add up to the composite strain. The principal strains in the 2/3-plane of both slabs must all be identical and equal to the principal strain of the arrangement in this plane. This follows from the compatibility condition due to the tight bonding and from the uniformity of strain. The principal strains are:

$$\varepsilon_1 = f_m \varepsilon_{1m} + f_r \varepsilon_{1r} \qquad \textbf{(6-2 a)}$$

$$\varepsilon_2 = \varepsilon_{2m} = \varepsilon_{2r} \qquad \textbf{(6-2 b)}$$

$$\varepsilon_3 = \varepsilon_{3m} = \varepsilon_{3r} \qquad \textbf{(6-2 c)}$$

The subscripts m and r stand for the matrix and reinforcement phases, f_m and f_r are the volume fractions of these constituents. They are represented by the relative thickness of the slabs in the model. The principal stresses σ_{ip} in the phases have to fulfil the equilibrium condition with the principal external stresses σ_i:

$$\sigma_1 = \sigma_{1m} = \sigma_{1r} \qquad \textbf{(6-3 a)}$$

$$\sigma_2 = f_m \sigma_{2m} + f_r \sigma_{2r} \qquad \textbf{(6-3 b)}$$

$$\sigma_3 = f_m \sigma_{3m} + f_r \sigma_{3r} \qquad \textbf{(6-3 c)}$$

where σ_1 is the external stress in the stacking direction. In order to calculate the strains in the phases from equations (6-1), the stresses in the phases have to be obtained first. The phase stresses σ_{1m} and σ_{1r} are simply given by Eq. (6-3a). The others can be obtained as follows: Introducing Eqs. (6-1b) in (6-2b) and substituting σ_{2r} by σ_{2m} and σ_{3r} by σ_{3m} from Eqs. (6-3b)

and (6-3c) gives an equation that contains only σ_{2m} and σ_{3m} as unknowns. An equivalent equation can be obtained from the iso-strain condition (6-2c). Substituting σ_{3m} from the latter leads to a rather long equation for one of the in-plane phase stresses:

$$\left(\frac{1}{A} - A \cdot B^2\right) \cdot \sigma_{2m} = (ABC + C) \cdot \sigma_1 + (D - ABE) \cdot \sigma_2 + (ABD - E) \cdot \sigma_3 + (AB + 1) \cdot (\alpha_r - \alpha_m)\Delta T + AB \cdot \left(\varepsilon_{3r}^{inel} - \varepsilon_{3m}^{inel}\right) + \left(\varepsilon_{2r}^{inel} - \varepsilon_{2m}^{inel}\right) \quad \textbf{(6-4)}$$

with

$$A = \left(\frac{1}{E_m} + \frac{f_m}{E_r f_r}\right)^{-1} \qquad B = \frac{\nu_m}{E_m} + \frac{\nu_r f_m}{E_r f_r} \qquad C = \frac{\nu_m}{E_m} - \frac{\nu_r}{E_r} \qquad D = \frac{1}{E_r f_r} \qquad E = \frac{\nu_r}{E_r f_r}.$$

The other in-plane phase stresses are easily obtained by exchanging the indices for the principal directions (*2* and *3*) and for the phases (*m* and *r*).

The next section will describe how these equations can be utilized together with suitable expressions for the inelastic deformation to simulate the strain evolution of the slab arrangement under load.

6.1.2 Implementation

It is the objective of the model to determine a global strain history under changing external stresses and temperature. This requires calculating the evolution of the internal stresses under consideration of all phase strains, including inelastic strains, which are in turn strongly dependent on the internal stress state (see above). Such problems are analytically tractable only for very restrictive assumptions, which is why they are usually solved numerically.

Basic Concept

The slab model is implemented in an incremental manner, similar to implementations of other models for the evolution of internal stresses reported in literature (e.g. Daehn and Gonzalez-Doncél (1989), Furness and Clyne (1991b)). For sufficiently small increments in time, the elastic, thermal and inelastic strain increments are calculated, based on the changes in external stress, the temperature change and the current phase stresses. Knowing these strain increments, the increments in the principal phases stresses can be calculated from (6-3a) and (6-4). After each step, the new composite strain and the new phase stresses are obtained by adding the stress and strain increments.

The simulation program is written in the programming language *Visual Basic for Applications* as it is supplied with the widespread spreadsheet program *Microsoft Excel*. The input of parameters and the output of the simulation are done via *Microsoft Excel* worksheets, which

greatly eases further processing of the results. A detailed flow-chart of the implementation is given in Figure 6.2.

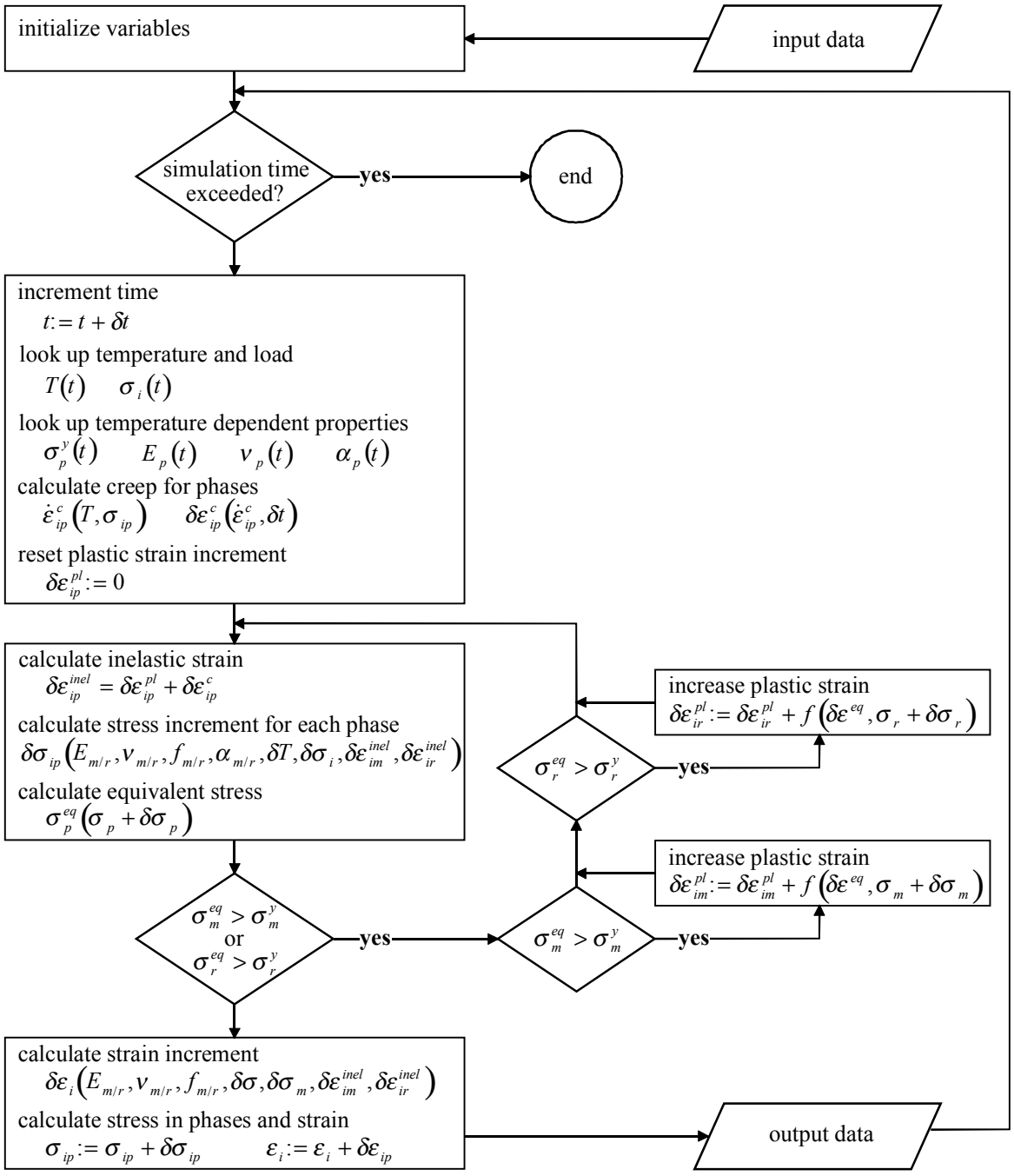

Figure 6.2: *Flow-chart, showing the implementation of the slab-model.*

Implementation of Steady State Creep

The inelastic deformation of the slabs was modeled by employing a steady-state power-law creep expression. For the uniaxial case the creep law is formulated as follows:

$$\dot{\varepsilon}_{SS} = B \cdot \sigma^n , \qquad \textbf{(6-5)}$$

where $\dot{\varepsilon}_{SS}$ is the uniaxial steady-state creep rate, σ is the uniaxially applied stress and n is the stress exponent. B contains the proportionality constant A and the thermal activation term with the activation energy Q, Gas constant R and temperature T:

$$B = A \cdot \exp\left(-\frac{Q}{RT}\right) \qquad \textbf{(6-6)}$$

According to Soderberg (1936) (as cited in Finnie and Heller (1959)) such a creep expression can be used under a triaxial state of stress, if the following assumptions are made: 1) the directions of the principal strains coincide with the principal stresses; 2) the volume remains constant; 3) the principal shear strains are proportional to the principal shear stresses and 4) the relation of the equivalent strain rate to the von–Mises equivalent stress is the same as for the uniaxial case. Soderberg's derivation as it is reviewed in several textbooks (see e.g. Finnie and Heller (1959) or Oding (1965)) leads to the following equations for the principal creep rates $\dot{\varepsilon}_{SS,ip}$ in a phase p:

$$\dot{\varepsilon}_{SS,1p} = B \cdot \sigma_p^{eq(n-1)} \cdot \left[\sigma_{1p} - \frac{1}{2}\left(\sigma_{2p} + \sigma_{3p}\right)\right], \qquad \textbf{(6-7 a)}$$

$$\dot{\varepsilon}_{SS,2p} = B \cdot \sigma_p^{eq(n-1)} \cdot \left[\sigma_{2p} - \frac{1}{2}\left(\sigma_{3p} + \sigma_{1p}\right)\right], \qquad \textbf{(6-7 b)}$$

$$\dot{\varepsilon}_{SS,3p} = B \cdot \sigma_p^{eq(n-1)} \cdot \left[\sigma_{3p} - \frac{1}{2}\left(\sigma_{1p} + \sigma_{2p}\right)\right], \qquad \textbf{(6-7 c)}$$

where σ_p^{eq} is the von-Mises equivalent stress in the phase p defined as

$$\sigma_p^{eq} = \sqrt{\frac{1}{2}\left[\left(\sigma_{1p} - \sigma_{2p}\right)^2 + \left(\sigma_{2p} - \sigma_{3p}\right)^2 + \left(\sigma_{3p} - \sigma_{1p}\right)^2\right]}. \qquad \textbf{(6-8)}$$

The creep contribution to the inelastic deformation can now be calculated from the creep rates in the phases by integrating (6-7) over the time increment of the simulation, using the current temperature and stress state in the phase.

Implementation of Rate-Independent Plastic Deformation

For some simulations, it was useful to additionally consider rate-independent plasticity as a source of inelastic strain in the slabs. For ideal plastic deformation, the directional contribution of rate-independent plastic flow can be obtained from the Levy-von-Mises equations as they are found in numerous textbooks (see e.g. Dieter (1988)):

$$\delta\varepsilon_{1p} = \frac{\delta\varepsilon_p^{eq}}{\sigma_p^{eq}}\left[\sigma_{1p} - \frac{1}{2}\left(\sigma_{2p} + \sigma_{3p}\right)\right] \qquad \textbf{(6-9 a)}$$

$$\delta\varepsilon_{2p} = \frac{\delta\varepsilon_p^{eq}}{\sigma_p^{eq}}\left[\sigma_{2p} - \frac{1}{2}\left(\sigma_{3p} + \sigma_{1p}\right)\right] \qquad \textbf{(6-9 b)}$$

$$\delta\varepsilon_{3p} = \frac{\delta\varepsilon_p^{eq}}{\sigma_p^{eq}}\left[\sigma_{3p} - \frac{1}{2}\left(\sigma_{1p} + \sigma_{2p}\right)\right] \qquad \textbf{(6-9 c)}$$

They specify the principal phase strain increments $\delta\varepsilon_{ip}$ if under a certain state of stress the equivalent strain is changed by $\delta\varepsilon_p^{eq}$ (the equivalent strain is defined in analogy to Eq. (6-8)).

In the simulation, this is considered as follows: For each time step, the creep strain and the resulting stress increments in the phases are computed and from this a preliminary phase stress is obtained. If the von-Mises equivalent stress in one phase exceeds the uniaxial yield stress of the material, a small increment in the equivalent plastic strain is assumed (typically 10^{-6}) and its directional components are calculated according to Eqs. (6-9). The plastic strain increments are now added to the inelastic strain increments and a new preliminary phase stress is calculated. If the equivalent phase stress is still in excess of the uniaxial yield stress, the equivalent plastic strain is again increased by a small increment. The whole procedure is repeated until the equivalent phase stress falls below the yield stress. In this way, a stress increment that causes the stress in a phase to cross the yield surface is relaxed by plastic flow within the same time-step, until the yield surface is reached again.

Temperature Dependent Properties

The elastic properties, the thermal expansion coefficient and the uniaxial yield stress of each phases were implemented as temperature dependent properties. They are supplied as a table of values for certain temperatures, between which the simulation program interpolates linearly. The temperature dependence for each property and for each phase can be switched off at will, if simulation time is to be saved.

6.1.3 Basic Limitations

To avoid misinterpretation, basic limitations of the slab model are summarized in the following. These limitations also have consequences for the way in which the slab model has to be calibrated in order to simulate the real composite material.

Reinforcement Texture

The slab model is highly anisotropic. Its geometry together with the strain-compatibility conditions (Eqs. 6-2) excludes strain mismatch and internal stresses in 1-direction. This will especially affect the thermoelastic properties, such as the Young's modulus or the CTE. In comparison to a material with discontinuous fibers in an ideal 2D-random arrangement, the slab model can be expected to over-estimate the anisotropy of these thermoelastic properties. The inelastic strain components are mainly determined by the von-Mises equivalent stress and

they are thus distributed more evenly in the 3 principal directions. In 1-direction, however, the generated inelastic strains produce no strain mismatch and no associated counteracting stress. As a consequence, the slab-model can be expected to over-estimate inelastic deformation in the 1-direction.

The experimentally studied reinforced piston alloy does not have an ideal 2D-random reinforcement texture. It was shown in the previous chapter that although the fibers were preferentially oriented in the yz-plane, the fiber orientation component in x-direction, though smaller, was also considerable. This weaker structural anisotropy tends to lower the mean stresses and strains compared to a strongly textured composite.

After all, the slab-model direction 1 matches best with the x-direction of the real composite and the y- and z-directions correspond to directions in the 2/3-plane. One has to be aware of the fact that internal stresses in 2/3 direction are over-estimated and are not present in the 1-direction. Furthermore, strains in 1-direction can be expected to be over-estimated.

Homogeneity

A severe simplification in the slab-model is the assumption of homogeneous deformation. In a real composite, stresses are expected to concentrate at reinforcement angularities and inelastic strains will occur there first. This has been shown in a vast number of FEM investigations. Because of the local stress concentrations, dynamic processes, such as creep under an increasing thermal misfit strain, will occur relatively widespread over the duration of the process. However, macroscopically, these local stresses and strains are noticeable only as a volume average. In contrast to the homogeneously deforming slabs, the inelastic response of a real composite will start earlier (because of the stress concentrations), but will be possibly less noticeable macroscopically (because of the volume average).

In the case of global plastic deformation, where regions of long-range dislocation glide get interconnected, plasticity can be thought of being uniform (Withers et al. (1989)). Then, the simplifying assumption of homogeneity of the slab-model is an appropriate one. The microstructural inhomogeneity of a real composite, which can for example influence the matrix yield stress and flow behavior, is, however, not captured in the slab-model.

Inelastic Deformation

The continuity of the slabs together with the strain compatibility condition introduces a fundamental limitation in the slab-model: If one slab is assumed to behave purely elastically, like an individual fiber in an MMC, inelastic deformation of the whole arrangement in 2/3 plane is completely disabled (because of the iso-strain assumption). In the real composite, however, the discontinuous nature of the fibers allows for global inelastic deformation of the matrix in the direction of the main reinforcement orientation. As far as creep deformation is concerned, this problem can be overcome by attributing creep properties not only to the matrix

but also to the reinforcement slab. This is a meaningful assumption: The slab-model is an abstraction of the real composite and in this abstraction, no individual fibers are considered but rather their collective coaction as a reinforcing phase, and this phase can deform inelastically. In a sense, the inelastic deformations of the matrix and the reinforcement slab represent two parts of matrix strain in the real material: Matrix (slab) deformation is the part of the global strain which creates fiber/matrix misfit. Reinforcement (slab) deformation represents the part of global strain which occurs without generation of misfit. Flow around fiber ends, for example, could be considered as a process which aids elongation of the composite but which does not transfer load to the fibers. It will be shown later how the creep properties of the slab model can be calibrated with experimental matrix and composite creep data.

Plastic deformation underlies the same limitations: When the reinforcement slab is purely elastic, plastic deformation of the matrix slab cannot cause permanent deformation of the whole slab arrangement because of the strain compatibility condition. The problem can in principle be overcome in the same way as for creep deformation. This was not done in this work because of lack of calibration data.

Sign of Loading

The slab model is insensitive to the sign of loading. Predictions of compressive and tensile creep rates, for example, differ only in their sign but not in the absolute values. This is because none of the assumed strain contributions contains a tension-compression inequity. Of course, internal stresses lead to indirect differences in the tensile and compressive response of the simulation, so that Bauschinger-like effects can be simulated. However, no real sign-dependent deformation mechanisms, such as reinforcement damage proposed by Bidlingmaier for the MMC under investigation (Bidlingmaier et al. (1998) cf. Section 3.5), are included.

6.2 Parameters for the Slab Model

Most of the properties of the matrix and reinforcement slabs were copied directly from the properties of the M124 matrix alloy and the Saffil fibers. These properties are listed in Section 6.2.1. The creep properties, however were calibrated so that the steady state isothermal creep behavior of the slab model matched the creep behavior of the real composite as closely as possible.

The reinforcement volume fraction was set to 15%, which is the nominal fraction of Saffil fibers in the investigated composite.

6.2.1 Properties of the Composite Constituents

In this sub-section, all those properties are summarized that were taken directly from the properties of the constituents and attributed to the slabs without further modification. These are the elastic constants, the CTEs and the matrix yield stress.

Elastic Properties

For the matrix slab, the room-temperature elastic properties of the matrix alloy M124 were taken from Table 3.3. Poisson's ratio was assumed to be constant for all temperatures and the elastic modulus for higher temperatures was taken from Figure 3.8. The values for the Saffil reinforcement were taken from Table 3.2 and assumed to be constant over the whole temperature range.

T [°C]	20	250	350	400	650
E_m [GPa]	80	71.6	65.2	59.4	0
ν_m []	0.325	–	–	0.325	0
E_r [GPa]	285	–	–	–	–
ν_r []	0.2	–	–	–	–

Table 6.1: *Elastic properties of the matrix and reinforcement slabs*

Thermal Expansion

The coefficients of thermal expansion were taken from Table 3.4 (matrix) and from Table 3.2 (reinforcement). Again, a temperature dependence was considered only for the matrix slab.

T [°C]	0	20	50	250	400	450
α_m [10^{-6}/K]	18.5	18.9	19.5	24.7	25.5	25.1
α_r [10^{-6}/K]	–	7.7	–	–	–	–

Table 6.2: *Thermal expansion coefficients of the matrix and reinforcement slabs*

Yield Stress

Only the matrix slab was allowed to yield. The uniaxial compressive 0.2%-yield stress of the over-aged matrix material, as it was shown in Figure 3.7b, was taken as yield stress for the matrix slab.

T [°C]	0	200	300	400	500	650
σ_m^y [MPa]	90	90	50	30	10	0

Table 6.3: *Uniaxial yield stress of the matrix slab*

6.2.2 Creep Parameters

The creep parameters were chosen such that the isothermal minimum composite creep rate was reproduced by the slab-model. This means that in the calibration not only constituent properties were used but also experimentally determined properties of the real composite. It is described in the following how this was done.

Matrix Creep

First, the matrix creep parameters for a power-law creep expression according to Eqs. (6-5) and (6-6) had to be determined. For this, the experimental tensile creep data by Bidlingmaier that were shown in section 3.5, Figure 3.10a were analyzed as follows: Rearranging (6-5) and using (6-6) gives

$$\ln \dot{\varepsilon}_{SS} + \frac{Q}{RT} = n \cdot \ln \sigma + \ln A \,. \qquad \textbf{(6-10)}$$

The left hand side of this equation was then plotted against $\ln\sigma$ by using experimental data for $\dot{\varepsilon}_{SS}$, σ and T and a rough estimate for Q. Next, Q was varied until a best fit to a straight line was achieved in the resulting diagram. The slope of this line finally yielded n and from the intercept, A could be calculated. The analysis is shown in Figure 6.3.

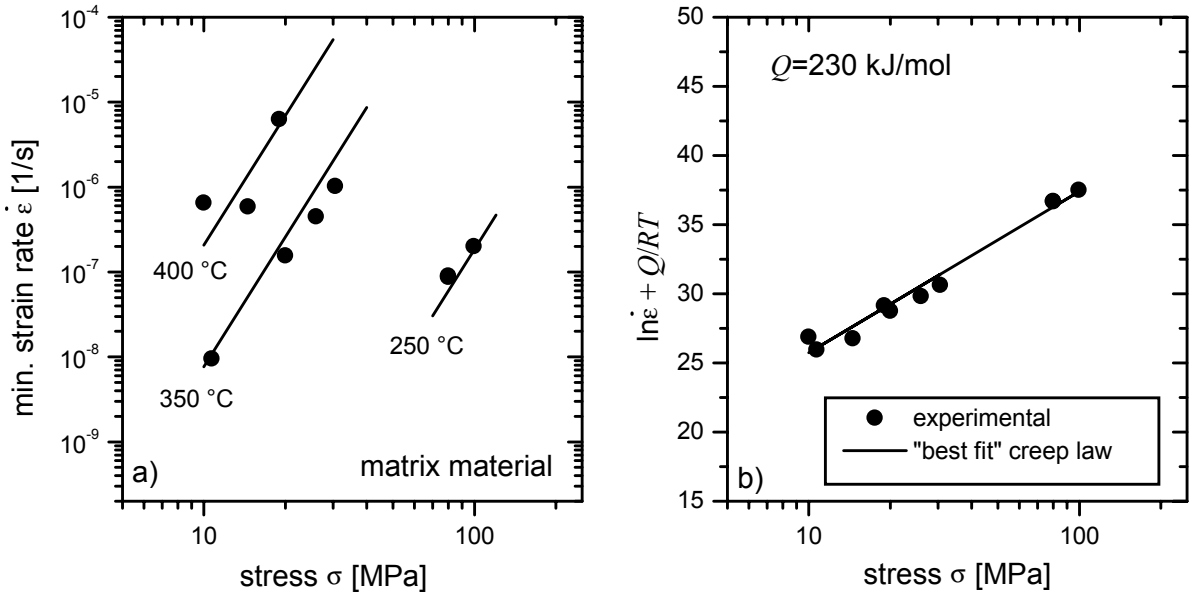

Figure 6.3: *a) Isothermal creep data for the matrix material in a classical Norton-type plot (cf. Fig. 3.10a). b) Best fit of creep data to a straight line after varying the activation energy Q.*

The analysis yielded the following creep parameters for the matrix slab:

Q_m [kJ/mol]	230
n_m []	5.07
A_m [MPa^{-n}s^{-1}]	$1.27 \cdot 10^6$

Table 6.4: *Creep parameters for the matrix slab according to (6-5)*

Reinforcement Creep

As pointed out in Section 6.1.3 it is useful to attribute creep properties to the reinforcement slab. The reinforcement slab is an abstraction of the collective effect of all fibers on the composite behavior and it must therefore have the ability to deform inelastically together with the composite.

As mentioned above, the creep parameters of the reinforcement slab were chosen such that the isothermal minimum composite creep rate was reproduced by the slab-model. They were determined from the experimental creep data of the composite material and the known creep law of the matrix. Based on the insight that if the phases of a composite can develop a steady state creep rate individually, the composite will also exhibit steady state creep, a simple rule of mixtures can be applied McLean (1994). The steady state is reached, when both phases are deforming with the same creep rate. The stresses in the phases that are necessary to sustain this creep rate have to fulfil the equilibrium condition:

$$\sigma(\dot{\varepsilon},T) = f_m \cdot \sigma_m(\dot{\varepsilon},T) + f_r \cdot \left[\frac{\dot{\varepsilon}}{A_r \exp(-Q_r/RT)}\right]^{1/n_r} \qquad \textbf{(6-11)}$$

The applied stress σ and the composite creep rate $\dot{\varepsilon}$ were given by experimental data points for various temperatures T. The stress $\sigma_m(\dot{\varepsilon},T)$ that has to be applied to the matrix in order to yield the composite creep rate was given by the matrix creep law that has been established above. The parameters that remained to be determined were A_r, Q_r and n_r. Rearranging (6-11) gives an equation analogous to the one that was used for the determination of the matrix creep parameters:

$$\left(\ln\dot{\varepsilon} + \frac{Q_r}{RT}\right) = n_r \cdot \ln\left(\frac{1}{f_r}\sigma - \frac{f_m}{f_r}\sigma_m(\dot{\varepsilon},T)\right) + \ln A_r \qquad \textbf{(6-12)}$$

Again, the left hand side of the equation was plotted against the stress dependent term on the right hand side of the equation. Then Q_r was varied, until a best fit to a straight line was obtained. From this fit, n_f and A_r were determined as before. The analysis is shown in Figure 6.4. There was one data point for creep at 250 °C and 180 MPa that could not be brought to agreement with the assumed creep law. This data point was excluded from the analysis. It is worth noting that the stress/strain-rate lines for various temperatures in Figure 6.4a are not

straight. For the composite creep law according to a simple rule of mixtures of power-laws, it is expected that the apparent stress exponent as well as the apparent activation energy both vary with stress and temperature McLean (1994).

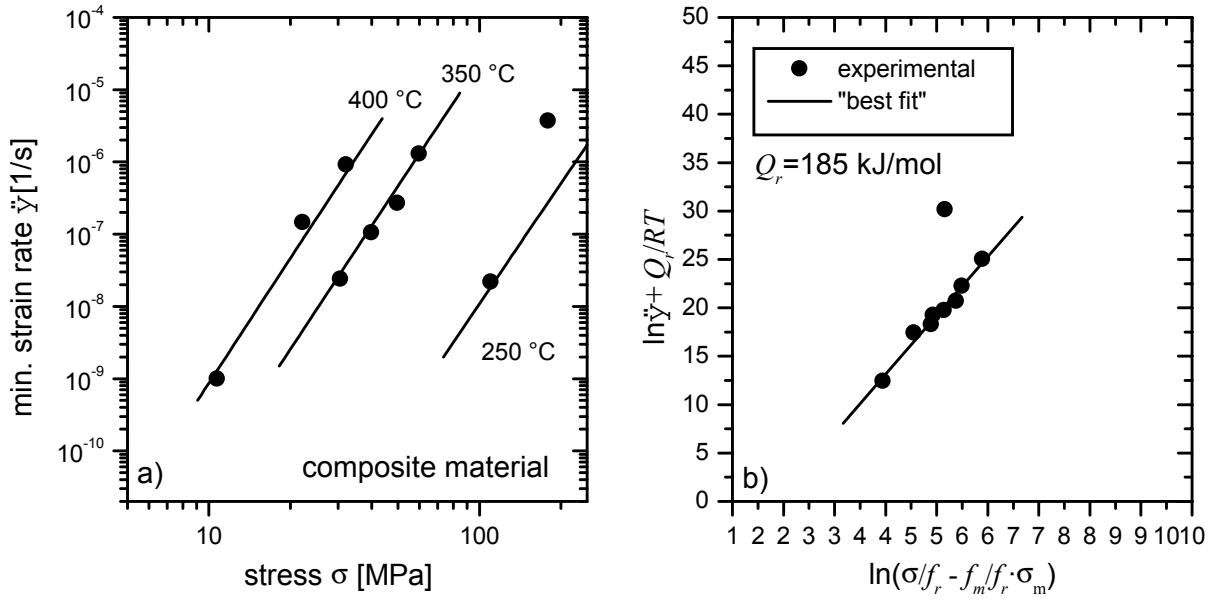

Figure 6.4: *a) Isothermal creep data for the composite material in a classical Norton-type plot (cf. Fig. 3.10b). Note that the lines that are drawn for the different temperatures are not straight. b) Best fit of creep data to a straight line after varying the activation energy Q_r.*

The analysis yielded the following parameters for power-law creep of the reinforcement slab:

Q_r [kJ/mol]	185
n_r []	6.08
A_r [MPa^{-n}s^{-1}]	$1.39 \cdot 10^{-5}$

Table 6.5: *Creep parameters for the reinforcement-slab according to (6-5).*

It is to be noted here that the rule of mixtures-approach (see Eq. (6-11)) that was applied in this analysis is not an approximation for the slab model. For uniaxial steady state creep of the slab arrangement under consideration of the triaxiality of the phase stresses, exactly the same formulation is obtained. This is shown in Section 6.3.3.

Tension / Compression Asymmetry of Creep Properties

It has been pointed out in Section 6.1.3 that the slab model is insensitive to the sign of loading and it can therefore not rationalize a tension / compression asymmetry of isothermal creep rates as found experimentally. The creep properties of the slab-model were calibrated with composite creep data for tensile loading. Because the measured tensile creep rates were always higher than the compressive ones, the slab model simulations will generally over-estimate creep rates when the reinforcement slab is mainly loaded in compression. The proper

way to overcome this problem would be to find a suitable model that is able to describe the experimentally observed inequity (possibly by taking into account reinforcement damage) and implement it in the slab-model. A crude alternative would be to re-calibrate the reinforcement creep properties using the compressive creep data of the composite. This set of parameters should then be used exclusively for simulations, where the reinforcement slab experiences mainly compressive loading. Unfortunately the compressive creep rates measured by Wolf (1997) were not sufficient in quantity and showed a considerable amount of scatter, so that they could not be analyzed adequately with the above method. Nevertheless, such a calibration was tried and the parameters found are given in Table 6.6. They can serve merely as an estimate and should only be used for simulations under constant compressive loading

Q_r [kJ/mol]	283
n_r []	5.98
A_r [$MPa^{-n}s^{-1}$]	$5.7 \cdot 10^1$

Table 6.6: *Estimate of creep parameters for the reinforcement-slab under monotonic compressive loading according to Eq. (6-5).*

6.2.3 Refinement: Primary Creep

In the results section, pronounced transient creep behavior was reported for many different experiments. In single phase materials, such behavior is usually attributed to primary creep. In composites, transitions in creep rates are also expected due to progressive load transfer from the creeping matrix to the reinforcement. The incorporation of a primary creep law for the matrix slab can help to study the interplay of the two effects – matrix primary creep and load transfer.

In order to do this, first, Bidlingmaier's (1996a) and Wolf's (1997) isothermal creep experiments for the matrix material (see Section 3.5) will be re-analyzed with respect to the creep behavior at low strains. Next, a primary creep law is set up on this basis, which in the last section is implemented into the slab model.

Analysis of Isothermal Creep Curves

It is often found in metals and alloys at elevated temperatures that the biggest portion of primary creep strain follows a power-law in time, such as

$$\varepsilon \propto t^a . \qquad \textbf{(6-13)}$$

For most pure metals at temperatures above $0.5 \cdot T_M$, the exponent a is 1/3 (Andrade (1910)). At lower temperatures or for alloyed metals, the time exponent can become higher. Dobson

and Greenwood (1996), for example, reported a time exponent of a=0.55 for pure aluminum at low stresses and below $0.45 \cdot T_M$. In the same work, they also found that the temperature dependence of primary creep had the same activation energy as the steady state creep law – a result which is also common for other metals (see e.g. Argon and Bhattacharya (1987)).

The power-law in time relationship can also be applied to the matrix material M124. In Figure 6.5, the initial portion of compressive creep curves, measured by (Wolf (1997)), are shown as a double-logarithmic plot of creep strain against a combined time-temperature parameter. It can be seen that the curves for different temperatures fall into the same narrow band, indicating that the transitional region has the same activation energy as the steady state creep law (Q_{app} = 294 kJ/mol for compressive matrix creep, cf. 3.5). In the region from 0.1% to 0.4%, the curves are linear with a time exponent of about 0.6. For lower strains, elastic and anelastic deformation can be assumed to contribute and beyond 0.4%, steady state and later on tertiary creep take over. It was tried to analyze Bidlingmaier's tensile creep data in the same way. As he mainly focused on the determination of the steady state creep rate, his data are not well resolved at low strains (see Section 3.5) so that only general trends can be given: The time exponent for tensile creep seems to be lower than in the compressive case (about 0.3) and the thermal activation energy again is roughly the same as for steady state creep (230 kJ/mol for tensile matrix creep). Primary creep seems to last only up to a very small strain, approximately 0.2%.

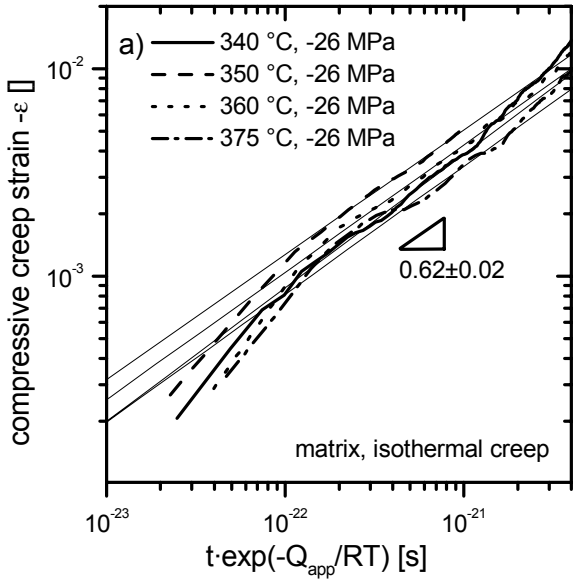

Figure 6.5: *Primary creep of the matrix material (compression). The creep curves follow a power-law in time with a time exponent of about 0.6 from 0.1% to 0.4% creep strain. The temperature dependence is roughly the same as for the steady state creep rates (Q_{app}=294 kJ/mol)*

In summary, the primary creep regime of the matrix alloy can be described by an equation of the following type:

$$\varepsilon = A^* t^a = A' \cdot D_{act} \cdot t^a \qquad \textbf{(6-14)}$$

ε is the primary creep strain at time t, $D_{act} = \exp(-Q/RT)$ is the thermal activation term and A' is a proportionality factor which is a function of stress. In order to use an equation of this type

in the slab model, the proportionality factor has to be determined in a way so that the creep laws for primary and secondary creep fit together.

Equation for Primary Creep

For later implementation in the slab-model simulation program, it is desirable to have a formulation for primary creep in terms of strain rate as a function of strain $\dot{\varepsilon}(\varepsilon)$ and not of strain as a function of time $\varepsilon(t)$. Differentiating Eq. 6-14 and substituting t for ε leads to

$$\dot{\varepsilon} = A^* \cdot a \cdot t^{a-1} = A^* \cdot a \cdot \left(\varepsilon / A^*\right)^{(1-1/a)} = A^{*1/a} \cdot a \cdot \varepsilon^{(1-1/a)}, \qquad \textbf{(6-15)}$$

which is valid for a certain combination of temperature and stress.

From isothermal creep tests of the matrix, it is known that primary creep is confined to low strains up to a limiting strain which we will call $\varepsilon_{prim,max}$. In Figure 6.5 it was shown that for compressive creep $\varepsilon_{prim,max}$ is approximately 0.4%. For higher strains, a steady-state power law in stress (Eq. 6-5) was assumed to be valid. At $\varepsilon_{prim,max}$ the two laws should give identical strain rates:

$$\dot{\varepsilon} = \dot{\varepsilon}_{ss} = A^{*1/a} \cdot a \cdot \varepsilon_{prim,max}^{(1-1/a)}, \qquad \textbf{(6-16)}$$

where $\dot{\varepsilon}_{ss}$ is the steady state creep rate given by the power-law in stress. From Eq. 6-16, the factor $A^{*1/a} \cdot a$ can be substituted in Eq. 6-15 so that we end up with the following simple formulation for the primary creep strain rate of a strain hardening material:

$$\dot{\varepsilon} = \dot{\varepsilon}_{ss} \cdot \left(\varepsilon / \varepsilon_{prim,max}\right)^{(1-1/a)} \qquad \textbf{(6-17)}$$

Altogether the creep rate is:

$$\dot{\varepsilon} = \begin{cases} \dot{\varepsilon}_{ss} \cdot \left(\varepsilon / \varepsilon_{prim,max}\right)^{(1-1/a)} & \text{for } \varepsilon_{inel} < \varepsilon_{prim,max} \\ \dot{\varepsilon}_{ss} & \text{for } \varepsilon_{inel} > \varepsilon_{prim,max} \end{cases} \qquad \textbf{(6-18)}$$

Application of this creep-law in its integrated form is shown in Figure 6.6. Three selected compressive creep curves by Wolf are compared to the creep curves according to Eq. 6-18. The parameters that were used were a=0.6 and $\varepsilon_{prim,max}$=0.4%. The parameters for steady-state creep were taken from Table 6.4. For these values, the agreement is quite satisfying.

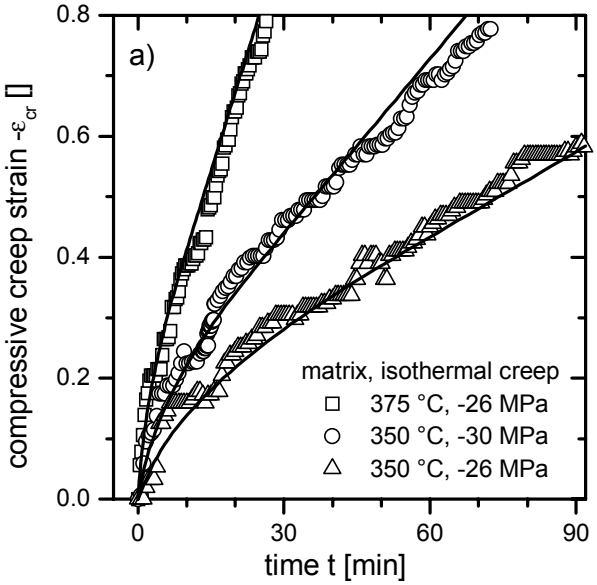

Figure 6.6: *Comparison of experimental creep curves (matrix, compression, Wolf (1997)) with creep curves according to Eq. 6-18 with a=0.6 and $\varepsilon_{prim,max}$=0.4%.*

Implementation

For the matrix slab, the creep law from Eq. 6-18 can be adapted to triaxiality when $\dot{\varepsilon}_{SS}$ is replaced by $\dot{\varepsilon}_{SS,i,m}$ from Eqs. 6-7a-c and all uniaxial strains are replaced by the appropriate equivalent strains. For the maximum primary creep strain this means that $\varepsilon_{prim,max}$ has to be changed to $\varepsilon^{eq}_{prim,max}$. For plastic flow (Poisson's ratio ν=0.5), the equivalent maximum primary creep strain is related to the uniaxially measured strain by $\varepsilon^{eq}_{prim,max} = \sqrt{3} \cdot \varepsilon_{prim,max}$. The same applies to the primary creep strain.

At very low values of inelastic strain (at the very beginning of creep), the creep rate has to be limited, because extremely high creep rates cause instabilities in the numerical simulation. Primary creep enhancement was therefore cut off below a critical strain $\varepsilon^{eq}_{prim,min}$. The following creep law was used for the phase *p* and the principal direction *i*:

$$\dot{\varepsilon}_{ip} = \begin{cases} \dot{\varepsilon}_{SS,ip} \cdot \left(\varepsilon^{eq}_{prim,min} \,/\, \varepsilon^{eq}_{prim,max} \right)^{(1-1/a)} & \text{for} \quad \varepsilon^{eq}_{p} \le \varepsilon^{eq}_{prim,min} \\ \dot{\varepsilon}_{SS,ip} \cdot \left(\varepsilon^{eq}_{p} \,/\, \varepsilon^{eq}_{prim,max} \right)^{(1-1/a)} & \text{for} \quad \varepsilon^{eq}_{p} < \varepsilon^{eq}_{inel} \le \varepsilon^{eq}_{prim,max} \\ \dot{\varepsilon}_{SS,ip} & \text{for} \quad \varepsilon^{eq}_{pl} > \varepsilon^{eq}_{prim,max} \end{cases}$$

(6-19)

At last, the slab-model simulation program has to be extended to keep track of the inelastic strain that has accumulated since ε_{inel}=0, so that it can decide, whether the primary or steady-state creep law is to be applied.

Great care has to be given to the evolution of the equivalent inelastic strain, especially when load or temperature are not held constant. Removing the load during a creep simulation, for example, could reduce the equivalent inelastic strain to low values so that primary creep suddenly reappears in the unloading curve. Such behavior has to be carefully considered, before attributing physical meaning to the simulation results.

6.2.4 Limitations Introduced by the Choice of Parameters

In addition to the basic limitations of the slab-model that were discussed in Section 6.1.3, the choice of parameters introduces further uncertainties.

Matrix Properties

A known problem in determining composite matrix properties from unreinforced material is that the matrix microstructure can be changed by the incorporation of a reinforcing phase. In the present case, the most apparent differences between the unreinforced alloy and the composite matrix are the grain and particle sizes. It must be assumed that those materials parameters which strongly depend on microstructure, such as the yield stress and the creep properties are changed due to the presence of the reinforcement. Increases in the apparent creep stress exponent and activation energy, for example, were frequently attributed to dispersion strengthening of the matrix, where the dispersoids were introduced during a powder metallurgical production route (e.g. Park et al. (1990)). The effect of a reduced subgrain size due to pinning by these dispersoids has also been discussed (e.g. Mishra and Pandey (1990)). This effect is assumed to be subordinate for the piston alloy, because of the employed casting route, which is less likely to introduce oxide particles into the matrix. Moreover, as was already mentioned in Section 3.2, the aging behavior was not significantly influenced by the presence of the reinforcement. As far as plastic yielding is concerned, the reduction in grain size, precipitation particle size and interparticle spacing (see Section 3.2) can be assumed to raise the yield stress of the composite matrix compared to the monolithic matrix alloy.

The microstructural changes in the matrix are complex. The matrix slab properties were thus adopted unchanged from the unreinforced material.

Plastic Deformation

In the current implementation, plastic deformation is confined to the matrix slab. Because of the strain compatibility condition, plastic matrix deformation does not cause direct plastic deformation of the whole slab arrangement, it only helps to reduce the internal elastic strain mismatch. Cyclically repeated plastic deformation of the matrix, for example, would lead to no permanent deformation if the reinforcement slab remained entirely elastic. In the current implementation, plastic deformation of the matrix causes permanent deformation of the slab arrangement only indirectly by increasing the stresses that drive creep in the reinforcement.

This is a crucial point for modeling thermal cycling creep. It will be shown later on (Section 6.3.4) that thermal cycling induces stresses in the matrix that exceed the yield stress – especially at the low-temperature end of the cycle where the matrix stresses become highly tensile. When matrix plasticity is permitted in the simulation, the stresses at the low temperature end are limited by the yield stress (because the thermal misfit is accommodated plastically). For the above reasons, however, the big effect of plasticity on the overall stress

evolution is not reflected in the strain evolution. Nevertheless, simulations incorporating matrix plasticity are still useful. Under thermal cycling conditions, it is e.g. possible to quantify the amount of plastic deformation by calculating the accumulated equivalent inelastic matrix strain in one cycle. When the cycle amplitude / frequency / temperature etc. is altered, this quantity will change and these changes can be expected to correlate with changes in the deformation rate of the real material.

6.3 Basic Results

In this section the slab model, fed with the parameters from the last section, is used to calculate basic physical properties and behavior of the composite material. The calculations of the elastic properties and the thermal expansion in the first two sub-sections are predictions based on the constituent properties. These are compared to predictions based on Eshelby-type models. In the third sub-section, the isothermal creep behavior is simulated.

6.3.1 Elasticity

If only elastic strains are considered, the slab-model yields the following expressions for Young's modulus in 1-direction and in the 2/3-plane :

$$E_1 = \left[\left(\frac{f_m}{E_m} - \frac{f_r}{E_r} \right) - 2 f_m C^2 \cdot (AB+1) \cdot \left(\frac{1}{A} - AB^2 \right) \right]^{-1} \qquad \textbf{(6-20)}$$

$$E_{2/3} = \frac{\frac{1}{A} - AB^2}{\frac{1}{E_m}(D - ABE) - \frac{\nu_m}{E_m}(ABD - E)} \qquad \textbf{(6-21)}$$

The terms A, B, C, D and E were defined previously for Eq. (6-4). These two equations are derived in Appendix C. They contain only the elastic constants and the volume fractions of the slabs. The variation of both moduli with the reinforcement volume fraction are shown in Figure 6.7. They are compared to predictions based on the equivalent elastic inclusion method by Eshelby. Predictions using the mean-field approach (see Section 2.1.2) have been made with three different Eshelby (S-) tensors: The first was an S-tensor for discs parallel to the 2/3 plane. This represents the same geometry as the slab model and the use of this tensor therefore led to exactly the same thermoelastic predictions as the slab-model*. For the case of *fibrous* reinforcement, a composite structure which comes closest to the slab-model arrangement is the arrangement of continuous fibers in a 2D random planar array. The S-tensor for such an

* This applies only to Eshelby-modeling of non-dilute systems using the mean-field approach.

arrangement was given by Johannesson and Ogin (1995). Predictions with this "random-planar" *S*-tensor have also been made. Both Eshelby tensors – for discs and the random planar arrangement – are listed in Appendix A.1. Finally, an average Eshelby tensor has been calculated which represents the fiber orientation distribution of the real composite under investigation. The procedure with which this "average" *S*-tensor was determined is outlined in Appendix A.2. Predictions based on the average *S*-tensor are also given. It must be noted that the Eshelby-model is strictly valid only for entirely elastic problems of an ellipsoidal inclusion in an infinite matrix. For non-dilute systems, like in the present case, the matrix has to be approximated by an effective medium and this mean-field approach leads to lower bound estimates of the composite properties (Withers et al. (1989)).

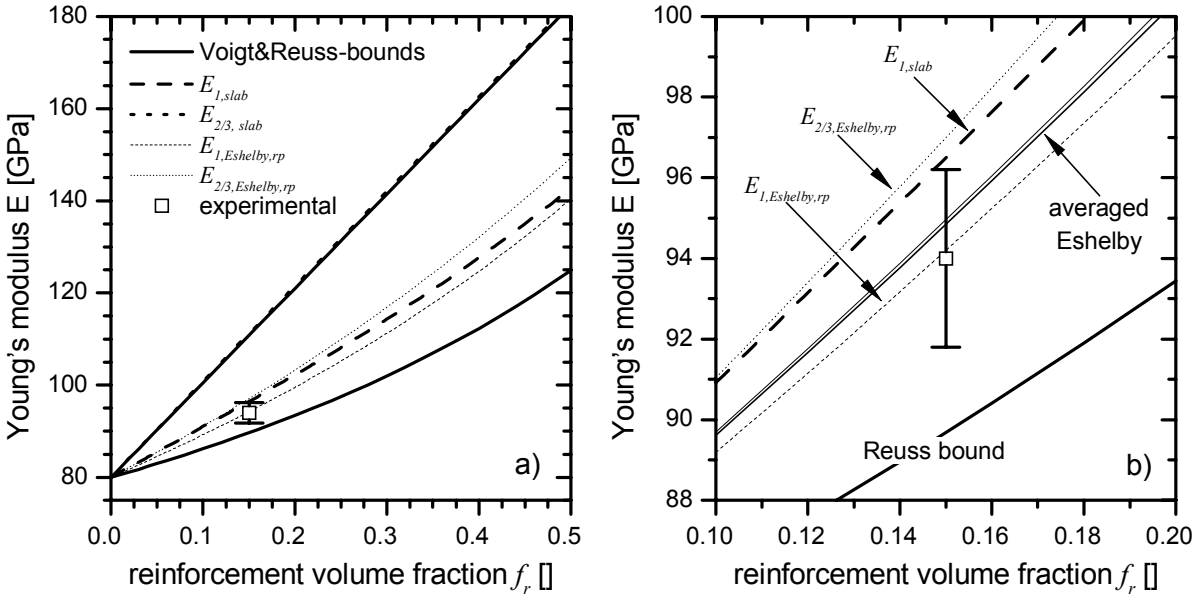

Figure 6.7: *The predicted Young's moduli for two-phase composites and different models (room-temperature). a) A rough estimate is given by the iso-strain (Voigt) and iso-stress (Reuss) rule of mixtures. The in-plane (2/3 plane) Young's modulus of the slab model shows only very little deviations from the linear rule of mixtures. In the stacking direction, the slab-model prediction lies in between the Voigt- and the Reuss-bounds. Predictions from an Eshelby-type model assuming a random planar arrangement of continuous fibers for the in-plane and the perpendicular (1-) direction both lie close to the slab-model prediction in stacking direction. The experimental value lies in between the Eshelby-predictions. b) Magnified version of a). In b) Eshelby-predictions for the average S-tensor which closely describes the real fiber orientation distribution are additionally given. Note that the moduli in 1-direction and in the 2/3 plane are almost the same for this averaged tensor.*

It can be seen that the prediction of the Young's modulus in the direction of stacking is close to the prediction of an Eshelby-based model for continuous fibers in random-planar arrangement. At a reinforcement volume fraction of 15% the values for the slab model lie closer to the Eshelby-prediction in 2/3-plane than to the Eshelby-prediction perpendicular to the fiber-plane. The in-plane slab-model prediction shows only very little deviation from the linear rule of mixtures. The stiffness is bigger due to the additional internal stresses caused by the different Poisson's ratios of the slabs. Eshelby-predictions for the averaged *S*-tensor reveal a negligible macroscopic elastic anisotropy. The predictions deviate from the experimental data (Bidlingmaier (1999)) by less than 1% and are well within the range of the measurement error.

The low amount of elastic anisotropy led Bidlingmaier to the conclusion that the fiber orientation distribution is 3D random.

The slab model over-estimates Young's modulus of a composite. This general trend is also seen in the comparison with the experimental Young's modulus of the composite. As pointed out in Section 6.1.3, the slab-arrangement obviously over-estimates the effectiveness of the reinforcement in impeding the matrix elastic expansion – especially in the 2/3-plane. However, the prediction for the 1-direction is quite satisfactory.

6.3.2 Thermal Expansion

If inelastic strains are excluded, the thermal expansion of the slab arrangement without external load is given by

$$\alpha_1 = f_m\alpha_m + f_r\alpha_r + 2f_m\left(\frac{\nu_r}{E_r} - \frac{\nu_m}{E_m}\right)\cdot\left[\frac{1-\nu_m}{E_m} + \frac{f_m}{f_r}\cdot\frac{1-\nu_r}{E_r}\right]^{-1}(\alpha_r - \alpha_m) \qquad \textbf{(6-22)}$$

and

$$\alpha_2 = \alpha_m + \frac{1-\nu_m}{E_m}\cdot\left[\frac{1-\nu_m}{E_m} + \frac{f_m}{f_r}\cdot\frac{1-\nu_r}{E_r}\right]^{-1}\cdot(\alpha_r - \alpha_m) \qquad \textbf{(6-23)}$$

Again, the results are compared to predictions of an Eshelby-type model for continuous fibers in a random-planar arrangement. The comparison is shown in Figure 6.8. The composite CTE tensor was calculated using Eq. 2-2. The Eshelby tensor used was also the one for a random-planar arrangement of continuous fibers in the 2/3-plane.

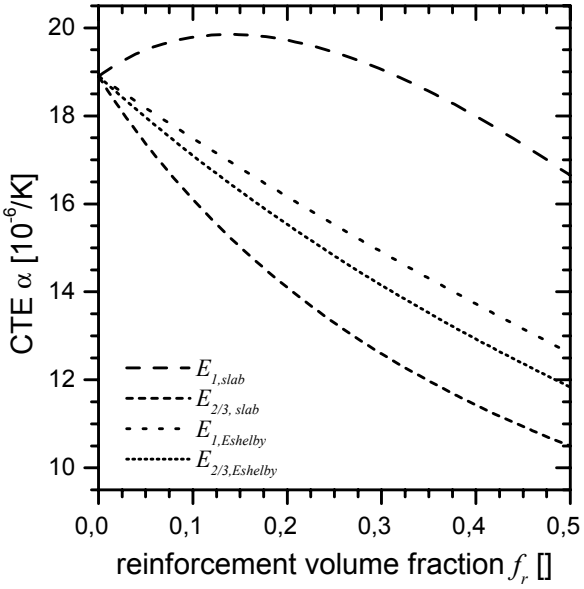

Figure 6.8: *The predicted thermal expansivities for two-phase composites according to the slab model and an Eshelby-type model assuming a random planar arrangement of continuous fibers in the 2/3-plane. It can be seen that the slab model gives only very rough estimates of the composite CTE. At the relevant reinforcement volume fraction of 15%, the predicted composite CTE in the 1-direction is higher than the matrix CTE (α_m= 18.5 10^{-6}/K).*

The slab-model predictions for the 1-direction and the 2/3-plane differ largely from each other and are in both cases far off the predictions from the Eshelby-type model. The CTE in 1-

direction even assumes a maximum for reinforcement volume fractions around 15%. The aforementioned high effectiveness of the reinforcement slab in the 2/3-plane is the reason for the strong impediment of matrix expansion in this direction. The matrix reacts with an enhancement of the expansion in the 1-direction.

6.3.3 Isothermal Creep

During creep of the slab arrangement, load is progressively transferred from one slab to the other. A steady state is reached when both slabs deform at the same rate under their individual (and then constant) state of stress. For uniaxial loading in 1-direction, this creep rate can be easily calculated: At steady state the creep rates have to be equal in the two slabs

$$\begin{aligned}\dot{\varepsilon}_1 &= \dot{\varepsilon}_{1m} = \dot{\varepsilon}_{1r} \\ &= B_m \cdot \sigma_m^{eq\,(n_m-1)} \cdot \left[\sigma_{1m} - \frac{1}{2}\left(\sigma_{2m} + \sigma_{3m}\right)\right] \\ &= B_r \cdot \sigma_r^{eq\,(n_r-1)} \cdot \left[\sigma_{1r} - \frac{1}{2}\left(\sigma_{2r} + \sigma_{3r}\right)\right]\end{aligned} \qquad \textbf{(6-24)}$$

and with the conditions for the external stresses $\sigma_1=\sigma_{1m}=\sigma_{1r}$ and $\sigma_2=\sigma_3=0$ and the phase stresses $\sigma_{2m}=\sigma_{3m}$ and $\sigma_{2r}=\sigma_{3r}$ this equation simplifies to

$$\dot{\varepsilon}_1 = \dot{\varepsilon}_{1m} = \dot{\varepsilon}_{1r} = B_m \cdot \left(\sigma_1 - \sigma_{2m}\right)^{n_m} = B_r \cdot \left(\sigma_1 - \sigma_{2r}\right)^{n_r}. \qquad \textbf{(6-25)}$$

With the equilibrium condition (6-3b) we arrive at

$$\dot{\varepsilon}_1 = B_r \cdot \left[\frac{\sigma_1}{f_r} - \frac{f_m}{f_r}\left(\frac{\dot{\varepsilon}_1}{B_m}\right)^{1/n_m}\right]^{n_r} \qquad \textbf{(6-26)}$$

which can be solved for $\dot{\varepsilon}_1$ numerically. This equation is essentially identical to Eq. (6-12) if $\dot{\varepsilon}_1$ is replaced by $\dot{\varepsilon}$ and σ_1 by σ and because $\left(\dot{\varepsilon}/B_m\right)^{1/n_m} = \sigma_m$. This means that the slab model yields exactly the same steady-state creep rate as the simple rule of mixtures that was applied for the determination of the creep parameters (page 97). The same creep rate is obtained numerically with the slab-model for uniaxial loading in the 2/3-plane. In summary, the steady-state creep-rate is dependent only on the external uniaxial stress, the temperature and the creep properties of the slabs. The transitional behavior from the moment of loading until the steady state is reached, however, additionally depends on the elastic properties, the direction of loading and on the existence of internal stresses. In Figure 6.9, experimental and simulated creep curves are compared. The experimental and the simulated creep rates coincide in the steady state region as they should according to the calibration. It can be seen that the slab model predicts the existence of a primary creep regime although only steady-state creep laws are used for the individual slabs. Yet it strongly under-estimates the creep rate in the transient

region. When primary creep is additionally considered, transient creep becomes more pronounced, the experimental creep rates are, however, still not reached.

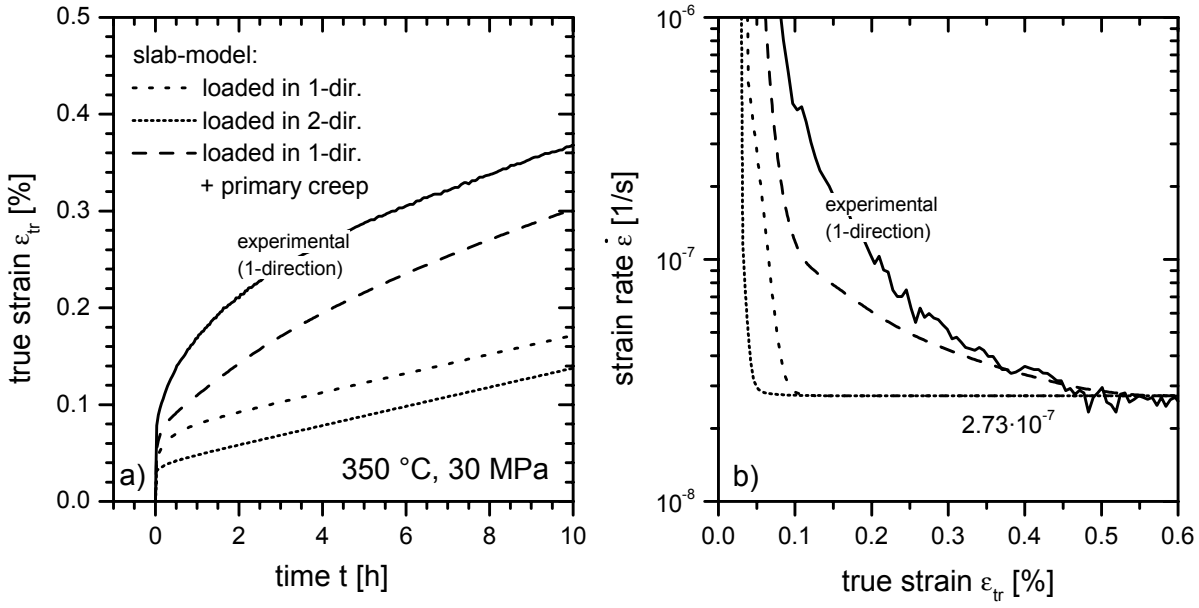

Figure 6.9: *Experimental and modeled creep curves for 350 °C and 30 MPa. The strain vs. time curves (a) include the elastic stain on loading. The dashed and dotted lines show the simulated strain evolution (in the direction of loading) for loading in 1- and 2-direction. Additionally, a simulated curve for loading in 1-direction and considering primary creep is shown. The slabs were assumed to be stress-free prior to loading. In b) the evolution of strain rate with strain is shown. It can be seen that the modeled creep curves exhibit very distinct transient creep behavior, depending on the loading direction and the presence of internal stresses (not shown). They all, however, converge to a common creep rate of $2.73 \cdot 10^{-7}$ 1/s because of the calibration of the slab-model. When no primary creep is considered, the transitional regime lasts up to 0.2% at maximum. The experimental creep curve in contrast displays a much more pronounced transitional behavior, as the steady state is reached not before 0.5%.*

6.3.4 Thermal Cycling

The Thermoelastic Coefficient of Stress

The stresses that are generated in the slab arrangement by changing the temperature are easily calculated from Equation 6-4. When no external stresses are applied and no inelastic deformation is allowed, the stress change upon a temperature change in the matrix is given by

$$\frac{d\sigma_{m2/3}}{dT} = \frac{(AB+1)}{\left(1/A - AB^2\right)} \cdot (\alpha_r - \alpha_m) \qquad \textbf{(6-27)}$$

This quantity is called *thermoelastic coefficient of stress* (see 2.1.1, page 4) because the thermal expansion mismatch is accommodated purely elastically. It represents the slope of a line in a diagram of induced stress vs. temperature, which is often called the *thermoelastic line*. Neglecting the differences between the Poisson's ratios and substituting the reinforcement modulus by $E_r = k_E \cdot E_m$, where k_E is the factor by which the reinforcement is stiffer than the matrix, then Eq. 6-27 simplifies to:

$$\frac{d\sigma_{m2/3}}{dT} = \frac{E_m}{(1-\nu)} \cdot \frac{f_r \cdot k_E}{1+f_r(k_E-1)} \cdot (\alpha_r - \alpha_m). \qquad \textbf{(6-28)}$$

It is apparent from this formula that the thermally induced stress is not only proportional to the difference in CTE but also depends on the modulus mismatch (measured by k_E). For very low reinforcement volume fractions ($f_r \to 0$), the thermally induced stresses depend linearly on k_E, i.e. the stiffer the reinforcement is, the higher are the matrix stresses. Higher reinforcement volume fractions diminish the influence of the modulus mismatch. For ($f_r \to 1$), the influence vanishes. All this applies only to the simplified geometry of the slab-model. In a real composite, the TECS depends additionally on the reinforcement shape and the orientation distribution.

The TECS can also be calculated with the elastic inclusion-theory by Eshelby (see Section 2.1.2, page 5). In Figure 6.10, values for $(d\sigma_m/dT)_{el}$ are calculated for the slab-model and the Eshelby model (using again the Eshelby tensor for a random-planar array of continuous fibers and the averaged Eshelby-tensor for the fiber orientation distribution of the investigated material). The temperature dependence is caused by considering the temperature dependence of the matrix Young's modulus (decreasing with temperature) and the matrix CTE (increasing with temperature). It can be seen that the slab model predicts much higher stress changes for a given temperature change than the Eshelby model. Again, the effectiveness of the reinforcement is over-estimated in the 2/3-plane and not present perpendicular to the stacking direction. The Eshelby model, in contrast, takes into account the thermal strain misfit in all directions, including the one perpendicular to the main reinforcement direction. This leads to a considerable amount of hydrostatic stress in the mean matrix stress state and to relatively low equivalent stresses. For the real fiber orientation distribution, the Eshelby-model predicts almost entirely hydrostatic thermally induced stresses. This is a direct consequence of volume averaging and it can be expected that predictions of creep deformation, based on Eshelby-type mean matrix stresses under-estimate the real composite behavior.

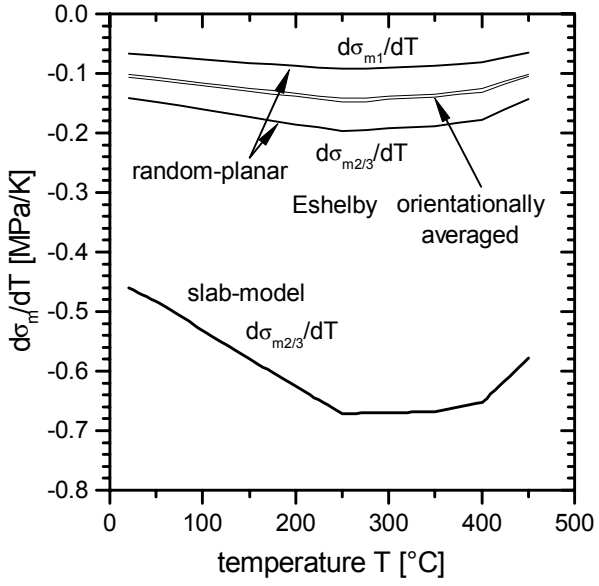

Figure 6.10: *Stress change due to thermoelastic strain misfit induced by temperature changes. The slope of the so-called thermoelastic line (thermoelastic coefficient of stress $(d\sigma_m/dT)_{el}$) is given for the slab-model and for Eshelby-type modeling assuming a random planar arrangement of continuous fibers in the 2/3-plane and for the averaged S-tensor which describes the fiber orientation distribution of the investigated material. For the slab model, only stresses in the 2/3-plane are generated by thermal strain misfit. For the Eshelby-type model, stresses in 2/3- and 1-direction are shown.*

Thermally Induced Stresses for Elastic Accommodation

The absolute value of the internal stresses during thermal cycling is not only dependent on the thermal excursion and the TECS but also on the reference temperature, where the internal stresses are zero. This temperature is called the effective stress free temperature T_{esf}. The lowest tensile and compressive stresses are induced when the stress-free temperature lies in the middle of the thermal cycle. For higher T_{esf}, the tensile stresses in the low-temperature part of the cycle become higher on the expense of the compressive stresses at high temperatures. In Figure 6.11, this is shown for a 450↔150 °C cycle where the T_{esf} is arbitrarily set to 400 °C. The thermoelastic lines for the slab model and for the mean-field Eshslby model were calculated by numerically integrating over the values for the TECS given in Figure 6.10. In the slab model, with no external load applied, the stress in the 1-direction is always zero and thus the equibiaxial matrix stress in the 2/3-plane is identical to the von-Mises equivalent stress. With the Eshelby method, the principal thermoelastic matrix stresses are lower in the 2/3-plane but higher in the 1-direction. Therefore the mean equivalent matrix stresses are very low. As mentioned above, for the case of the averaged Eshelby tensor which represents the fiber orientation distribution of the investigated material, the mean matrix stress state is almost entirely hydrostatic. This reveals a serious drawback of the mean-field approach in Eshelby-type modeling: the implicit volume averaging leads to low deviatoric stresses although locally, highly deviatoric stress states are present. In the extreme case of spherical inclusions or a 3D random orientation distribution of any kind of reinforcement, an entirely hydrostatic stress state would be predicted. These models are thus not very useful for the prediction of inelastic deformation.

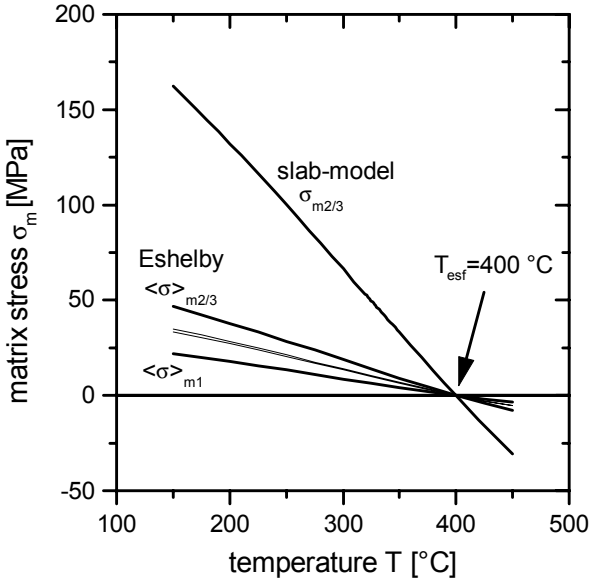

Figure 6.11: *Thermoelastic lines for a 450↔150 °C cycle with the effective stress free temperature T_{esf} set to 400 °C. Given are the slab-model matrix stresses in the 2/3-plane (in 1-direction the matrix stress is zero by definition) and the mean principal matrix stresses calculated with the Eshelby model, using the S-tensor for a random planar arrangement of continuous fibers and the average S-tensor for the composite fiber orientation tensor. The lines were obtained by integrating the TECS values from Figure 6.10.*

The stresses calculated with the slab model are very high compared to the mean-field-predictions. For the given cycle, they reach up above 150 MPa in tension and down to –30 MPa in compression. These stresses are high enough to cause considerable creep or plastic

deformation. When these deformation mechanisms are considered in the slab model simulation, the matrix stress changes. This will be addressed in the next paragraph.

Stress Evolution Including Creep and Plasticity

In Figure 6.12 the slab-model simulations of the internal matrix stress, now considering inelastic deformation, are shown. The thermal cycle was the same as above. Stress-temperature curves are given for creep relaxation enabled and for combined creep and plasticity. For comparison, the thermoelastic line from the previous paragraph is also given. Only stable stress-temperature hystereses are shown. In this context, the term "stable" means that the evolution of stress and strain is identical for the present and subsequent cycles. For the given cycle and the high temperatures, this stable hysteresis is reached after the very first cycle already. For lower temperatures it can take many more cycles until the stress evolution, originating from the initial stress state, assumes a steady state.

For the simulation with only creep contribution the cycle starts at 450 °C with compressive stresses. In this temperature range, creep causes the stress to deviate from the thermoelastic line. During cooling, a state of zero matrix stress is assumed. At this point, creep ceases and thus the material behavior becomes thermoelastic. As the stresses rise further, the stresses again deviate from the thermoelastic line until at a temperature of around 300°C, the creep contribution to the deformation becomes negligible and the slope of the curve again assumes the slope of the thermoelastic line. In principle the same things happen on re-heating: The thermoelastic line is left at around 300 °C but the slope becomes thermoelastic again as the stress approaches zero (at around 390°C). For further increasing temperature and stress, creep comes into effect once more and relaxes the compressive stress partly, until the maximum temperature is reached again.

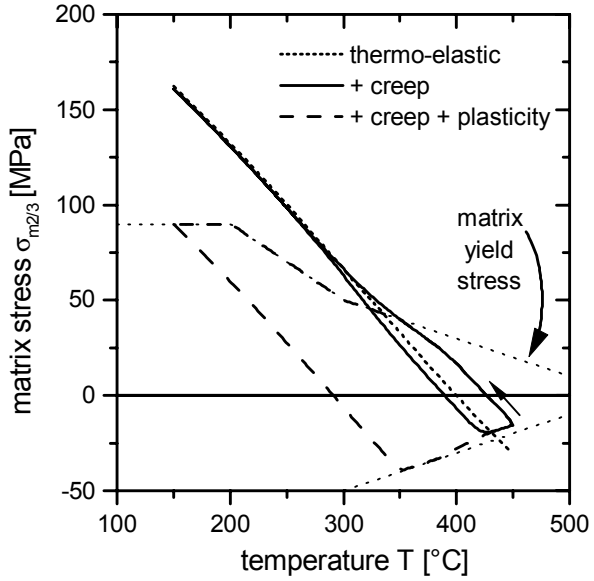

Figure 6.12: *Slab model simulations of the matrix stress in 2/3 direction for thermal cycling from 450°C to 150 °C. Ramp rates were ±50 K/min, no external load was applied. Only stable cycles are shown.*

The implemented matrix yield stress as a function of temperature is also shown in Figure 6.12 (values are given in Tab. 6.3). The stress-temperature curve (including creep) impinges on the yield stress-curve slightly above 350 °C. If matrix plasticity is also taken into account, the stress-temperature curve follows the yield stress curve from that point on downwards to 150 °C, because the thermoelastic coefficient of stress is more negative than the slope of the yield-stress curve (note again that for the case of a slab-arrangement with no external load applied, the stress in 1-direction is always zero and thus the matrix stress in the 2/3-plane is identical to the equivalent stress and can be compared directly to the uniaxial yield stress). On re-heating from 150 °C, the compressive yield stress is reached at around 350 °C. The stress follows the yield stress curve up to 380 °C, where creep becomes strong enough to relax the stress quickly to absolute values below the yield stress.

Shakedown

In the discussion of the internal stress evolution in MMCs, it is useful to adopt some of the terminology from the continuum mechanics literature in the field of fatigue modeling and ratcheting, as it was done by Elfishawy and Daehn (1995). In this field, the term *shakedown* is frequently used for the phenomenon that cyclic plastic deformations (usually modeled on the basis of the Levy-von-Mises flow rule) lead to a redistribution of internal stresses in a way so that a stable cyclic stress evolution in the elastic regime is achieved. Shakedown occurs frequently, when a composite is cooled from production temperature (initially stress free) and the induced stresses cause the matrix to yield. The term *thermal shakedown* is often used for this behavior. Along with shakedown, two other terms are often used to qualify cyclic behavior: *Cyclic plasticity* and *ratcheting*. These are used to qualify the case that a stable internal stress evolution is reached where the yield surface bounds the stable stress-cycle at two ends, in tension and compression. *Ratcheting* is used when the repeated plastic deformation leads to stable permanent changes in the external dimensions. *Cyclic plasticity* is used when the deformation is entirely “internal” i.e. permanent macroscopic deformation does not occur at all or maybe only in the first few cycles. Elfishawy and Daehn (1995) additionally introduce the term *isolated plasticity*, which describes the behavior in real composites that stable plastic zones are formed during thermal cycling, but that these zones do not interconnect. In this case the material is dimensionally stable. Based on this classification of composite deformation behavior, Elfishawy and Daehn (1995) have proposed composite behavior maps for simple composite geometries.

The above terminology is confined to the case of elastic-plastic behavior. Creep is usually not taken into account. Under creep conditions, inelastic strains will also lead to a redistribution of internal stresses, even if the plastic yield stress is not reached. This will also lead to a stable stress-temperature cycle sooner or later (depending on how big the contribution of inelastic deformation is). We will call this phenomenon *creep shakedown*. If stresses and temperature during the cycle are high enough to cause considerable creep deformation, creep shakedown

will occur in the first or after a few cycles (like in the example form the last paragraph). If the creep contribution in the cycle is small, creep shakedown can take very long times but it will eventually happen.

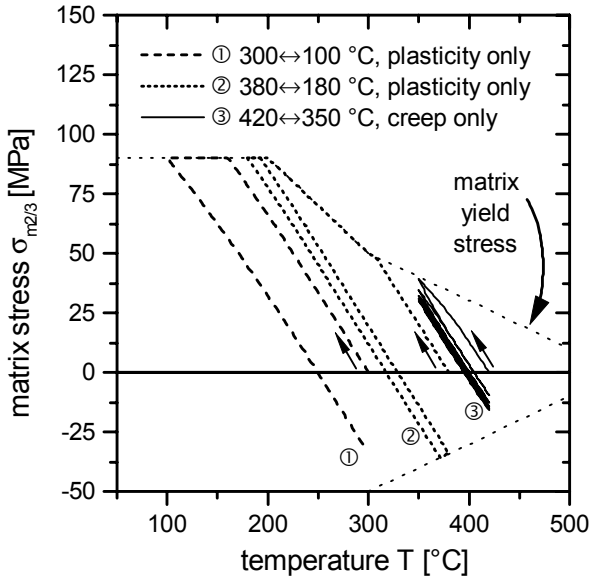

Figure 6.13: *Simulated examples for thermal shakedown (①), cyclic plasticity (②) and creep shakedown (③). Cycling starts at T_{max} with no internal stresses. Shakedown: For the 300↔100 °C cycle, the yield stress is reached during the cooling of the first cycle. Subsequent cycles are entirely elastic. Cyclic plasticity: For the 380↔180 °C cycle, again, the yield stress is reached during cooling and also upon re-heating in the first cycle. Stresses in subsequent cycles are bound by the yield stress in tension and compression. Creep shakedown: For the 420↔350 °C cycle, only creep deformation takes place. It takes several cycles (here: 6) until the stress evolution has assumed a steady cycle.*

Strain Evolution

The strain evolution for two stable unloaded thermal cycles corresponding to the above simulation incorporating creep deformation is shown in Figure 6.14. As expected, the strain-temperature evolution is linear in regions where the composite response is thermoelastic. The strain evolution deviates from a straight line whenever inelastic deformation takes place. It can be seen that the biggest part of the accumulated strain in one half-cycle is recovered during the other half-cycle. However, the strains are not fully reversed, i.e. the strain-temperature hysteresis does not close so that a small amount of strain is accumulated during each cycle. The slab model thus predicts thermal ratcheting, because all this happens without an external load applied. This is a direct consequence of the two slabs having different creep properties. When creep of one phase is disabled or when both phases are given the same creep properties, the strains become fully reversed so that the strain per cycle becomes zero. This sometimes unwanted effect must be considered when cyclic strains are calculated for applied loads. Thermal cycling creep rates under applied loads can be corrected for the influence of thermal ratcheting by subtracting the creep rate for unloaded cycling. This can be done, when the external load is small so that the stress evolution is not changed too much compared to unloaded cycling. As the ratcheting strain rate is usually low, its influence is only relevant at low applied stresses, where the TCC rate is also low.

The strain evolution is clearly dominated by the thermal expansion/contraction strain and effects of inelastic deformation are comparatively small. Therefore, as it was already said in

Section 4.3.1, page 53, the strain evolution is best analyzed in terms of the instantaneous CTE, which will be done in Chapter 7.

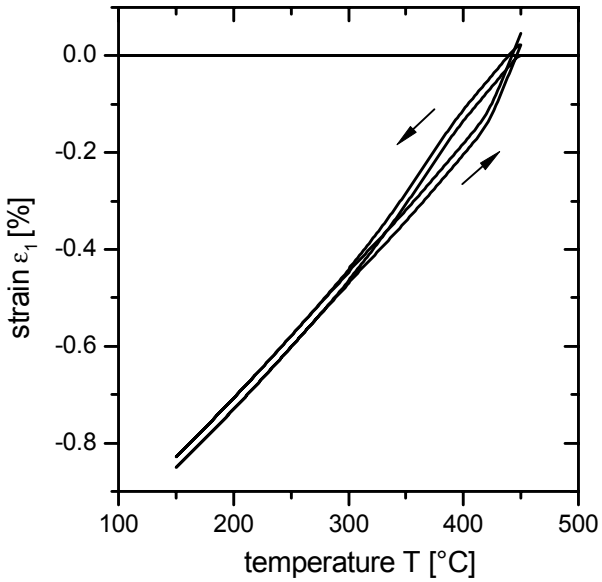

Figure 6.14: *Evolution of strain in stable cycles, calculated with the slab model for an unloaded 450↔150 °C cycle. Only thermoelastic and creep deformation are considered. Note that the cyclic strain is not fully reversed.*

7 Discussion

The experimental results will be discussed in three different stages. In the first two sections, the discussion will be limited to the minimum strain rate data from the thermal cycling creep experiments, for the unreinforced and the composite material. The TCC rates will be compared to the isothermal creep rates as well as to literature data. It will be analyzed which classical features of thermal cycling creep are found in the technical material under investigation and where its behavior differs from the expected behavior. Comparison to slab model simulations will be of great help here. In the third section, the strain evolution in individual cycles will be discussed and again, slab model simulations will be presented for comparison. The concept of load transfer and progressive damage of the reinforcement will be discussed in the fourth and fifth section. The isothermal, stress cycling creep experiments are interpreted in the fourth section and the conclusions from these experiments will be used in the fifth section, where the overall form of the thermal cycling creep curves is discussed. The influence of specimen orientation and the sign of loading will also be discussed there.

7.1 Thermal Cycling Creep of the Unreinforced Material

In Section 5.2.3 it was shown that even the unreinforced matrix material exhibits accelerated creep deformation under thermal cycling conditions. This behavior will be now discussed in comparison to literature data.

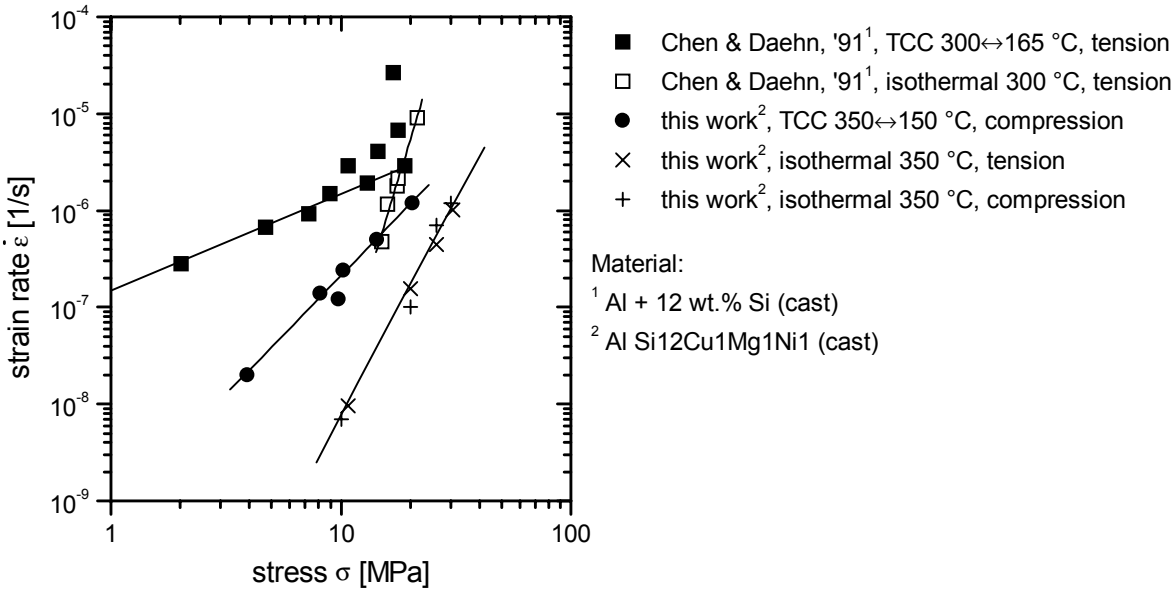

Figure 7.1: *Comparison of matrix TCC rates to literature data for a eutectic binary Al-Si alloy*

The eutectic matrix material can be considered as a composite of aluminum with silicon platelets. It is thus not surprising that this alloy shows thermal cycling creep acceleration at low loads. The only investigation of thermal cycling creep with an Al-Si "composite" that was

found in the available literature was performed by Chen and Daehn (1991). They tested a sand-cast binary eutectic Al-12 wt.%Si (13.6 vol.%) isothermally and under thermal cycles of 165↔300 °C at various tensile loads. They found "classical" thermal cycling creep behavior at low loads with an apparent stress exponent of one and negligible transitional behavior upon load changes. Their results are shown in Figure 7.1 in comparison to data from Section 5.2.3.

The two composites have the same amount of Si as reinforcement and, apart from the additional intermetallic precipitates, differ only in the constitution of the matrix. The M124 alloy studied in the present work has an aluminum matrix which is precipitation hardening and which has been optimized for yield strength and creep resistance. The matrix in Chen and Daehn's material was aluminum of commercial purity. It is thus not surprising that, despite the higher temperature (350 °C instead of 300 °C), the M124 alloy exhibits lower creep rates than the binary eutectic. For the same reason, the technical alloy also performs better under TCC conditions, with lower creep rates at the same stresses and even higher T_{max} and larger thermal excursions. The TCC rates were found to approach an apparent stress exponent of one only when T_{max} was increased to 450 °C and the thermal excursion was raised to 300 °C.

These findings may be relevant for the application of the matrix alloy in engine environments. Thermal cycling creep of the matrix alloy was, however, not the subject of the present work and will not be discussed further. Based on these general findings, however, a more detailed discussion will be made regarding the effect of the silicon platelets on thermal cycling creep of the fiber-reinforced material in Section 7.2.3.

7.2 Thermal Cycling Creep Rates of the Composite

7.2.1 Comparison to Isothermal Creep

Equivalent Strain Rates

In Chapter 5, the minimum creep rates from all thermal cycling creep tests were compared to creep rates from isothermal tests at the maximum cycle temperature. From an engineering point of view, this is a useful comparison because it involves the two most severe temperature conditions in an automotive engine environment: Permanent operation at a peak temperature and steadily repeated cycling to a peak temperature. It is also a very direct and easy to understand comparison and the observed creep enhancements are intuitively striking.

The real extent of thermal cycling creep enhancement, however, can only be seen when comparison is made to the isothermal creep rate at an equivalent temperature T_{eq}, which takes into account the influence of the varying temperature during the cycle. This equivalent temperature is usually taken as the average temperature of the cycle, weighted for the diffusion coefficient

and is therefore often called “diffusional mean temperature”. It can be calculated for a temperature profile $T(t)$ and an activation energy Q with the following formula (solving for T_{eq}):

$$\exp\left[-Q/\left(R \cdot T_{eq}\right)\right] = \frac{1}{t_c} \cdot \int_0^{t_c} \exp\left[-Q/\left(R \cdot T(t)\right)\right] dt \qquad \textbf{(7-1)}$$

Comparison to isothermal creep can then be made by measuring the isothermal creep rates at the diffusional mean temperature (e.g. Gordon and Clyne (1993)). An equivalent approach makes use of isothermal creep data obtained at T_{max}: One can calculate a diffusivity-compensated strain rate $\dot{\varepsilon}/D$ for cyclic and isothermal tests, where D is the diffusion coefficient for creep. For thermal cycling experiments, an effective diffusion coefficient has to be determined then by again averaging the temperature dependence of the diffusion coefficient over the whole thermal cycle (usually done by graphical integration (e.g. Hong et al. (1988)).

In both cases it is assumed that the temperature dependence of composite creep can be described by a single thermally activated process. This is not necessarily so, if the reinforcement itself shows thermally activated deformation or it the reinforcement introduces stress relaxation processes with a different thermal activation than that for matrix creep. In the slab model, presented in Chapter 6, this is considered by attributing separate creep properties to the reinforcement slab. It has been pointed out there already that this causes the apparent activation energy to be no longer independent of temperature, although the activation energies for creep of the two constituents are constant. Maybe this is the reason why the direct comparison of thermal cycling creep rates to creep rates at T_{max} is more widespread in the literature dealing with thermal cycling of composites (Wu and Sherby (1984), Pickard and Derby (1990), Wakashima et al. (1986), Goncales-Doncel and Sherby (1996)). In contrast, most investigations of thermal cycling of single-phase materials make use of effective temperatures or diffusivity-compensated strain rates (Lobb et al. (1972), Wu et al. (1987), Dunand and Bedell (1996)).

In this work the thermally equivalent isothermal strain rates were determined with the aid of the slab model simulation program. Loaded thermal cycling was simulated with the thermal expansion coefficients of the phases set to zero, so that no thermal strain mismatch was present. A net equivalent creep rate can be determined when a steady state is achieved. At this point, it has to be pointed out again that, as the slab model is insensitive to the sign of loading and as it was calibrated with tensile composite creep data, the simulation will over-estimate creep rates of compressive tests. In Section 6.2.2, page 98, a re-calibration with isothermal compressive creep data was proposed to overcome this drawback. This re-calibration can be applied here, because the absence of thermal cycling stresses ensures that the stress components in the reinforcement stay compressive.

Basic Results, Compared to Isothermal Creep Rates

In Figure 7.2, TCC rates from selected experiments from Chapter 5 (all for x-orientation) are compared to isothermal creep rates at the equivalent temperatures. Thermal cycling in any case led to higher creep rates than for isothermal creep at T_{max}. Of course, the increase in strain rate is even more drastic when compared to creep at the equivalent temperature: In the tensile case, creep is accelerated by a factor of at least 10 for the standard cycle (350↔150 °C) and by a factor of at least 30 for the high-temperature cycle (450↔120 °C). The compressive TCC rates exceed the estimated isothermal creep rates at T_{eq}, by a factor of around 35.

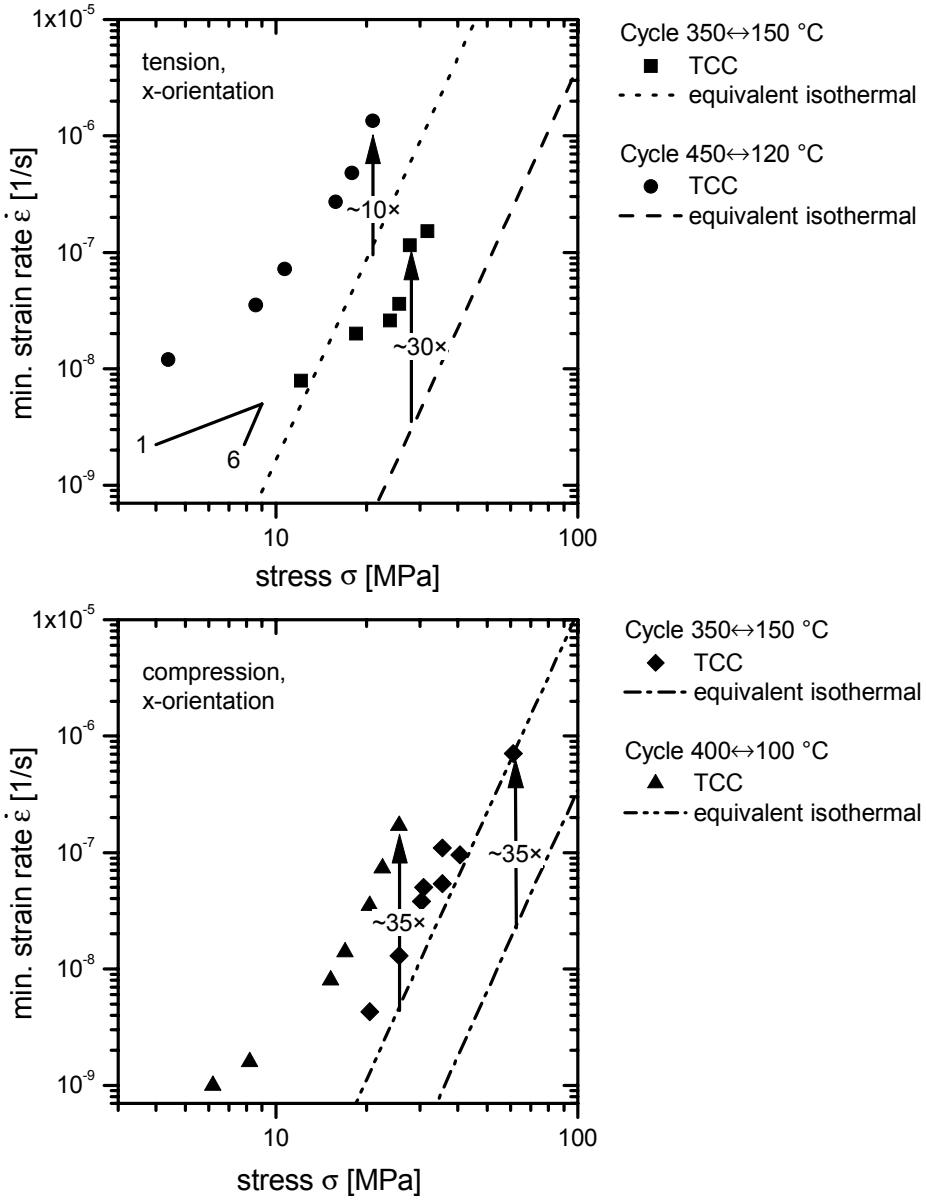

Figure 7.2: *Thermal cycling creep rates for different thermal cycles, compared to isothermal creep rates at equivalent (diffusional mean) temperatures.*

The overall stress dependence of the TCC rates was found to be similar to literature results for other MMCs: At high stresses, the stress exponent matches the one for isothermal creep. At

lower stresses, it continuously decreases towards unity, except for the compressive tests with standard cycles, where no such reduction of the stress exponent was found. It is remarkable that none of the curves displayed approaches the isothermal strain rate values for high stresses as reported in literature (e.g. Kitazono and Sato (1999)). Instead, the TCC strain rate vs. stress curves seem to be offset relative to the isothermal curves by a certain factor.

This disparity at high stresses is not caused by measurement errors or systematic failures in the conduction of the experiments. Errors in the measurement of stresses and strains are far below the observed shift of data: Stresses were constant within ±0.5 MPa. The failure in the determination of a strain rate of, say, 10^{-7} 1/s is only about 10 percent, based on a maximum strain measurement error of $\Delta\varepsilon=\pm 4\cdot 10^{-5}$ (see Section 4.2.5), measured over one hour. Basic material differences could also be excluded as a source of error. All specimens were manufactured from the same batch of material and thus had undergone the same processing.

After all, for the material under investigation, the acceleration of creep by thermal cycling was not limited to very low stresses but was present over the whole range of stresses.

7.2.2 Comparison to Literature Data

Comparison to Literature Data: Al/Al_2O_{3f}-Composites

The only study of thermal cycling creep of aluminum reinforced with discontinuous alumina (Saffil) fibers that could be found is the thesis by Furness (Furness (1991)). He investigated, amongst other systems, aluminum of commercial purity, reinforced with 10 and 20% δ-Al_2O_3-fibers (Saffil). The composites were produced in two different ways. One was a powder metallurgical route, involving dry blending of the powder and the reinforcement, followed by cold compaction and hot extrusion. The second route was squeeze infiltration of fiber-preforms, again followed by hot extrusion. During the extrusion process, the Saffil fibers broke to pieces with a mean aspect ratio of 3.5 to 5 and were aligned in the extrusion direction. From these composites, tensile specimens were machined with the fibers aligned in the loading direction. Tensile isothermal creep as well as thermal cycling creep tests were performed, employing the technique of laser scanning extensometry (Furness and Clyne (1991a)). The thermal cycle employed by Furness was identical to the standard cycle that was used in this work, except that T_{max} and T_{min} were 340 and 140 °C respectively. In Figure 7.3, the strain rates reported by Furness are compared to the tensile TCC-rates (standard cycle, *x*-orientation) from the present work. Also given are isothermal creep rates at 300 °C. It can be seen that the powder-route material has similar creep rates at 300 °C as the composite used in the present work (extrapolated from Bidlingmaier's creep results). The same applies to the TCC rates. For a composite with a pure aluminum matrix, this is a comparatively high creep strength. Furness attributed this to matrix strengthening by a fine oxide dispersion that was introduced by the powder-route processing. The composite made by squeeze casting contained

no comparable oxide dispersion and thus exhibited a substantially lower creep strength. Both composites showed considerable TCC-enhancement by factors comparable to those for the reinforced piston alloy.

The composites investigated by Furness show the same overall behavior as the reinforced Al-Si alloy investigated in the present study: no extreme change in the stress exponent and a considerable difference between the TCC- and isothermal creep rates at high stresses were found. A thermal cycling stress exponent tending towards unity was not reported. It has to be noted that Furness found no measurable permanent creep deformation at a load of 8 MPa for the powder-route material. He attributed this to the possible existence of a creep threshold stress (as proposed by Park et al. (1990), see 2.2.1,).

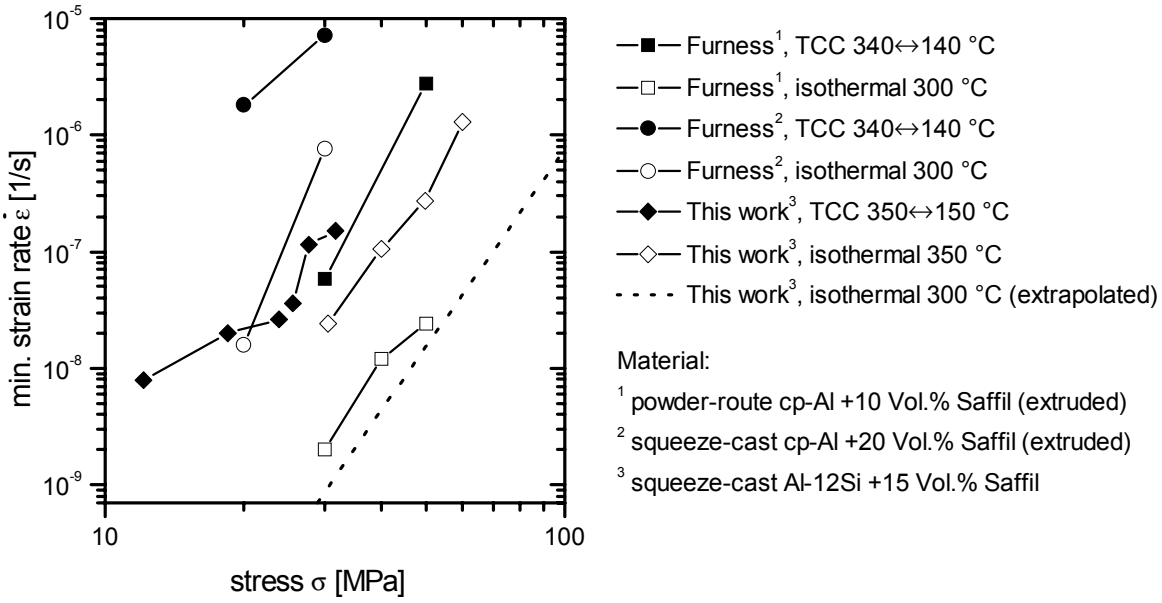

Figure 7.3: *Comparison of TCC rates to data from Furness (1991).*

Comparison to Literature Data: Al/SiC-Composites

As already mentioned in Section 0, the bulk of the experimental work in the field of TCC has been performed on the composite system Al/SiC. In this and the following sections, TCC behavior as it has been found in the literature for the Al/SiC system will be compared to the behavior of the Al/Al_2O_3 system used in this work. One can expect that the two systems exhibit substantially different TCC rates: For SiC reinforcement, the CTE mismatch is much larger, resulting in higher internal strain mismatches. Therefore only general trends and dependencies in the TCC properties will be compared.

Pure and alloyed aluminum matrices reinforced by different volume fractions of SiC particles or whiskers in various sizes have been investigated. In most of these studies, the basic phenomenology of the thermal cycling creep behavior of pure metals with anisotropic CTEs (Zn, U) or with phase transformations (U, Ti) was reproduced. This includes that TCC rates

and equivalent isothermal creep rates coincide at high applied stresses and that TCC rates have a stress exponent close to unity at low stresses. In Figure 7.4 some examples for this behavior from the works of Daehn and Gonzalez-Doncél (1989) and Goncales-Doncel and Sherby (1996) are given.

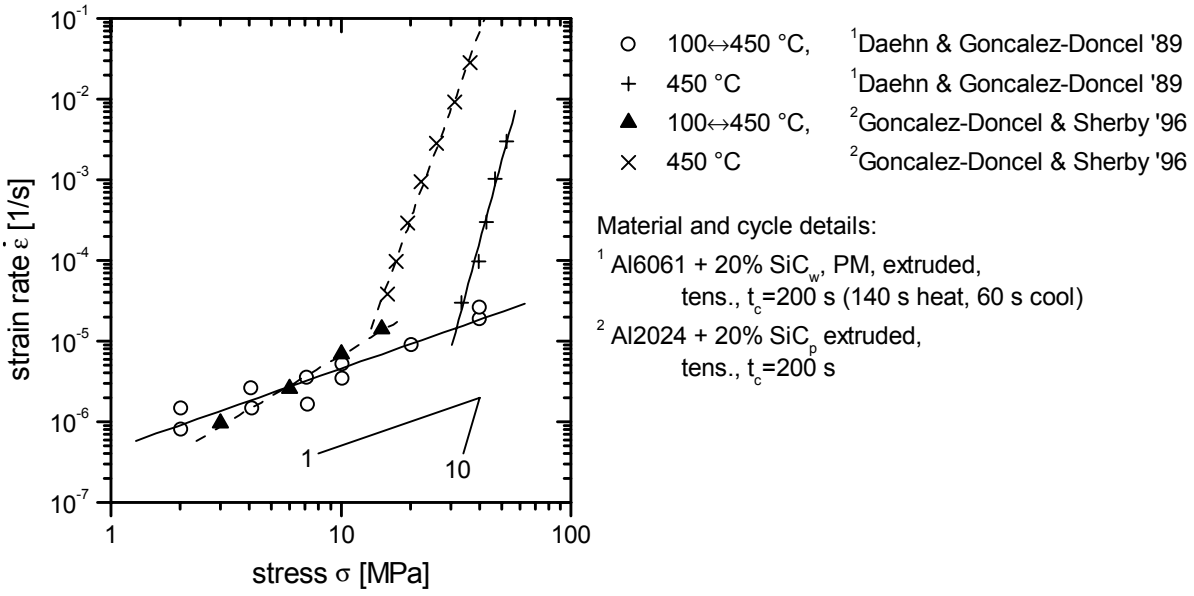

Figure 7.4: *TCC data for Al/SiC composites, taken from Daehn and Gonzalez-Doncél (1989) and Goncales-Doncel and Sherby (1996). The TCC rates have a stress exponent close to unity up to at least the isothermal creep rates at T_{max}. Creep is only accelerated by thermal cycling at low stresses. At high stresses, isothermal creep at T_{max} leads to higher creep rates.*

In these studies, it has been shown that the stress exponent for TCC is about unity over the whole range of stresses up to the isothermal creep rates at T_{max}. The lines for TCC and isothermal creep intersect and it can be assumed that the TCC-rates coincide with the equivalent isothermal creep rates at higher stresses.

There are, however, also reports of TCC behavior for Al/SiC systems that show a disparity between the TCC rates and isothermal creep rate curves, similar to he one reported in the present work. These are given in Figure 7.5. Only Hong et al. (1988) mentioned this discrepancy, but the authors did not discuss its origin or offer an explanation. They investigated aluminum systems with 10 and 20 vol.% of aligned SiC whiskers under longitudinal and transverse compressive loading. In all cases, the TCC rates deviated from the slope-1 behavior at stresses far below those stresses that cause comparable isothermal creep rates at T_{max}. The offset was even more drastic when diffusivity compensated strain rates were compared (see Hong et al. (1988)). A similar but less pronounced offset was found in the work of Wu and Sherby (1984), but again, it was not addressed by the authors. Unfortunatly, there is a lack of experimental studies that include comparisons to isothermal data. Therefore no clear statements can be made about the origin of the displacement between the TCC rates and the isothermal creep rates.

Even slight changes in one of the parameters can obviously influence the creep behavior strongly. This is illustrated in Figure 7.5. In both of the cited investigations, most of the material and test parameters seem to be the same, except for the T6 treatment that was applied to the material in the investigation by Hong et al. (1988). Surprisingly, the isothermal creep strength of the age hardened material was lower than for the material studied by Wu and Sherby (1984). This is probably due to differences in the processing route that were not reported in the cited investigations. In the light of this, the fact that the TCC rates fall onto the same line for lower stresses can be mere coincidence.

The most prominent difference between the experiments shown in Figure 7.4 and 7.5 is the loading direction: The two investigations, in which a large stress displacement between TCC and isothermal creep was found, were conducted under compressive loading. Such a difference between tensile and compressive loading was not found in the present work (see Figure 7.2), where such a displacement was observed under both types of loading. No comparative study of TCC under various loading directions has been found in the literature. Apart from that, no definite distinction between the results in Figure 7.4 and Figure 7.5 could be found, which could give indications about the origin of the disparity between the creep rate vs. stress curves.

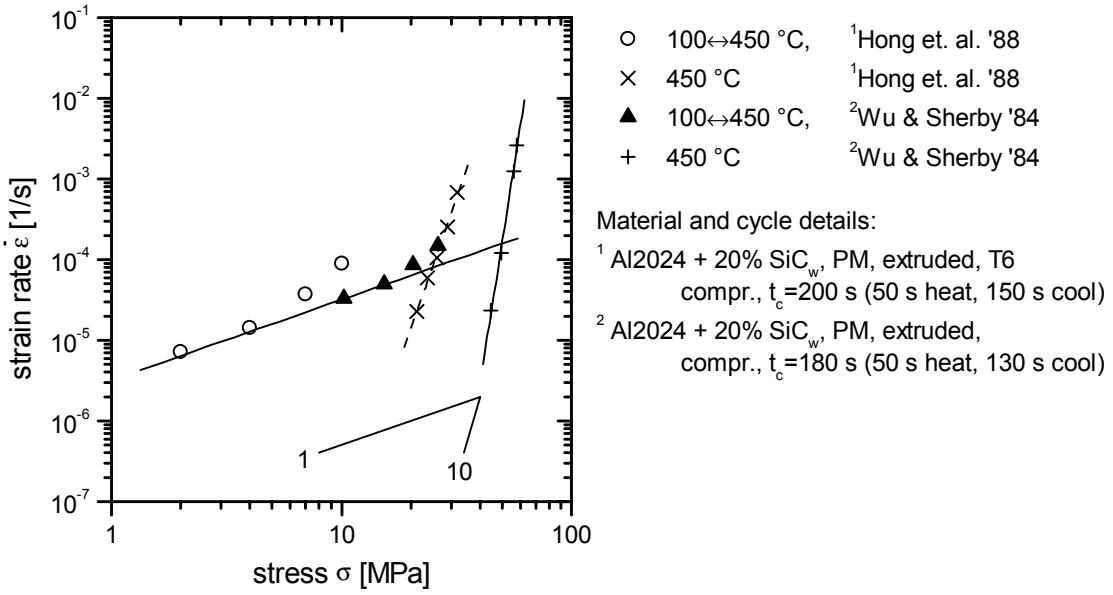

Figure 7.5: *TCC and isothermal creep data for Al/SiC composites, by Hong et al. (1988) and Wu and Sherby (1984). The TCC rates have a stress exponent close to unity at very low stresses. However, the stress exponent starts to increase at stresses below those that are needed for comparable isothermal creep rates at T_{max}.*

From an engineering point of view, it is interesting to know which material performs better under thermal cycling creep conditions: the piston alloy reinforced with Al_2O_3 fibers or the precipitation hardening alloys with SiC reinforcement. In Figure 7.6 such a comparison is made for intermediate temperatures (T_{max} = 350 °C) and high temperature cycles (T_{max} = 450 °C). One of the very few investigations of TCC in Al/SiC systems where also cycles with

low T_{max} were investigated is the work by Pickard and Derby (1990). They performed their experiments on commercially pure aluminum, reinforced with various amounts of SiC-particles (powder-metallurgical processing). In Figure 7.6a, TCC data are shown for a material with 20 vol.% reinforcement that was tested in tension with a 7-minute thermal cycles from 350 to 120 °C (including a long upper dwell-time). Isothermal creep rates at 350 °C are given as well. It can be seen that the thermal cycling creep rates are at least two orders of magnitude higher than for the alumina fiber reinforced piston alloy. The isothermal creep rates are also higher in the investigated range of stress. For higher temperatures, the results of Daehn and Gonzalez-Doncél (1989) (cf. Figure 7.4) are compared to high-temperature TCC rates from this work. Again, it is obvious that the TCC rates are considerably higher for the Material with SiC reinforcement. For isothermal creep, no definite statement can be made, because the 450 °C creep rates for the fiber-reinforced piston alloy were not measured experimentally but were extrapolated from lower temperatures. It is likely that the isothermal creep strength at lower stresses is higher for the SiC-reinforced material owing to the higher stress exponent.

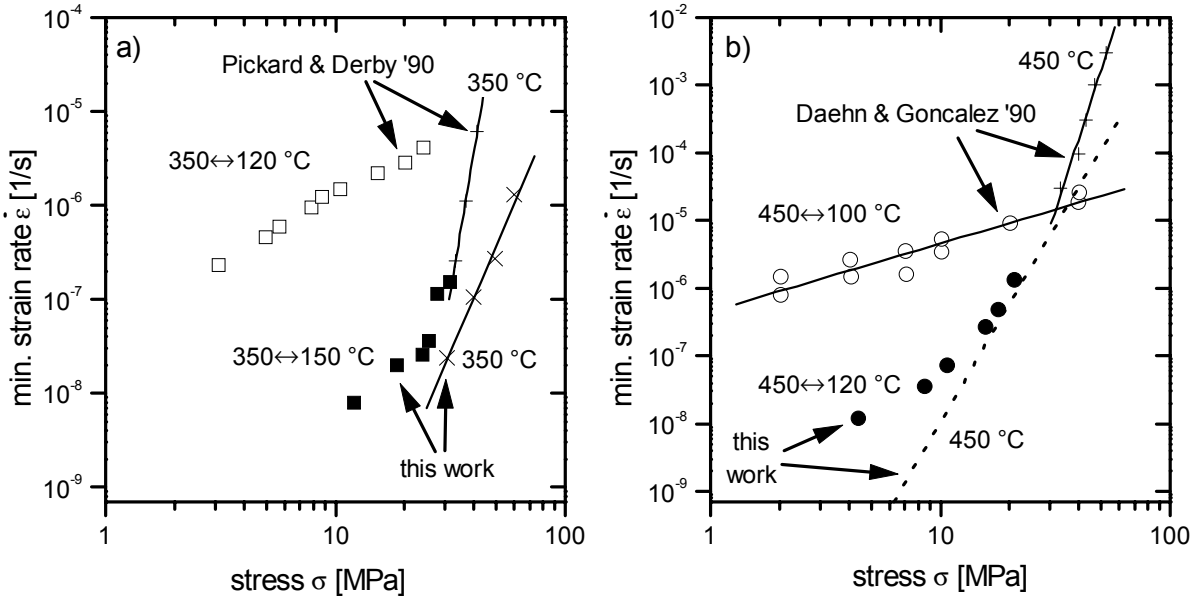

Figure 7.6: *Comparison of TCC rates from this work to TCC rates of Al/SiC systems from the literature. Experiments with similar thermal cycles are compared.a) Thermal cycles with T_{max}=350 °C, Literature data were taken from Pickard and Derby (1990), who investigated cp-Al with 20 vol.% SiC_p (2.3 µm) in tension. The thermal cycles had a duration of 7 minutes and included a long upper dwell time. b) Thermal cycles with T_{max}=350 °C, Literature data were taken from Daehn and Gonzalez-Doncél (1989) (see Figure 7.4).*

The explanation for the worse TCC performance of composites with SiC reinforcement lies in the higher thermoelastic mismatch. The shape of the reinforcement – high aspect ratio fibers as compared to short whiskers – may additionally play a role for the distribution of the internal stresses. In the following section, the influence of the constituent properties and the reinforcement shape on the induced internal stresses will be analyzed in more detail.

7.2.3 Stresses Induced by Thermal Cycling

In this sub-section, the influence of the type of reinforcement on the thermally induced stresses will be investigated. At first, the basic influence of the material combination will be addressed and secondly, the influence of the reinforcement morphology is considered. Finally, the statements will be used to judge the relevance of the silicon platelets in the matrix material for the thermal cycling creep acceleration.

Influence of Material Combination

The influence of the physical properties of the constituents on the thermally induced stresses can be conveniently quantified in terms of the thermoelastic coefficient of stress $(d\sigma/dT)_{el}$ (TECS) for the simplified geometry of the slab model. It has been shown in Section 6.3.4 how the TECS can be calculated and this will be now done for different material combinations using Eq. 6-27. In this work, the combinations Al/Al_2O_3 and Al/Si are relevant. For comparison with literature, we will also take into account the system Al/SiC. Textbook values for essential thermoelastic properties of these materials are listed in Table 7.1. The respective thermoelastic coefficients of stress for the different combinations with Al and for a volume fraction of 15 % are also listed. It is apparent from the calculated TECS that the highest stresses will be induced in the material combination Al/SiC, while for the combination Al/Si, the thermally induced stresses will be rather low. At first sight this seems surprising because the difference in CTE is similar for both composites. However, as it was pointed out in Section 6.3.4, the thermally induced stresses do not only depend on the difference in CTE between the phases but also on the differences between the elastic moduli. It is apparent that at comparable volume fractions, the combination Al/Si, despite the slightly bigger CTE-difference, will cause lower matrix stresses during thermal cycling than the combination Al/SiC or even Al/Al_2O_3 with its even lower $\Delta\alpha$. This is because of the low modulus mismatch between Al and Si.

For the behavior under external load, it is also important to consider how effective the reinforcement is in shielding the applied stresses against the matrix. For a given volume fraction and matrix modulus, the matrix stress is the lower the higher the reinforcement modulus is. Among the material combinations considered, SiC, with the highest modulus, is therefore the most effective reinforcement in terms of reducing the matrix stress.

All the above considerations are strictly valid only for the slab-model. The qualitative results are, however, believed to apply also for real composites with a more complex reinforcement geometry. The additional influence of the reinforcement shape will be addressed next.

Material	Properties			Slab-model Al / 15 vol.% X
	E [GPa]	ν	α [10^{-6}/K]	$d\sigma_{m2/3}/dT$
Al	70 [(a)]	0.33 [(a)]	23.6 [(a)]	–
Al_2O_{3f} (Saffil)	285 [(b)]	0.20 [(b)]	7.7 [(a)]	-0.62
Si	107 [(c)]	0.27 [(c)]	3.5 [(d)]	-0.42
SiC_w	450 [(a)]	0.17 [(a)]	4.0 [(a)]	-0.85

Table 7.1: *Textbook values for thermoelastic properties of selected materials. [(a)] Clyne and Withers (1993), [(b)] ICI (1982), [(c)] Courtney (1990), [(d)] Ebert (1971). Also given are the thermoelastic coefficients of stress, calculated with the slab model for combinations of 15% reinforcement with aluminum.*

Influence of Reinforcement Shape

The influence of the reinforcement shape on the internal stresses is also studied by calculating the TECS first. The slab-model with its fixed geometry is of no great use here. Instead, Eshelby-based mean-field predictions are employed with *S*-tensors according to different reinforcement geometries. Results from calculations of the mean matrix stress for aligned spheroidal inclusions of different aspect ratio are given in Table 7.2. It can be seen that platelets induce larger mean stresses during thermal cycling than fibers.

Shape (of ellipsoid)	Aspect ratio	TECS (thermoelastic coefficient of stress)			Elastic load transfer (share of mean matrix stress)	
		1-direction	2/3-plane	von-Mises	1-direction	2/3-plane
	s	$d\langle\sigma\rangle_{m1}/dT$	$d\langle\sigma\rangle_{m2/3}/dT$	$d\langle\sigma\rangle_m^{eq}/dT$	$\langle\sigma\rangle_{m1}/\sigma_{A1}$	$\langle\sigma\rangle_{m2/3}/\sigma_{A2/3}$
Platelets	0.01	-0.28	-0.97	0.69	0.91	0.38
	0.1	-0.29	-0.81	0.57	0.86	0.49
Spheres	1	-0.31	-0.31	0	0.80	0.80
Fibers	10	-0.70	-0.21	0.49	0.49	0.87
	100	-0.75	-0.21	0.54	0.45	0.88

Table 7.2: *Thermoelastic coefficient of stress and amount of elastic load transfer calculated with the Eshelby method (mean-field approximation) for aligned spheroids with different aspect ratios. Note that the highest stresses due to thermal misfit are induced by platelets. The 1-direction is the axis of rotational symmetry. The physical properties of the constituents were taken from Tables 6.1 and 6.2; the volume fraction was 15%. The appropriate S-tensors for aligned prolate and oblate spheroids are listed in Appendix A.1.*

The reinforcement shape is not only important for the thermally induced stresses but also when the effectiveness of shielding the matrix against externally applied loads is considered. The mean matrix stress that arises under external loading can be calculated with Eq 2-3. Mean matrix stresses under uniaxially applied loads have been calculated for the same reinforcement morphologies as above and the results are also listed in Table 7.2. The platelets are very effective in reducing the matrix stress when they are oriented parallel to the applied load – more effective than parallel aligned fibers. They are, however, much less effective when they are oriented perpendicular to the loading axis (like fibers under transverse loading). Platelets are the slightly more effective form of reinforcement in terms of elastic load transfer when they are compared to fibers with the same aspect ratio and volume fraction. The same result has been obtained by Brown and Clarke (1975) who calculated the effectiveness of various reinforcements against plastic flow of the matrix. All these considerations have been made for the thermoelastic case. Under TCC conditions, however, inelastic effects are important. It was already noted in Chaper 6 that the Eshelby-method using the mean-field approach has the major drawback of averaging out localized deviatoric stress states and therefore leads to a high hydrostatic component. Such stress predictions are therefore not the best choice for calculating effects of inelastic deformation. A frequently applied alternative is modeling of deformation using FEM models. Bao et al. (1991), for example, investigated the effectiveness of different reinforcement shapes and aspect ratios against plastic flow with a unit-cell FEM model. They found that the composite limit flow stress was higher for needle-like particles aligned parallel to the loading direction than for platelets aligned perpendicular to the loading direction. This result also complies to the above thermoelastic calculations. The authors stated further that for randomly oriented packets of needles or platelets, the needles were the slightly more efficient reinforcement.

No literature studies were found regarding the influence of particle shape on the amount of the thermally induced stresses.

Relevance of Silicon Precipitates for TCC of the Composite

The findings of thermal cycling creep acceleration due to the presence of silicon platelets in aluminum raise several questions regarding the TCC behavior of the fiber-reinforced piston alloy: Could it be that TCC acceleration in the fiber reinforced composite is entirely due to Si-particles? If not, can their presence be neglected?

From the above considerations it is known that the material Si introduces a 50 % lower thermoelastic misfit than Al_2O_3 does. However, the platelet morphology of the Si precipitates is – according to the mean-field predictions – more effective in inducing high stresses than fibrous reinforcements. This is expected even for the given microstructure, in which the aspect ratio of the Saffil fibers is much higher than that of the Si platelets (s≈50 for the Saffil fibers and s≈10 for the Si platelets (see Figure 3.5)). The higher effectiveness of the platelets is

probably not sufficient to outweigh the 50% lower thermoelastic misfit. It is therefore reasonable to assume that the presence of the Si platelets adds considerable stresses upon thermal cycling but that it cannot dominate TCC behavior alone. In the investigated stress range, the thermally induced stresses are significant in size and the contribution of the Si-particles is also significant but it is still the Saffil reinforcement which introduces most of the stresses during thermal cycling.

In all considerations of this sub-section, we have concentrated on the induced stresses. The influence of the reinforcement morphology on impeding macroscopic strain was not addressed. Doing this quantitatively would have been beyond the scope of the present work. It seems, however, intuitively clear that a network of relatively long fibers is more effective in impeding a given global inelastic strain than small platelets.

7.2.4 Comparison to Simulations

The standard as well as the high temperature cycles were simulated with the slab model simulation program and corrected for thermal ratcheting (the simulated strain rates for load-free cycling were subtracted as outlined in Section 6.3.4, Page 113). The results are compared to experimental data in Figure 7.7. The calculations show the expected TCC behavior. At low loads, the apparent stress exponent is unity and at high loads the strain rates coincide with those at the equivalent temperature.

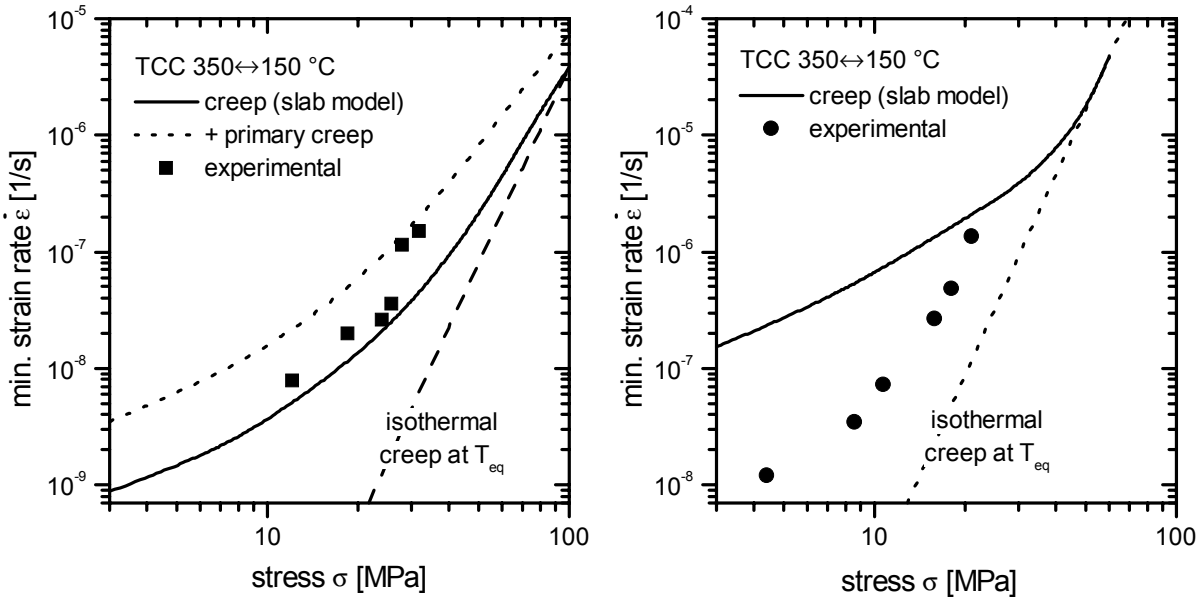

Figure 7.7: *Comparison of experimental and simulated TCC rates. For the low temperature cycles, the agreement is quite good (a), for the high temperature cycles (b), the TCC rate is largely over-estimated. Applying a primary creep law which is re-initiated in each thermal cycle, the creep rates are further increased irrespective of the applied stress (shown in a). In this case, the simulated TCC rate and the isothermal minimum creep rate at the equivalent temperature do not coincide at high stresses.*

For the standard cycles, the agreement between calculated and measured TCC rates is quite good. This is rather surprising, considering the over-estimation of the matrix stresses due to the model geometry and the neglect of the stresses that are introduced by the silicon platelets. It can be speculated that these two counteracting inaccuracies cancel each other for the standard cycle, leading to a good prediction. For the high temperature cycles, the slab-model over-estimates the TCC rates. The over-estimation of thermally induced stresses may weigh stronger under these conditions. Another reason could be the neglect of plasticity in the slab model simulations (due to the mentioned incapability of the slab model to determine total strains when plasticity is involved): It will be shown later in this chapter that plastic deformation can influence the in-cycle strain evolution in a way that the net strain per cycle is reduced.

A comparison between the simulated TCC rates for the standard (low-temperature) cycles and the isothermal creep rates at T_{eq} in Figure 7.7a shows that the transition between isothermal creep behavior and slope-1 behavior takes place over a wide range of stresses: Agreement between the curves is found not below 100 MPa and an apparent stress exponent of one is reached at stresses below 10 MPa. In the investigated stress range, the applied stresses are not high enough to outweigh the (simulated) thermally induced stresses. This raises the question if the disagreement between the experimentally measured TCC rates and the (extrapolated) isothermal creep rates at high stresses is really so remarkable. Maybe the maximum applied stresses were simply not high enough and for higher stresses, the creep rates would have been equal. This assumption is contradicted by the strong variation in the apparent stress exponent for TCC. The apparent stress exponent for TCC had reached values that were already very close to the ones for isothermal creep. It is therefore likely that the strain rate difference at high stresses is real, i.e. that thermal cycling enhances creep beyond the mere introduction of internal stresses.

Effects of Primary Creep

Primary creep has been attributed to a vast amount of microstructural processes. One of the common explanations is that the initial dislocation and subgrain structure gradually transforms into an arrangement in which mobile dislocations move in a dynamic equilibrium between the applied stress and counter-acting internal stresses on the micro-scale (e.g. dislocation pile-ups) (Derby and Ashby (1987)). A high temperature anneal can be applied to recover the initial dislocation arrangement, e.g. by dissolving pile-ups and subgrain walls., One can speculate that such a transient creep behavior also takes place under thermal cycling conditions: Whenever the maximum temperature of the cycle is reached, the microstructural creep state is "reset" and primary creep starts over. Experimental findings that support such a view can be found in the work by Pickard and Derby (1990) (Al/SiC$_p$). They state that the dislocation microstructure at room temperature showed only little change over a large number of loaded thermal cycles. Cyclic re-initiation of transient creep would lead to an increase of creep rate irrespective of the applied stress. Such a scenario was set up using the slab model: For stan-

dard cycles, primary creep deformation was enabled and whenever T_{max} was reached, the internal variable that measured the inelastic strain evolution was set to zero, resetting the primary creep process. The results of this simulation are also shown in Figure 7.7a. It is found that creep is indeed accelerated over the whole stress range, so that at high stresses the creep rates do not agree with the creep rates at the equivalent temperature. The predicted difference in creep rates at high stresses is smaller than it was observed experimentally. Rather than leading to a more perfect agreement with the experiment, this approach clearly shows the following: A continuum mechanics approach which focuses on the evolution of internal stresses alone is well suited to describe TCC in the present case. However, micromechanical effects that influence the kinetics of creep directly can be additionally taken into account to indicate the origin of discrepancies.

7.2.5 Influence of Cycling Amplitude

In the experiments described in Section 5.2.2, where T_{max} was fixed at 450 °C and T_{min} was varied, it was found that the investigated material, after an initial increase, showed a more or less constant low strain per cycle ε_{pc} up to thermal excursions of ΔT=250 °C. For higher cycle amplitudes (to lower temperatures) the strain per cycle started to increase significantly. Such behavior has been explained by models for internal stress driven plasticity (e.g. Greenwood and Johnson (1965), Derby (1985)). In these models, a critical thermal excursion ΔT_c is required to induce stresses high enough to cause plastic flow. For higher excursions, a linear dependence of thermal cycle amplitude and strain per cycle is predicted. However, it has been pointed out by Furness (1991) already that except for data published by Daehn and Gonzalez-Doncél (1989), almost all investigations on MMCs showed a *non*-linear dependence of ε_{pc} on ΔT.

For insights into the processes that control the influence of the thermal excursion on the strain per cycle for the material under investigation, some slab model calculations will be presented next. It will be elucidated what the thermal cycle of an experiment with changing cycle amplitude should look like to achieve maximum comparability of the results. As we have seen in the previous section, TCC rates are highly over-estimated for high temperature cycles. We will therefore focus on principal effects of internal stresses and the relative contribution of creep and plasticity rather than predicting the strains per cycle quantitatively.

Influence of the Equivalent Temperature

When the amplitude of a thermal cycle is changed, the diffusional mean temperature also changes. This alone alters the average creep rate – even if no internal stresses are involved. This fundamental influence of amplitude on creep rate can be easily calculated. The strain rates at the equivalent temperatures are calculated as explained in Section 7.2.1 and then divided by the cycle duration t_c. The results are shown in Figure 7.8. At zero thermal ampli-

tude, the cycle consists only of two dwell times of 60 seconds at 450°C, so that the strain per cycle is given by the isothermal strain rate at 450 °C divided by 120 seconds. As T_{min} decreases, the diffusional mean temperature is reduced and along with it the strain rate. Below a temperature of around 350 °C, the thermal activation becomes very low and the strain contribution of the low temperature part of the cycle becomes negligible. Therefore the strain per cycle becomes constant. It becomes clear that the decrease of the diffusional mean temperature has no influence on the strain per cycle for high excursions. This advantageous feature is a direct consequence of the way the experiment is conducted, namely with a fixed upper temperature and constant ramp rates. The majority of experiments reported in the literature were done with a fixed lower temperature or with a fixed cycle duration. In the results from such experiments, the effects of equivalent temperature and internal stresses are intermixed and it is complicated to separate them.

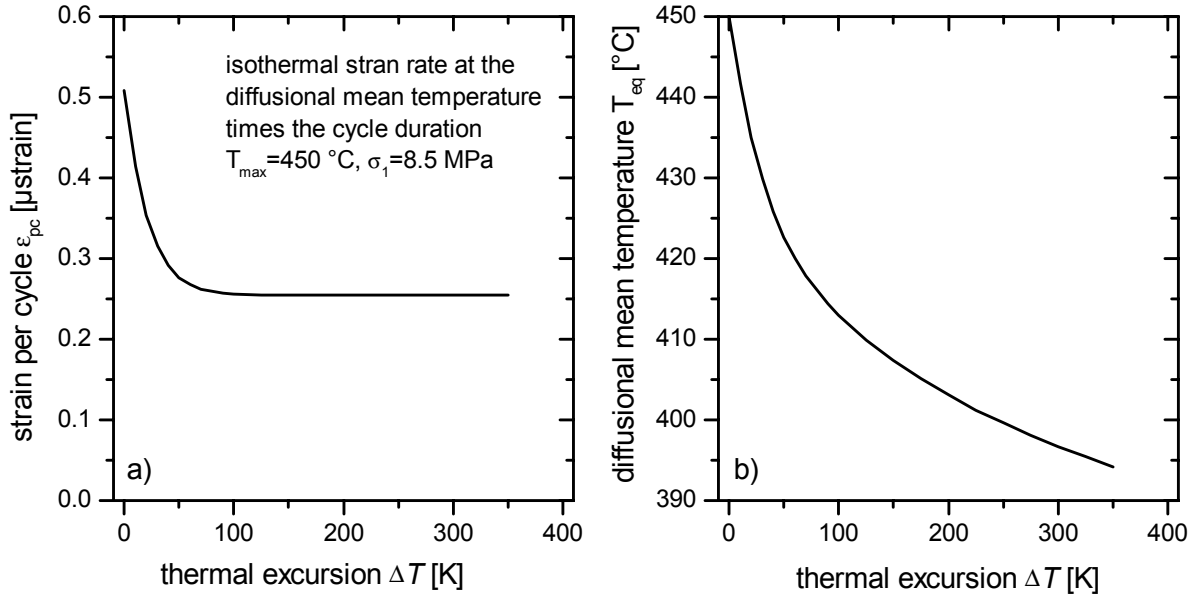

Figure 7.8: *Diffusional mean strain and temperature for different thermal cycles. The thermal cycle consisted of 1 min. dwell at T_{max}=450 °C, cooling with 50 K/min to T_{min}=T_{max}-ΔT, 1 min. dwell at T_{min} and again heating to T_{max} with 50 K/min. a) Strain per cycle at the diffusional mean temperature b) diffusional mean temperature.*

Internal Stress Evolution and Inelastic Strains

The presence of internal stresses is considered next. The general trend for the thermal cycling evolution of the internal matrix stress in the slab model was already calculated in Section 6.3.4. This calculation is repeated for the cycle shape used here. Because we are mainly interested in the relative importance of creep and plasticity, depending on the cycle amplitude, we confine the analysis to the simple case of thermal cycling without external load. Slab model calculations were done using creep and plasticity. The calculated internal matrix stress evolution is shown for three prominent thermal cycles in Figure 7.9a. In Figure 7.9b, the equivalent inelastic matrix strain per cycle is given as a function of the cycle amplitude. These values were determined by adding up the inelastic matrix strain increments over a complete

stable cycle. For comparison, the inelastic matrix strains were also calculated for the cases when only creep is allowed and when only plasticity is allowed.

The first cycle shown (①, 450↔350 °C) has an amplitude at which the matrix yield stress is just reached at the low temperature end (tensile). In cycles with lower amplitudes, only creep but no plasticity occurs. For higher amplitudes, the yield surface is hit during the low temperature end and thermal strain misfit is accommodated by plastic deformation. The second stress-temperature curve (②, 450↔300 °C) denotes a transition in the temperature dependence of the matrix yield stress. The third curve (③, 450↔185 °C) finally shows the case where the matrix yield surface is reached additionally on heating (in compression).

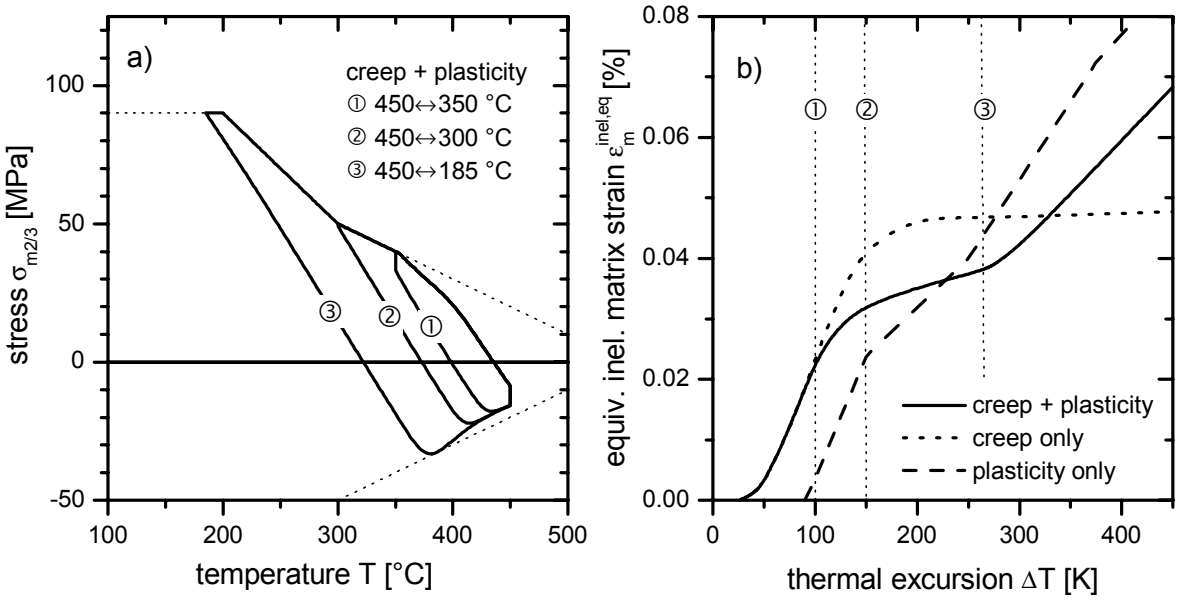

Figure 7.9: *a) Matrix stress evolution for stable thermal cycles to 450 °C without external load (slab-model simulation incorporation creep and plasticity). Three distinct cycles are shown: ① impingement on the yield surface in tension, ② change of matrix yield stress dependence and ③ impingement on the yield surface in compression. b) net equivalent inelastic matrix strain (per cycle) as a function of the thermal excursion. For comparison, simulation results are also given for the cases of only creep (stable cycles) and only plasticity (second cycles) allowed.*

The inelastic matrix strain variations with changing amplitude can only be understood when one realizes that part of the inelastic matrix strain that accumulates during the cooling half cycle is reversed during heating. Full reversal does not occur because 1) the reinforcement slab does also deform and 2) unconstrained matrix flow can take place in 1-direction (see Section 6.3.4). We will first look on the simulated matrix inelasticity for the case of "creep-only" and "plasticity-only" deformation. For creep, the inelastic strain rises sharply as the thermal cycle amplitude is increased. With the described setup, the forward creep contribution during cooling is larger than the reverse component during heating so that a positive net inelastic strain results. Beyond amplitudes of around 175 K, the inelastic strain stagnates because the cycle is purely elastic for lower temperatures. When only plastic deformation is considered, inelastic strains (in the second thermal cycle) do not occur if ΔT is smaller than 90 K. In this regime, the deformation is entirely elastic or shakedown to elastic deformation

occurs in the very first cycle. For higher amplitudes, cyclic plasticity takes place as the yield surface is hit in tension and compression. Again, the inelastic strain contribution of the cooling half cycle outweighs the contribution of the heating half cycle. The inelastic strain rises with further increasing amplitudes and the rate of increase is determined by the temperature dependence of the matrix yield stress.

Now for the case of combined creep and plasticity. For low amplitudes, the stresses do not reach the yield surface and the inelastic behavior is determined by creep only. The yield stress is reached at around $\Delta T = 100$ K. For higher excursions, the inelastic matrix strain falls short behind the creep-only simulation, although for the latter the amount of stress relaxed during cooling is lower. The reason is that plastic yielding on cooling shifts the stresses for heating downwards, so that the compressive stresses during heating become much higher than for pure creep. This means that plasticity does not only introduce more forward straining but also more reverse creep. The (relative) enhancement of the reverse portion weighs stronger so that the overall inelastic strain per cycle is reduced compared to the creep-only simulations. Yet the inelastic strains for combined creep and plasticity are still larger than those for the plasticity-only simulations due to the additional inelastic creep contribution. As the forward creep contribution stays constant and the reverse creep contribution becomes more pronounced with increasing ΔT, the plasticity-only simulations soon gives higher inelastic strains than the combination of creep and plasticity. For high amplitudes, plasticity dominates the inelastic strain behavior but the presence of creep in compression still keeps the inelastic strain below the values for pure plasticity.

The findings can be summarized as follows: Starting from very low cycle amplitudes, the amount of equivalent inelastic strain rises steeply as the internal stresses enhance creep deformation. Cyclic plasticity balanced by creep relaxation leads to a stagnation of this increase at intermediate cycle amplitudes. When the amplitude becomes high enough to cause plastic yielding on both heating and cooling, the deformation increases again and the creep influence is diminished. Another important point is that although the inelastic matrix strains in an individual cycle may be very large when plasticity is involved, they can cancel each other. It is the balance between forward and reverse inelastic deformations during the half-cycles that counts. The coaction of creep and plasticity can shift this balance in favor of lower net strains.

All the above findings have been obtained for the case of thermal cycling without external load. If a (low) external load is applied, the stress evolution changes only slightly. The characteristic temperatures of the strain evolution curves (Fig. 7.9b ①/②/③) are shifted accordingly, but this shift is not very pronounced when the applied load is low. The cyclic inelastic deformations are biased in a certain direction by this external load. When the equivalent inelastic strains per cycle is large, one can expect that the net external strain due to biasing is also large. The strain per cycle (under small loads) will thus vary with thermal

amplitude in the same way as the equivalent inelastic matrix strains that were shown in Figure 7.9b:

1) For very low amplitudes the strain per cycle rises steeply because of creep deformation assisted by the growing internal stresses.

2) When the thermal amplitude becomes high enough that the yield stress is reached during cooling (at $\Delta T \approx 100$ K), reverse creep deformation (during heating in compression) is enhanced and therefore the increase of the strain per cycle stagnates.

3) For high thermal amplitudes, plastic deformation (in tension and compression) dominates and the strain per cycle is expected to rise again. The yield surface is hit in tension and compression when $\Delta T \approx 265$ K.

Of course all those predictions are subject to the limitations of the slab model and the known inaccuracies. Additionally the critical temperatures are slightly shifted due to the applied load. Nevertheless, the predictions are qualitatively consistent with the measured strains per cycle as they are shown in Figure 7.10 (data taken from Figure 5.11). Even the predicted temperatures for the transitions between the regimes of different behavior seem to match well with the ones that were found experimentally.

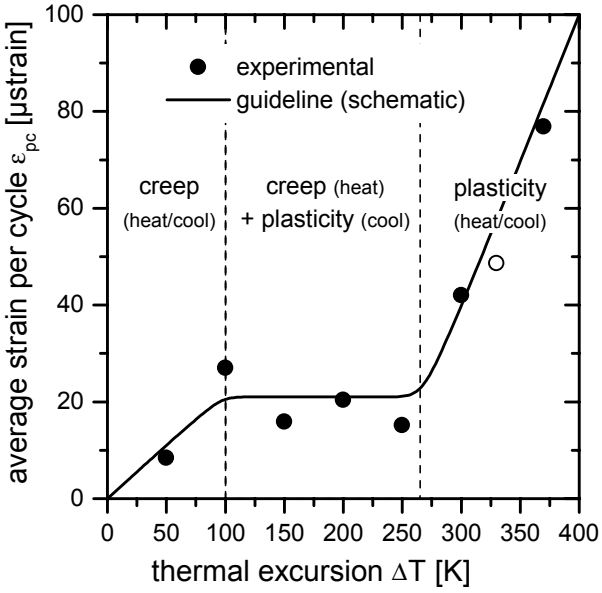

Figure 7.10: *Average strain per cycle for increasing thermal amplitude (cf. Figure 5.11). A schematic guideline is drawn which is subdivided into three distinct sections with different dominating deformation mechanisms. The temperatures for the transition between these sections were deduced from slab model simulations.*

These findings are important because they show that the concept of a critical thermal amplitude for cyclic plasticity may be too crude a simplification. The presence of creep relaxation can cause relatively low strains per cycle even when cyclic plasticity is already present. A neglect of this effect can lead to misinterpretations of TCC experiments with varying amplitudes.

7.2.6 Summary of Discussion Regarding the Composite TCC-Rate

At low stresses, the TCC rates were increased compared to the isothermal creep rates at the equivalent temperature as it is well established in literature. What is remarkable here is that this acceleration was also present at higher stresses, where the apparent stress exponents for isothermal and thermal cycling creep were the same i.e. the creep rates did not coincide at high stresses. This behavior has also been found in reports of TCC for other MMCs but it has not been explained yet. It was speculated in the present work that micromechanical effects which enhance the kinetics of creep could directly cause a creep acceleration beyond the mere introduction of internal stresses. As an example, cyclically re-initiated primary creep was additionally considered in the slab model and this led indeed to a TCC acceleration over the whole stress range.

Comparison to literature data revealed that the fiber reinforced piston alloy was less susceptible to TCC than MMCs with the material combination Al/SiC. An analysis of the thermoelastic stresses, which are thought to be the driving force for TCC acceleration, showed that SiC reinforcements induce substantially higher stresses than Al_2O_3, which is essentially the reason for the worse TCC performance of MMCs with SiC reinforcement. In the same analysis it was found that Si reinforcements induce lower thermoelastic stresses than Al_2O_3 but also that platelets induce higher stresses than fibers. For the analyzed reinforcements, the material combination has a stronger effect on the thermoelastic stresses than the reinforcement morphology. Based on the thermoelastic considerations it was concluded that the silicon platelets add stresses to the MMC that are significant in size but that theses stresses are most probably not high enough to dominate TCC behavior. The Saffil fibers still remain the main source of thermally induced matrix stresses.

The slab model simulations of TCC rates gave fair agreement with the experimental data for standard (350↔150 °C) TCC tests. It was found that agreement with equivalent isothermal creep rates could not be expected below 100 MPa and that a stress exponent of one is not reached for stresses higher than 10 MPa. For the high-temperature cycles, the agreement between experimental and simulated TCC rates was less good. This was mainly attributed to the neglect of plasticity in the slab-model.

The slab model was also used to interpret the results from TCC experiments with increasing thermal amplitudes. An important finding was that, in order to avoid misinterpretation, it is necessary to compare only experiments with thermal cycles that have the same T_{max} and the same heating and cooling rates. Creep deformation at the high temperature leads to measurable strains per cycle even at low thermal amplitudes. The slab model simulations showed that a large part of the inelastic matrix strain that accumulates during the cooling half cycle is reversed during heating. The balance between forward and reverse inelastic deformations during the half-cycles determines the net strain per cycle. The occurrence of plasticity in addition to creep can shift the balance in favor of *low* strains per cycle. Only when the thermal

amplitude becomes high enough so that plastic deformation gains dominance above the creep contribution, does the strain per cycle increase substantially. This contradicts the established simplified concept of a critical thermal amplitude ΔT_c beyond which matrix plasticity and thus rapid TCC deformation is induced and below which no deformation happens at all.

7.3 In-Cycle Strain Evolution

In the present work, the concept of instantaneous CTE was used to present the in cycle strain evolution. This was investigated at high an low temperatures, at varying amplitudes, with and without load, for different reinforcement orientations and finally for different cycle shapes. In this section, the experimental findings are compared to slab model calculations. These will help in the interpretation of distinct features in the evolution of instantaneous CTEs. This will give more information on the contribution of creep and plasticity to the inelastic deformation and will lead to a better understanding of how the strains accumulate during thermal cycling creep.

7.3.1 Literature

As it was pointed out in Section 0, only very few studies of the in-cycle strain evolution during loaded thermal cycling creep of MMCs can be found in the literature. Furness and Clyne (1991b) used the technique of laser-extensometry to accurately measure the in-cycle strain evolution for cp-Al (*cp* = ”commercial purity”) reinforced with 10 and 20 vol.% of aligned δ-Al_2O_3-fibers (aspect ratio *s*=5). The thermal cycle went from 340 to 140 °C. They subtracted calculated thermoelastic strains from the measured data to obtain the inelastic strain contribution. Under tensile loading they found reverse inelastic strains at the beginning of the cooling ramp and a slight acceleration of deformation at the end of the heating ramp. They modeled the strain evolution based on a thermoelastic strain misfit (calculated with the Eshelby method) relative to a fixed stress-free temperature. Deviatoric stresses were calculated from the misfit and creep strains were calculated based on these stresses. The major drawback of their modeling is that they did not correct the strain misfit for the accumulated creep strain i.e. the creep strain is not treated as additional misfit strain. Therefore, the strain evolution is always the same on heating and cooling and the effective stress-free temperature stays fixed.

Daymond and Withers (1997) also used a laser scanning extensometer to measure in-cycle strains for TCC with cp-Al/ 10 vol.% SiC_w (aligned whiskers) in the temperature range between 400 and 175 °C. They also measured the internal elastic strains in the matrix and the reinforcement with a stroboscopic neutron diffraction technique (see Section 0). They introduced the concept of instantaneous CTE to present their findings of the macroscopic strain evolution. They found that the instantaneous CTEs during heating and cooling deviated

from the calculated thermoelastic behavior especially at high temperatures in the cycle. The CTEs were increased above the thermoelastic values at the high temperature end of the heating ramp and they were lower than the thermoelastic CTE at the beginning of the cooling ramp. Daymond and Withers set up a unit-cell FEM model to calculate the internal elastic strains and the instantaneous CTEs and achieved fair agreement with the experimental data. They also used the FEM calculations to predict the relative contribution of creep and non-hardening plastic deformation to the overall strain evolution. They found that a substantial portion of strain in one half cycle was recovered in the other half cycle. In the case of plasticity-only deformation this led to low overall strains per cycle. This overall strain per cycle increased when power-law creep deformation was additionally considered. Creep contributed especially at the high temperature end of the heating ramp, and this increase also led to an enhancement of plasticity at the end of the cooling ramp.

7.3.2 Cycles to High Temperatures

A typical cycle from a TCC-experiment with a high maximum temperature will be considered in this section. The thermal cycle consisted of 1 min. dwell at T_{max}=450 °C, cooling to T_{min}=120 °C in 4 minutes, 1 min. dwell at T_{min} and again heating to T_{max} within 4 minutes. This cycle was simulated with the slab-model including creep. The results from the simulation with and without external load are compared to experimental findings in the following two sections.

Unloaded Cycles

The simulated evolution of the matrix stress for unloaded thermal cycling is shown in Figure 7.11. Without external load, the stress in 1-direction is zero by definition so that only the stress in the 2/3-plane is given. Along with this, the instantaneous CTE in 1-direction for heating and cooling are plotted. Also shown is the composite CTE for purely elastically accommodated misfit. The instantaneous CTE curves deviate from the “elastic” CTE whenever both temperature and stress are high enough to cause creep deformation. These calculated CTE curves will now be discussed in detail. Certain characteristics of the simulated curves will afterwards be correlated to similar features in the experimentally measured CTE curves.

The cycle in Figure 7.11 is a stable cycle for which creep shakedown has already occurred. For this cycle, shakedown occurs in the very first cycle no matter what the initial internal stresses are. The simulation was started with a stress free slab model and after two cycles, the internal matrix stress was $\sigma_{m2/3}$=–8.9 MPa (after the high temperature dwell).

We will now start at T_{max} with the cooling half-cycle. The matrix stresses are slightly compressive, but decreasing the temperature raises them towards zero. The response of the composite is essentially elastic, because the stresses are not high enough to cause substantial creep deformation in this region. As the stresses rise progressively, creep comes into effect

and the matrix slab has to follow the deformation of the stiff elastic reinforcement. This means that in the reinforcement-direction (2/3-plane), the matrix does no longer contract as fast as it should (in the elastic case). Instead, it shrinks faster perpendicular to the reinforcement (1-direction), because the volume has to stay constant*. This is why the CTE in the 1-direction suddenly rises during cooling. It indicates that matrix creep sets in. Simultaneously, matrix creep reduces the thermal strain misfit and so the rate of stress-increase drops. At low temperatures, the thermal activation for creep becomes very small, so that both the CTE and the rate of stress-change assume their purely elastic values. On re-heating, the matrix slab again experiences creep relaxation. As the matrix is still under tension in the 2/3-plane, the inelastic strain is positive in the direction of the reinforcement and negative perpendicular to it. This time the creep deformation in 1-direction opposes the thermal expansion strain, so that the CTE is diminished. When the matrix stress approaches zero, creep ceases again and the composite response becomes elastic. Creep sets in soon after the matrix stress has reverted to compressive, because the temperature is now very high. The compressive nature of the matrix stress leads to a negative inelastic strain in the 2/3-plane and consequently to an enhanced expansion in 1-direction. This is reflected in the steep increase in CTE at the end of the heating cycle. In this final phase of the cycle and during the high-temperature dwell time, creep deformation reduces the strain misfit and so the internal stresses relax towards lower absolute values.

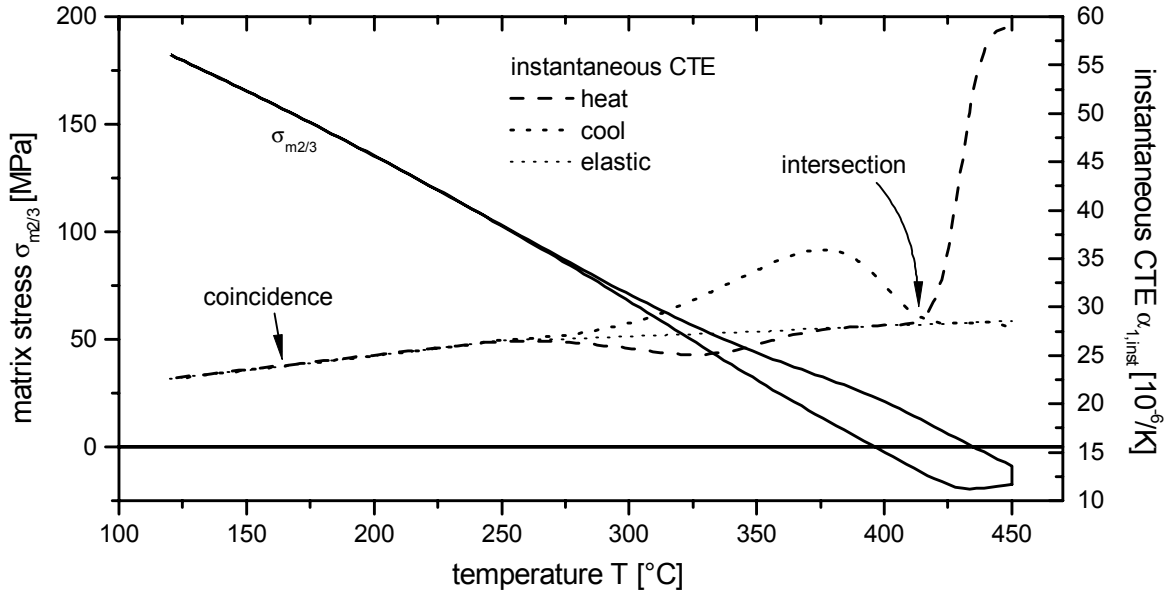

Figure 7.11: *Slab-model simulation of an unloaded thermal cycle 450↔120 °C. The stress in the 2/3-plane is given along with the instantaneous CTE in 1-direction for heating and cooling and for purely elastic deformation.*

* The very small effects of elastic volume change are neglected in this explanation, although they are included in the simulation.

At a given temperature, the instantaneous CTE is given by the slope of the thermoelastic line (rate of thermal misfit generation) and by the rate of inelastic deformation (creep rate). While the slope of the thermoelastic line is independent of the current stress, the creep rate depends strongly on the von-Mises equivalent stress. It can be concluded that, whenever the CTE curves for heating and cooling intersect or fall together, the creep rates must be the same and thus the equivalent stresses must be the same. On the other hand this means that differences in the heating and cooling CTEs at a given temperature indicate that inelastic deformation is taking place at different rates. Furthermore it can be concluded that when the heating and cooling CTE curves cross each other (instead of just coinciding), the stresses have the same amount but different signs during heating and cooling, while they are identical in amount and sign when the curves coincide.

The sign of CTE deviations from the thermoelastic values is determined by the sign of the temperature change (heating or cooling), by the average hydrostatic matrix stress (tension or compression) and by the orientation of CTE measurement relative to the reinforcement texture. This can be summarized in a simple equation:

$$-\operatorname{sgn}\left(\alpha_{i,inst}-\alpha_{i,inst}^{thermoelastic}\right)=\operatorname{sgn}\left(\dot{T}\right)\cdot\operatorname{sgn}\left(\left\langle\sigma\right\rangle_{m}^{hydrostatic}\right)\cdot\operatorname{sgn}\left(\left(\frac{d\left\langle\sigma\right\rangle_{m}}{dT}\right)_{i}^{deviatoric}\right) \qquad \textbf{(7-2)}$$

Here, $\left\langle\sigma\right\rangle_{m}^{hydrostatic}$ is the hydrostatic component of the volume averaged matrix stress and $\left(d\left\langle\sigma\right\rangle_{m}/dT\right)_{i}^{deviatoric}$ is the deviatoric component of the matrix TECS in the direction *i*. The latter quantity introduces the orientational dependence in the formula. It tells us whether the thermally induced misfit in the measured direction is larger or smaller than perpendicular to it. The sign of this deviatoric component becomes apparent from the calculated TECS values in Table 7.2. The following table summarizes the possible deviations from thermoelastic behavior for the slab model arrangement:

Sign of temperature change	Hydrostatic matrix stress	Orientation (deviatoric TECS)	Sign of CTE deviation from thermoelastic behavior
heating (+)	tensile (+)	x (+)	-
		y (-)	+
	compressive (-)	x (+)	+
		y (-)	-
cooling (-)	tensile (+)	x (+)	+
		y (-)	-
	compressive (-)	x (+)	-
		y (-)	+

Table 7.3: *Sign of deviation of the instantaneous CTE from thermoelastic behavior for various conditions.*

Table 7.3 can be of great help in the interpretation of instantaneous CTE curves. If for example the instantaneous cooling CTE in y-direction shows a sudden increase, one can conclude that the internal matrix stresses are probably compressive.

In Figure 7.12 experimentally determined CTEs of the short fiber composite are compared to the slab-model predictions. The general trend of both the heating and cooling curves is reproduced by the simulation. At high temperatures, the heating CTE rises steeply above the cooling CTE-curve and at low temperatures the heating CTEs lie below the ones for cooling. The simulated CTEs are generally higher than the experimental ones. This is not unexpected. In Chapter 6 it was already mentioned that the CTE in the main reinforcement direction is under-estimated and perpendicular to it over-estimated. The rather high degree of misalignment of the fibers in the real composite additionally reduces this directional CTE-inequity. Despite these minor shortcomings of the simulation, important things can be learned from the comparison to the experimental data. Regions can be estimated, where the composite exhibits an almost elastic response to temperature changes. From the above analysis of the simulated CTEs it is know that the equivalent stresses for heating and cooling are the same at the temperature where the CTE curves intersect. In the experiment, this is at around 370 °C. We can be sure that at this temperature the matrix stress in the *y/z*-direction is tensile for cooling and compressive for heating (see above). At temperatures slightly below this point, it can be expected that the heating CTEs come close to an “elastic” CTE while for the cooling curves the rather elastic response should lie at higher temperatures.

Unlike in the simulation, no pronounced increase in the experimental cooling CTE is found at temperatures below the intersection of the curves. This is probably due to the inhomogeneous reinforcement distribution in the technical material and due to non-homogeneous deformation.

Both effects will tend to “smear out” pronounced changes in the CTE as they are predicted by the slab-model with its idealized geometry and homogeneity.

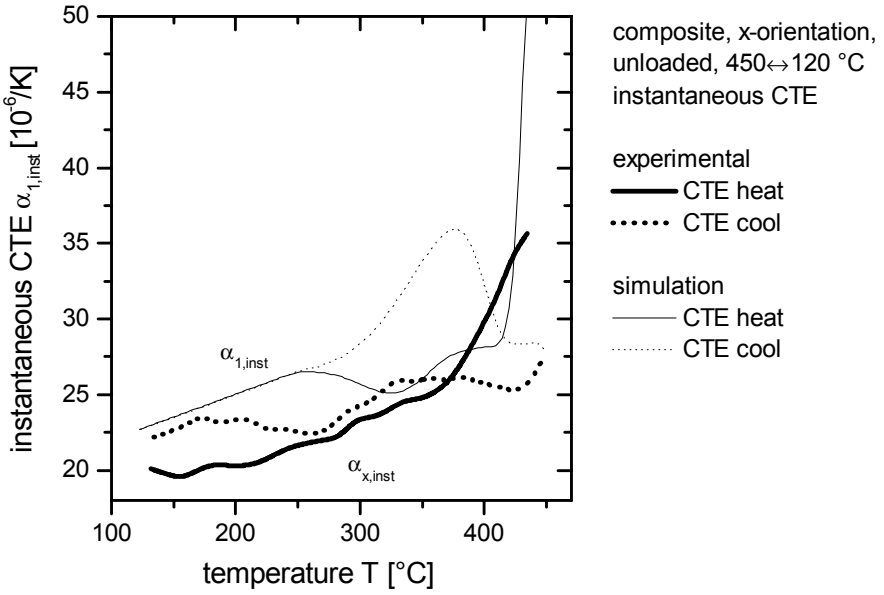

Figure 7.12: *Comparison of the instantaneous CTEs from experiments (thick lines) and Slab-model simulations (thin lines). Unloaded thermal cycling 450↔120 °C.*

Another interesting feature is that the measured heating and cooling CTEs do not agree at low temperatures. This deviation from the predictions will be addressed next.

Plasticity Induced by Thermal Cycling

Upon reversal of the temperature ramp at T_{min}, the CTE jumps to lower values. This indicates the presence of inelastic processes. Global creep deformation is not likely to be happening in this regime because the temperature is too low to provide sufficient thermal activation. Yet, time dependent relaxation of internal stresses at room temperature has been reported e.g. for the system cp-Al +5vol.% SiC_w in the literature (Withers et al. (1987)). However, such inelastic deformation occurs over several hours up to days and not within the duration of a single 10-minute thermal cycle. It is concluded that it is not creep but rather time-independent plastic deformation which influences the CTE at the low-temperature end of the cycle. It is expected that the internal stresses in the matrix are tensile. In this case, re-heating leads to a reduction in the effective stress and thus cannot give rise to further plastic deformation. It can be concluded that at low temperatures, the heating response is essentially elastic. In the same regime, the CTE for cooling is increased in 1-direction. This is because the matrix yields plastically under high tensile stresses in the 2/3-plane and contraction perpendicular to this plane is enhanced.

The curve of the cooling CTE almost meets the one for heating at around 260 °C. This temperature might be associated with the onset of plastic flow in the material. In a slab-model simulation one would expect a sudden jump in the instantaneous CTE to values that are pro-

portional to the thermoelastic coefficient of stress $(d\sigma/dT)_{el}$, when homogeneous non-hardening plastic deformation sets in. In the real composite, the state of stress is not homogeneous in the matrix. Plastic deformation will start in highly stressed regions and extend from there for further cooling. In addition, strain hardening could raise the yield stress until a dynamic equilibrium between hardening and recovery is established. This is reflected in the slow deviation of the cooling CTE towards higher values. After cooling by another 60 K (to 200 °C), an almost constant difference in the CTEs between heating and cooling is established. It can be speculated that at this temperature, the whole matrix experiences global plastic yielding with negligible further strain hardening. In Section 7.2.5 (Figure 7.10) it was shown that a significant increase in the average strain per cycle was found when thermal cycles reached down to below 200 °C (ΔT>250 °C), which is roughly the temperature at which supposedly global plastic deformation is established.

Plastic yielding at low temperatures causes further deviations from the simulations: When the heating curve starts from a lower internal stress at T_{min}, the point of zero stress will be reached at a lower temperature during re-heating. Moreover, inelastic deformation during the tensile part of the heating curve (at intermediate temperatures) will be reduced because the stresses at a given temperature are lower. The associated drop in CTE will be reduced. Conversely, in the compressive regime, creep deformation will start earlier because the compressive stresses are higher at a given temperature so that the terminal increase of CTE starts at lower temperatures. All these effects are indeed found when the experimental heating CTE is compared to the simulated one: The CTE-drop at intermediate temperatures is absent and the CTE-increase is found at lower temperatures.

Loaded Cycles

When a small tensile load is applied perpendicular to the main reinforcement direction (samples loaded in x-orientation or the slab-model in 1-direction), the effective matrix stress can be reduced or increased, depending on whether the present thermally induced stresses are tensile (at lower temperatures) or compressive (at higher temperatures). In those parts of the cycle where the thermal mismatch stresses in the matrix are tensile, the application of a small external load will tend to decrease the deviatoric stress and reduce the deviations from elastic behavior. Tensile matrix stresses can only cause a reduction of the strain in 1-direction and the external load will reduce this tendency. The opposite is true in the compressive parts of the cycle. The deviatoric matrix stresses are increased by the tensile load and inelastic deformation is enhanced. This happens at the high-temperature end of the heating cycle.

For the high-temperature cycles, the stresses that are commonly applied are small compared to the maximum thermally induced stresses. In this case, the effect on the instantaneous CTE is not very pronounced. The inelastic deformation that is present under unloaded thermal cycling is only biased by the small external load. Experimentally, the cooling CTE curves were the

same for load-free cycling and for an applied load of 8.5 MPa. The heating curves differed only at the high-temperature end, where the CTE was marginally higher in the case of an applied load. Furthermore, it was predicted and found experimentally that, in the loaded case, the CTE-curves intersect at slightly lower temperatures. The experimentally determined and the calculated CTE-evolution are compared to the results from load-free cycling (see the previous section) in Figure 7.13.

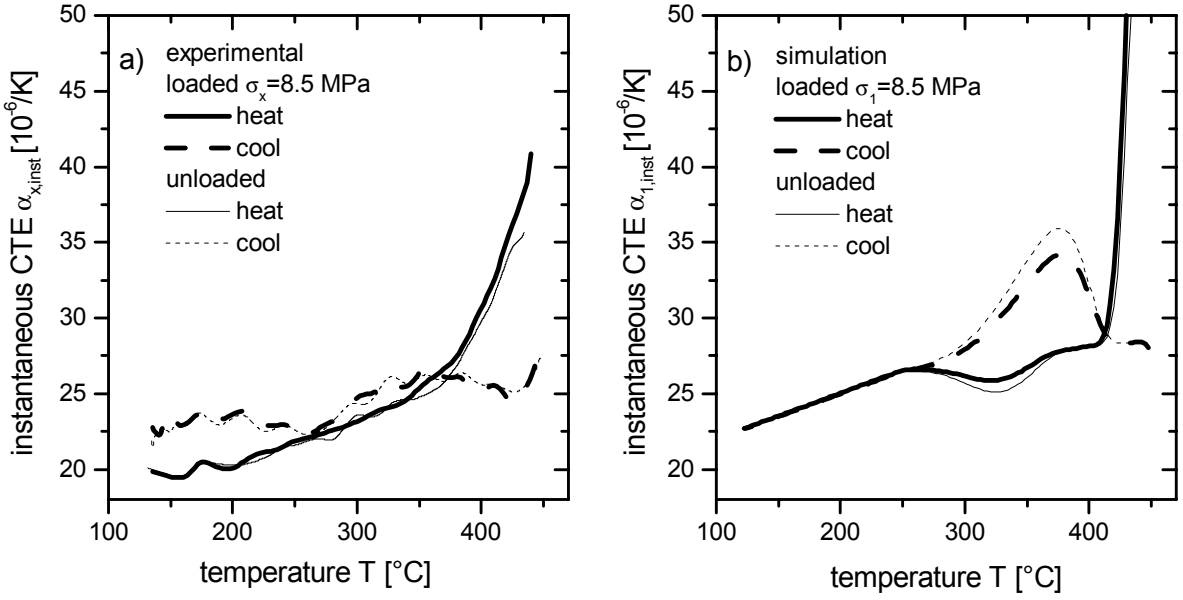

Figure 7.13: *Comparison of instantaneous CTEs for loaded and unlaoded thermal cycles 450↔120 °C. a) Experimental data. b) Slab-model simulation.*

The same considerations as above can be made for compressive loading. Now the external compressive load increases deviatoric stresses where a tensile load would have decreased them and vice-versa. The same applies to the CTEs: they are increased, where tensile loading led to a decrease and vice-versa. The bias of the inelastic deformation acts just in the opposite direction. Of course all these propositions are only valid for the slab-model simulations and only for small stresses. For thermal cycles where the maximum temperature is lower and the inelastic deformation processes are slower, the applied stresses are usually higher and they exceed the internal stresses over a considerable part of the cycle. Such effects are discussed in Section 7.3.3 for the standard TCC cycles.

Influence of Cycle Amplitude

In Section 5.3.2 it was shown that changing the cycle amplitude (at constant ramp rates and T_{max}) did not change the CTE during cooling. One can conclude that the stress state at the start of the cooling ramp is always very similar. The heating CTEs, in contrast, were very different. The point at which the curves crossed was shifted to higher temperatures with sinking amplitudes. At a given temperature, the heating CTE was lower, the lower the amplitude of the cycle was. Both phenomena, the invariant cooling CTE curves and the systematically reduced heating CTEs, could be reproduced with the slab model. Simulations of thermal amplitudes of

50, 100 and 300 K are shown in Figure 7.14. All cooling curves agree because the stress states after the high-temperature dwell are essentially identical. Lower cycle amplitudes lead to higher matrix stresses on heating. This increases the creep rate in the 2/3-plane at a given temperature and thus the CTE in 1-direction is reduced. The state of zero stress is reached at progressively higher temperatures and for further heating the internal stresses become compressive. The higher the cycle amplitude is, the higher are the compressive internal stresses at a given temperature. Higher compressive stresses lead to enhanced contraction in the 2/3-plane and thus the expansion in 1-direction is increased. This effect will be enhanced further when plastic yielding is induced for the high thermal amplitudes, as this shifts the stresses on heating to even lower temperatures.

In summary, the cooling CTEs are identical because the stress state after the high-temperature dwell is essentially the same. The heating CTEs are lower the lower the cycling amplitude is, because low amplitudes lead to higher tensile and lower compressive internal stresses.

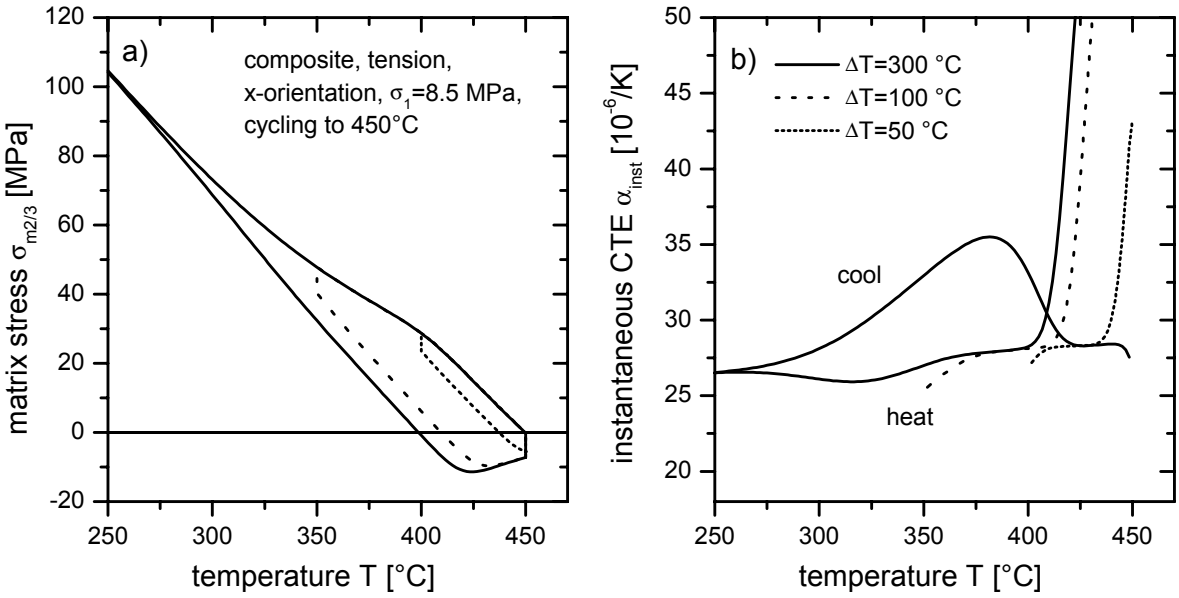

Figure 7.14: *Slab model simulations of thermal cycling creep under an external load of σ_1=8.5 MPa. Thermal cycles to 450 °C with a ramp rate of 50 K/min and upper and lower dwell times of 1 minute were simulated for thermal excursions of 50, 100 and 300 K. a) matrix stress in* 2/3-plane *($\sigma_{m1}=\sigma_1$=8.5 MPa) and b) instantaneous CTE for heating and cooling. The cooling curves all agree.*

Influence of Orientation

Both the simulated and measured CTE curves are substantially different when the responses in *y*- or 2-direction are considered. Nevertheless, for unloaded thermal cycling, the slab-model simulations of the CTE in 1-direction and the 2/3-plane are closely related. We have seen that deviations form the "elastic CTE" are caused mainly by inelastic deformation of the matrix slab. The inelastic deformations in the principal directions are related via the conservation of volume. A relative contraction in the 2/3-plane is always accompanied by an expansion in 1-direction. For the CTE curves, this means that whenever $\alpha_{1,inst}$ deviates from the correspond-

ing elastic value, $\alpha_{2/3,inst}$ will deviate in the opposite direction. This is illustrated in Figure 7.15, where experimental and simulated instantaneous CTEs in y-direction and the 2/3-plane are shown for load-free cycling. The curves can be compared to the corresponding data in Figure 7.12. Differences between the experimental results and the simulated data can be explained in the same way: Inhomogeneous reinforcement distribution and non-homogeneous deformation in the technical material tend to "smear out" pronounced changes as they are predicted from the slab-model simulations. Plastic yielding during cooling to low temperatures reduces the internal stresses for heating. This diminishes the inelastic deformation in the tensile regime and the compressive regime is entered at lower temperatures, so that inelastic deformation at the end of the heating half-cycle starts earlier.

It is interesting to note that the instantaneous CTE is elevated at the start of cooling. Obviously, the matrix stresses (in y-direction) are compressive in this regime and they are high enough to cause negative creep deformation in y-direction. This leads to an acceleration of the contraction in y-direction and so $\alpha_{y,inst}$ is higher than for elastic response. This indicates that the relaxation of the internal stresses during the high-temperature dwell is not as pronounced as it is predicted from the slab-model simulations. The particular influence of this dwell time is addressed in the next section.

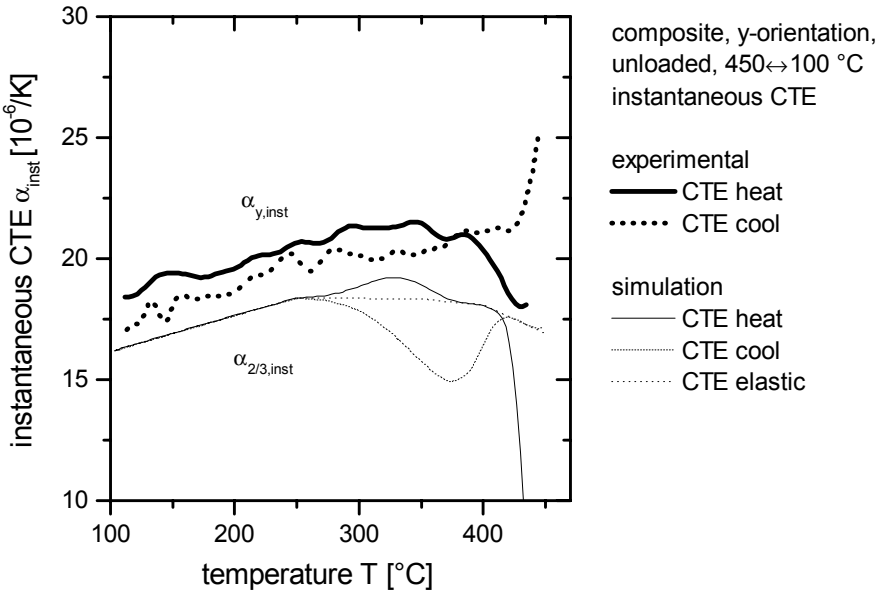

Figure 7.15: *Comparison of the instantaneous CTEs from experiments on y-oriented samples (thick lines) and to CTEs in the 2/3-plane from a slab-model simulation (thin lines). Unloaded thermal cycling 450↔100 °C. Comparison can be also made to the related data for x- or 1-direction in Figure 7.12.*

Influence of High-Temperature Dwell

It was found experimentally (Section 5.3.2, Figure 5.20) that the duration of the high-temperature dwell had no measurable effect on the instantaneous CTE curves. The major differences can therefore be expected to be located directly in the strain evolution during the

high-temperature dwell. This strain evolution was shown in Figure 5.21 (and it is repeated in Figure 7.17).

The loaded thermal cycles used in the above mentioned investigation were also simulated with the slab model. The predictions for the evolution of the internals stresses and the instantaneous CTEs are shown in Figure 7.16a and b. In contrast to the experimental findings, the simulated evolution of the cooling curves is significantly influenced by the dwell time; the heating curves stay unaffected – just like in the experiments. The main difference between the simulated and the measured instantaneous cooling CTE curves is found at the high temperature end of the cooling ramp. In the experiment, all cooling ramps start with the same high CTEs. This suggests that the stress state at the beginning of the cooling ramp is not essentially different for the three different cycles because no differences in the inelastic behavior were found. The slab model predicts high CTEs at the start of the cooling ramp only for the cycle without dwell time. In the other two cases, the internal matrix stresses relax towards an equibiaxial state during the dwell time so that no high driving force for deformation is present when cooling starts.

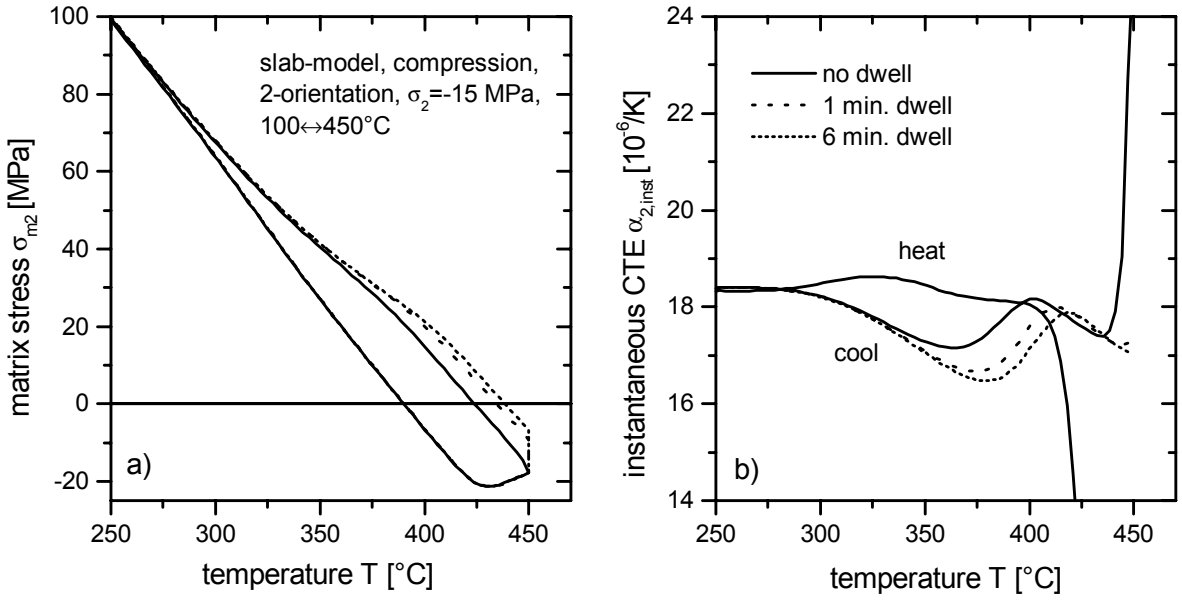

Figure 7.16: *Slab-model simulations of the influence of the high temperature dwell time on the stress and strain evolution with temperature. a) matrix stress in 2-direction for thermal cycles with dwell times of 0, 1 and 6 minutes. b) calculated instantaneous CTE in 2-direction. Note that the dwell time affects only the evolution of the cooling curves.*

Better agreement between experiments and simulations is found for the strain evolution during the high temperature dwell. The measured and the simulated curves have very similar shape (see Figure 7.17). The slab model over-estimates the amount of strain a little, most probably because of the well-known over-estimation of the internal stresses. The two experimentally determined strain curves agree well with each other and this suggests that the initial stress state was the same in both cases. This was also found in the slab model simulations.

We therefore have indications for two phenomena: 1) The stress state at the beginning of the dwell time is always the same irrespective of the dwell time. This is substantiated by the slab model simulations and by the agreement between the two measured strain curves during two different dwell times. 2) The stress state at the end of the dwell time is also constant. This was concluded from the agreement of the instantaneous CTEs at the beginning of the cooling ramp. The slab model simulations contradict this and based on the current considerations no explanation for this unexpected effect was found.

It was found in the experiments that the strain during the upper dwell time was larger than the overall strain of the cycle. This indicates that part of the strain that is accumulated during the dwell time is recovered in the following cycle. This can only happen in the tensile region, because only there the internal matrix stress opposes the applied (compressive) stress so that reverse deformation can happen. The slab model simulations did not predict such a behavior most probably because no plastic deformation was considered. It was shown before both experimentally and in simulations that the thermally induced stresses become high enough to cause plastic deformation during the cooling ramp (see Section 7.2.5). Plastic flow in this region would induce additional backward strain which is not considered in the simulations.

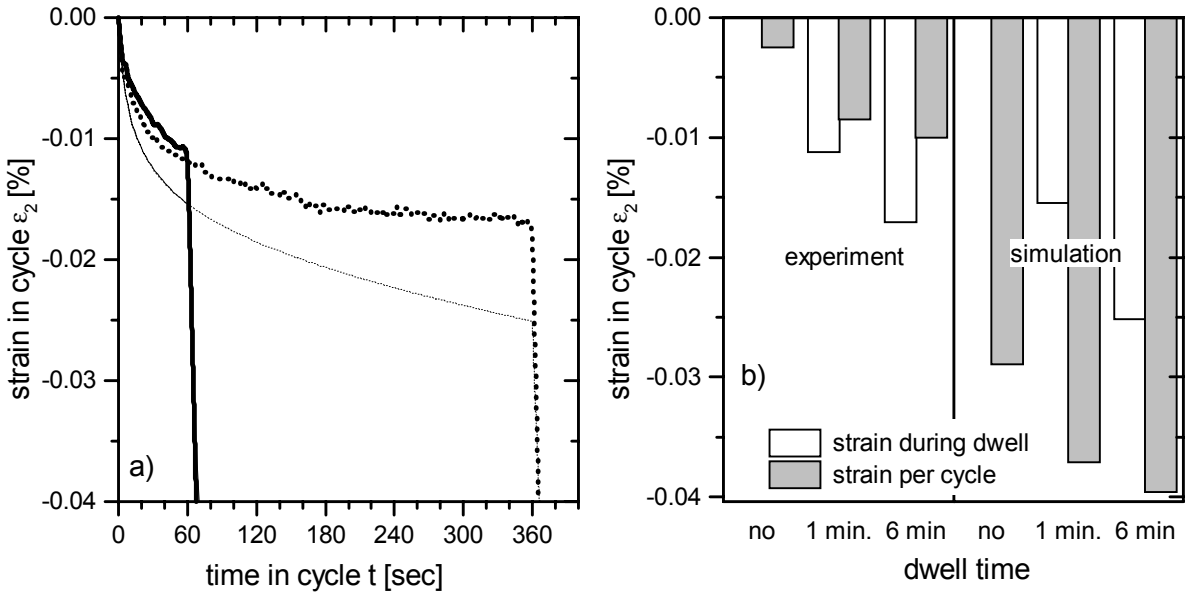

Figure 7.17: *Strain evolution during the high temperature dwell. a) comparison of measured and simulated strain evolution with time during the high temperature dwell. b) simulated and measured strains per cycle compared to the strains that are accumulated during the high temperature dwell. Note that in the experiments, the strain during the dwell time was larger than the overall strain per cycle.*

7.3.3 In Cycle Strain Evolution in Standard Cycles (150↔350 °C)

Unloaded Cycles

There are some basic differences between the standard cycles and the cycles to high temperatures. In the standard cycles, much less evidence is found for inelastic deformation, which is

due to the overall lower temperature: The strain-temperature hystereses are rather narrow, the instantaneous CTEs exhibit lower variations and it takes many more cycles to achieve creep shakedown than for high-temperature cycles. These basic findings are qualitatively reproduced by the slab-model. In the simulations of standard cycling, only a small part of the internal stress is relaxed in each cycle and it takes many more cycles until a steady stress-temperature-hysteresis is achieved (creep shakedown). The initial internal stresses* that are present in the material as a result of production and heat-treatment play now a more important role than for the high-temperature cycles. At the beginning of the first cycle, the internal stresses in the slab model were set to $\sigma_{m2/3}$ = 16.4 MPa and $\sigma_{f2/3}$ = -92.8 MPa. They were determined with the slab model with a sequence that simulated production and heat treatment (see Section 3.3) and the initial over-aging treatment which was part of every experiment (see Section 4.3.1).

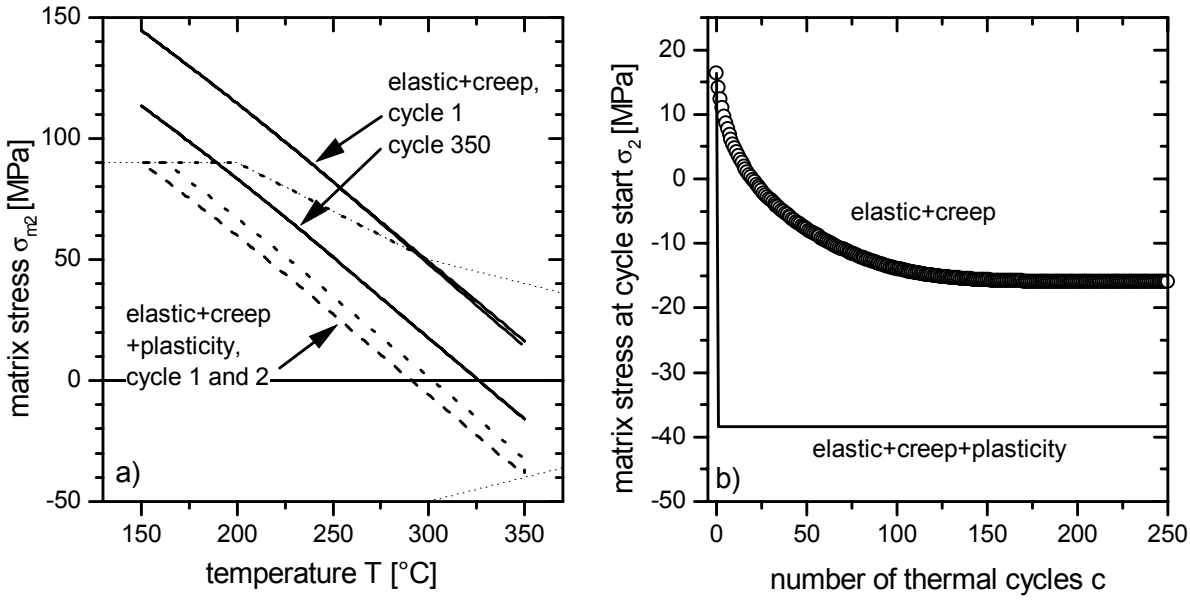

Figure 7.18: *Simulated matrix stresses for standard 350↔150 °C cycles. a) The stress- temperature curves show no resolvable hysteresis, when only creep is considered as a deformation mechanism. Including plasticity in the simulation leads to immediate plastic shakedown so that in the first half-cycle, a stable but narrow stress-temperature hysteresis is established. b) Evolution of the matrix stress at the start of the cycle (350°C) for an increasing number of cycles. Very low amounts of inelastic deformation lead to a progressive relaxation of internal stresses during creep shakedown.*

In Figure 7.18a the evolution of the matrix stress $\sigma_{m2/3}$ in a slab-model simulation incorporating creep deformation is shown. Even in the very first cycle the deviations from a thermoelastic line can hardly be resolved within the line-width of the graph. It can be seen that only a small fraction of the internal stress has been relaxed until the end of the cycle. A very late cycle (No. 350) is also given. This cycle starts at a compressive stress of $\sigma_{m2/3}$ = -16.0 MPa and ends at the same value, i.e. the cycle is stable. No hysteresis in the

* These internal stresses after cooling from production temperature are often called *residual stresses* because they reside in the material at low temperature when no external load is applied and further inelastic deformation is negligible.

stress-temperature curve can be resolved in this graph. The maximum calculated difference between the stress on heating and on cooling is only 0.113 MPa at 310 °C. The simulation results become substantially different when matrix plasticity is also taken into account. The matrix yield stress is reached on cooling and for further decreasing temperature the internal matrix stress follows the expanding yield surface (the yield surface expands due to sinking temperature, not because of hardening). Because no hardening is considered, plastic shake-down occurs in the very first cycle, i.e. all subsequent cycles are bound in tension by the same yield stress and thus have the same stress evolution.

The evolution of the matrix stress at the beginning of each cycle is shown in Figure 7.18b. When only creep deformation is considered, it takes around 200 cycles until a stable hysteresis is reached. When plasticity is included, the cycles are stable right after the first cycle.

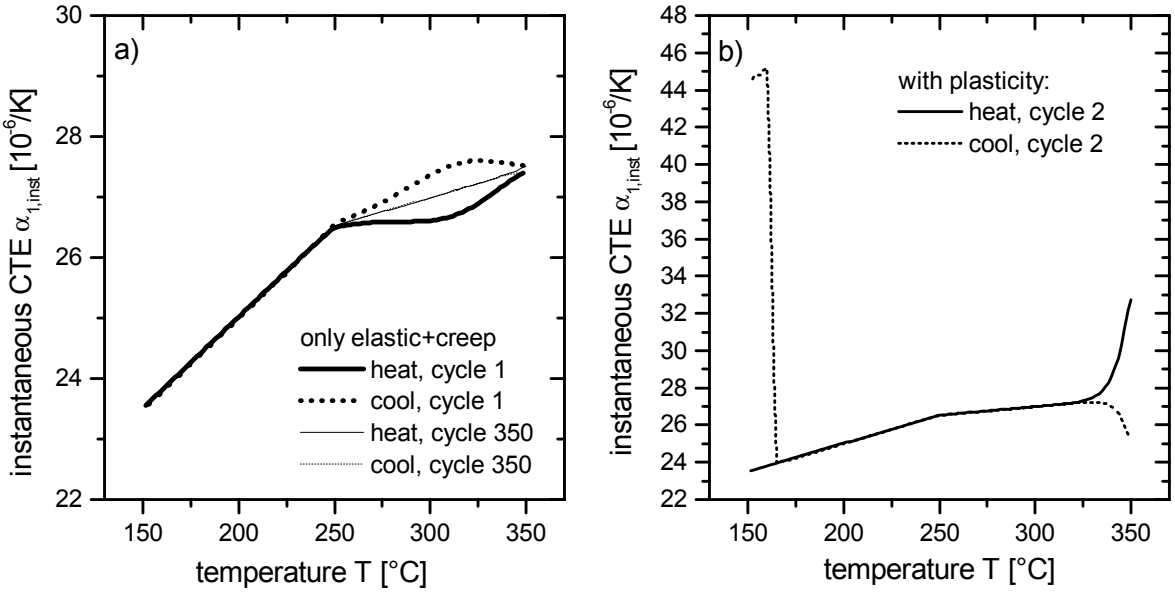

Figure 7.19: *Evolution of the Instantaneous CTE corresponding to the stress evolutions from Figure 7.18. a) Simulation with creep deformation only, b) simulation including plasticity.*

The calculated instantaneous CTEs corresponding to the stress evolutions in Figure 7.18 are shown in Figure 7.19. The first cycle for the simulation with only creep deformation considered exhibits slight deviations of the CTE from thermo-elastic behavior (Figure 7.19a). During heating, the CTE is reduced at high temperature, because the matrix slab relaxes under tension in the 2/3-plane. It shows a relative contraction normal to the direction of the internal stresses and so the CTE in 1-direction is reduced. On cooling, the CTE is enhanced in the same region for the same reason. For the stabilized cycle, no deviation from thermoelastic behavior can be resolved in the graph. For the simulation including plasticity (Figure 7.18b), the instantaneous cooling-CTE jumps to high values when the yield stress is reached at low temperatures. Again, the matrix slab yields under tensile stresses in the 2/3-plane and thus contracts in the 1-direction. On re-heating, the compressive stresses at the high-temperature end become high enough to cause compressive creep relaxation in the 2/3-plane and enhanced expansivity in 1-direction. During the high-temperature dwell, the matrix stress relaxes further

and there is still some relaxation going on when the cooling ramp is started. It must be noted that the distinct bend in the CTE-curves at 250 °C is due to the discretization of the temperature-dependent matrix-CTE (see Tables 6.1 and 6.2) and no result of inelastic deformation.

Experimentally determined instantaneous CTEs for load-free standard cycles were shown in Section 5.3.1, Figure 5.14. They are compared to CTE-curves for high-temperature cycles in Figure 7.20. The measured curves show more evidence of inelastic deformation than expected from the above simulations. Nevertheless, the discussion of these curves is started with elastic behavior.

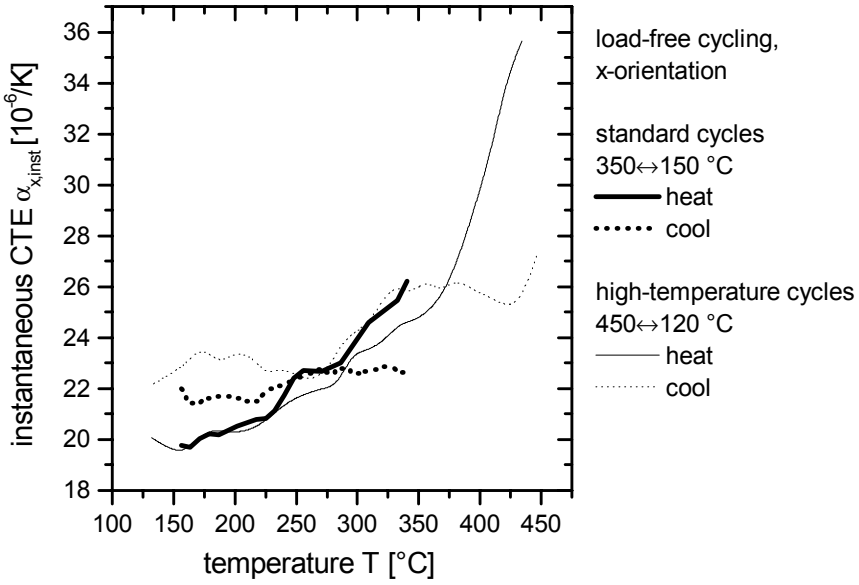

Figure 7.20: *Comparison of the instantaneous CTE for load-free cycling in standard cycles and in cycles to high temperatures.*

The heating CTE curves of the standard and high-temperature cycles agree at low temperatures. Obviously, the response of the composite is thermo-elastic for both cycles in this low-temperature region. On heating, the CTE curve for the standard cycle starts to rise at lower temperatures. The region where the heating and cooling CTEs are equal is also shifted to lower temperatures and it extends over a range of 50 K, whereas for the high-temperature cycles a clearly defined intersection of the curves was found. If the composite has equal CTEs on heating and cooling over a relatively wide temperature range of temperature, it can be concluded that no temperature dependent inelastic processes are involved in this region. Otherwise, the CTE would deviate in different directions for heating and cooling. Again, at high temperatures, the heating CTE rises, indicating creep relaxation under compression in the main reinforcement direction. The increase, however, is by far lower than for the high-temperature cycle. The temperature at which the average internal stresses on heating become zero lies supposedly in the middle between 250 and 290 °C. This can be concluded from the above finding that in this region, the composite response is thermo-elastic and from the fact that the CTE rises at higher temperatures, which indicates that the stresses in the matrix are compressive.

The cooling curves also show substantial differences between standard and high-temperature cycles – especially at low temperatures, where plastic yielding is expected. The cooling CTE, for example, starts to deviate from the heating CTE at lower temperatures. Moreover, it is not risen as much above the heating CTE than for the high-temperature cycles. This indicates that plasticity is less prominent and possibly confined to regions of high stresses (e.g. around fiber ends). It is also possible that the yield stress is higher for the standard cycles, because recovery of the microstructure at the high-temperature end of the cycle is less pronounced.

The agreement between measured and simulated CTEs is not as good as for high-temperature cycles. The measured stress-temperature and strain-temperature hystereses show much more evidence for inelastic deformation than the slab-model predicts. This is probably due to the enforced homogeneous deformation in the model.

For high-temperature cycles, where the stresses are high and the thermal activation is sufficient, inelastic deformation can be assumed to take place in the whole composite matrix and the homogeneous deformation of the matrix in the slab-model seems to be a good approximation for this. In the real composite, the overall stresses are lower. Global inelastic deformation cannot be expected. One can speculate that instead, the inelastic strains will tend to be more localized because of stress concentrations at reinforcement angularities. Although these inelastic strains will be confined to a low fraction of volume, they have a big effect on the macroscopic behavior because they widen up the thermal strain hysteresis. As before, the biggest part of the inelastic strains cancel out over the cycle, so that the accumulated net macroscopic strain is comparatively low. This is found in both the simulation and for the real composite.

Loaded Cycles

The experimentally determined instantaneous CTEs for loaded cycles differed from those for unloaded cycles only at high temperatures: loaded heating curves deviated from those for load-free cycling above 270 °C for tension and above 290 °C for compression. Tensile loading led to an increase in the heating CTE, compressive loading to a decrease. The loaded cooling curves differed from the unloaded ones only within the first 20 to 30 K of cooling. The relative difference in the CTEs between loaded and unloaded cycles is larger for the standard cycles than for the high-temperature cycles. This is due to the applied stresses which in the case of the standard cycles are comparable in magnitude to the thermoelastically induced stresses.

Simulated loaded cycles displayed the same principal behavior but again with much less inelastic strains involved. For tensile loading, the temperature, where the equivalent stress becomes zero (hydrostatic stress state), shifts to lower and for compressive loading to higher temperatures. This corresponds well to the experimentally found difference in the temperature, where the loaded heating CTE curves deviate form the unloaded ones. However, the point

where the hydrostatic stress state is reached is predicted to lie at around 325 °C. In the experiments it lies certainly below 280 °C – at least for heating.

Summary of the In-Cycle Strain Evolution for Standard Cycles

In summary, it can be said that despite the low thermal amplitude and temperature, creep and time-independent plasticity both play a considerable role during thermal cycling. From the characteristic evolution of the instantaneous CTE it can be seen that the stresses in the matrix are compressive at high temperatures and tensile at low temperatures. A state of zero internal stress is estimated to be between 250 and 290 °C for heating, which is relatively low compared to the simulations.

The wide strain hysteresis (big differences in the instantaneous heating and cooling CTEs) suggest that a considerable amount of inelastic deformation is induced by thermal cycling. Plasticity occurs at the low temperature end of the cooling ramp. The low strains per cycle, however, indicate that the strains are localized and do not lead to strong global inelastic deformation.

7.3.4 Summary of Discussion Regarding the In-Cycle Strain Evolution

It was found that presenting the in cycle strain evolution in the form of instantaneous CTE curves is a good way to visualize the sometimes subtle differences in deformation behavior for various test conditions. The approach works well for both experimental and simulated results.

Qualitative agreement between simulated and experimental instantaneous CTE curves was found throughout so that the simulations could be used for the interpretation of the measurements. Especially the comparison of simulations with inelastic deformation to simulated thermoelastic instantaneous CTEs (for purely elastically accommodated misfit) helped to set up some simple rules for the interpretation of instantaneous CTE curves:

1) The instantaneous CTE at a given temperature is representative for the rate of composite deformation and thus for the internal equivalent matrix stress.

2) When the instantaneous CTE curves for heating and cooling cross each other (instead of just coinciding), the matrix stresses have the same amount but different signs during heating and cooling. The internal stresses are identical in amount and sign when the curves coincide over an extended temperature range.

3) The sign of CTE deviations from the thermoelastic values is given by a simple equation which depends on the sign of the temperature change (heating or cooling), the sign of the average hydrostatic matrix stress (tension or compression) and by the orientation of CTE measurement relative to the reinforcement texture.

With the aid of these rules, the in-cycle strain evolution could be successfully explained in most cases. Pronounced differences between simulated and measured CTEs were found at the low temperature end of the cooling cycles. These were explained by the presence of plastic deformation. The temperatures at which this happened agreed well with the analysis of the amplitude influence on TCC rates from Section 7.2.5.

For standard thermal cycles (low thermal amplitudes and low T_{max}, 350↔150 °C), the measured strain-temperature hysteresis showed much more evidence of inelastic strains than the simulations predicted. This was explained with strong localization of inelastic strains e.g. at reinforcement angularities.

The external stresses that were usually applied were low enough so that they did not influence the instantaneous CTEs strongly. This was found both experimentally and in the simulations. Analysis of the in-cycle strain evolution can therefore be also accomplished with data from unloaded cycles. The orientational dependence of the instantaneous CTE curves was also successfully predicted by the slab model. This again confirms the presence and nature of a preferential reinforcement orientation, and it shows that the slab model reflected this texture correctly.

7.4 Stress Cycling Creep

Within this section, a simple qualitative scheme is proposed to explain the experimentally found stress cycling creep behavior that was presented in Chapter 5. This will mainly give information on the processes of load transfer and damage and how these are linked to the amount of total strain.

The literature on stress cycling creep (see Section 2.3) focused mainly on the question if isothermal creep was accelerated (CCA) or retarded (CCR) due to comparatively fast cyclic loading. In most cases CCA occurs at rather low temperatures and high stresses, while CCR is mostly found at high temperatures and low stresses (Lee and Nam (1988)). All stress cycling creep investigations on MMCs have in common that short cycle times were used. They do not consider effects of load transfer and strain energy storage in the reinforcement, probably because these are believed to gain importance only at very low frequencies with long relaxation times. No investigations of stress cycling creep on MMCs with long recovery times, like it was done in this work, have been found in literature.

The stress cycling creep experiments in this work were conducted with a fixed forward strain at creep load, followed by a 6-hour period of recovery at almost zero external stress. It was found that the amount of recovered strain per cycle increased with increasing total strain up to an almost constant value. For high total strains, the amount of back creep decreased only slightly.

7.4.1 General Considerations

In this sub-section, a scheme for the strain evolution under stress cycling creep conditions is lined out.

Recoverable and Non Recoverable Strain

The basic assumption is that the total accumulated strain can be split up in a recoverable and a non recoverable part. The same underlying assumption has been made by Dlouhy and Eggeler in their work (see e.g. Dlouhy and Eggeler (1994)) and by Kimmerle and co-workers (Kimmerle et al. (1986, Kimmerle et al. (1987)). The recoverable part is the one that stores elastic strain energy in the reinforcement while the non-recoverable strain does not. The nature of non-recoverable strain will be discussed later on. These two strain contributions have been previously called "misfit-generating" and "non-misfit-generating". Together with the elastic contribution, the forward strain increment in a stress cycling creep test can be expressed as

$$\Delta\varepsilon_f = \Delta\varepsilon^{el} + \Delta\varepsilon^{inel} = \varepsilon^{el} + \varepsilon^{anel} + \Delta\varepsilon_{rbl} + \Delta\varepsilon_{n-rbl}, \qquad \textbf{(7-3)}$$

where $\Delta\varepsilon^{el}$ is the instantaneous elastic strain on loading which is fully recovered when the load is removed. $\Delta\varepsilon_{rbl}$ is the inelastic but recoverable and $\Delta\varepsilon_{n\text{-}rbl}$ is the non recoverable strain increment. The backward strain upon load removal can be expressed as

$$\Delta\varepsilon_b = \Delta\varepsilon^{el} + \Delta\varepsilon_{rec}, \qquad \textbf{(7-4)}$$

where $\Delta\varepsilon_{rec}$ is the amount of inelastic backflow* strain during the time given for recovery. All strain quantities are defined relative to the state before the load change. It shall be noted that, unlike in the scheme proposed by Kimmerle et al. (see above), $\Delta\varepsilon_{rbl}$ and $\Delta\varepsilon_{n\text{-}rbl}$ occur simultaneously and not successively. For the moment, it shall be assumed that no damage occurs in the reinforcement or the matrix. The recoverable strain increment will then rise with increasing forward strain increment. The fraction of non-recoverable strain will depend on the underlying deformation process.

Possible Deformation Processes for Non Recoverable Strain

One such process could for example be plastic deformation in fiber free zones (as they are present in the material under investigation). Strain tends to concentrate in these weak regions but it is constrained by the surrounding reinforced material. The easily deforming fiber free zones cause a strain misfit and thus stress concentration in neighboring reinforced regions. This in turn causes highly localized (not global) reinforcement damage so that a contiguous

* In the literature regarding the material response after creep unloading, the terms "backflow", "recovery", and "anelasticity" are often used interchangeably. In this discussion, the term "recovery" or alternatively "back creep" is preferred because the term "backflow" suggests the presence of time-independent plasticity and the term "anelasticity" is more frequently used in conjunction with short-term behavior such as damping.

network of highly deformed zones is formed. This is schematically illustrated in Figure 7.21a. According to this idea, the recoverable and non-recoverable parts of the total strain are located in separate regions of the specimen volume. Apart from the strain accommodation problems, deformations in the reinforced and unreinforced regions are independent of each other. The non recoverable strain process takes part in the overall straining of the composite by a certain fraction and if no time dependent processes are involved, the non recoverable strain is proportional to the total creep strain. Under the conditions used in this work, time dependent (creep) deformation definitely plays a role. During the load transfer process it will therefore take progressively more time to strain the reinforced regions to larger strains. This increases the relative share of the total strain for the unreinforced regions.

The evolution of recoverable and non-recoverable creep is visualized in the curves on the right hand side of Figure 7.21. The lower curve shows the amount of recoverable strain as a function of the accumulated inelastic strain. The upper line depicts the summation of recoverable and non-recoverable creep. these two contributions add up to the total inelastic strain so that a straight line with a slope of one is obtained.

Another process that can accumulate non recoverable creep is reinforcement relaxation driven by interface diffusion (Rösler et al. (1991)). This process was proposed as a possible source of non-recoverable strain by Dlouhy and Eggeler (Dlouhy and Eggeler (1994)). The matrix stress state around a fiber is different near the fiber end and midway along its length. The resulting gradient in stress perpendicular to the fiber (inclusion) surface gives rise to diffusional mass transport between these regions and this relaxes the strain misfit[*]. This diffusional flow is proportional to the stress gradient which is given by the load transfer process and depends non-linearly on the misfit strain. The misfit strain represents the amount of recoverable deformation and the misfit reduction by diffusional flow represents the non-recoverable strain. Their relative contribution depends on many parameters, the most important ones being those that control the diffusional relaxation process (temperature, reinforcement size, matrix stress state etc.). The share of non-recoverable strain will again increase with increasing total strain.

A third possibility is that non-recoverable creep occurs by global fracture of fibers. This process is not initiated before a critical misfit strain is reached. For progressively increasing strain, more and more fibers break according to the fracture statistics and the share of non recoverable creep increases. For high strains, the amount of recoverable creep can be expected to decrease because the load carrying ability of the reinforcement decreases. This process is not likely to occur alone, because non-recoverable creep is already found at very low forward strain increments. It rather provides an upper limit for the recoverable strain.

[*] In the extreme case that the diffusional relaxation is fast enough to balance matrix creep (small particles, high temperatures), load transfer can no longer take place and the reinforcement does no longer contribute to strengthening.

It must be noted here that the three processes mentioned above differ in their contribution during the relaxation phases: While deformation in fiber free regions and fiber fracture cease as soon as the external load is removed, diffusional relaxation around fibers can still take place as long as there is a strain misfit between the phases, i.e. also during the recovery period. The three processes also differ in their dependence on the internal stresses: Fiber fracture and diffusional relaxation of the fibers depend directly on the strain misfit between the matrix and the fibers. Deformation in the separate fiber free regions, however, depends on the total accumulated strain. It therefore depends only indirectly on the fiber-matrix misfit in reinforced regions.

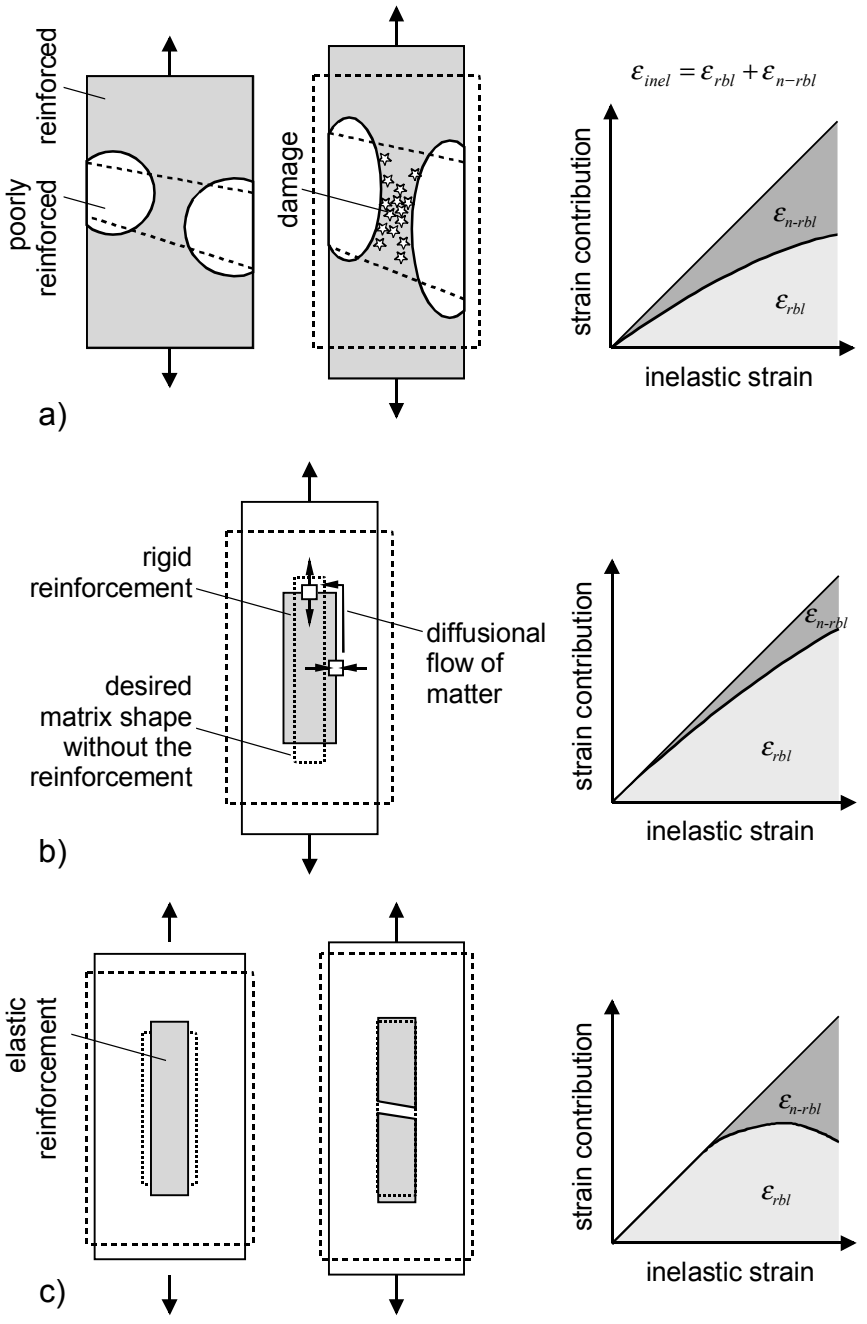

Figure 7.21: *Possible mechanisms for non-recoverable creep.*

a) Deformation of fiber free regions.

The share of non-recoverable strain increases with increasing inelastic strain because strain concentrates in unreinforced regions.

b) diffusional relaxation of reinforcement misfit strain, driven by a gradient in the normal stress along the reinforcement interface.

Large misfit strains accelerate relaxation and so the share of $\varepsilon_{n\text{-}rbl}$ increases with increasing inelastic strain.

c) Global fiber fracture, starting at a critical misfit strain.

At low total strains (no fractures), all strain is recoverable. At very high strains, the amount of recoverable strain decreases because the load carrying ability of the reinforcement is reduced.

Evolution of Recoverable and Non Recoverable Strain with Total Strain

It shall now be discussed how the recoverable and non recoverable strain together with the recovered strain interact to yield the overall strain evolution during stress cycling creep. The evolution of the recoverable strain for the first two load changes is shown schematically in Figure 7.22a. The elastic strain contribution is omitted in this graph.

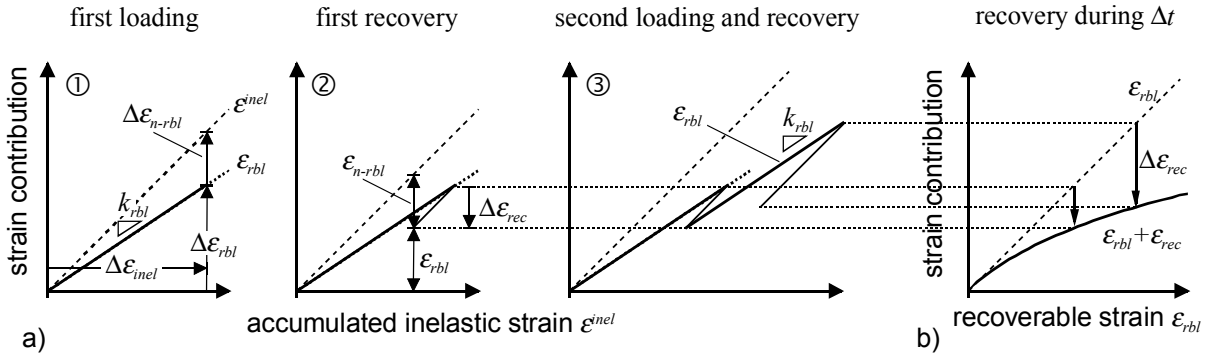

Figure 7.22: *Schematic evolution of recoverable strain during a stress cycling creep test. a) recoverable strain evolution for the first two load changes. b) Amount of recovery as a function of the total recoverable strain. See text for details.*

Figure 7.22a ①: During the first forward creep segment, both the recoverable and non-recoverable strains increase. For simplicity, it is assumed for the moment that the recoverable and non-recoverable strain contributions are proportional to each other so that

$$\Delta\varepsilon_{rbl} = k_{rbl} \cdot \Delta\varepsilon^{inel} \qquad \textbf{(7-5)}$$

and

$$\Delta\varepsilon_{n-rbl} = \left(1 - k_{rbl}\right) \cdot \Delta\varepsilon^{inel}, \qquad \textbf{(7-6)}$$

with k_{rbl} being a constant smaller than unity. As seen above, this is most probably not the case in a real composite but the basics of strain recovery under stress cycling creep conditions can still be demonstrated.

Figure 7.22a ②: When the load is removed, the material creeps backwards. During this backward creep, only the recoverable strain is reduced – the non recoverable strain stays constant.

Figure 7.22a ③: Upon reapplying the load, the recoverable and non-recoverable strains increase again according to the factor k_{rbl}. At the end of the second loading segment, the recoverable strain is lower than it would have been if the total strain had been accumulated without the interim recovery. During the second recovery phase, the recoverable strain is reduced again, but now by a larger amount than during the first recovery time. The reason for this is given in the following:

The amount of recovered strain is determined by the time given for recovery Δt and by the driving force for recovery. For the investigated material, the elastic strain mismatch between the fibers and the matrix (the recoverable strain) suggests itself as a probable driving force for

back creep. The strain recovery therefore depends on the amount of recoverable strain. This is shown schematically in Figure 7.22b for a given Δt. It is important that the strain recovery increases with increasing amount of recoverable strain (i.e. with increasing load transfer). The dependencies can be expressed as:

$$\Delta\varepsilon_{rec} = -k_{rec} \cdot \varepsilon_{rbl} \qquad \textbf{(7-7)}$$

Here, k_{rec} is a factor which increases with Δt from zero to 1 as Δt goes to infinity. For a given Δt, k_{rec} increases with increasing ε_{rbl}.

$$k_{rec} = f(\Delta t, \varepsilon_{rbl}) \qquad \textbf{(7-8)}$$

The evolution of recoverable and non recoverable strain for further loading and unloading segments, is shown in Figure 7.23a.

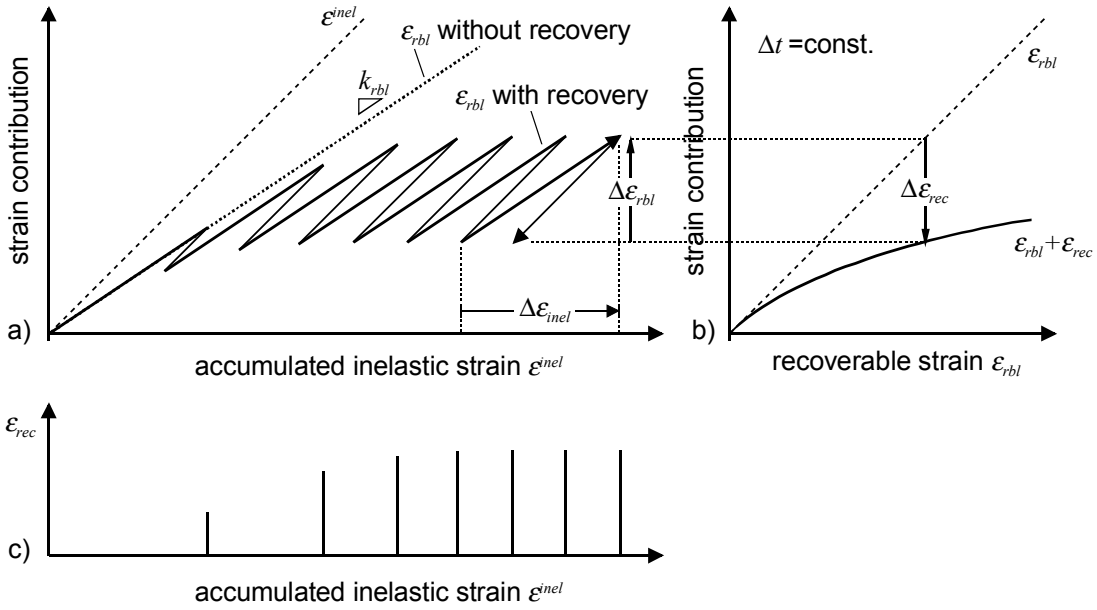

Figure 7.23: *Schematic evolution of recoverable strain during a stress cycling creep test. a) Stress cycling and static creep (with and without recovery). The recoverable strain increment is assumed to be proportional to the inelastic strain increment. b) Amount of recovery for a given Δt as a function of the total recoverable strain. c) Recovered strain in each cycle plotted against the total accumulated inelastic strain. The recoverable strain after a forward creep increment approaches a value where the build-up of recoverable strain in the loaded phase is exactly balanced by the recovery during the unloaded phase.*

The amount of back creep, which is shown in 7.23c), rises cycle by cycle as the recoverable strain gets bigger. The recoverable strain asymptotically approaches a value where the back creep tendency is large enough to cause recovery which exactly balances the previous increment of recoverable creep:

$$\Delta\varepsilon_{rbl}(\Delta\varepsilon^{inel}) + \Delta\varepsilon_{rec}(\Delta t, \varepsilon_{rbl}) = 0 \qquad \textbf{(7-9)}$$

This is why the increase in recovery seems to stop after a number of cycles. The rate at which the equilibrium is approached (in terms of strain increment per cycle) and the amount of inelastic strain accumulated during the cycles depends on the amount of forward creep strain

and on the time given for recovery. With large forward strain increments, the maximum load transfer is reached at larger strains than with smaller forward strain increments. The final degree of load transfer is also higher the larger the forward strain increment is.

Up to now, it has not been considered that the reinforcement can have a limited capacity to store recoverable strain, i.e. the load transfer to the reinforcement is somehow limited. The consequences of such a limit for stress cycling creep experiments are shown in Figure 7.24. It is the same schematic as in Figure 7.23 but now the recoverable strain is limited to an arbitrarily chosen maximum value. When this value is reached during stress cycling creep, the amount of back creep becomes constant immediately, irrespective of the forward strain increment. This happens at a total strain which lies above the point of maximum load transfer for uninterrupted deformation.

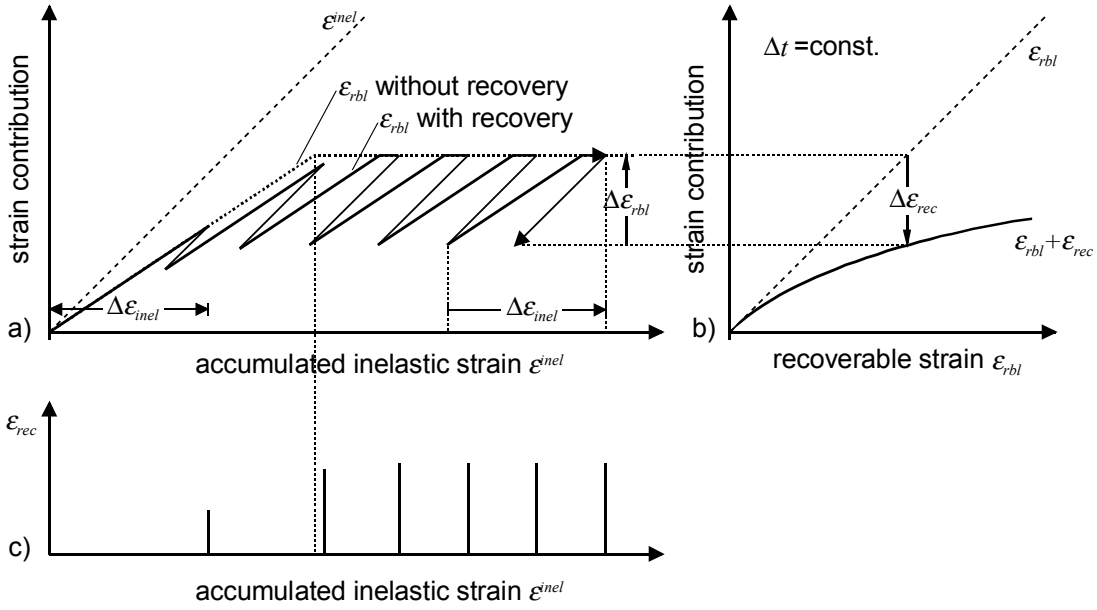

Figure 7.24: *Same schematic as in Figure 7.23 but now, the recoverable strain (e.g. due to reinforcement damage) is limited at large strains. The corresponding back-creep becomes constant in this case, irrespective of the prior forward creep strain. Note that the point at which the back-creep becomes constant is always found at larger strains than the point of maximum load transfer for static creep.*

Two essential points can be extracted from the above considerations:

1) For stress cycling creep experiments like they were done in this work (fixed amount of forward strain, fixed recovery time), the amount of back-creep becomes constant sooner or later. Either a limiting recovery strain is approached asymptotically which balances the increase in recoverable strain during loaded creep. Or, for larger forward strain increments, the maximum load carrying capacity in the reinforcement is reached.

2) The evolution of back creep in stress cycling creep experiments cannot provide a measure for load transfer under static creep conditions. The total strain at which a constant amount of back creep is reached are not correlated to the conditions under static creep.

The concept that was developed here will be utilized in the following to interpret the stress cycling creep results from Section 5.3.3.

7.4.2 Interpretation of Experiments

Before the amount of observed back creep is looked at in more detail, its origin is to be clarified.

Origin of Back Creep

As it was already pointed out above, the elastic strain mismatch between the matrix and the fibers suggests itself as a probable driving force for back creep for the material under investigation. However, comparatively large amounts of creep recovery after unloading have also been observed in pure polycrystalline metals (e.g. Gibeling and Nix (1981), Dobson and Greenwood (1996)). It has been commonly attributed to the presence of internal "dislocation back stresses" that act on mobile dislocations (un-bowing of dislocations, recovery of pile-ups, subgrain boundary migration). For example, the anelastic backflow strain for pure polycrystalline aluminum at 400 °C and at very low stresses has been reported to be 5 times the elastic strain at maximum (Gibeling and Nix (1981)). The amounts of back-creep that were observed on the composite material in this work were even larger than 5 times the elastic strain. Within six hours, strains above 0.6% could be recovered upon unloading from a stress of –63 MPa. This amounts to ten times the expected elastic strain at this temperature, based on dynamic measurements of the Young's modulus of the composite. The amount of backflow in our study is therefore substantially bigger and occurs over a much larger time-scale than "dislocation back-stress" driven back creep. It can be concluded that the elastic strain energy stored in the reinforcement provides a vital and maybe the major driving force for back creep.

Saturation of Back Creep

In Chapter 5 it was shown that back creep became constant after a certain amount of strain had accumulated. It was shown above that this can have two reasons: 1) The amount of recoverable strain becomes such that the amount of back creep during the recovery phase exactly balances the increase in recoverable strain during the subsequent loading phase. 2) The maximum load carrying capacity of the reinforcement is reached and therefore the recoverable strain is limited to a certain value. In the first case the constant back creep strain will depend on the forward strain increment. In the second case, it is expected that the amount of back-creep becomes constant and that additionally its amount is independent of the forward strain increment. In the experiments, the back creep strain saturated to more or less constant values but these values were different for different forward strain increments. No limit in the back creep strain was found, even not for forward creep strain increments as large as 3%. This suggests that at least up to this value, the load carrying capacity of the reinforcement is not

reached. Instead, the saturation seems to be due to the above mentioned balancing between the recovered strain and the increment of the recoverable strain.

A forward strain increment of up to 3% without reaching the load carrying limit of the reinforcement seems relatively large. The average fracture strain of the Saffil fibers is around 0.7% in tension (see Table 3.2) or maybe a little higher if the elastic modulus decreases with increasing temperature. Even under compressive loading, where the fibers oriented perpendicular to the loading axis experience a tensile strain which is only half of the external compressive strain, the applied strain at which fibers will start to fracture amounts to only -1.4% (iso-strain condition assumed). This is still half of the largest forward strain increment that was applied and at which still a further increase in back creep was observed. This means that at least half of the total strain was contributed by non-recoverable strain. Of course, all the above considerations are only rough estimates and, taking into account the simplicity of the assumptions, it is clear that the general statements cannot be quantitative. Yet, some important conclusion can be drawn: 1) During creep deformation, the contribution of non-recoverable strain is at least comparable in size to the recoverable strain contribution. 2) The global load carrying limit of the reinforcement is not reached below strains of 3% (behavior for larger strains has not been verified experimentally). This can be concluded from the absence of a common back creep limit for different forward creep strains. This indicates that fiber fracture is probably no major source of non-recoverable creep. For static isothermal creep this means that load transfer to the fibers is not complete or limited in any way up to comparatively high strains – strains that are higher than the strains at which the minimum strain rate is observed.

It must be noted that the above conclusions were drawn based on compressive cyclic creep experiments with a creep stress of –63 MPa. For smaller absolute stresses, absolute and relative quantities may change but the above reasoning predicts no changes in the qualitative behavior.

Nature of Non-Recoverable Creep

In the introductory part of this section, three possible mechanisms have been proposed by which non-recoverable strain could accumulate: Deformation in fiber free zones, diffusional relaxation of fiber stresses and fiber fracture. It was concluded in the previous subsection that fiber fracture is probably no major source of non-recoverable creep.

The remaining two mechanisms represent two fundamentally different types of deformation with respect to their time dependence. In the case of diffusional relaxation of fiber stresses, the time dependence of non-recoverable strain is a function of the stress gradient along the fiber interface and thus a function of the momentary recoverable strain. The creep rate for this mechanism does depend on the elastic strain misfit between the fibers and the surrounding matrix. The deformation in fiber free zones is mainly dominated by matrix creep. It takes place in separate regions of the material and apart from strain accommodation problems, its

deformation is independent of the deformation of the fiber reinforced regions. This also means that the elastic strain mismatch between the fibers and the matrix in the reinforced regions does not influence non recoverable creep.

For the material under investigation, it is observed that the rate of back-creep does not depend on the rate of forward creep. This is shown in Figure 7.25, where two loading / unloading cycles for intermediate and high total strains are compared. In both cycles, the recovery segments are virtually identical and therefore the internal stresses are the same. The forward creep segments, however, differ substantially in duration. At the smaller total strain, the forward strain rate is much higher than for the cycle at the large strain. This is a clear indication that at least part of the forward strain occurs at a rate which does not depend on the reinforcement stress state. Deformation of fiber free zones therefore seems to be a more probable source of non-recoverable creep than other processes which are associated with the reinforcement stress. Besides, the lack of a time dependence could also be made out in another interesting feature: When the specimen was pre-deformed by various types of experiments, the subsequent stress cycling creep tests showed almost identical amounts of back creep. It did not matter whether the pre-deformation was applied slowly (e.g. by stress cycling creep) or fast (e.g. by compressive deformation at room temperature): The subsequent back creep was always the same. This also suggests that only the total strain but not the time needed to accumulate it controls the evolution of recoverable creep.

The idea that fiber free zones are a major source of non recoverable creep is additionally substantiated by microscopical observations of strain localization in these zones (see Figure 5.30).

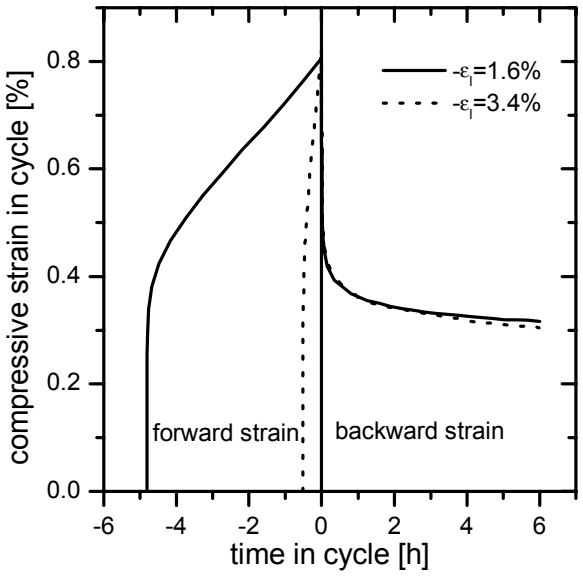

Figure 7.25: *Two loading / unloading cycles for different total strains from a stress cycling creep test with a forward strain increment of 0.8%. Note that despite the different forward creep rates, the back creep behavior is almost identical.*

Notes on Reinforcement Damage

It was stated above that reinforcement damage is probably no major source of non-recoverable creep. If during tertiary creep the reinforcement gets massively damaged, one would expect that the ability to store elastic strain energy would decrease, and so the tendency for back-creep should be reduced. The experimental findings in cyclic creep tests provide no strong evidence for this. The recovery strain showed only a very moderate decrease with increasing total creep strain, even when the specimen was pre-deformed to large strains (see Figure 5.22). Even after a supposedly highly damaging room temperature compression test up to -2%, the specimen showed no pronounced reduction of its ability to restore creep strain. A very straightforward explanation for this would be that the reinforcement just does not get damaged globally. Tertiary creep would then be caused exclusively by damage in fiber free zones. It has to be clarified then, where the small but still measurable decrease of back creep comes from.

It was also stated above that the deformation in fiber free regions is most probably constrained by surrounding reinforced material. The strain concentration in the fiber free regions causes localized (not global) reinforcement damage in their vicinity and especially in regions that link up fiber free zones. Under these conditions, reinforcement damage is related to the total amount of non-recoverable strain $\varepsilon_{n\text{-}rbl}$. This reasoning leads to the surprising result that the extent of damage is high when the share of recoverable strain is small.

Reinforcement damage in the form of fiber fractures was indeed found in the material. The fragmentation of fibers was, however, not pronounced, and it was not obvious, whether the concentration of fiber fractures was at all higher than in the untested material. Similar findings have been reported in Section 5.5.2 for TCC tests. Dedicated image analyses for damage assessment have not been conducted in this work. Evidence of reinforcement damage under compression in the form of fiber fractures was given by Wolf (1997). He investigated the orientational distribution of fiber cracks with respect to the loading axes after compressive creep loading to -1,5% at 350 °C and various stresses. He found a significantly higher amount of fractures in those fibers that were oriented perpendicular to the loading direction.

From the stress cycling creep experiments, it cannot be determined when reinforcement damage sets in. The fact that a decrease in back creep occurs only at large strains does not necessarily mean that damage does not occur at small strains already. Recently, Bidlingmaier et al. (1999) observed very early initiation of damage in the form of fiber fractures at strains only slightly above the elastic loading strain, which was observed with acoustic emission techniques on a Pb/Al_2O_{3f} model composite.

In summary it can be said that 1) reinforcement damage does take place and it is probably mainly dependent on the amount of non-recoverable strain. 2) Strain accommodation problems are likely to cause reinforcement damage in zones adjacent to the fiber-free regions. It is the accumulation of non-recoverable creep that drives this damage process. 3) Global

damaging of the reinforcement by loading it up to its maximum load carrying capacity is probably no governing damage mechanism.

7.4.3 Evolution of Stress Cycling Creep Rate as Compared to the Static Case

Now the consequences of the above findings for the time dependent strain and strain rate evolution shall be discussed. It was shown in Chapter 5 that introducing recovery phases during creep enhances the creep rates in the loaded periods (see Section 5.3.3). This can also be explained on the basis of the previously proposed scheme. It was shown that the amount of recoverable strain is reduced by the recovery phases compared to the case of static creep (see Figure 7.23). This has consequences for the creep rates: Large recoverable strains are tantamount to a high degree of load transfer from the matrix to the fibers. This load transfer is, however, believed to control the initial decrease of the creep rate. Reducing the load transfer by introducing recovery phases does therefore increase the creep rate. Moreover, the point of maximum load transfer may be shifted to larger total strains under stress cycling conditions.

It was also shown that recovery promotes non-recoverable creep, which occurs probably by deformation of fiber-free zones and reinforcement damage around them. The degree of weakening / damage is supposedly correlated to the amount of accumulated non-recoverable creep. Stress cycling creep does therefore not only enhance the creep rate in the initial stage but also the degree of damage at larger strains. This is schematically illustrated in Figure 7.26.

When the loaded phases of the stress cycling creep curves are concatenated and compared to the isothermal creep curve (strain rate vs. strain), it was seen that for both types of experiment the principal evolution of strain rate with strain was the same (around 1.2%). The strain to minimum strain rate, was also apparently the same. This is surprising since the evolution of load-transfer with strain is different for the two tests. A possible reason for this finding is that the joint enhancement of creep rate by reduced load transfer and increased damage leaves the point of minimum strain rate apparently unaltered (see Figure 7.26d). This can only happen when damage starts at very low creep strains, so that the initial transient is immediately followed by tertiary creep without a pronounced steady state creep regime. This is also substantiated by the lack of a steady state in the experimentally determined creep curves.

The creep enhancement due to repeated unloading as it was found here cannot be compared directly to the CCA behavior as it is commonly discussed in literature. The used loading/ recovery cycle was not symmetrical and the time for recovery was unusually large. If the stress cycling creep rates were calculated from the strain per cycle with a cycle time that includes the recovery phase, extremely low creep rates would be obtained. It can be speculated that reduction of the recovery time together with very low forward strain increments (i.e. low stresses and short loading times) could lead to a saturation of recoverable creep to very low values. In

this case, a high amount of creep acceleration is expected – maybe high enough to over-compensate the reduction in creep rate due to the off-load periods.

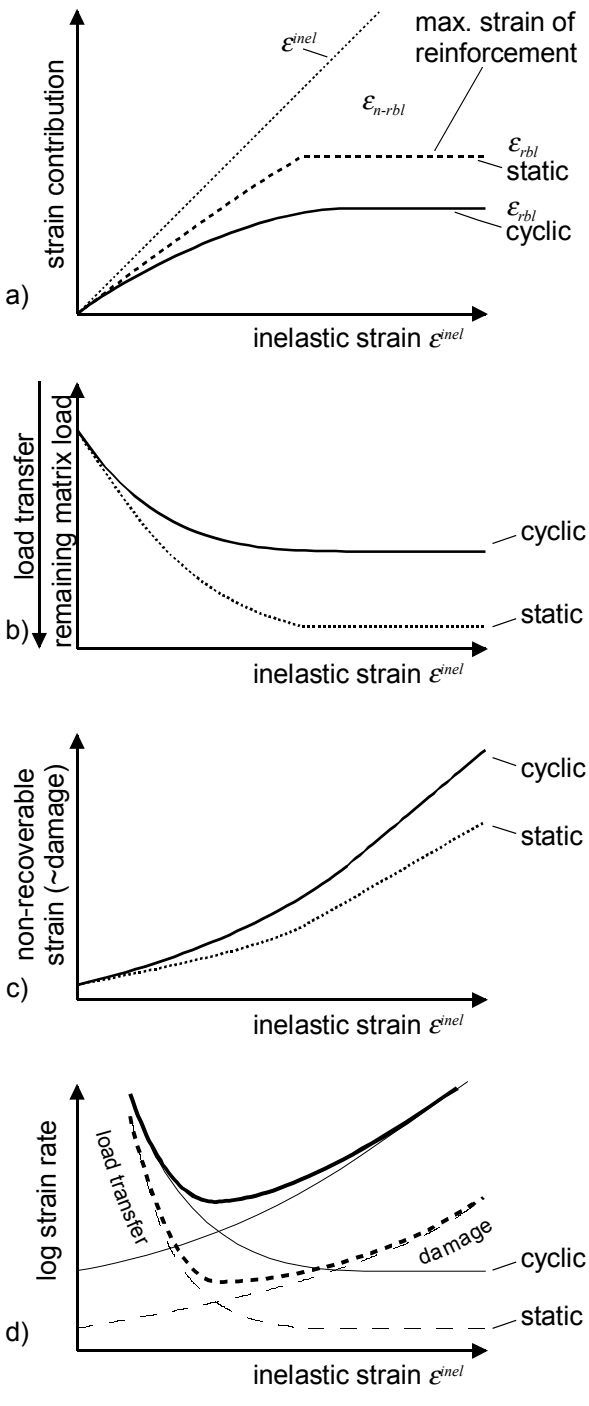

Figure 7.26: *Scheme for the explanation of strain rate evolution for static and stress cycling creep*

a) Contributions of recoverable and non recoverable strain. Static creep: $\varepsilon_{n\text{-}rbl}$ is limited at large strains due to reinforcement damage. For the cyclic case, the detailed forward and backward evolution is omitted for simplicity. ε_{rbl} (cyclic) saturates to lower values than in the static case because equilibrium is reached between $\Delta\varepsilon_{rbl}$ and $\varepsilon_{rec}(\varepsilon_{rbl})$.

b) Large recoverable strains are tantamount to a high degree of load transfer from the matrix to the fibers. The evolution of matrix stress is therefore correlated to the negative evolution of ε_{rbl}.

c) It was found that tertiary creep is probably linked to the amount of non-recoverable strain and not to the amount of load transfer. The evolution of non recoverable strain is given here. Degradation of the reinforcement at large strains is neglected. This additional effect would increase the share of non recoverable strain further.

d) For small strains, the creep rate evolution is given by the evolution of the matrix stress i.e. it decreases due to load transfer. At large strains, load transfer is completed and the creep rate evolution is dominated by weakening of the fiber free regions and beginning fiber damage. For stress cycling creep, load transfer is reduced and weakening is enhanced. This leads to an acceleration of creep at both ends of the creep curve. Under these circumstances, the strain to minimum strain rate might stay constant apparently.

7.4.4 Summary of Discussion Regarding the Stress Cycling Creep Behavior

The basis of the interpretation of the stress cycling creep experiments is the assumption that the inelastic strain can be split up into a recoverable and a non-recoverable part. The following conclusions were drawn based on the evaluation of the stress cycling creep experiments.

1) A major driving force for back creep is the elastic strain energy which is stored in the fibers. It is built up by recoverable strain. Back creep in the composite material was shown to be larger than typical anelastic strains for pure metals and alloys.

2) A substantial part of the forward creep strain cannot be recovered.

3) A maximum load carrying capacity of the fibers is not reached, not even for large forward strains. This was verified for compressive strains up to –3%. Based on this one can speculate that global reinforcement damage (fiber fragmentation, debonding etc.) does not take place because this should limit the load carrying capacity.

4) Among three proposed mechanisms for non recoverable creep, deformation in fiber free zones was found to be the most probable one. Non recoverable creep by global reinforcement damage was ruled out in point 3). Diffusional relaxation around the fibers could be ruled out because non recoverable creep occurred at a rate which did not depend on the elastic strain mismatch between the fibers and the matrix. Additionally, metallographic investigations revealed evidence of strain localization in fiber free regions.

5) Reinforcement damage does nevertheless occur and it is probably located around and between fiber free regions.

6) Cyclic recovery accelerates creep under load by a) reducing the amount of load transfer from the matrix to the fibers and b) by increasing damage caused by strain concentration.

7.5 Thermal Cycling Creep Curves

Up to now we have discussed the minimum creep rates during thermal cycling creep, the effect of the thermal amplitude and the stress and strain evolution within single thermal cycles. In this Section, the overall envelope of the thermal cycling creep curve will be looked at.

It is widely accepted that the form of an isothermal creep curve of a composite is given essentially by the two counteracting processes of load transfer (dominating the primary stage and damage (dominating the tertiary stage). From the above discussion of stress cycling creep experiments it is known that “damage” does not necessarily mean “global damage of the whole reinforcement”. Instead, weakening of the material in, around and in between fiber free zones can be expected to contribute largely to tertiary creep. In the case of isothermal stress

cycling creep and isothermal static creep, the creep curves had almost identical shape. It was shown previously in this work that the form of the thermal cycling creep curve for standard cycles (150↔350 °C) was also not very much different from isothermal creep curves (apart from the higher creep rate, of course). One can therefore speculate with some degree of confidence that the same processes of load-transfer and damage do determine the creep curves for the three types of tests. The relative contributions of load transfer and damage effects seem to be similar in all these cases. The TCC experiments with high temperature cycles have different creep curves. The cyclically induced plasticity leads to very quick load transfer and therefore to much shorter transients. Moreover, the experiments have been conducted with incrementally increased stresses so that no long-term creep curve at a certain stress was determined.

These two processes of load transfer and damage and the effect of stress, sign of loading and reinforcement orientation on them shall be discussed here. Many creep curves under TCC conditions have been presented in this work. As they have been obtained under most different conditions, they are scattered throughout the results chapter. To ease discussion, these creep curves will be brought together and presented so that they can be compared to each other. Then, the phenomenological influence of various testing parameters on their shape will become distinguishable.

Next, the insights that were gained from the stress cycling creep experiments will be used together with general considerations for load transfer and damage evolution in order to obtain a final scheme with which the form of TCC curves can be explained.

7.5.1 Characteristics of Creep Curves

In the following Figure 7.27, a compilation of isothermal and thermal cycling creep curves is given. They are presented in order to illustrate the effect of stress, sign of loading and reinforcement orientation on their shape. Part of the isothermal curves were taken from Bidlingmaier's work as cited in Section 3.5 (Bidlingmaier et al. (1996a)). These are displayed as dotted lines. The rest of the isothermal and TCC curves were taken from the present experimental work (solid lines).

For isothermal creep, the tensile creep curves had the typical shape with an initial transient regime, an extended secondary regime and a pronounced tertiary regime. A weak dependence of the strain $\varepsilon_{to\ min}$ to minimum strain rate on the applied stress was detected. A change in reinforcement orientation from *y*- to *x*-orientation did not change the creep curve in tension; both minimum strain rate and the creep transients were the same. Things were different in compression. Here the strain to minimum strain rate was shifted to smaller strains when the material was loaded in y-direction. The sign of loading had a huge effect: Compressive loading at comparable absolute stresses led to lower strain rates and much stronger initial transients. Tertiary creep was much more pronounced under tensile loading.

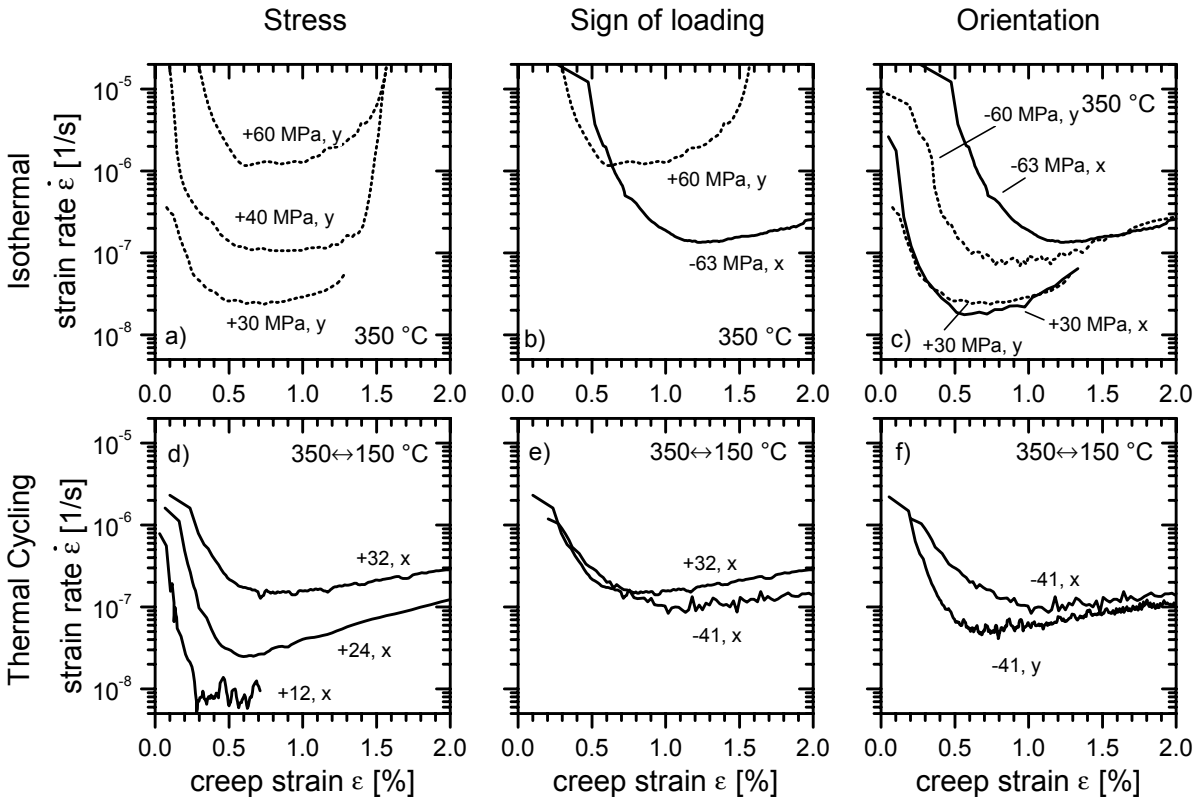

Figure 7.27: *Selected isothermal and thermal cycling creep curves to illustrate the effect of stress, sign of loading and orientation on their shape. All strains include elastic strains from the application of load, supposedly also the curves taken from Bidlingmaier et al. (1996a) (dotted lines), for which, however, some uncertainty exists on the origin of time and strain.*

Under TCC conditions, the stress dependence of $\varepsilon_{to\,min.}$ was more pronounced. Compressive loading, again, led to lower strain rates and higher values of $\varepsilon_{to\,min.}$. Just like in the compressive isothermal case, the reinforcement orientation affects the creep curve under TCC: For *y*-orientation, the minimum strain rate is slightly lower and it is reached at substantially lower strains than for *x*-orientation.

One thing is quite remarkable about the tertiary creep regime: For identical stresses, the creep curves coincide at larger strains, irrespective of the orientation or the sign of loading.

7.5.2 Load transfer

Isothermal Creep

We shall now discuss the strain rate evolution when damage processes are neglected. It has been shown in Chapter 6 that a slab-model like composite of two creeping phases assumes a steady state sooner or later. The final creep rate only depends on the creep properties and the volume fraction of the constituents. The orientation of the external load or the sign of loading have no effect on the final absolute creep rate. Only the transition to this steady state is influenced. One can speculate that the real composite with its comparatively long fibers also

behaves like this. Experimental findings suggest that this is really the case: In Figure 7.27c and 7.27f, one can see that for identical stresses, the creep curves coincide at larger strains, irrespective of the orientation or the sign of loading.

It was found experimentally that applying larger stresses leads to larger strains until minimum strain rate. This finding can be explained with the concept of progressive load transfer. Consider a composite with continuous elastic reinforcement. At loading, an elastic strain misfit between the phases is introduced which is larger the larger the applied stress is. During creep, this misfit is reduced by the deforming matrix, which simultaneously sheds load onto the reinforcement. Creep ceases at infinite time when the whole elastic misfit is made up by matrix creep strain and the reinforcement carries all the load. The stress equilibrium (simple rule of mixtures) changes from

$$\sigma = f_m \sigma_m + f_r \sigma_r \qquad \text{to} \qquad \sigma = f_r \sigma_{r,SS}$$

The total strain to minimum creep rate is then

$$\varepsilon = \varepsilon_m = \varepsilon_r = \sigma_{r,SS} / E_r = \sigma / f_r E_r \,, \tag{7-10}$$

i.e. it is proportional to the applied stress. For the case of a creeping reinforcement, the strain to minimum creep rate can be calculated numerically. This was done here with the aid of the slab model. The results are given in Figure 7.28. In 7.28a simulated isothermal creep curves are shown for various loads in 1-direction. Only steady state matrix and reinforcement creep was considered (no primary creep) and no initial internal (residual) stresses were assumed. In Figure 7.28b it is seen that the strain to minimum strain rate is also proportional to the applied stress. As the proportionality constant, we can define a load transfer modulus $M_{LT} = \sigma / \varepsilon_{to\ min.}$. It was found to be 27 GPa for loading the slab model in 1-direction and 35 GPa for loading in the 2/3-plane. For the case of a non-creeping reinforcement M_{LT} can be calculated from Eq. 7-10 and is 42 GPa. The elastically more compliant direction has a lower load transfer modulus because more misfit strain is generated upon loading and therefore more creep strain has to accumulate to accommodate it.

It can be noted here that the kinetics of the creep process has no influence on the strain to minimum strain rate. The initially induced elastic misfit has to be accommodated with one and the same amount of creep strain, no matter how fast it is accumulated. Changing the temperature, for example, has no effect except for the temperature dependence of the elastic properties. This underlines the necessity to look at creep curves in the form of strain rate vs. strain curves and not vs. time.

The above results are important because they explain why in the experiments the minima of the creep curves occur at different strains. On the other hand, the shift in the minimum of the creep curves should be a good indicator of the relative importance of the load transfer process.

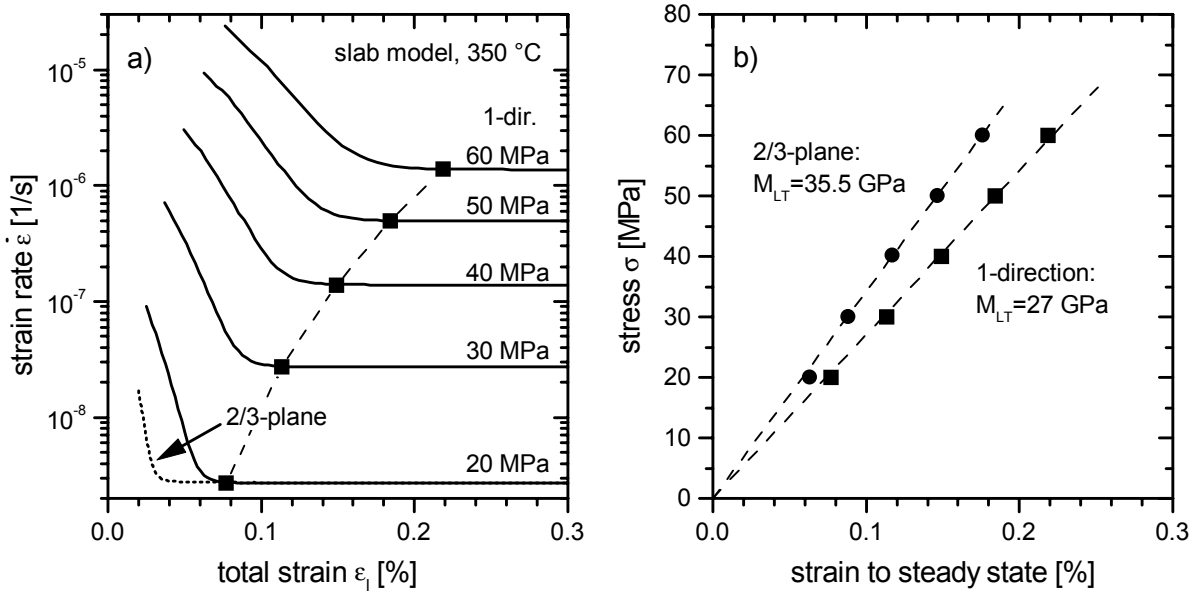

Figure 7.28: *Slab model simulations of isothermal creep at 350 °C. a) Creep curves with points of minimum strain rate indicated (0.1% deviation from analytically calculated steady state creep rate). Only one curve is given for loading in 2/3-plane. b) Plot of applied stress vs. the strain to steady state for both loading directions. Linear dependence is clearly seen. The modulus of load transfer is given as the slope of the line.*

Thermal Cycling Creep

Under thermal cycling conditions, cyclic thermal stresses are superimposed on the stresses due to the static external load. The material deformation is such that starting from a certain internal stress, the cyclic stress evolution finally reaches a stable stress-temperature cycle, which is then associated with a steady state creep rate (creep shakedown). This is a load transfer process in which the creeping phase sheds load on the reinforcement until a stable cycle is established. For the standard cycles this process can take a large number of cycles (cf. Section 7.3.3 Figure 7.18) so that a pronounced transitional behavior is observed during creep loading. A comparison of slab model simulations of isothermal and thermal cycling creep shows that the strain to minimum strain rate is the same for both simulations. This is again because the initially applied stress creates a defined misfit strain which is accommodated by inelastic straining. The inelastic process or the rate by which it occurs have no influence on the strain to minimum strain rate.

It is not clear whether the real composite also shows such a linear dependence between the external stress and the strain to minimum strain rate. It was mentioned in Chapter 6 that the slab-model was well set up and calibrated to simulate composite creep rates. It is less good in predicting creep strains. Therefore the load transfer moduli calculated above are not relevant as quantitative predictions, yet they are interesting as a concept.

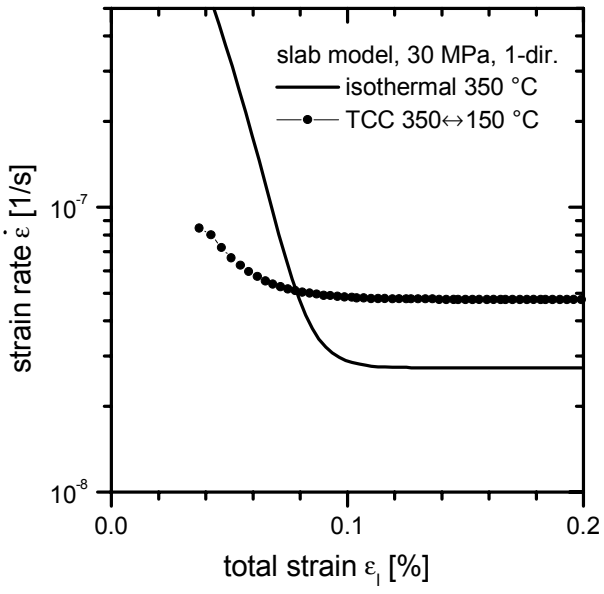

Figure 7.29: *Isothermal (350 °C) and thermal cycling creep curves (standard cycles) at 30 MPa, simulated with the slab model. Despite the different rate, both curves reach the steady state at the same strains.*

In Figure 7.30, an apparent load transfer modulus is shown. It was determined from the strains to minimum strain rates for tensile and compressive TCC tests at various loads. The associated creep curves were shown in Figures 5.7b and 5.9b. Low absolute values for M_{LT} of only 4.5 GPa for loading in *x*-direction and 5 GPa for loading in *y*-direction can be estimated. This rough trend reflects that loading in the less compliant direction leads to higher load transfer moduli. The assessed load transfer moduli are merely upper bound estimates, because the strain to minimum strain rate is possibly smaller than the strain at which the load transfer is completed. The reason for the upper bound is that damage processes, which start early in creep life, can raise the strain rate above the steady state level before load transfer is complete.

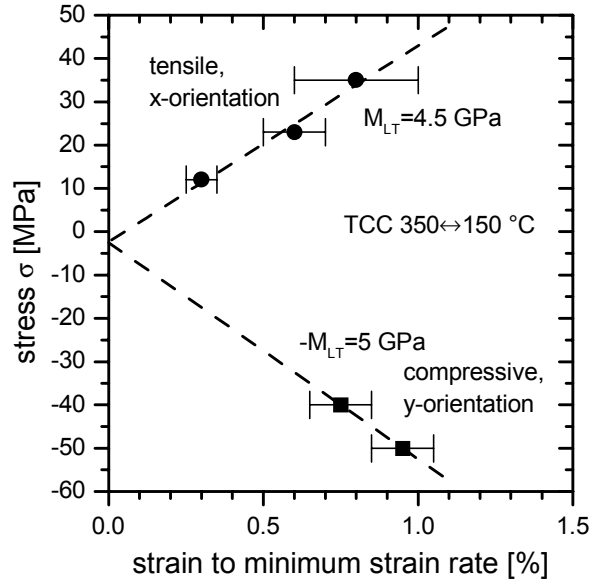

Figure 7.30: *Upper-bound estimate of the load transfer modulus in the tested material for tensile and compressive standard TCC. Note that the absolute load transfer modulus is higher for loading in y-direction.*

It is worth noting that the stress axis intercept is negative for both fitted lines in Figure 7.30. The absolute value is too low to be significant (-1.9 MPa for tension and –2.5 MPa for compression), the statistics is rather poor, the existence of a linear dependency is not proved and

the influence of damage is also not considered. Nevertheless, the finding of a non-zero intercept raises questions about the initial stress state in the material. This is addressed next.

Internal stresses

Internal (residual) stresses that are present in the material before loading can additionally influence the initial strain mismatch and thus the strain to minimum strain rate. Whether the strain to minimum strain rate is increased or decreased depends on the sign of loading: For tensile loading, a residual tensile matrix stress will increase the initial misfit and a compressive residual matrix stress will decrease it. In Figure 7.30, a slightly negative intercept was found which is probably not significant. Nevertheless, such a negative intercept suggests that the residual matrix stress is tensile: The strain needed to accommodate the initial misfit is larger than expected under tension and it is smaller than expected under compression.

Considerations of the internal matrix stress evolution during heat treatment substantiate the existence of tensile residual stresses at the testing temperature. The thermal pre-treatment includes heating to 400 °C and It can be expected that the tensile matrix stresses revert to compression. During the following dwell time, these stresses relax towards zero. Subsequently, the temperature is reduced to the testing temperature of 350 °C and the matrix stresses again become tensile. The then present misfit strain is reduced further during the load-free cycling phase but the overall evolution of misfit strain is such that still some misfit remains. This residual misfit must be small but it has the same sign as an elastic misfit due to an external tensile load. The strain to minimum strain rate will be increased in this case.

7.5.3 Damage

Damage processes in the constraining zones around fiber free zones have been neglected so far but they obviously influence the strain rate evolution. These are considered in the following. Damage was observed in the material in the form of fiber fracture, creep porosity (tension only) and fracture of matrix precipitates. The latter contribution is not considered further. Its effect may be considered together with the effects of fiber fracture.

Fiber fracture

The stress cycling creep experiments as well as the metallographic investigations suggest that reinforcement damage is localized around fiber free zones due to the necessary strain accommodation. The fiber free zones have no preferential orientation and they are uniformly distributed. The size of the constraining zones where damage is induced can therefore be expected to be independent of the loading direction. The amount of damage in these constraining zones should also be only weakly dependent on the specimen orientation.

Damage around fiber free zones is a matter of strain accommodation and the amount of damage therefore depends only on the accumulated strain. The applied stress plays a subordinate role for this. The time needed for strain accommodation is of course shorter for higher stresses but the strain that has to be accommodated is the same.

Based on the above considerations it is expected that the evolution of damage with strain under compression is roughly the same for all stresses, orientations, and types of tests. This is indeed found: Beyond the minimum all the compressive creep curves exhibit the same slight increase in strain rate. When the stresses are also the same, the curves even coincide irrespective of the reinforcement orientation. The increase in strain rate appeared to follow a linear dependence of $\log(\dot{\varepsilon})$ on ε up to at least 2%.

Creep Porosity

Under tensile loading, pore growth has also been found as a damage mechanism. It was clearly visible especially for the high strains that could be achieved under thermal cycling deformation. The metallographic investigations showed that pores aligned perpendicular to the loading direction especially around fiber free regions or in regions connecting fiber free zones. The pores were thus found exactly at those sites in which the highest degree of strain incompatibility was expected.

Creep pores can grow from infiltration micropores which are widespread throughout the material. There is thus no nucleation time or strain and pore growth can take place right from the beginning of loading.

The growth of creep pores is accelerated with increasing pore size in principle because the external load acts on a remaining uncavitated area which becomes progressively smaller.

7.5.4 Summary of the Interpretation of Thermal Cycling Creep Curves

Load transfer takes place because strain misfit between the phases is accommodated by inelastic deformation. The strain that accumulates during the load transfer process is determined by the initial strain misfit in the material immediately after load application. The initial misfit strain is influenced by the applied stress, the orientation (and morphology) of the reinforcement and by residual strains. Their influence is summarized in the following schematic graph.

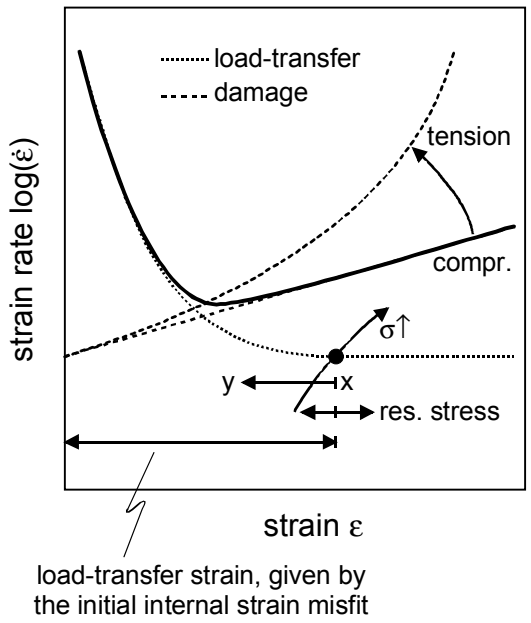

Figure 7.31: *Influence of testing parameters on the shape of the isothermal or thermal cycling creep curve (350↔150°C).*

The load-transfer strain (and thus the strain to minimum strain rate) is determined by the initial misfit strain after load application. Larger applied stresses increase the misfit and thus the load transfer strain. The presence of residual stresses and the reinforcement orientation do also influence the initial misfit strain.

The strain to minimum strain rate is also influenced by the damage evolution and therefore by the sign of loading. Tensile loading increases the strain rate and shifts the strain to minimum strain rate to lower values.

From the stress cycling creep experiments it is known that a substantial amount of inelastic strain is probably located in fiber free regions. This part of the strain was important when back-creep phenomena were investigated. It has, however, subordinate importance for the evolution of strain rate. The deformation in the fiber free regions is constrained by the surrounding reinforced material. The creep rate of these constraining zones thus determines the overall creep rate of the composite. The load transfer process in the reinforced zones is thus still of prime importance for the evolution of the creep rate. Damage in the form of fiber fracture or cavitation accumulates in the constraining zones and progressively increases the strain rate. In the tensile case it appeared that damage had a more pronounced effect on the tertiary strain rate. This is most probably due to cavitation damage that partly replaces fiber fracture in the constraining zones.

8 Summary and Conclusions

An industrially used metal matrix composite has been widely investigated in the present work regarding its behavior under thermal cycling creep conditions. The composite consisted of an eutectic Al-Si matrix with 15 vol.% of discontinuous alumina fibers. Standard experimental techniques were adapted to purpose and suitable test procedures for testing under thermal cycling conditions were developed to measure the stress dependent rate of deformation. The thermal cycling creep (TCC) behavior was determined for thermal cycles to very high temperatures and under moderate thermal cycling conditions, for various high-temperature dwell times, for changing thermal amplitudes, under tensile and compressive loading, and for different orientations of the reinforcement. This provided a uniquely comprehensive set of experimental data of thermal cycling creep in a fibrous MMC.

In some important aspects, the TCC behavior of the investigated composite matched the classical phenomenology established in literature: At low stresses, a creep acceleration compared to isothermal conditions was found and the apparent stress exponent decreased to low values. However, the following differences to the classical behavior appeared on closer examination: The stress exponent did not decrease to 1 and no superplastic deformation was observed (although the ductility of the material was slightly enhanced). Moreover, pronounced transitional behavior upon load changes was found. These discrepancies to classical behavior could be attributed to a) too low internal stresses because of the relatively small thermoelastic misfit strain for the material combination Al/Al_2O_3 and b) an effective impediment of strain by the relatively long fibers. In fact, the performance under TCC conditions of the present MMC investigated in this work was excellent (in technical terms). It exhibited the lowest TCC rates compared to all published investigations of TCC on aluminum based MMCs at comparable conditions. The fiber reinforcement improved the MMC's behavior compared to the matrix material, even under thermal cycling at very low stresses, because the Al-Si matrix material alone did also exhibit TCC behavior. It was shown theoretically that the Si platelets from the matrix material probably introduce additional stresses in the fiber reinforced piston alloy but that the overall TCC behavior is probably still dominated by the Al_2O_3 fibers.

An important deviation from classical TCC behavior, which had hitherto not been addressed in literature, was that the TCC rates were increased compared to the isothermal creep rates not only at low applied stresses but also at high stresses, where the apparent stress exponents for isothermal and thermal cycling creep were the same. It was speculated in the present work that micromechanical effects which enhance the kinetics of creep directly could cause such a creep acceleration beyond the mere introduction of internal stresses. Cyclically re-initiated primary creep was proposed as such a mechanism which could indeed lead to a substantial TCC acceleration in the whole stress range (and not only at low stresses).

The experimental setup had been optimized among other things for precise strain measurement and this allowed for analysis of the strain evolution in individual cycles. It was found that presenting the in-cycle strain evolution in the form of strain differentials with respect to temperature ("instantaneous CTE") was a good way to visualize effects of inelastic straining. Simple rules for the interpretation of such instantaneous CTE curves were set up and with them it was possible to define the temperatures at which the average internal matrix stresses were zero ("effective stress-free temperatures") or where matrix plasticity set in. The measurements showed evidence of substantial inelastic deformation under thermal cycling conditions. An important finding was that most of the inelastic strain which had accumulated in one half cycle was recovered by reversed inelastic deformation in the other. It was shown with the aid of a self-developed numerical simulation program how the combined action of creep (mainly at the high temperature end of the heating half-cycle) and plasticity (mainly at the low temperature end of the cooling half-cycle) could lead to a well balanced cycle with a low net strain per cycle. Theses findings contradict former theories, in which the onset of plastic deformation beyond a critical thermal amplitude was believed to cause a strong increase of the net accumulated strain per cycle.

The composite exhibited a weak reinforcement texture. In a quantitative analysis of the fiber orientation distribution it was found that a plane of preferential fiber orientation existed, but that the degree of alignment was relatively weak so that still a substantial amount of fibers were oriented randomly. This texture did not affect measurements of the Young's modulus or the isothermal creep rates. It however largely influenced the behavior under thermal cycling conditions: For example, the TCC rates in the direction perpendicular to the preferential plane were generally higher than for loading parallel to this plane. In order to describe the fiber orientation distribution quantitatively, the concept of orientation tensors was adapted from the field of polymer matrix composites and for the first time applied to MMCs. With the aid of a measured second-order orientation tensor, it was possible to determine an averaged Eshelby tensor with which in turn thermoelastic properties (such as the Young's modulus) of the composite material could be estimated and compared to the experimental findings.

For thermal cycles which came close to use conditions (cycling between 350 and 150 °C), the investigated composite exhibited pronounced transient creep behavior and the overall envelope shape of the thermal cycling creep curve was very similar to the shape of an isothermal creep curve. The mechanisms that led to this form of the creep curve were further investigated with a newly developed experimental procedure of isothermal stress cycling creep. In contrast to conventional stress cycling creep experiments that resemble slow fatigue tests, particularly long relaxation times were employed alternating with defined creep straining. The phenomenon of back-creep (strain recovery after removing a creep load) was utilized to investigate effects of load transfer from the matrix to the fibers and to conclude on the overall evolution of the composite strain rate. An important finding of this investigation was that a substantial part of the creep strain was probably concentrated in regions of low fiber content. This led

also to the unexpected finding that reinforcement damage in the form of fiber fracture was not widespread in the whole microstructure but that it was rather localized in those reinforced regions that had to accommodate the strain concentrations. Metallographic investigations supported these suggestions. It is expected that creep rates would be more effectively reduced when zones that concentrate strains such as fiber free regions were avoided. This applies to isothermal and thermal cycling conditions.

A simple continuum mechanical model has been set up which approximated the investigated composite by a stack of two homogeneous and tightly bonded deforming slabs. The slabs were attributed the thermoelastic properties of the matrix and the reinforcement material and the creep properties of the slabs were calibrated with the known isothermal creep properties of the matrix and the composite. The problem of the impediment of deformation by a continuous and elastic reinforcement was overcome by attributing creep properties not only to the matrix but also to the reinforcement slab. The slab model was implemented in a computer program and it was used to predict the creep rates and the in cycle strain evolution under thermal cycling creep conditions. Due to its geometrical simplicity, the slab model yielded no quantitatively exact predictions but excellent qualitative agreement with the experimental findings was found throughout. The simulations proved to be of great help in the interpretation and explanation of the observed phenomena. Furthermore, the calculations showed that a continuum mechanics approach which focuses on the evolution of internal stresses alone is well suited to describe TCC behavior in the present case.

In the present work, established knowledge from the literature of isothermal and thermal cycling creep of MMCs, from the field of continuum mechanics and from polymer composite engineering were brought together to explain the thermal cycling creep behavior of a technical metal matrix composite. Almost all deviations from the idealized behavior could be resolved by carefully refining or correcting established concepts and sometimes by proposing reasonable new concepts. The challenging task was to clarify the complicated relations between different aspects of the external and internal stresses and strains, their evolution within single cycles and their long-term evolution so that finally a concise picture of the deformation behavior for a special technical MMC emerged.

Appendix A Eshelby Tensors

A.1 Eshelby Tensor for Aligned Discs and Spheroids and for a Planar Array of Continuous Fibers

In Table A.1 the Eshelby (*S*-)tensor for prolate spheroids with an aspect ratio *s*, which are aligned in 1-direction and the *S*-tensor for discs aligned in the 2/3-plane are listed (taken from Clyne and Withers (1993)). The geometry of aligned discs is identical to the geometrical setup of the slab model. The thermoelastic predictions from a mean-field Eshelby model using the S-tensor for aligned discs are thus identical to thermoelastic slab-model predictions.

For the case of *fibrous* reinforcement, a composite structure which, regarding the symmetry and overall constraints, comes closest to the slab-model arrangement is the arrangement of continuous fibers in a 2D random planar array. The Eshelby tensor for such an arrangement (fibers in the 2/3 plane) has been given by Johannesson and Ogin (1995). The tensor components are listed in the widely accepted notation by Brown and Clarke (1975).

Tensor notation	Matrix notation	Spheroids	Discs	2D random
S_{1111}	S_{11}	$\frac{4}{3}Q + RI_3 + 2s^2P$	1	$\frac{5-4\nu}{8(1-\nu)}$
$S_{1122} = S_{1133}$	$S_{12} = S_{13}$	$-RI_3 - P$	0	$\frac{8\nu-1}{16(1-\nu)}$
$S_{2211} = S_{3311}$	$S_{21} = S_{31}$	$-RI_1 - s^2P$	$\frac{\nu}{1-\nu}$	$\frac{4\nu-1}{16(1-\nu)}$
$S_{2233} = S_{3322}$	$S_{23} = S_{32}$	$\frac{1}{3}Q - RI_1 + \frac{4}{3}P$	0	$\frac{16\nu-3}{64(1-\nu)}$
$S_{2222} = S_{3333}$	$S_{22} = S_{33}$	$Q + RI_1 + \frac{3}{4}P$	0	$\frac{23-16\nu}{64(1-\nu)}$
S_{2323}	$\frac{1}{2}S_{44}$	$\frac{1}{3}Q + RI_1 + \frac{1}{4}P$	0	$\frac{13-16\nu}{64(1-\nu)}$
$S_{1313} = S_{1212}$	$\frac{1}{2}S_{55} = \frac{1}{2}S_{66}$	$2R - \frac{RI_1}{2} - \frac{1+s^2}{2}P$	$\frac{1}{2}$	$\frac{5-6\nu}{16(1-\nu)}$

Table A.1: *Eshelby tensors for a) spheroids with aspect ratio s, oriented in 1-direction, b) discs parallel to the 2/3-plane (taken from Clyne and Withers (1993)) and c) a planar array of continuous fibers in the 2/3-plane (Johannesson and Ogin (1995))*

The used constants are:

$$I_1 = \frac{2s}{\left(s^2-1\right)^{2/3}} \cdot \left[s \cdot \left(s^2-1\right)^{1/2} - \cosh^{-1} s \right] \qquad \text{for prolate spheroids } (s>1)$$

$$I_1 = \frac{2s}{\left(1-s^2\right)^{2/3}} \cdot \left[\cos^{-1} s - s \cdot \left(1-s^2\right)^{1/2} \right] \qquad \text{for oblate spheroids } (s<1)$$

$$I_3 = 4 - 2I_1 \qquad Q = \frac{3}{8(1-\nu)} \qquad R = \frac{(1-2\nu)}{8(1-\nu)} \qquad P = Q\,\frac{(4-3I_1)}{3\left(s^1-1\right)}$$

A.2 Estimation of the Eshelby Tensor from an Orientation Tensor

For calculations of thermoelastic composite properties, it would be desirable to have an Eshelby tensor not for aligned fibers but for the individual reinforcement texture of the material investigated in this work. This requires the orientational averaging of the fourth-rank Eshelby tensor for the aligned reinforcement according to the reinforcement orientation distribution. Setting up such an averaged tensor is not an easy task. It has been pointed out by Johannesson and Pedersen (1998) that for the calculation of an average Eshelby *S* tensor for arbitrarily oriented inclusions, *"it is necessary to carry out 3^8=6561 complicated trigonometric triple integrals"*. In the same paper, they have given a computer algebra solution for the determination of the average *S* tensor for a transversely isotropic reinforcement orientation distribution function (ODF). This solution shall be applied to the material from this work. In order to do so, we have to approximate the measured reinforcement orientation distribution by a transverse isotropic one. We can do this by omitting the off-diagonal elements and by averaging over the 2/3 components. The transverse isotropic approximation of the orientation tensor would then be:

$$\begin{pmatrix} 0.20 & -0.045 & 0.003 \\ -0.045 & 0.35 & 0.003 \\ 0.003 & 0.003 & 0.44 \end{pmatrix} \qquad \begin{pmatrix} 0.20 & 0 & 0 \\ 0 & 0.40 & 0 \\ 0 & 0 & 0.40 \end{pmatrix}$$

Measured second-order orientation tensor — *Approximated transversely isotropic orientation tensor*

The next task is to recover the fiber ODF from the approximated orientation tensor. Advani and Tucker (1987) have shown how this can be done. Because of the low order of the orientation tensor, only limited information about the real ODF is stored in it. The recovered ODF will thus be only a second-order approximation. Better results can be obtained when higher-order orientation tensors are also taken into account. The second-order approximation of the distribution function is given by the formula

$$\psi(p) = \frac{1}{4\pi} + \frac{15}{8\pi} b_{ij} f_{ij}(p), \qquad \textbf{(A-1)}$$

where

$$b_{ij} = a_{ij} - \frac{1}{3}\delta_{ij} \qquad \textbf{(A-2)}$$

is the deviatoric version of the orientation tensor and

$$f_{ij}(p) = p_i p_j - \frac{1}{3}\delta_{ij} \qquad \textbf{(A-3)}$$

are tensor basis functions of the vector p (δ_{ij} is the Kronecker-delta). The ODF for fibers perpendicular to the plane of transverse isotropy is shown in Figure A.1. It is compared to the histogram of fiber inclinations towards the (global) *x*-axis as they were measured from section ellipsoids in the *yz*-plane. The agreement between the measured and the recovered ODF is not perfect but still quite reasonable.

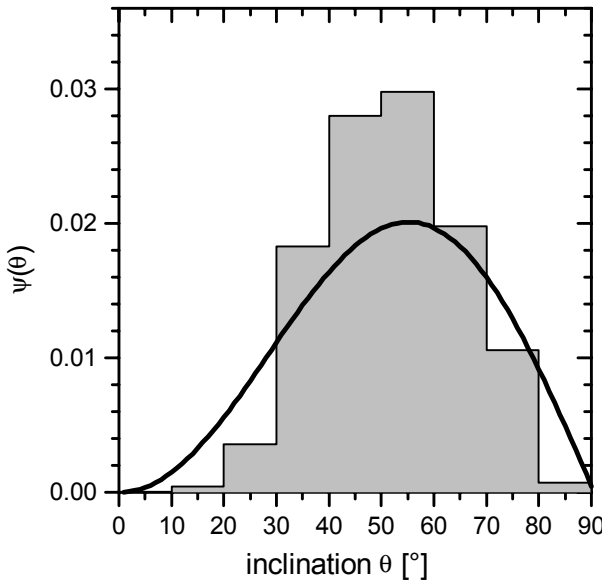

Figure A.1: *Fiber ODF (thick line), recovered from the approximated transversely isotropic orientation tensor, compared to the histogram of the fiber inclinations towards the x-axis (measured from the aspect ratio of ellipsoidal fiber sections in the microscope). The ODF-curve has been corrected by sin(θ) for the realization probabilities of the angle θ in spherical coordinates. The histogram was corrected with the weighting function for different section-realization probabilities (see Section 4.1.3).*

Now that we have obtained a transverse isotropic fiber ODF, we can apply Johannesson and Pedersen's analytical recipe for averaging any Eshelby tensor. Their solution is given in the form of numerous lengthy formulas in their paper Johannesson and Pedersen (1998). The appropriate Eshelby tensor to be averaged was considered to be the tensor for aligned fibers with an aspect ratio of 50. Finally, after orientational averaging, the averaged Eshelby tensor for the fiber reinforced piston alloy is:

Tensor notation	Matrix notation	S tensor
S_{1111}	S_{11}	0.548
$S_{1122} = S_{1133}$	$S_{12} = S_{13}$	0.052
$S_{2211} = S_{3311}$	$S_{21} = S_{31}$	0.053
$S_{2233} = S_{3322}$	$S_{23} = S_{32}$	0.051
$S_{2222} = S_{3333}$	$S_{22} = S_{33}$	0.538
S_{2322}	S_{44}	0.322
$S_{1313} = S_{1212}$	$\frac{1}{2} S_{55} = \frac{1}{2} S_{66}$	0.450

Table A.2: *Eshelby tensor for the fiber-reinforced piston alloy investigated in this work. The tensor was determined from an approximated transversely isotropic second-order orientation tensor.*

Appendix B Accuracy of Orientation Measurement

It is obvious that the determination of the fiber orientation from its elliptic cross section lacks accuracy for certain angular ranges. The error for the calculation of θ from a measured aspect ratio of the ellipse $s_e=a/b$ with an error in length measurement Δl can be calculated by the law of error propagation from equation 4-1:

$$\Delta\theta = \left|\frac{d\theta}{da}\right|\Delta a + \left|\frac{d\theta}{db}\right|\Delta b = \frac{\Delta l}{\sqrt{1-(1/s_e)^2}} \cdot \frac{(s_e+1)}{s_e^{\,2}} \cdot \frac{1}{b}, \qquad \textbf{(B-1)}$$

(for the definition of the angles θ and ϕ see Figure 4.3). One can assume a standard error of one pixel in length ($2\Delta l = 0.17$ µm) for the measurement of $2a$ and $2b$. The variation of calculated θ with measured s_e is shown in Figure B.1. The upper and lower error bounds according to equation B-1 for a fiber with a thickness d of 3 µm ($b = 1.5$ µm) are also shown there. It can be seen that for low aspect ratios, the error for θ becomes quite significant: For an ellipse aspect ratio below $s_e = 1.41$ ($\theta < 45°$), the relative error is larger than 12% ($\Delta\theta > 5.5°$). Above 60° ($s_e = 2$), the error drops below 5% ($\Delta\theta < 2.8°$). Another error arises from the finite length of the fibers or from the fact that long fiber sections have a high probability to be clipped by the image frame. According to equation 4-1, even those fibers that lie perfectly perpendicular to the z-axis would be measured with $\theta < 90°$, just because the aspect ratio of the fiber section is finite. Section aspect ratios of up to ten are usually not limited by the image frame or the length of the fibers – provided that the fibers themselves have a fairly large aspect ratio. Therefore this error has to be accounted for only at larger aspect ratios ($\theta > 85°$).

The error for the determination of the angle ϕ can only be roughly estimated, because the software algorithm for the measurement of ϑ is not given by the manufacturer. It is evident that as the section aspect ratio approaches unity, the uncertainty in the measurement of ϑ increases to a maximum of ±90°. For aspect ratios of more than 1.5, however, the accuracy of the angular measurement was found to be better than ±2.5°.

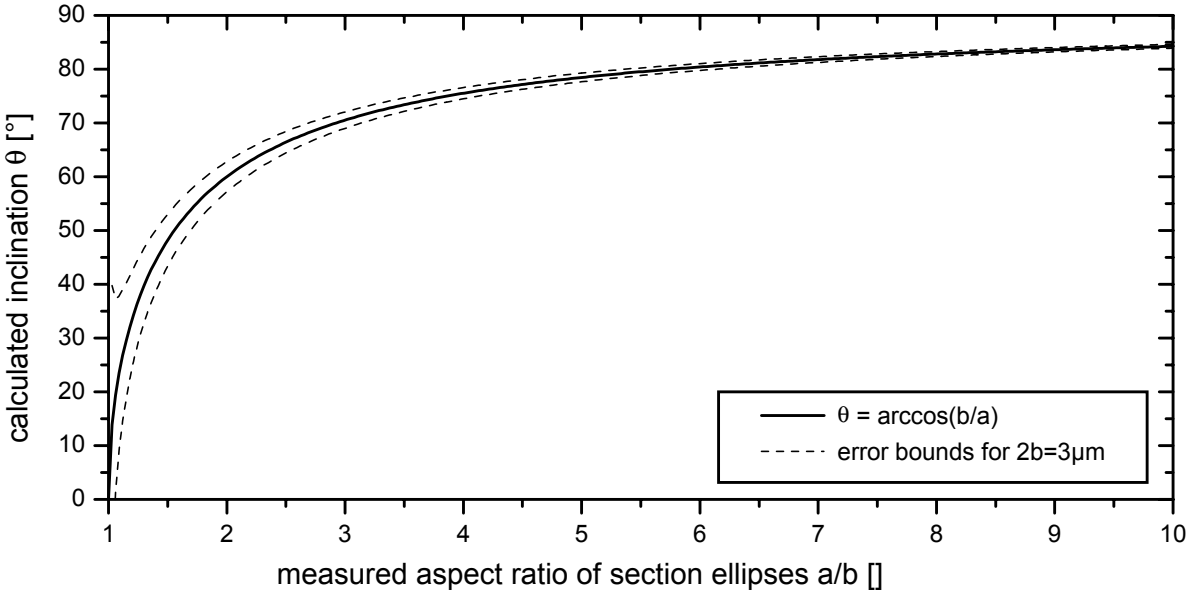

Figure B.1: *Inclination θ of fibers, calculated from the aspect ratio of their section ellipses. The error bounds are calculated for a fiber with a thickness of 3 µm and for an absolute error of 0.17 µm in the spatial resolution of the image analysis.*

Appendix C Slab Model: Derivation of Young's Modulus

If only elastic strains are considered, Eq. 6-1a) in 6-2a) simplifies to

$$\varepsilon_1 = f_m\varepsilon_{1m} + f_r\varepsilon_{1r} = \frac{f_m}{E_m}\sigma_1 - \frac{f_m\nu_m}{E_m}\cdot 2\sigma_{2m} + \frac{f_r}{E_r}\sigma_1 - \frac{f_r\nu_r}{E_r}\cdot 2\sigma_{2r}. \qquad \textbf{(C-1)}$$

Substituting σ_{2r} for σ_{2m} using Eq. 6-3b) and σ_2=0 yields

$$\varepsilon_1 = \sigma_1\left(\frac{f_m}{E_m} + \frac{f_r}{E_r}\right) + 2f_m\cdot\left(\frac{\nu_r}{E_r} - \frac{\nu_m}{E_m}\right)\cdot\sigma_{2m}. \qquad \textbf{(C-2)}$$

σ_{2m} is given by Eq. 6-4 which simplifies to the following equation when again inelastic and thermal strain terms are omitted and σ_2=σ_3=0:

$$\cdot\sigma_{2m} = \left(\frac{1}{A} - A\cdot B^2\right)^{-1}\cdot\left(ABC + C\right)\cdot\sigma_1. \qquad \textbf{(C-3)}$$

The terms A, B, C and D have been defined in Chapter 6 for Eq. 6-4. Equation C-3 can be susbstituted in C-2 so that we obtain an equation which directly relates ε_1 to σ_1 and from which we can obtain the slab model's Young's modulus E_1 (cf. Eq. 6-20):

$$E_1 = \left[\left(\frac{f_m}{E_m} - \frac{f_r}{E_r}\right) - 2f_mC^2\cdot\left(AB+1\right)\cdot\left(\frac{1}{A} - AB^2\right)\right]^{-1}. \qquad \textbf{(C-4)}$$

Young's modulus for the in-plane-direction can be derived in a similar manner. The strain compatibility condition 6-2b) with Eq. 6-1b) simplifies to

$$\varepsilon_2 = \frac{1}{E_m}\sigma_{2m} - \frac{\nu_m}{E_m}\sigma_{3m}, \qquad \textbf{(C-5)}$$

considering that σ_1=σ_3=0. Equations for σ_{2m} and σ_{3m} can be obtained again from Eq. 6-4:

$$\sigma_{2m} = \left(\frac{1}{A} - A\cdot B^2\right)^{-1}\cdot\left(D - ABE\right)\cdot\sigma_2, \qquad \textbf{(C-6)}$$

and

$$\sigma_{2m} = \left(\frac{1}{A} - A\cdot B^2\right)^{-1}\cdot\left(ABD - E\right)\cdot\sigma_2. \qquad \textbf{(C-7)}$$

Substituting these into Eq. C-5 gives a direct relation between ε_2 and σ_2 which yields the slab model's Young's Modulus $E_{2/3}$ (cf. 6-21).

$$E_{2/3} = \frac{\frac{1}{A} - AB^2}{\frac{1}{E_m}(D - ABE) - \frac{\nu_m}{E_m}(ABD - E)}. \qquad \textbf{(C-8)}$$

Appendix D Tables of Experimental TCC Data

Standard Cycles

specimen	orientation	sign of loading	applied stress [MPa]	min. strain rate [s^{-1}]
Standard cycle 350↔150 °C, t_c=600 sec., 60 sec. dwell at T_{max} and T_{min}				
* denotes tests with incremental loading				
V20_3	x	tensile	12.1	$7.9 \cdot 10^{-9}$
V19_1	x	tensile	18.4	$2.0 \cdot 10^{-8}$
V19_3	x	tensile	23.9	$2.6 \cdot 10^{-8}$
V20_1	x	tensile	25.6	$3.6 \cdot 10^{-8}$
V19_2	x	tensile	27.8	$1.2 \cdot 10^{-7}$
V18_2	x	tensile	31.7	$1.5 \cdot 10^{-7}$
V22x08	x	compressive	-20.0	$-4.3 \cdot 10^{-9}$
V22x08	x	compressive	-25.0*	$-1.3 \cdot 10^{-8}$
V22x08	x	compressive	-30.0*	$-5.0 \cdot 10^{-8}$
V22x01	x	compressive	-30.4	$-3.8 \cdot 10^{-8}$
V22x03	x	compressive	-40.7	$-9.5 \cdot 10^{-8}$
V22x11	x	compressive	-35.6	$-5.4 \cdot 10^{-8}$
V22x11	x	compressive	-61.1*	$-7.1 \cdot 10^{-7}$
V22y03	y	compressive	-40.7	$-4.7 \cdot 10^{-8}$
V22y01	y	compressive	-50.8	$-1.4 \cdot 10^{-7}$

Table C.1: *Minimum TCC rates for standard thermal cycles with the composite material.*

Standard Cycles with Isothermal Pre-Creep

Note that these experimental data were not presented or discussed in the present work. In these tests, an isothermal creep segment at test load was introduced between the initial load free cycling and the loaded thermal cycling segments. The measurements suggest that isothermal pre-deformation increased the minimum creep rates mainly by initiation of creep damage. The overall effect of pre-creep was not pronounced.

specimen	orientation	sign of loading	applied stress [MPa]	min. strain rate [s^{-1}]	pre creep [%]
Standard cycle 350↔150 °C, t_c=600 sec., 60 sec. dwell at T_{max} and T_{min} All test were done with isothermal pre-creep before TCC					
V12_3	x	tensile	20.9	$5.3 \cdot 10^{-7}$	0.60
V11_3	x	tensile	23.7	$2.8 \cdot 10^{-8}$	0.30
V17_2	x	tensile	26.9	$4.0 \cdot 10^{-8}$	0.30
V10_2	x	tensile	30.4	$2.6 \cdot 10^{-7}$	0.78
V18_3	x	tensile	31.3	$9.7 \cdot 10^{-8}$	0.20
V17_3	x	tensile	34.6	$1.9 \cdot 10^{-7}$	0.30
V11_2	x	tensile	40.7	$4.0 \cdot 10^{-7}$	0.60
V12_1	x	tensile	51.6	$7.5 \cdot 10^{-7}$	0.60
V2_xc1	x	compressive	-39.8	$-1.9 \cdot 10^{-7}$	-0.60
V2_xc2	x	compressive	-50.2	$-5.4 \cdot 10^{-7}$	-0.60
V2_xc3	x	compressive	-50.3	$-4.7 \cdot 10^{-7}$	-0.60
V2_xc4	x	compressive	-60.5	$-1.2 \cdot 10^{-6}$	-0.60
V2_yc4	y	compressive	-39.9	$-5.0 \cdot 10^{-8}$	-0.60
V2_yc2	y	compressive	-50.2	$-1.0 \cdot 10^{-7}$	-0.60
V2_yc3	y	compressive	-60.4	$-2.1 \cdot 10^{-7}$	-0.60
V2_zc1	z	compressive	-50.2	$-1.0 \cdot 10^{-7}$	-0.60
V2_zc2	z	compressive	-70.3	$-3.1 \cdot 10^{-7}$	-0.60

Table C.2: *Minimum TCC rates of the composite material for experiments with standard cycles and isothermal pre-creep.*

High-Temperature Cycles

specimen	orientation	sign of loading	applied stress [MPa]	min. strain rate [s^{-1}]
High-temp. cycle 400↔100 °C, t_c=600 sec., 60 sec. dwell at T_{max} and T_{min}				
* denotes tests with incremental loading				
V22x09	x	compressive	-6.2	$-1.0\cdot10^{-9}$
V22x09	x	compressive	-8.2*	$-1.6\cdot10^{-9}$
V22x09	x	compressive	-15.2*	$-8.0\cdot10^{-9}$
V22x09	x	compressive	-17.0*	$-1.4\cdot10^{-8}$
V22x09	x	compressive	-20.5*	$-3.5\cdot10^{-8}$
V22x09	x	compressive	-22.6*	$-7.3\cdot10^{-8}$
V22x09	x	compressive	-25.6*	$-1.7\cdot10^{-7}$
High-temp. cycle 450↔120 °C, t_c=600 sec., 60 sec. dwell at T_{max} and T_{min}				
v24_2	x	tensile	2.3	$2.0\cdot10^{-10}$
v24_2	x	tensile	6.5*	$2.2\cdot10^{-8}$
v24_2	x	tensile	12.7*	$1.3\cdot10^{-7}$
v24_2	x	tensile	17.8*	$4.0\cdot10^{-7}$
v24_1	x	tensile	4.4	$1.2\cdot10^{-8}$
v24_1	x	tensile	8.6*	$3.5\cdot10^{-8}$
v24_1	x	tensile	10.7*	$7.2\cdot10^{-8}$
v24_1	x	tensile	15.8*	$2.7\cdot10^{-7}$
v24_1	x	tensile	17.9*	$4.8\cdot10^{-7}$
v24_1	x	tensile	21.0*	$1.4\cdot10^{-6}$

Table C.3: *Minimum TCC rates for high temperature cycles with the composite material.*

Influence of High-Temperature Dwell

specimen	orientation	sign of loading	applied stress [MPa]	min. strain rate [s^{-1}]	strain per cycle [%]
High-temp. cycle 450↔100 °C, t_c=540 sec., no dwell at T_{max} and 60 sec dwell at T_{min}					
* denotes tests with incremental loading					
V22y05	y	compressive	-8.2	$-2.3\cdot10^{-9}$	$1.2\cdot10^{-6}$
V22y05	y	compressive	-10.2*	$-6.1\cdot10^{-9}$	$3.3\cdot10^{-6}$
V22y05	y	compressive	-15.3*	$-4.4\cdot10^{-8}$	$2.4\cdot10^{-5}$
V22y05	y	compressive	-17.5*	$-9.0\cdot10^{-8}$	$4.9\cdot10^{-5}$
V22y05	y	compressive	-20.6*	$-2.0\cdot10^{-7}$	$1.1\cdot10^{-4}$
High-temp. cycle 450↔100 °C, t_c=600 sec., 60 sec. dwell at T_{max} and 60 sec dwell at T_{min}					
V22y04	y	compressive	-8.2	$-2.0\cdot10^{-8}$	$1.2\cdot10^{-5}$
V22y04	y	compressive	-10.2*	$-4.0\cdot10^{-8}$	$2.4\cdot10^{-5}$
V22y04	y	compressive	-15.5*	$-1.4\cdot10^{-7}$	$8.4\cdot10^{-5}$
V22y04	y	compressive	-17.5*	$-2.4\cdot10^{-7}$	$1.4\cdot10^{-4}$
V22y04	y	compressive	-20.6*	$-3.4\cdot10^{-7}$	$2.0\cdot10^{-4}$
High-temp. cycle 450↔100 °C, t_c=600 sec., 360 sec. dwell at T_{max} and 60 sec dwell at T_{min}					
V22y07	y	compressive	-8.1	$-1.3\cdot10^{-8}$	$1.2\cdot10^{-5}$
V22y07	y	compressive	-10.1*	$-2.5\cdot10^{-8}$	$2.3\cdot10^{-5}$
V22y07	y	compressive	-15.2*	$-1.1\cdot10^{-7}$	$9.9\cdot10^{-5}$
V22y07	y	compressive	-17.3*	$-1.9\cdot10^{-7}$	$1.7\cdot10^{-4}$
V22y07	y	compressive	-20.3*	$-4.0\cdot10^{-7}$	$3.6\cdot10^{-4}$

Table C.4: *Minimum TCC rates for high temperature cycles with the composite material and various dwell times at the maximum cycle temperature.*

Matrix Material

specimen	sign of loading	applied stress [MPa]	min. strain rate [s^{-1}]
Cycle 350↔150 °C, t_c=600 sec., 60 sec. dwell at T_{max} and T_{min}			
* denotes tests with incremental loading			
u18_4	compressive	9.8	$1.2 \cdot 10^{-7}$
u18_5	compressive	3.9*	$2.0 \cdot 10^{-8}$
u18_5	compressive	8.1*	$1.4 \cdot 10^{-7}$
u18_5	compressive	14.3*	$5.0 \cdot 10^{-7}$
u18_5	compressive	20.4*	$1.2 \cdot 10^{-6}$
u18_5	compressive	10.2*	$2.4 \cdot 10^{-7}$
u18_7	compressive	1.5	$5.9 \cdot 10^{-8}$
Cycle 400↔200 °C, t_c=600 sec., 60 sec. dwell at T_{max} and T_{min}			
u18_7	compressive	4.0	$2.3 \cdot 10^{-7}$
u18_7	compressive	6.1*	$4.3 \cdot 10^{-7}$
u18_7	compressive	8.1*	$7.0 \cdot 10^{-7}$
u18_7	compressive	10.2*	$1.1 \cdot 10^{-6}$
u18_7	compressive	12.3*	$1.6 \cdot 10^{-6}$
u18_7	compressive	4.0*	$2.2 \cdot 10^{-7}$
Cycle 400↔100 °C, t_c=600 sec., 60 sec. dwell at T_{max} and T_{min}			
u18_6	compressive	1.5	$1.0 \cdot 10^{-7}$
u18_6	compressive	4.0*	$3.2 \cdot 10^{-7}$
u18_6	compressive	6.1*	$5.6 \cdot 10^{-7}$
u18_6	compressive	8.1*	$9.0 \cdot 10^{-7}$
u18_6	compressive	10.2*	$1.3 \cdot 10^{-6}$
u18_6	compressive	12.3	$1.9 \cdot 10^{-6}$
u18_6	compressive	4.0*	$3.3 \cdot 10^{-7}$

Table C.5: *Minimum TCC rates for the matrix material.*

References

Advani, S.G. and Tucker, I. (1987), *The Use of Tensors to Describe and Predict Fiber Orientation in Short Fiber Composites*, J. Rheology, **31,** 751.

Allen, A. J., Bourke, M. A. M., Dawes, S., Hutchings, M. T. and Withers, P. J. (1992), *The Analysis of Internal Strains Measured by Neutron Diffraction in Al/SiC Metal Matrix Composites*, Acta mater., **40,** 2361-2373.

Anderson, R.G. and Bishop, J.F.W. (1962), *The Effect of Neutron Irradiation and Thermal Cycling on Permanent Deformations in Uranium under Load*, In: Symposium on Uranium and Graphite , Institute of Metals, 17-23.

Andrade, E.N. da C (1910), *As Cited in Argon and Battacharya (1987)*, Proc. Roy. Soc., **A84**.

Argon, A.S. and Bhattacharya, A.K. (1987), *Primary Creep in Nickel: Experiments and Theory*, Acta metall., **35,** 1499-1514.

ASTM (1983), *Standard Practice for Conducting Creep, Creep-Rupture and Stress-Rupture Tests of Metallic Materials*, ASTM Standard, E139-83, American Society for Testing and Materials, Philadelphia.

Atkins, S.L. and Gibeling, J.C. (1995), *A Finite Element Model of the Effects of Primary Creep in an Al-SiC Metal Matrix Composite*, Metall. Mater. Trans., **26A,** 3067-3079.

Avery, D.H. and Backofen, W.A. (1964), *A Structural Basis for Superplasticity*, Trans. ASM, **58,** 551-562.

Bao, G., Hutchinson, J.W. and McMeeking, R.M. (1991), *Particle Reinforcement of Ductile Matrices against Plastic Flow and Creep*, Acta metall. mater., **39,** 1871-1882.

Bär, J. (1992), *Einfluß von Temperatur und Mikrostruktur auf die Ausbreitung von Ermüdungsrissen in faserverstärkten Aluminiumlegierungen*, Dissertation, Institut für Metallkunde, Universität Stuttgart, Stuttgart

Bär, J., Klußmann, H.G. and Gudladt, H.J. (1993), *Influence of Fibre-Reinforcement on the Microstructure of an Al-Si-Based Alloy*, Scripta metall. mater., **29,** 787-792.

Bay, R.S. and Tucker, C.L. (1992), *Stereological Measurement and Error Estimates for Three-Dimensional Fiber Orientation*, Polym. Eng. Sci., **32,** 240-253.

Bidlingmaier, T. (1999), *Anwendung der Schallemissionsanalyse zur Charakterisierung der Schädigung in Verbundwerkstoffen mit duktiler Matrix*, Dissertation, Institut für Metallkunde, Universität Stuttgart, Stuttgart

Bidlingmaier, T., Akhizina, S. and Wanner, A. (1999), *Ongoing work*

Bidlingmaier, T., Vogt, D., Wanner, A. and Arzt, E. (1996a), *Schädigungsentwicklung bei der Kriechbeanspruchung einer kurzfaserverstärkten Aluminiumlegierung*, In:

Werkstoffwoche '96, Vol. 7 (Eds. Aldinger, F. and Mughrabi, H.), DGM Informationsgesellschaft mbH, 493-498.

Bidlingmaier, T., Vogt, D., Wanner, A. and Arzt, E. (1996b), *Unpublished Results*

Bidlingmaier, T., Wanner, A. and Arzt, E. (1997), *Charakterisierung des Schädigungsverlaufs in Faserverbundwerkstoffen mittels Zerstörungsfreier Prüfung - Teilprojekt A1*, Sonderforschungsbereich 381, Ergebnisbericht 1994-1997, Teilprojekt A1, Universität Stuttgart, Stuttgart.

Bidlingmaier, T., Wolf, A., Wanner, A. and Arzt, E. (1998), *Einfluß des Vorzeichens der mechanischen Spannung auf das Fließverhalten von kurzfaserverstärkten Metallmatrix-Verbundwerkstoffen*, In: Werkstoffwoche ’98 , DGM Informationsgesellschaft, .

Brechet, Y., Embury, J.D., Tao, S. and Luo, L. (1991), *Damage Initiation in Metal Matrix Composites*, Acta metall. mater., **39,** 1781-1786.

Bressers, J. (1995), *A Code of Practise for the Measurement of Misalignment Induced Bending in Uniaxially Loaded Tension-Compression Test Pieces*, Code of practise, EUR 16138 EN, European Comission, Luxembourg.

Brown, L.M. and Clarke, D.R. (1975), *Work Hardening due to Internal Stresses in Composite Materials*, Acta metall., **23,** 821-830.

Ceretti, M., Kocsis, M. and Lodini, A. (1994), *Analysis of Internal-Stress Relaxation in an Al/SiC Composite by Neutron-Diffraction*, Sci. Eng. Comp. Mater., **3,** 167-176.

Chen, K.-C. and Chao, C.-G. (1995), *Effect of delta Alumina Fibers on the Aging Characteristics of 2024-Based Metal-Matrix Composites*, Metall. Mater. Trans., **26A,** 1035-1943.

Chen, Y.C. and Daehn, G.S. (1991), *The Deformation of an Aluminum-Silicon Eutectic Alloy under Thermal Cycling Conditions*, Metall. Trans., **22A,** 1113-1115.

Christman, T., Needleman, A. and Suresh, S. (1989), *An Experimental and Numerical Study of Deformation in Metal-Ceramic Composites*, Acta metall., **37,** 3029-3050.

Clyne, T.W. and Withers, P.J. (1993), *An Introduction to Metal Matrix Composites,* Cambridge University Press, Cambridge.

Cottrell, A.H. (1955), *Creep of Alpha Uranium During Irradiation or Thermal Cycling*, Harwell Report, AERE M/M 102, A.E.R.E. Harwell (UK), .

Courtney, T.H. (1990), *Mechanical Behavior of Materials,* McGraw-Hill, Singapore.

Daehn, G.S. and Gonzalez-Doncél, G. (1989), *Deformation fo Whisker-Reinforced Metal-Matrix Composites under Changing Temperature Conditions*, Metall. Trans., **20A,** 2355-2368.

Dakshinamurthy, V.K. and Pollock, T.M. (1998), *Numerical Modelling of the Creep Behavior of Unidirectional Eutectic Composites*, Acta mater., **46,** 2859-2876.

Davis, L.C. and Allison, J.E. (1995), *Micromechanics Effects in Creep of Metal-Matrix Composites*, Metall. Mater. Trans., **26A,** 3081-3089.

Daymond, M.R. and Withers, P.J. (1996), *A Synchrotron Radiation Study of Transient Internal Strain Changes During the Early Stages of Thermal Cycling in an Al/SiC$_W$ MMC*, Scripta mater., **35,** 1229-1234.

Daymond, M.R. and Withers, P.J. (1997), *In Situ Monitoring of Thermally Cycled Metal Matrix Composites by Neutron Diffraction and Laser Extensometry*, Appl. Comp. Mater., **4,** 375-93.

De Silva, A.R.T. (1968), *A Theoretical Analysis of Creep in Fibre Reinforced Composites*, J. Mech. Phys. Solids, **16,** 169-186.

Derby, B. (1985), *Internal Stress Superplasticity In Metal Matrix Composites*, Scripta metall., **19,** 703-707.

Derby, B. (1991), *Thermal Cycling of Metal Matrix Composites*, In: 12th Risø International Symposium on Materials Science: Metal Matrix Composites - Processing, Microstructure and Properties (Eds. Hansen, N., Juul Jensen, D., Leffers, T., Lilholt, H., Lorentzen, T., Pedersen, A. S., Pedersen, O. B. and Ralph, B.), Risø National Laboratory Roskilde, Denmark, 31-49.

Derby, B. and Ashby, M.F. (1987), *A Microstructural Model for Primary Creep*, Acta metall., **35,** 1349-1353.

Dieter, G.E. (1988), *Mechanical Metallurgy,* McGraw-Hill, London.

Dlouhy, A. and Eggeler, G. (1994), *Recovery Processes and Backflow after Creep Unloading of Short Fibre Reinforced, Squeeze Cast Aluminium Alloys*, Scripta metall. mater., **30,** 1161-1165.

Dlouhy, A., Eggeler, G. and Merk, N. (1995), *A Micromechanical Model for Creep in Short Fibre Reinforced Aluminium Alloys*, Acta metall. mater., **43,** 535-550.

Dlouhy, A., Merk, N. and Eggeler, G. (1993), *A Microstructural Study of Creep in Short-Fiber-Reinforced Aluminum-Alloys*, Acta metall. mater., **41,** 3245-3256.

Dobson, S.J. and Greenwood, G.W. (1996), *Primary Creep and Anelastic Behaviour of Aluminium at Low Strains and Temperatures below 0.45 T_m*, Mater. Sci. Tech., **12,** 139-142.

Dragone, T.L. and Nix, W.D. (1990), *Geometric Factors Affecting the Internal Stress Distribution and High Temperature Creep Rate of Discontinuous Fiber Reinforced Metals*, Acta metall. mater., **38,** 1941-1953.

Dragone, T.L. and Nix, W.D. (1992), *Steady State and Transient Creep Properties of an Al Alloy Reinforced with Alumina Fibers*, Acta metall. mater., **40,** 2781-2791.

Dunand, D.C. and Bedell, C.M. (1996), *Transformation-Mismatch Superplasticity in Reinforced and Unreinforced Titanium*, Acta mater., **44,** 1063-1076.

Durodola, J.F., Ruiz, C. and Derby, B. (1994), *Uniaxial Creep of Long-Fiber Reinforced Metal-Matrix Composites*, Compos. Engng., **4,** 1241-1255.

Ebert, H. (1971), *Dichte, Ausdehnung und Kompressibilität*, In: Landoldt-Börnstein Eigenschaften der Materie in ihren Aggregatzuständen 1.Teil Mechanisch-Termische Zustandsgrößen (Ed. Schäfer, K.) Springer Verlag, Berlin, pp. 429.

Eggeler, G. (1994), *On the Mechanism of Creep in Short-Fiber-Reinforced Aluminum-Alloys*, Z. Metall., **85,** 39-46.

Elfishawy, K.F. and Daehn, G.S. (1995), *An Approach to the Design of Composites for Service at Elevated and Nonsteady Temperatures*, Metall. Mater. Trans., **26A,** 3091-3105.

Elzey, D.M. (1989), *Mechanismen der Ermüdung und Kriech-Ermüdung in dispersionsgehärteten Superlegierungen,* VDI Verlag, Stuttgart, Germany.

Ericsson, T., Ohlsson, A. and Persson, C. (1993), *Measurements And Prediction Of Residual Stress In Metal Matrix Composites*, In: Advances in X-Ray Analysis, Vol. 36 (Ed. Gilfrich, J. V.) Plenum Press, New York, pp. 461-471.

Eshelby, J.D. (1957), *The Determination of the Stress Field of an Ellipsoidal Inclusion, and Related Problems*, Proc. Roy. Soc., **A241,** 376-396.

Favier, S., Canova, G.R. and Baudelet, B. (1995), *A Micromechanical Incremental Model of Damage in Materials Containing Second Phase Particles*, Acta metall. mater., **43,** 1249-1258.

Finnie, I. and Heller, W.R. (1959), *Creep of Engineering Materials,* McGraw-Hill, New York.

Furness, J.A.G. (1991), *Thermal Cycling Creep of Aluminium Based Composites*, Dissertation, Downing College, University of Cambridge, Cambridge

Furness, J.A.G. and Clyne, T.W. (1991a), *The Application of Scanning Laser Extensometry to Explore Thermal Cycling Creep of Metal Matrix Composites*, Mater. Sci. Eng., **141,** 199-207.

Furness, J.A.G. and Clyne, T.W. (1991b), *Thermal Cycling Creep of Short Fibre MMCs - Measurement and Modelling of the Strain Cycle*, In: 12th Risø International Symposium on Materials Science: Metal Matrix Composites - Processing, Microstructure and Properties (Eds. Hansen, N., Juul Jensen, D., Leffers, T., Lilholt, H., Lorentzen, T., Pedersen, A. S., Pedersen, O. B. and Ralph, B.), Risø National Laboratory Roskilde, Denmark, 349-354.

Gibeling, J.C. and Nix, W.D. (1981), *Observations of Anelastic Backflow Following Stress Reductions During Creep of Pure Metals*, Acta metall., **29,** 1769-1784.

Goncales-Doncel, G. and Sherby, O.D. (1996), *Tensile Ductility and Fracture of Superplastic Aluminum-SiC Composites Under Thermal Cycling Conditions*, Metall. Mater. Trans., **27A,** 2837-2841.

Gordon, F.H. and Clyne, T.W. (1993), *Thermal Cycling Creep of Ti-6Al-4V/SiC Monofilament Composites under Transverse Loading*, In: Residual Stresses in Composites - Measurement, Modeling & Effects on Thermo-Mechanical Behavior (Eds. Barrera, E. V. and Dutta, I.), The Minerals, Metals & Materials Soc, 293-304.

Goto, S. and McLean, M. (1991a), *Role of Interfaces in Creep of Fibre-Reinforced MMC - I Continuous Fibres*, Acta metall. mater., **39,** 153-164.

Goto, S. and McLean, M. (1991b), *Role of Interfaces in Creep of Fibre-Reinforced MMC - II Short Fibres*, Acta metall. mater, **39,** 165-177.

Greenwood, G.W. and Johnson, R.H. (1965), *The Deformation of Metals Under Small Stresses during Phase Transformations*, Proc. R. Soc. Metals A, **283,** 403.

Hegeler, H., Buschmann, R. and Elstner, I. (1994), *Herstellung von faserverstärkten Leichtmetallen unter Verwendung von Faserkeramischen Formkörpern (Preforms); Herstellung, Eigenschften und Anwendung von Kurz- und Langfaserpreforms*, In: Metallische Verbundwerkstoffe (Ed. Kainer, K. U.), DGM Informationsgesellschaft mbH, Oberursel, 101-116.

Henning, W. and Neite, G. (1994), *Eigenschaften und Anwendungen von kurzfaserverstärkten Aluminiumlegierungen*, In: Metallische Verbundwerkstoffe (Ed. Kainer, K. U.), DGM Informationsgesellschaft mbH, Oberursel, 169-191.

Hong, S.H., Sherby, O.D., Divecha, A.P., Karmarkar, S.D. and MacDonald, B.A. (1988), *Internal Stress Superplasticity in 2024 Al-SiC Whisker Reinforced Composites*, J. Comp. Mater., **22,** 102-123.

Humsicker, H.Y., Mondolfo, L.F. and Tomblin, P.A. (1979), *Properties of Pure Metals - Aluminum*, In: Metals Handbook Ninth Edition Volume 2 – Properties and Selection: Nonferrous Alloys and Pure Metals, Vol. 2 (Eds. Chubberly, W. H., Baker, H., Benjamin, D., Unterweiser, P. M., Kirkpatrick, C. W., Knoll, V. and Niemann, K.) American Society for Metals, Metals Park, Ohio, pp. 715.

ICI (1982), *Saffil RF Data Sheet*, Data Sheet, ICI Mod Division, Runcorn, Cheshire, UK.

Johannesson, B. and Pedersen, O.B. (1998), *Analytical Determination of the Average Eshelby Tensor for Transversely Isotropic Fiber Orientation Distributions*, Acta mater., **46,** 3165-3173.

Johannesson, S. and Ogin, S.L. (1995), *Internal Stresses in Planar Random Fibre Aluminium Composites-I. Tensile Tests and Cyclic Bauschinger Experiments at Room Temperature and 77K*, Acta metall. mater., **43,** 4337-4348.

Joos, R. (1995), *Thermomechanische Ermüdung von ODS-Superlegierungen,* VDI Verlag, Stuttgart, Germany.

Kelly, A. and Street, K.N. (1972), *Creep of Discontinuous Fibre Composites II - Theory for the Steady State*, Proc. Roy. Soc., **A328,** 283-293.

Kimmerle, W.L., Nardone, V.C. and Tien, J.K. (1986), *Cyclic Creep and Anelastic Relaxation of an ODS Superalloy*, Metall. Trans., **17A,** 1577-1583.

Kimmerle, W.L., Nardone, V.C. and Tien, J.K. (1987), *The Effect of the Lower Stress Level on the Cyclic Creep Behavior of an ODS Superalloy*, Metall. Trans., **18A,** 1029-1033.

Kitazono, K. and Sato, E. (1999), *Internal Stress Superplasticity in Directionally Solidified Al-Al_3Ni Eutectic Composite*, Acta mater., **47,** 135-142.

Kitazono, K., Sato, E. and Kuribayashi, K. (1996), *Internal Stress Superplasticity Induced by Thermal Cycling in Metal Matrix Composites*, Mat. Trans., JIM, **37,** 345-348.

Komenda, J. and Henderson, P.J. (1993), *Quantification of Fiber Distribution in a Metal Matrix Composite and Its Effect on Creep-Rupture Properties*, Scripta metall. mater., **28,** 553-558.

Le Flour, J.C. and Locicéro, R. (1987), *Influence of Internal Stresses Induced by Thermal Cycling on the Plastic Deformation Resistance of an Al/SiC Composite Material*, Scripta metall., **21,** 1071-1076.

Lee, J.K. and Nam, S.W. (1988), *Effects of Cyclic Stress on the Creep Behaviour and Dislocation Microstructure of Pure Copper in the Temperature Range 0.4 to 0.5 T_m*, J. Mater. Sci., **23,** 2051-2058.

Li, H., Li, J.B., Wang, Z.G., Chen, C.R. and Wang, D.Z (1998), *Dependence of Thermal Residual Stress on Temperature in a SiC Particle Reinforced 6061 Al Alloy*, Metall. Mater. Trans., **29A,** 2001-2009.

Liu, P.L., Wang, Z.G., Toda, H. and Kobayashi, T. (1997a), *Effect Of Cyclic Stress On the High Temperature Creep Behavior Of SiCw/6061Al Composite*, Scripta mater., **36,** 807-812.

Liu, P.L., Wang, Z.G., Toda, H. and Kobayashi, T. (1997b), *Effect Of Frequency On Cyclic Creep Of SiCw/6061Al Composite At High Temperatures*, J. Mater. Sci. Letters, **16,** 1603-1605.

Liu, X.C. and Bathias, C. (1994), *Creep features of Al2O3-Al alloy composites*, J. Mater. Sci., **29,** 4618-4624.

Llorca, J. (1995), *An Analysis of the Influence of Reinforcement Fracture on the Strength of Discontinously-Reinforced MMC*, Acta metall. mater., **43,** 181-192.

Lobb, R.C., Sykes, E.C. and Johnson, R.H. (1972), *The Superplastic Behavior of Anisotropic Metals Thermally Cycled Under Stress*, Metal Sci. J., **6,** 33-39.

Majumdar, S., Singh, J.P., Kupperman, D. and Krawitz, A.D. (1991), *Application of Neutron-Diffraction to Measure Residual Strains in Various Engineering Composite-Materials*, J. Eng. Mater. Tech., **113,** 51-59.

McLean, D (1972), *Viscous Flow of Aligned Composites*, J. Mater. Sci., **7,** 98-104.

McLean, M. (1994), *Creep of Composites*, In: Concise Encyclopedia of Composite Materials (Ed. Kelley, A.) Pergamon, pp. 67-69.

Mileiko, S.T. (1970), *Steady State Creep of a Composite Material with Short Fibres*, J. Mater. Sci., **5,** 254-261.

Mishra, R.S. and Pandey, A.B. (1990), *Some Observations on the High-Temperature Creep Behaviour of 6061Al-SiC Composites*, Metall. Trans. A, **21A,** 2089-2090.

Mlekusch, B. (1999), *Fibre Orientation in Short-Fibre-Reinforced Thermoplastics II: Quantitative Measurements by Image Analysis*, Compos. Sci. Techn., **59,** 547-560.

Mori, T., Tanaka, K., Nakasone, Y., Huang, J. and Taya, M. (1997), *Creep of a metal matrix composite with or without diffusion and sliding on matrix/reinforcement interfaces*, Key Engineering Materials, **127-131,** 1145-1152.

Müller-Schwelling, D. and Röhrle, M.D. (1988), *Verstärkung von Aluminiumkolben durch neuartige Verbundwerkstoffe*, Motortechnische Zeitschrift, **49,** 59-62.

Mura, T. (1987), *Micromechanics of Defects in Solids,* Martinus Nijhoff Publishers, Dordrecht.

Nam, H.W. and Han, K.S. (1998), *Creep Rupturte Life Predictions of Short Fiber-Reinforced Metal Matrix Composites*, Metall. Mater. Trans. A, **29A,** 1983-1989.

Nardone, V.C. and Prewo, K.M. (1986), *On the Strength of Discontinuous Silicon Carbide Reinforced Aluminium Composites*, Scripta metall., **20,** 43-48.

Nieh, T.G. (1984), *Creep Rupture of a Silicon Carbide Reinforced Aluminum Composite*, Metall. Trans. A, **15A,** 139-146.

Noyan, I.C. and Cohen, J.B. (1987), *Residual Stress - Measurement by Diffraction and Interpretation,* Springer-Verlag, Berlin.

Oding, I.A. (1965), *Creep and Stress Relaxation in Metals,* Oliver and Boyd, Edinburgh and London.

Park, K.T., Lavernia, E.J. and Mohamed, F.A. (1990), *High-Temperature Creep of Silicon Carbide Particulate Reinforced Aluminium*, Acta metall. mater., **38,** 2149-2159.

Paul, J. and Exner, H.E. (1990), *Microstructure and Mechanical Properties of the Age-Hardening Eutectic Aluminium-Silicon Alloy G-AlSi12(CuMgNi)*, Z. Metall., **81,** 816-825.

Pedersen, O.B. (1983), *Thermoelasticity and Plasticity of Composites - I. Mean Field Theory*, Acta metall., **31,** 1795-1808.

Pickard, S.M. and Derby, B. (1990), *The Deformation of Particle Reinforced Metal Matrix Composites During Temperature Cycling*, Acta metall. mater., **38,** 2537-2552.

Pickard, S.M. and Derby, B. (1991), *The Influence of Microstructure on Internal-Stress Superplasticity in Polycrystalline Zinc*, Scripta metall. mater., **25,** 467-472.

Rösler, J., Bao, G. and Evans, A.G. (1991), *The Effects of Diffusional Relaxation on the Creep Strength of Composites*, Acta metall. mater., **39,** 2733-2738.

Sato, E. and Kuribayashi, K. (1993), *A Model of Internal Stress Superplasticity Based on Continuum Micromechanics*, Acta mater., **41,** 1759-1767.

Sato, E., Ookawara, T., Kuribayashi, K. and Kodama, S. (1998), *Steady-State Creep in an Inclusion-Bearing Material by Plastic Accomodation*, Acta mater., **46,** 4153-4159.

Schuh, C. and Dunand, D.C. (1998), *Transformation superplasticity of super α_2 titanium aluminide*, Acta mater., **46,** 5663-5675.

Seitz, T., Bär, J. and Gudladt, H.-J. (1991), *Low-Cycle Fatigue Behaviour of Fibre-Reinforced Al-Si-Based Alloys at Ambient and Elevated Temperatures*, In: 12th Risø International Symposium on Materials Science: Metal Matrix Composites - Processing, Microstructure and Properties (Eds. Hansen, N., Juul Jensen, D., Leffers, T., Lilholt, H., Lorentzen, T., Pedersen, A. S., Pedersen, O. B. and Ralph, B.), Risø National Laboratory Roskilde, Denmark, .

Sherby, O.D., Klundt, R.H. and Miller, A.K. (1977), *Flow Stress, Subgrain Size and Subgrain Stability at Elevated Temperatures*, Metall. Trans. A, **8A,** 843-850.

Soderberg, C.R. (1936), Trans. ASME, **58**.

Sorensen, N. (1991), *Effects of Clustering on the Creep Properties of Whisker Reinforced Aluminium*, In: 12th Risø International Symposium on Materials Science: Metal Matrix Composites - Processing, Microstructure and Properties (Eds. Hansen, N., Juul Jensen, D., Leffers, T., Lilholt, H., Lorentzen, T., Pedersen, A. S., Pedersen, O. B. and Ralph, B.), Risø National Laboratory Roskilde, Denmark, 667-673.

Sorensen, N.J. (1993), *A Planar Model Study of Creep in Metal Matrix Composites with Misaligned Short Fibres*, Acta metall. mater., **41,** 2973-2983.

Tjong, S.C., Ma, Z.Y. and Wang, Z.G. (1999), *Static and Cyclic Creep Behavior of SiC Whisker Reinforced Aluminium Composite*, Mater. Sci. Tech., **15,** 666-672.

Toitot, D., Andrieu, E. and Jarry, P. (1990), *Thermal Ratchetting of a Metal Matrix Composite-Material - Study of the Transient and Steady-States*, Mémoires et Études Scientifiques Revue de Métallurgie, **87,** 761-768.

Tucker, C.L. and Advani, S.G. (1994), *Processing of Short-Fiber Systems*, In: Flow and Rheology in Polymer Composites Manufacturing (Ed. Advani, S.) Elsevier Science, pp. 147-202.

Wakashima, K., Choi, B.H. and Lee, S.H. (1986), *Temperature Cycling-Induced Superplasticity in Metal Matrix Composites*, In: Third Japan-US Conference of Composite Materials, CCM-III (Eds. Kawata, K., Umekawa, S. and Kobayashi, A.), Japan Society for Composite Materials, 579-584.

Weiland, A. and Ericsson, T. (1995), *Elevated temperature X-ray measurement of residual stresses in a fibre reinforced Al alloy*, J. Mater. Sci., **30,** 1046-1052.

Weiland, A., Hultman, L., Wahlstrom, U., Persson, C. and Johannesson, T. (1998), *Internal stress and microstructure of SiC reinforced aluminium alloy 2014*, Acta mater., **46,** 5271-5281.

Weiland, A. and Johannesson, T. (1995), *Residual-Stresses in Fiber-Reinforced and Whisker-Reinforced Aluminum-Alloys During Thermal Cycling Measured by X-Ray-Diffraction*, Mater. Sci. Eng., **190,** 131-142.

Whitehouse, A.F. and Clyne, T.W. (1993), *Cavity Formation During Tensile Straining of Particulate and Short Fibre Metal Matrix Composites*, Acta metall. mater., **41,** 1701-1711.

Whitehouse, A.F. and Winand, H.M.A. (1999), *The Tensile Creep Response of Al-SiC Particulate and Whisker Composites*, Scripta mater., **41,** 817-822.

Whitehouse, A.F., Winand, H.M.A. and Clyne, T.W. (1998), *The Effect of Processing Route and Reinforcement Geometry on Isothermal Creep Behaviour of Particulate and Short Fibre MMCs*, Mater. Sci. Eng., **242,** 57-69.

Withers, P.J., Jensen, D.J., Lilholt, H. and Stobbs, W.M. (1987), *The Evaluation of Internal Stresses in a Short Fibre MMC*, In: ICCM VI / ECCM2 (Eds. Matthews, F., Buskell, N., Hodgkinson, J. and Mortensen, J.), Elsevier, 255-264.

Withers, P.J., Stobbs, W.M. and Pedersen, O.B. (1989), *The Application of the Eshelby Method of Internal Stress Determination to Short Fibre Metal Matrix Composites.*, Acta metall. mater., **37,** 3061-3084.

Wolf, A. (1997), *Untersuchung des Kriechverhaltens der faserverstärkten Gußlegierung M124*, Diplomarbeit, Institut für Metallkunde, Universität Stuttgart, Stuttgart

Wu, M.Y. and Sherby, O.D. (1984), *Superplasticity in a Silicon Carbide Whisker Reinforced Aluminium Alloy*, Scripta metall., **18,** 773-776.

Wu, M.Y., Wadsworth, J. and Sherby, O.D. (1987), *Internals Stress Superplasticity in Anisotropic Polycrystalline Zinc and Uranium*, Metall. Trans., **18A,** 451-462.

Zhang, H.Y., Daehn, G.S. and Wagoner, R.H. (1991), *Simulation of the Plastic Response of Whisker Reinforced Metal Matrix Composites Under Thermal Cycling Conditions*, Scripta metall. mater., **25,** 2285-2290.

Zwigl, P. and Dunand, D.C. (1997), *A Non-Linear Model for internal stress superplasticity*, Acta mater., **45,** 5285-5294.

Zwigl, P. and Dunand, D.C. (1998), *Transformation Superplasticity of Iron and Fe/TiC Metal Matrix Composites*, Metall. Mater. Trans., **29A,** 565-575.